

Constitutive Modeling of Soft Sandstone Degradation under Cyclic Conditions

by

Mojtaba Rahimi

A thesis submitted in partial fulfillment of the requirements for the degree of

Doctor of Philosophy
in
Petroleum Engineering

Department of Civil and Environmental Engineering
University of Alberta

© Mojtaba Rahimi, 2014

ABSTRACT

The near wellbore region is subjected to cyclic loads due to repeated changes of the mean effective stress. These repeated loads result in plastic deformation and sanding problems which can occur in injection or production wells. The difficulty is more pronounced in weakly consolidated reservoirs since they are more prone to sanding. Therefore it is required to investigate the material response to cyclic loading.

In this research, the mechanical behaviour of uncemented and cemented sands under monotonic and cyclic loading are studied. Emphasis is placed on the constitutive modeling. A critical state constitutive model which was developed at the University of Alberta for monotonic behavior of cohesionless sands was chosen as the base model.

First with modification of the hardening law, plastic volumetric strain increment and unloading plastic modulus, the original model was modified to describe sand behavior under cyclic loading. The modified model was calibrated and validated against triaxial cyclic loading tests for Fuji River sand, Toyoura sand and Niigata sand. Comparison between the measured and predicted results suggests that the model can capture the main features of sands under cyclic loading. Second the original model was modified for cemented sands. Formulation of the yield function, elastic moduli, plastic modulus, flow rule and other components of the original model were modified. Having incorporated these changes, the radial mapping formulation of bounding surface plasticity was incorporated in the model. The modified model was assessed against monotonic triaxial tests. Third

to simulate the mechanical behaviour of cemented sand/soft sandstone under cyclic loading, some further modifications were incorporated into the model. Destruction of the cementation bonds by plastic deformation was considered as the reason for the mechanical degradation of cemented sands. To model cyclic response, the unloading plastic and elastic moduli were formulated based on those of loading. The proposed model was evaluated against laboratory triaxial tests, and the model agreed with experimental observations. Fourth the application of the proposed constitutive model was ultimately extended to cases that are not under conventional triaxial conditions. This was performed by incorporating the inherent anisotropy and b -parameter into formulation of the proposed model.

ACKNOWLEDGMENTS

I would like to express my greatest appreciation to my supervisor (Professor Dave Chan) and my co-supervisor (Professor Alireza Nouri) who supported me constantly and never endingly throughout my Ph.D. term. Their unparalleled scientific helps, encouragements, and purposeful technical advices were remarkable motivations for me to follow through my research actively. I am deeply grateful of them for their helps and supports in all aspects.

I would like to thank Dr. Reza Imam and Rouzbeh Rasouli for providing technical helps and scientific discussions on the original model. Their helps are highly appreciated.

I acknowledge NSERC and BP for providing funding for this research. I am thankful for their financial support.

I profoundly thank my wife for accompanying me and for tolerating all difficulties encountered during my Ph.D. period. Accomplishing my Ph.D. term was not possible without her collaboration. I thank my parents also for their lasting support. Starting my Ph.D. term was not feasible without their helps.

Ultimately, I thank all those who helped me by any means to pass this chapter of my life.

TABLE OF CONTENTS

CHAPTER 1: INTRODUCTION.....	1
1.1 Sand production.....	1
1.1.1 Sanding in production wells	1
1.1.2 Sanding in injection wells.....	3
1.1.2.1 Injection start-up and shut-in cycles	4
1.1.2.2 Injection pressure	4
1.1.2.3 Backflow	5
1.1.2.4 Cross flow	5
1.1.3 Field observations of sanding	6
1.2 Degradation of weak Sandstone around petroleum wells under cyclic conditions	7
1.3 Determination of the magnitude and direction of in-situ stresses.....	9
1.4 Problem statement and significance	11
1.5 Research objectives	12
1.6 Thesis structure	14
1.7 References	16
CHAPTER 2: LITERATURE REVIEW.....	19
2.1 Introduction	19

2.2 Numerical models of sanding.....	20
2.3 Slow cyclic loading vs. fast cyclic loading	25
2.4 Cyclic loading modeling by classical plasticity framework.....	28
2.5 Bounding surface plasticity concept.....	33
2.5.1 Mapping rule.....	36
2.5.2 Plastic modulus at the image point	37
2.5.3 Plastic modulus at the current stress point.....	38
2.6 Cyclic plasticity theories	40
2.6.1 Single surface kinematic hardening theory.....	40
2.6.2 Multi-surface plasticity theory.....	45
2.6.3 Bounding surface plasticity theory	49
2.7 Volume change and stress-strain behaviour of sand and cemented sand....	53
2.8 Methodology	60
2.9 Conclusion.....	62
2.10 References	63
CHAPTER 3: CONSTITUTIVE MODEL FOR CYCLIC BEHAVIOUR OF COHESIONLESS SAND	71
3.1 Introduction	71
3.2 Brief overview of the original model	73
3.3 A bounding surface model for the cyclic response of sand.....	76

3.3.1 Elasticity	76
3.3.2 Stress-dilatancy relationship	76
3.3.3 Loading surface and bounding surface	76
3.3.4 Stress-strain relationships	79
3.3.5 Loading criterion and loading direction	81
3.4 Performance of the proposed bounding surface model	81
3.4.1 Drained cyclic loading test on Fuji River sand	82
3.4.2 Drained and undrained cyclic loading tests on Toyoura sand	83
3.4.3 Undrained cyclic loading test on Niigata sand	87
3.5 Conclusion	89
3.6 References	90

**CHAPTER 4: A BOUNDING SURFACE CONSTITUTIVE MODEL FOR
CEMENTED SAND UNDER MONOTONIC LOADING 94**

4.1 Introduction	94
4.2 Brief description of the original model	97
4.3 A critical state framework for bonded sand	101
4.3.1 Elasticity	105
4.3.2 Yield function	106
4.3.3 Flow rule	107
4.3.4 Hardening modulus	109

4.3.5 Material parameters	110
4.4 A bounding surface model for cemented sand	111
4.4.1 Elasticity and flow rule.....	111
4.4.2 Bounding and loading surfaces.....	111
4.4.3 Projection rule.....	114
4.4.4 Hardening modulus.....	115
4.5 Assessment of the proposed bounding surface model	116
4.6 Conclusion.....	123
4.7 References	124
CHAPTER 5: CONSTITUTIVE MODEL FOR MONOTONIC AND CYCLIC RESPONSE OF LOOSELY CEMENTED SAND FORMATIONS	128
5.1 Introduction	128
5.2 Cemented sand	134
5.3 Brief review of the original model	136
5.4 A two-surface model for cemented sand.....	140
5.4.1 Bounding and loading surfaces.....	141
5.4.2 Elastic properties	144
5.4.3 Flow rule.....	145
5.4.4 Stress-strain relationships	146

5.4.5 Material parameters	148
5.4.6 Model performance.....	150
5.5 Conclusion.....	157
5.6 References	157
CHAPTER 6: INHERENT FABRIC ANISOTROPY	161
6.1 Introduction	161
6.2 Fabric tensor	162
6.3 Anisotropic state variable.....	163
6.4 Modification of the constitutive model using anisotropic state variable...	168
6.5 Model performance	169
6.6 Conclusion.....	188
6.7 References	189
CHAPTER 7: CONCLUSIONS	191
7.1 Summary and conclusions.....	191
7.2 Recommendations	193
APPENDIX A: 1D ANALYSIS OF CLASSICAL ELASTO-PLASTIC CONSTITUTIVE MODEL.....	195
A.1 Isotropic Hardening.....	195
A.1.1 Elasticity	195
A.1.2 Yield function	196

A.1.2.1 Drucker-Prager	196
A.1.2.2 Mohr-Coulomb	196
A.1.3 Plastic potential function	197
A.1.4 Hardening law	198
A.1.5 Stress-strain relationships	199
A.1.6 Verification	202
A.1.7 Results	203
A.2 Kinematic Hardening	205
A.2.1 Elasticity	205
A.2.2 Yield function	205
A.2.3 Plastic potential function	206
A.2.4 Stress-strain relationships	206
A.2.4.1 Prager's rule	207
A.2.4.2 Armstrong and Frederick's rule	207
A.2.4.3 Ziegler's rule	207
A.2.4.4 Derivations	208
A.2.4.5 Model predictions	209
APPENDIX B: GENERAL FORMULATION OF THE CRITICAL STATE	
CONSTITUTIVE MODEL	215
B.1 Constitutive modeling	215

B.2 Model ingredients	219
B.2.1 Bounding surface and loading surface	220
B.2.2 Flow rule	224
B.2.3 Hardening rule.....	225
B.2.4 Elastic properties.....	226
B.3 Model Calibration.....	226
BIBLIOGRAPHY	230

LIST OF TABLES

Table 3-1 Material parameters used for calibration of Fuji River sand, Toyoura sand and Niigata sand	82
Table 4-1 Material parameters used for the calibration of cemented Ottawa sand (1%), $p^* = p + pt$	117
Table 4-2 Material parameters used for calibration of artificially cemented Portaway sand (5%)	120
Table 5-1 Material parameters used for calibration in Figs. 8-9, $p^* = p + pt$...	156
Table 5-2 Material parameters used for calibration in Figs. 10-12, $p^* = p + pt$	156
Table 6-1 Material parameters used for calibration of undrained HC tests on Toyoura sand.....	171
Table 6-2 Material parameters used for calibration of hypothetical drained HC tests on cemented sand in Figs. 6-23 to 6-24	182
Table A2.1 Material parameters used for calibration of cyclic loading using pure kinematic hardening law (2 cycles). N indicates number of cycles.....	210
Table A2.2 Material parameters used for calibration of cyclic loading using pure kinematic hardening law (4 cycles)	213

LIST OF FIGURES

Fig. 1-1 Relationships needed to be addressed for full description of a mechanical process.....	16
Fig. 2-1 Perfect hysteresis loop in a two-way cycle	29
Fig. 2-2 Predicted response of a normally consolidated clay to undrained cyclic loading by Cam Clay [Wood 1990]	30
Fig. 2-3 Plastic loading under constant p stress path in compression plane for Cam Clay model. URL and ICL are abbreviations for unloading-reloading line and isotropic compression line	32
Fig. 2-4 Typical response of a normally consolidated clay/loose sand observed under undrained cyclic loading [Wood 1990].....	32
Fig. 2-5 Schematic illustration of the bounding lines in uniaxial stress-plastic strain curve [modified after Dafalias and Popov 1977].....	35
Fig. 2-6 A typical bounding surface model in conventional triaxial stress space for cohesionless sands	35
Fig. 2-7 Isotropic hardening for an assumed circular yield surface.....	41
Fig. 2-8 Kinematic hardening for an assumed circular yield surface	42
Fig. 2-9 Combined isotropic-kinematic hardening for an assumed circular yield surface.....	42
Fig. 2-10 Schematic representation of the approach used for single surface kinematic hardening.....	45

Fig. 2-11 Schematic representation of assumed movement of a circular yield locus during cyclic loading.....	45
Fig. 2-12 Mroz's Translation rule.....	47
Fig. 2-13 Effect of initial void ratio on volume changes of sands during drained triaxial tests.....	54
Fig. 2-14 Pore pressure generation during undrained triaxial tests on loose and dense sands.....	55
Fig. 2-15 Typical stress-strain curves for sands under drained triaxial tests.....	57
Fig. 2-16 Typical stress-strain curves for sands under undrained triaxial tests....	58
Fig. 3-1 Unloading and reloading from an elasto-plastic state: idealized stress-strain curve using traditional plasticity.....	72
Fig. 3-2 Schematic representation of change in position and size of the loading surface and bounding surface during elasto-plastic deformation.....	78
Fig. 3-3 Measured and predicted response of Fuji River sand during drained cyclic loading.....	83
Fig. 3-4 Measured and predicted response of Toyoura sand during drained cyclic loading with an initial void ratio of 0.845 and confining pressure of 98 <i>KPa</i>	85
Fig. 3-5 Measured and predicted behaviour of Toyoura sand during drained cyclic loading with an initial void ratio of 0.865 and confining pressure of 98 <i>KPa</i>	86

Fig. 3-6 Measured and predicted response of Toyoura sand during undrained cyclic loading with an initial void ratio of 0.798 and confining pressure of 98 <i>KPa</i>	87
Fig. 3-7 Measured and predicted response of Niigata sand during undrained cyclic loading	89
Fig. 4-1 Idealized representation of compression response for bonded soil	102
Fig. 4-2 Effect of cement content on the initial yield point of cement treated Portaway sand [modified after Marri 2010]	102
Fig. 4-3 Effect of cement content on the location of the initial yield point (small bold circles): a) triaxial tests with confining pressure of 1 <i>MPa</i> b) triaxial tests with confining pressure of 4 <i>MPa</i> [Marri 2010]	104
Fig. 4-4 Schematic representation of the modified yield surface	105
Fig. 4-5 Schematic representation of the proposed bounding surface model within a conventional triaxial p, q space	113
Fig. 4-6 Radial mapping rule for a conventional triaxial p, q space	114
Fig. 4-7 Measured and predicted response of cemented Ottawa sand for deviator stress vs. axial strain curve under different cement contents	118
Fig. 4-8 Measured and predicted response of cemented Ottawa sand for void ratio vs. axial strain curve under different cement contents	119
Fig. 4-9 Measured and predicted response of cemented Ottawa sand for volumetric strain vs. axial strain curve under different cement contents	119

Fig. 4-10 Measured and predicted response of cemented Portaway sand for deviator stress vs. axial strain curve under different cement contents.....	122
Fig. 4-11 Measured and predicted response of cemented Portaway sand for volumetric strain vs. axial strain curve under different cement contents.....	122
Fig. 4-12 Predicted response of cemented Portaway sand for void ratio vs. axial strain curve under different cement contents	123
Fig. 5-1 Unloading and reloading from an elasto-plastic state: perfect hysteresis loop in a complete cycle.....	129
Fig. 5-2 Single frictional block on a flat surface and corresponding force displacement response	130
Fig. 5-3a Four blocks in series where T is increased until movement occurs in all of the blocks	132
Fig. 5-3b T is decreased until the block 4 starts to move to the right.....	132
Fig. 5-3c T decreases to zero during unloading	132
Fig. 5-3d T increases during reloading	132
Fig. 5-4 Force displacement response of block 4 in the four-block system connected by springs.....	133
Fig. 5-5 Typical UESP in monotonic triaxial compressive loading on loose sands	137
Fig. 5-6 Schematic representation of the modified yield surface	141

Fig. 5-7 Schematic representation of the loading and bounding surfaces at the start of loading (solid surfaces) and immediately after plastic loading starts (dashed surfaces). In addition to change of position, size of two surfaces also changes with further plastic loading (isotropic hardening). Kinematic hardening has been significantly magnified for better illustration	142
Fig. 5-8 Measured and predicted response of Tehran Alluvium cemented sand for samples with 3% cement content	151
Fig. 5-9 Measured and predicted response of a slightly weathered rock under monotonic loading	152
Fig. 5-10 Measured and predicted response of a cemented carbonate sand in a triaxial drained cyclic compression test	153
Fig. 5-11 Measured and predicted response of rufous sandstone under a triaxial drained cyclic compression test	154
Fig. 5-12 Prediction of rufous sandstone behaviour using 1D model (reloading elastic moduli are defined similar to those of unloading conditions)	155
Fig. 6-1 Variations of anisotropic parameter A (vertical axis) with α and b (Rasouli 2010).....	167
Fig. 6-2 Schematic representation of hollow cylinder apparatus (Yoshimine et. al. 1998)	168
Fig. 6-3 Observed and predicted undrained response for deviator stress vs. shear strain curve under $b = 0$ and $\alpha = 00$ to 450	171

Fig. 6-4 Observed and predicted undrained response for deviator stress vs. mean effective stress curve under $b = 0$ and $\alpha = 00$ to 450.....	172
Fig. 6-5 Observed and predicted undrained response for deviator stress vs. shear strain curve under $b = 0.25$ and $\alpha = 00$ to 300.....	172
Fig. 6-6 Observed and predicted undrained response for deviator stress vs. mean effective stress curve under $b = 0.25$ and $\alpha = 00$ to 300.....	173
Fig. 6-7 Observed and predicted undrained response for deviator stress vs. shear strain curve under $b = 0.5$ and $\alpha = 150$	173
Fig. 6-8 Observed and predicted undrained response for deviator stress vs. mean effective stress curve under $b = 0.5$ and $\alpha = 150$	174
Fig. 6-9 Observed and predicted undrained response for deviator stress vs. shear strain curve under $b = 0.75$ and $\alpha = 300$ to 450	174
Fig. 6-10 Observed and predicted undrained response for deviator stress vs. mean effective stress curve under $b = 0.75$ and $\alpha = 300$ to 450	175
Fig. 6-11 Observed and predicted undrained response for deviator stress vs. shear strain curve under $b = 1.0$ and $\alpha = 450$	175
Fig. 6-12 Observed and predicted undrained response for deviator stress vs. mean effective stress curve under $b = 1.0$ and $\alpha = 450$	176
Fig. 6-13 Predicted drained behaviour for deviator stress vs. shear strain curve under $b = 0$ and $\alpha = 00$ to 450.....	176

Fig. 6-14 Predicted drained behaviour for volumetric strain vs. shear strain curve under $b = 0$ and $\alpha = 00$ to 450.....	177
Fig. 6-15 Predicted drained behaviour for deviator stress vs. shear strain curve under $b = 0.25$ and $\alpha = 00$ to 300	177
Fig. 6-16 Predicted drained behaviour for volumetric strain vs. shear strain curve under $b = 0.25$ and $\alpha = 00$ to 300	178
Fig. 6-17 Predicted drained behaviour for deviator stress vs. shear strain curve under $b = 0.5$ and $\alpha = 150$	178
Fig. 6-18 Predicted drained behaviour for volumetric strain vs. shear strain curve under $b = 0.5$ and $\alpha = 150$	179
Fig. 6-19 Predicted drained behaviour for deviator stress vs. shear strain curve under $b = 0.75$ and $\alpha = 300$ to 450	179
Fig. 6-20 Predicted drained behaviour for volumetric strain vs. shear strain curve under $b = 0.75$ and $\alpha = 300$ to 450	180
Fig. 6-21 Predicted drained behaviour for deviator stress vs. shear strain curve under $b = 1.0$ and $\alpha = 450$	180
Fig. 6-22 Predicted drained behaviour for volumetric strain vs. shear strain curve under $b = 1.0$ and $\alpha = 450$	181
Fig. 6-23 Sensitivity analysis for a cemented sand under HC tests with $\alpha = 00183$	
Fig. 6-24 Sensitivity analysis for a cemented sand under HC tests with $b = 0.25$	184

Fig. 6-25 Sensitivity analysis for cyclic HC tests with $\alpha = 0$ and $b = 0$ & 0.25	186
Fig. 6-26 Sensitivity analysis for cyclic HC tests with $\alpha = 0$ and $b = 0.25$ & 0.5	187
Fig. 6-27 Cohesion degradation during cyclic HC test with $\alpha = 0$ and $b = 0$..	188
Fig. A1-1 Linear isotropic deviator hardening law.....	198
Fig. A1-2 Schematic representation of isotropic hardening with friction angle and cohesion as hardening parameters.....	199
Fig. A1-3 The Mohr circle in $\tau - \sigma_n$ plane	203
Fig. A1-4 Deviator stress vs. deviator strain for hypothetical conventional drained triaxial compression test	204
Fig. A1-5 Deviator stress vs. axial strain for hypothetical conventional drained triaxial compression test	204
Fig. A1-6 Deviator stress vs. radial strain for hypothetical conventional drained triaxial compression test	204
Fig. A1-7 Volumetric strain vs. deviator strain for hypothetical conventional drained triaxial compression test	205
Fig. A1-8 Volumetric strain vs. axial strain for hypothetical conventional drained triaxial compression test	205
Fig. A2-1 Piecewise calibration of cyclic loading using Ziegler's pure kinematic hardening law	210

Fig. A2-2 Calibration of cyclic loading using Armstrong and Frederick's pure kinematic hardening rule with confining pressure of 3.45 MPa	211
Fig. A2-3 Movement of the yield locus during elastoplastic cyclic loading with confining pressure of 3.45 MPa	211
Fig. A2-4 Volumetric behaviour till the constant shear stress (for two complete cycles)	211
Fig. A2-5 Plastic volumetric strain during cyclic loading till the constant shear stress.....	212
Fig. A2-6 Plastic shear strain during cyclic loading till the constant shear stress	212
Fig. A2-7 Calibration of cyclic loading using Armstrong and Frederick's pure kinematic hardening rule with confining pressure of 13.79 MPa	213
Fig. A2-8 Movement of the yield locus during elastoplastic cyclic loading with confining pressure of 13.79 MPa	213
Fig. A2-9 Volumetric behaviour of the sample during cyclic loading	214
Fig. A2-10 Plastic volumetric strain during cyclic loading	214
Fig. B2-1 The loading surface in principal stress space (assume coordinate directions coincide with the principal directions).....	222

CHAPTER 1

INTRODUCTION

1.1 Sand production

Sand production (sanding) phenomenon occurs in two stages [Wu et. al. 2005, Servant et. al. 2007, Nouri et. al. 2009]:

- 1) Complete mechanical degradation of the rocks around the cavity (open hole or perforation) and hence, separation of the sand particles from the failed rock structure.
- 2) Transport of the detached sand particles into the wellbore by drag forces which come from pressure gradient induced fluid flow.

Completion strategy and production development plan for wells of a given reservoir can be optimized by predicting the locations and conditions that lead to the onset of sand production [Vaziri et. al. 2007, FJar et. al. 2008]. The sanding criteria used in sand models to predict onset of sand production mainly include shear failure, tensile failure, critical plastic deformation, and critical pressure draw-down [Nouri et. al. 2006]. These criteria are used to investigate the first stage of sanding (i.e. rock mechanical degradation). Erosion base criteria are used to study the second stage of sanding (i.e. mobilization of sand particles) [Vardoulakis et. al. 1996, Vardoulakis and Papamichos 2003]. Sand production can occur in both production and injection wells. They are briefly discussed here.

1.1.1 Sanding in production wells

The simultaneous movement of sand and reservoir fluids towards the production wells will occur at some points during the production life of most of worldwide sandstone reservoirs. Sand production is a major challenge in the petroleum industry due to its adverse effects on well performance and equipment. It costs the oil and gas industry tens of billions of dollars every year [Acock et. al. 2004]. The

historical background of sand production dates back to the 1900's when water wells were completed with sand control equipment [Nasr and Edbieb 2012]. The amount of produced solids ranges from insignificant, a few grams per cubic meter of reservoir fluids, causing slight problems to catastrophic resulting in choking and filling of the borehole which is called sand up [Veeken et. al. 1991, FJar et. al. 2008, Rahmati et. al. 2013]. Although most of solid production comes from sandstone reservoirs, carbonate reservoirs can also produce solids [FJar et. al. 2008, Bellarby 2009].

Borehole instability, formation collapse, plugging of the perforations, reduction in reservoir permeability and porosity due to blockage of pore space by mobile sands, erosion and failure of production pipelines and surface facilities, reduction in efficiency of the surface separators, additional costs of cleanup operation, and deferred production and also environmental problems with sand disposal are some adverse effects of sand production [Mathis 2003, FJar et. al. 2008, Rahmati et. al. 2013]. Justifying additional costs due to sand production becomes a greater problem during the life time of a reservoir due to decreasing trend of its reserve. To avoid the negative consequences of sand production, the preventive measure is a critical consideration in zones where there is high possibility for sand production. Screens and gravel packs which support wellbore wall and act as filters for produced sand are common approaches [Mathis 2003, FJar et. al. 2008]. However these methods are costly and usually lead to low productivity [FJar et. al. 2008]. Therefore, installing downhole sand control equipment may not always be the best solution for economic consideration of a petroleum project [Mathis 2003]. Strengthening of the wellbore wall with injection of a chemical agent, like resin, is also a sand control technique for open hole [Mathis 2003, FJar et. al. 2008]. The cased and perforated completion is used for weak formations to support well walls. However, application of this technique for very weak formations is risky because of the potential for the perforation collapse [Rahmati et. al. 2013]. Another well-known technique is frac packing in which a fracture from the well into the formation is created and then filled with proppants. Hydrocarbons are produced through highly permeable fracture while the

proppants resist the passage of sand grains and closure of the fracture [FJar et. al. 2008]. Additional completion costs and uncertainty in effective fracturing are paramount drawbacks of the frac pack operation [FJar et. al. 2008]. The selective perforating along stronger intervals combined with vertical fracturing is sometimes practiced to prevent sand production from weak intervals. This may be a possible solution provided that no significant barrier exists against vertical fracture propagation, otherwise the weak intervals remain unrecovered [Mathis 2003]. Utilization of an optimum perforation strategy (i.e. oriented perforation with smaller shots and large spacing) along the most stable direction is a suitable technique [Zoback 2007]. This requires the knowledge of in-situ stress directions and magnitudes. The perforations clearly should not be made perpendicular to the maximum horizontal in-situ stress since this is the direction of wellbore break out and high compressive stress [Zoback 2007].

1.1.2 Sanding in injection wells

Little attention has been dedicated to sanding problems in injection wells (injectors) in contrast to more reported studies of sanding in production wells. Sand production in injectors often goes on unnoticed until it is too late, i.e. when sand covers the perforated intervals, since there is usually no systematic monitoring of sanding in injectors [Vaziri et. al. 2007]. One major reason for the lack of enough research in the injectors probably comes from the negative pressure drawdown in injection wells. Therefore they are rarely back produced to display any sand in surface [Santarelli et. al. 1998]. This causes the near wellbore region in the injectors to be under high pore pressures and low effective stresses [Vaziri et. al. 2007]. Excess pore pressure is dissipated during shut-in period leading to increase in effective stresses. Hence, the rock around the cavity is exposed to repeated changes of mean effective stress. Additional damage is added to the rock matrix in every cycle, implying that the cementation in poorly consolidated formations can be totally destroyed by cycles of injection and shut-ins. Although fluid injection which acts against the formation provides enough force and pressure that prevent mobilization of failed sand grains [Bellarby 2009],

it gives rise to consistent loss of the rock strength. This occurs due to chemical reactions which take place by virtue of incompatibility in temperature, and pH of the injected fluid and formation fluids. The chemical reactions can result in dissolution and/or weakening of the cementation bonds especially if the cementation is clay rich [Skjaerstein et. al. 1997, Wu et. al. 2005, Vaziri et. al. 2007]. Capillary cohesion is also lost by increase in water saturation.

The factors affecting sanding in the injection wells include injection start-up and shut-in cycles, injection pressure, backflow and cross flow of injection/reservoir fluids. These factors are discussed here.

1.1.2.1 Injection start-up and shut-in cycles

In general, sanding in injectors usually occurs during or immediately after injection shut-ins [Morita et. al. 1998, Vaziri et. al. 2007]. Injection stops can be regular (for instance to clean up the perforations) or irregular (unplanned). The uncontrolled shut-ins of injection pumps take place in the case of unpredictable incident (i.e. dramatic reduction in injectivity) or loss of power during which pumps stop in few seconds [Vaziri et. al. 2007]. The rate of choke closure is small in controlled/planned shut-in leading to small changes in the flow velocity. However injection pump stops in a few seconds during uncontrolled/unplanned shut-in resulting in dramatic change in the flow velocity [Sadrpanah et. al. 2005, Vaziri et. al. 2007]. The so-called water hammer cyclic pressure pulses will be generated as a consequence of the rapid shut-ins [Jardine et. al. 1993, Santarelli et. al. 1998, Santarelli et. al. 2011]. Jardine et. al. (1993) discusses advantages and disadvantages of hard and soft shut-in during operational conditions. Note that (production) start-up and shut-in cycles can also occur in the production wells. In summary, slow injection start-up and shut-in cycles and chemical reactions combined with water hammer pressure waves can result in extensive rock degradation, possible liquefaction and massive sanding in injectors.

1.1.2.2 Injection pressure

Increase in injection pressures results in a reduction in mean effective stress and consequently a reduction in particle to particle frictional resistance [Vaziri et. al.

2007]. Higher injection pressures can also result in stronger water hammer wave loads in the case of hard shut-in [Vaziri et. al. 2007].

1.1.2.3 Backflow

Well pressure decreases after injection is halted and approaches static (steady state) reservoir pressure in a homogeneous reservoir. Back flow (flow from the formation to the injection well) can occur if well pressure lags behind the reservoir pressure, i.e. positive pressure drawdown. This can happen intentionally or un-intentionally during the injection process. Intentional back flow is usually performed to clean up the perforations. Back flow can transfer detached sand particles or suspended solids of injected fluid into the injection well and then move them several hundreds of meters above the top perforation [Santarelli et. al. 1998]. In addition to the likelihood for partial or entire blockage of the perforation tunnels, the solid particles tend to plug the pore throats especially in the near wellbore region and thus, to decrease the permeability and injectivity index.

1.1.2.4 Cross flow

Rate of the pressure drop at different depths of injection well after injection stop is not the same along the injected intervals of a heterogeneous reservoir. Layers with higher permeability containing clean sand loss pressure much faster than those with lower permeability containing dirty sand or shale. This leads to cross flow normally from low permeable layers towards the adjacent high permeable layers [Morita et. al. 1998, Vaziri et. al. 2007]. Cross flow is not limited to inter layer flow. Inter-wells and in-travel cross flow may occur as well. The inter-wells cross flow can occur when an injection well within a network of injectors is shut-in creating a pressure differential leading to flow from the surrounding injection wells towards the shut-in well [Sadranah et. al. 2005, Vaziri et. al. 2007, Bellarby 2009]. Major role of cross flow is in transferring the failed sand or eroded clay particles around the cavity [Santarelli et. al. 1998, Bellarby 2009].

If reinjection is procrastinated for several hours to let the produced particles enough time to settle down, they ultimately go down towards the bottom of the

well without leaving any evidence for the operators. This settling continues during subsequent injection stops and restarts until the perforation tunnels are blocked. The bottom line is that the first evidence of sanding in injectors is drastic fall in injection performance or complete loss of all injectivity due to plugging of the perforation intervals. This is unlike sanding in producers which can be detected by different methods such as sand detectors, collecting samples at the surface, and other evidences [FJar et. al. 2008].

1.1.3 Field observations of sanding

Field observations are used to establish a correlation between occurrence or non-occurrence of sand production due to change in influential parameter(s) [Veeken et. al. 1991]. In general, influential factors of sand production can be organized into the following categories [Veeken et. al. 1991]:

a) Geomechanical properties

The factors include the peak strength, vertical in-situ stress, horizontal in-situ stresses, cavity geometry, and depth.

b) Reservoir properties

Pore pressure which change during depletion/injection, viscosity and density of reservoir fluid, heterogeneity, and permeability/porosity which have an impact on the sanding process.

c) Completion procedures

Wellbore orientation and diameter, type of completion (open hole/cased and perforated), perforation strategy (size, density, under/overbalance), and use of sand control techniques can be considered in this category.

d) Production scheme

Production related factors include drawdown pressure, rate and velocity of reservoir fluid flow, shut-in and start-up cycles, fluctuations in rate of production or injection, and water cut.

1.2 Degradation of weak Sandstone around petroleum wells under cyclic conditions

Sand production cannot occur from intact sandstone regardless of intensity of bond between sand grains since the fluid flow cannot provide enough force to detach sand particles from rock structure. This means the cementation between sand grains in the neighborhood of the producing tunnels (cased hole completion) or around wellbore walls (open hole completion) should first disappear. Moreover, operational conditions of well also have to provide sufficient seepage force for displacing sand particles. The destruction of the cementation is caused by the effective stresses around the perforations or well walls [FJar et. al. 2008].

Sandstone is subjected to cyclic loading around petroleum wells during pressure maintenance projects or majority of improved/enhanced oil recovery (IOR/EOR) projects due to repeated changes of mean effective stress [Abdulazeez 1994]. It may experience many cycles due to injection start-up and shut-in cycles and injection/production rate fluctuations. Repeated injection/production shut-ins and start-ups, and fluctuations of injection/production rates give rise to plastic deformation and hence, degradation of the rock structure. This degradation which causes the breakage of cementation bonds and thus, loss of stiffness and strength, potentially can result in sanding problems in injection or production wells. The setback is more severe in loosely cemented sandstone reservoirs, which constitutes considerable portion of the sandstone reservoirs in the world, since they are more susceptible to full cohesion degradation and sanding. Therefore, it is required to understand the behavior of (very) weak sandstone under repeated loads prior to conducting IOR/EOR projects in the field.

Pore pressure fluctuations can occur due to changes in the reservoir pressure via production or injection, meaning sanding may materialize in both injection and production wells. The application can be extended to any injection scenario used for well maintenance by pressurization or for increasing recovery. The largest pore pressure changes occur around wells and decline with distance from the

wells implying that the near wellbore region is of the most interest. Hydrocarbon reservoir itself is also subjected to depletion and re-pressurization, but the intensity is less pronounced than the area around injection/production wells. Note that pore pressure changes do not occur simultaneously and uniformly within reservoir due to reservoir heterogeneity. Therefore effective stress gradient and shear stresses will develop within reservoir and specially around wellbore.

Cyclic steam stimulation (huff-and-puff), cyclic CO₂ injection and water injection are also scenarios in which the near wellbore region is subjected to the repeated loads. The two first cases are normally conducted for relatively shallow reservoirs which contain heavy oil. Note that other areas of engineering applications may also deal with the similar situations, for instance failure of the dam structure due to slow cyclic pressure variations.

There are two main areas of interest in studying sandstone degradation due to repeated loadings, namely cyclic loading laboratory tests and cyclic plasticity theories development. The majority of studies regarding cyclic loading of sandstone or cemented sand are limited to earthquake type (dynamic) of loading. Little attention has been paid so far to characterize deformation properties of sandstone under slow cyclic loading both theoretically and experimentally. It should be noted that the mechanical behaviours of geomaterials under dynamic cyclic loading are different from those of slow cyclic loading. This is due to the differences in the inertia effects.

Numerical approaches are adopted in this study to find a continuum rate independent elasto-plastic model suitable for modeling slow cyclic loading. Thus, the effects due to the frequency of cycles are not considered. Also analysis does not revolve around very large number of cycles implying that cyclic fatigue is neglected. The temperature changes coming from the difference between injected fluid temperature and reservoir temperature are neglected as well. Therefore, no temperature dependency is considered in decomposition of the total strain increment. The analysis is isothermal.

In order to analyze material behavior subjected to external (monotonic or cyclic) forces numerically, the following set of equations must be fulfilled [Atkinson 1993, Holland 1997, Khong 2004]:

- 1) Equilibrium equations
- 2) Compatibility equations
- 3) Constitutive equations

Fig. 1-1 demonstrates the relationships among these equations. If displacement formulation (displacement as primary unknown) is used, compatibility equations are not needed to be satisfied because strain and stress field can be determined using back-substitution in strain-displacement and constitutive equations, respectively.

It is assumed in this study that the equilibrium and compatibility equations have already been satisfied. Thus, the focus of this study is on the constitutive equations which describe the deformation of a material in response to imposed stresses (or vice versa).

1.3 Determination of the magnitude and direction of in-situ stresses

The in-situ vertical stress is dominated by the force of gravity. It is determined based on the weight of the overburden material by measuring the formation density from borehole density log [Santarelli et. al. 1998]. The vertical stress is usually assumed to be a principal stress. The hydrostatic pore pressure is obtained from calculating the weight of the water column from the surface to the targeted depth. In addition to vertical changes of the pore pressure with depth, there may be large lateral variations of pore pressure in some sedimentary formations. Actual pore pressure can be greater than the hydrostatic pressure (i.e. overpressure), or be less than the hydrostatic pressure (i.e. under pressure) in confined pore volumes which are hydraulically isolated from shallower depths (i.e. in compartmentalized reservoirs) [Zoback 2007]. If the pore pressure approaches the overburden pressure, it is referred to as hard overpressure. The in-situ stresses all become close to overburden stress in the case of hard overpressure

regardless of type of faulting regime [Zoback 2007]. Overpressure may occur when the rate of the stratigraphic layer burial is so rapid that the pore fluids cannot escape resulted in undrained conditions and thus, generating excess pore pressure. The undrained process is a constant volume process providing all the rock and also the pore fluids are incompressible [Wood 1990]. Drilling into an overpressured strata may lead to uncontrolled flow of reservoir fluids into the wellbore and even disastrously into the surface (i.e. blowout) if the drilling mud weight cannot balance the formation pressure (i.e. underbalanced drilling). In addition to the prevention of the possible blowout, overbalanced drilling also can decrease the risk of wellbore failure particularly in weak formations. However, operators simultaneously must take into consideration the probability of unplanned hydraulic fracturing and loss of mud circulation. Underpressure can occur in formations that have had depletion especially if they were under no pressure maintenance/improved recovery scenario. This causes the in-situ horizontal stress unusually low, implying that drilling new wells into greater depths is problematic in depleted reservoirs since drilling mud with lower unit weights should be used to prevent unintentional fracturing [Zoback 2007]. Wellbore instability becomes a pioneer issue at the case of the lower mud weights due to increase in the effective tangential stress. The pore pressure in interested depths of permeable formations can be obtained by drill-stem test or by wireline logging. However, it must be estimated before drilling as well to avoid possible blowout in overpressured zones. This is performed using seismic reflection data [Zoback 2007].

The in-situ minimum horizontal stress is obtained using mini-frac test, step rate test or (extended) leak-off test [Santarelli et. al. 1998, Zoback 2007]. The direction of maximum horizontal stress (σ_H) is obtained by the world stress map as an initial estimate [Hoek 2007] or the borehole break out for a vertical well since it occurs perpendicular to σ_H . It is known in geomechanics that estimation of the magnitude of σ_H is one of the most challenging task in determining in-situ stresses since it cannot be measured directly [Hoek 2007, Zoback 2007]. Drilling-induced tensile fractures in vertical wells occur when there is profound difference between horizontal stresses and can be detected by wellbore image devices.

Drilling induced tensile fractures may also be formed when the stress concentration around borehole exceeds the tensile failure limit of the wellbore wall. These fractures typically are approximately parallel to maximum horizontal stress orientation, which is as well in the direction of fast shear azimuth [Ostadhassan et. al. 2011]. This implies that sonic logs may also be used to determine direction of maximum horizontal stress because this direction is expected to coincide with that of fast component of a polarized flexural/shear wave. Acoustic (shear wave velocity) anisotropy can be measured by cross-dipole sonic logging tools [Syed et. al. 2011]. Magnitude of σ_H can be estimated for a vertical wellbore using the following equation [Zoback 2007]:

$$\sigma_H = 3\sigma_h - 2u - \Delta u - T - \sigma^{\Delta T} \quad (1.1)$$

in which u is the pore pressure, Δu is the difference between the drilling mud pressure in the wellbore and the pore pressure, T is the tensile strength, and $\sigma^{\Delta T}$ is the thermal stress caused by the difference between the mud temperature and formation temperature.

1.4 Problem statement and significance

If a material undergoes continuous increase in stresses along a given loading path without unloading and reloading, it is referred to as monotonic or virgin loading. The decrease in the stress beyond the peak point due to non-uniform deformation, however, is by virtue of the continuous loading and is not considered as unloading [Desai 2001]. Cyclic loading, however, is a term normally used by engineers to describe non-monotonic repetitive loading. That is, the emphasis by the term is more on non-monotonic nature of the loading than the cyclic nature [Reilly and Brown 1991]. Specifically speaking about the area of interest in this study, behavior of geomaterials under cyclic loading is remarkably complex. This may stem from the pressure and void ratio dependency of the constitutive relationship and the nonlinear behavior of the material matrix [Russel and Khalili 2004, Khalili et. al 2005, 2006].

Development or creation of a reliable model for modeling cyclic behavior of geomaterials is one of the most demanding tasks in constitutive modeling

[Vermeer and Borst 1984]. Even the most sophisticated constitutive models cannot provide accurate predictions under generalized cyclic loading [Reilly and Brown 1991].

In general, many constitutive models for cyclic loading have been proposed for cohesionless soils. Few developments, so far, have included cemented sand behaviour in response to slow cyclic loading. The lack of a critical state constitutive model for slow cyclic loading of cemented sand is noted in the literature. This is a need to develop a constitutive model that can capture the responses of artificially or naturally cemented sand under slow cyclic loading. During this research, the following questions will be addressed:

1. What are shortcomings of the proposed elasto-plastic theories rendered them likely to be unsuitable for describing sandstone response under slow cyclic loading?
2. How to modify existing bounding surface models to rectify the deficiencies?
3. How does slow cyclic loading influence sand/cemented sand deformation?

1.5 Research objectives

With a few exceptions, sanding analyses have been accomplished in the past using non-critical state constitutive models mainly by incorporation of the Mohr-Coulomb and/or Drucker-Prager yield functions. The major deficiency of these models is that unlike the critical state base models, void ratio is not included in these constitutive models, which is a major deficiency for any sand model [Jefferies 1993]. Moreover, Mohr-Coulomb yield function provides a linear failure envelope while geomaterials generally follow a curved failure envelope. Also the Drucker-Prager yield criterion does not provide a realistic representation of the failure condition for geomaterials since its yield locus gives rise to the symmetry of the yielding conditions in the deviatoric plane. The main objective of this study is to put forward a continuum critical state elasto-plastic model that will be used to predict cemented sand/soft sandstone behaviour under slow cyclic loading conditions. Bounding surface plasticity theory is used as the basic framework for the constitutive model. The inclusion of cohesion, inherent fabric

anisotropy and kinematic hardening in this framework makes the current development unique since the proposed model adopts simultaneously the concept of critical state, state parameter, kinematic hardening, inherent fabric anisotropy, non-associated flow rule, and material cohesion. A review of the historical development of the bounding surface theory in the next chapter will provide further insight on the deficiencies in existing models and the contribution of this work. For example many of the proposed models have not included cohesion in their formulations. Those that included cohesion have not been formulated using the concepts of critical state, state parameter, non-associated flow rule, inherent anisotropy, and kinematic hardening at the same time. The lack of at least one of the aforementioned concepts is noted in the models proposed so far in the framework of bounding surface plasticity theory.

The proposed model in this research will be used to simulate cemented sand response during slow cyclic loading. Analysis under drained conditions is preferred since sandstone reservoirs have relatively high permeability. Hence, fluid flow provides enough time to dissipate excess pore pressure. Normally the mean effective stress tends to increase gradually over the drainage period, but continuous fluid injection may decrease the rate of pore pressure dissipation. The partial undrained (no flow) conditions may exist if there is considerable amount of shale and clay materials in the sand reservoir. The rock compression in these situations causes the pore pressure to increase since the fluid cannot escape the pore space. The undrained conditions can also take place due to the dynamic loads induced by water hammer pressure pulses. The water hammer which is produced by unplanned shut-in referred in general to the generation, propagation and damping of unsteady flow of water within tubing [Vaziri et. al. 2007]. It creates dynamic type of wave loadings which are applied extremely rapidly to the rock causing the medium to react as if it were undrained. That is, the excess pressure cannot diffuse/drain in very short time period inside the reservoir resulting in the constant volume or more strictly speaking, the constant mass conditions. If the sand packing is loose enough and the amplitude of cyclic shear stress (created by the upward and downward propagation of the wave loadings) is large enough,

the pore pressure builds-up can continue until cyclic liquefaction occurs. If poroelasticity is assumed in liquefaction analysis, liquefaction takes place when the effective overburden stress becomes zero. The potential for liquefaction seems to be low for consolidated reservoirs due to the presence of bonding and high densities of these reservoirs. The likelihood decreases in deeper reservoirs because the in-situ rock is subjected to very high confining stresses leading to strain hardening behaviour. Moreover, if the over-pressured intervals are excluded, the effective overburden stress increases with depth since the average increment per meter of depth for the pore pressure is less than that of the overburden pressure. If liquefaction happens in poorly cemented reservoirs under cyclic wave loadings, it will most probably be due to cyclic mobility (i.e. limited liquefaction) since dense sands under cyclic loading tend to expand [Querol and Blázquez 2006, Lenart 2008, Elgamal et. al. 2003]. The reason for this behaviour is that dense sands dilate after an initial contractive response, the so-called phase transformation [Li and Ming 2000, Orense and Pender 2012].

1.6 Thesis structure

The thesis is organized in paper format. Chapters 3 to 5 are papers which either have been submitted or will be submitted to journals for publications. There are certain repetitions in each chapter since each chapter is a standalone paper.

The outline of the thesis is as follows:

Chapter 2 presents literature review on the sand production modeling and bounding surface plasticity theory. The chapter reviews numerical models of sanding, slow and fast cyclic loading, slow cyclic loading modeling by classical plasticity framework, bounding surface plasticity concept, and cyclic plasticity theories. The chapter also discusses typical stress-strain and volumetric behaviour of sand and cemented sand under triaxial conditions. Ultimately proposed methodology is discussed at the end of the chapter.

Chapter 3 introduces a critical state constitutive model for cohesionless sand under cyclic loading. The model, which is formulated using the bounding surface theory, uses the combined isotropic-kinematic hardening law and non-associated

flow rule. Predictions of the proposed model are compared and discussed against triaxial cyclic tests conducted under different initial conditions.

Chapter 4 describes a critical state constitutive model for cemented sand/soft sandstone under monotonic loading. The model is formulated using the radial mapping formulation of bounding surface plasticity theory. It is examined against monotonic tests of the sands with different cement contents under different initial conditions. The proposed model, however, is needed to be further modified in order to simulate cyclic response of cemented sand/very weakly cemented sandstones. This modification is discussed in Chapter 5.

Chapter 5 presents an elasto-plastic constitutive model for monotonic and cyclic behavior of (very) weakly cemented sandstones. In this model, destruction of the cementation bonds by plastic deformation is considered as the reason for mechanical degradation of rock and hence, the onset of sand production. After reviewing the mathematical formulation of the model, its performance is evaluated against monotonic and cyclic tests of several artificially and naturally cemented sands.

Chapter 6 extends the application of the constitutive model to cases that are not under conventional triaxial conditions. This is performed by incorporating an intrinsic/structural fabric anisotropy and the b -parameter into the formulation of the model. Performance of the proposed model is assessed against undrained monotonic hollow cylinder (HC) tests for a specific sand. The model also is used to predict the behavior of a weakly cemented sand under drained cyclic HC tests with different values of b .

Chapter 7 summarizes the major conclusions from the research and put forwards some suggestions for future works.

Two appendices also have been added at the end of the thesis. Appendix A presents formulation of a classical constitutive model with a Mohr-Coulomb type yielding criterion. It is formulated using both isotropic and kinematic hardening. Appendix B talks about formulation of the adopted critical state constitutive model for general stress space.

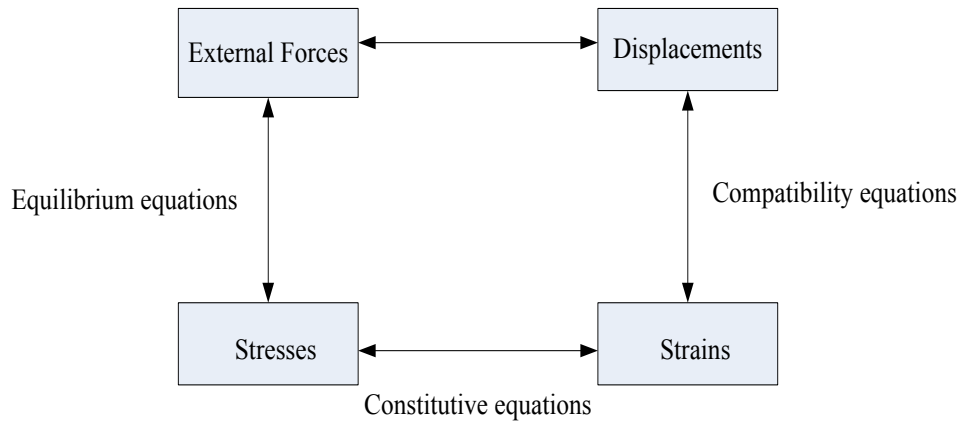


Fig. 1-1 Relationships needed to be addressed for full description of a mechanical process

1.7 References

Abdulazeez, A. (1994), Constitutive modeling of rocks and numerical simulation of oil reservoirs exhibiting pore collapse, Ph.D. thesis, The university of Oklahoma, Oklahoma, USA.

Acock, A., Alexander, J., Andersen, G., Kaneko, T., Venkitaraman, A., Lopez-de-Cardenas, J., Nishi, M., Numasawa, M., Yoshioka, K., Roy, A., Wilson, A. and Twynam, A. (2004), Practical approaches to sand management, *Oilfield Review*, pp. 10-27.

Atkinson, J. (1993), *An introduction to the mechanics of soils and foundations through critical state soil mechanics*, McGRAW-HILL Book Company, England.

Bellarby, J. (2009), *Well completion design*, Elsevier, Netherlands.

Desai, C. S. (2001), *Mechanics of materials and interfaces: the disturbed state concept*, CRC Press, USA.

Elgamal, A., Yang, Z., Parra, E. and Regheb, A. (2003), Modeling of cyclic mobility in saturated cohesionless soils, *International Journal of Plasticity*, Vol. 19, pp. 883-905.

Fjar, E., Holt, R.M., Horsrud, P., Raaen, A.M., and Risnes, R. (2008), *Petroleum related rock mechanics*, Elsevier, U.K.

Hoek E. (2007), *Practical Rock Engineering*, www.roscience.com.

Holland, T.J. (1997), Numerical methods for implementing the bounding surface plasticity model for clays, Ph.D. thesis, The University of California, Davis, USA.

Jardine, S.I., Johnson A.B., and Stibbs, W. (1993), Hard or soft shut-in: which is the best approach?, *SPE 25712*.

- Khalili, N., Habte, M. A., and Valliappan S. (2005), A bounding surface plasticity model for cyclic loading of granular soils, *International Journal For Numerical Methods In Engineering*, Vol. 63, pp. 1939–1960.
- Khalili, N., Habte, M. A., and Valliappan S. (2006), Monotonic and cyclic analysis of granular soils, *Computational Methods in Engineering And Science*, China, pp. 59-70.
- Lenart, S. (2008), The response of saturated soils to a dynamic load, *Acta Geotechnica Slovenica*, Vol. 5, No. 1, pp. 37-49.
- Li, X.S., Ming, H.Y.(2000), Unified modeling of flow liquefaction and cyclic mobility, *Soil Dynamics and Earthquake Engineering*, Vol. 19, pp. 363-369.
- Orense, R., and Pender M. (2012), Liquefaction characteristics of pumice sands, EQC project 10/589, The University of Auckland, Auckland, New Zealand.
- Ostadhassan, M., Zeng, Z., Jabbari, H. (2011), Using advanced acoustic data to determine stress state around wellbore, *ARMA*, pp. 1-7.
- Querol, S.L., and Blázquez, R. (2006), Liquefaction and cyclic mobility model for saturated granular media, *International Journal for Numerical and Analytical Methods in Geomechanics*, Vol.30, pp. 413-439.
- Mathis, S.P. (2003), Sand management: A review of approaches and concerns, *SPE 82240*, pp. 1-7.
- Morita, N., Davis, E., and Whitebay, L. (1998), Guidelines for solving sand problems in water injection wells, *SPE 39436*, pp. 189-200.
- Nasr, M.S., and Edbieb, S.M. (2012), Effect of sand production on the productivity of oil wells in unconsolidated sandstone reservoirs in Sirte basin Libya (field case study), 19th Annual India Oil & Gas Review Summit & International Exhibition, Mumbai.
- Nouri, A., Kuru, E. and Vaziri, H. (2009), Elastoplastic modeling of sand production using fracture energy regularization method, *Journal of Canadian Petroleum Technology*, Vol. 48, No. 4, pp. 64-71.
- Nouri, A., Vaziri, H., Kuru, E., and Islam, R. (2006), A comparison of two sanding criteria in physical and numerical modeling of sand production, *Journal of Petroleum Science and Engineering*, Vol. 50, pp. 55-70.
- Rahmati, H., Jafarpour, M., Azadbakht, S., Nouri, A., Vaziri, H., Chan, D., and Xiao, Y. (2013), Review of sand production prediction models, *Journal of Petroleum Engineering*, Review Article, pp. 1-16.
- Reilly, M.P.O, and Brown, S.F. (1991), *Cyclic loading of soils: from theory to design*, Blackie and son limited, U.K.

- Russel, A., and Khalili N. (2004), A bounding surface plasticity model for sands exhibiting particle crushing, *Canadian Geotechnical Journal*, Vol. 41, No. 6, pp. 1179-1192.
- Sadrpanah, H., Allam, R., Acock, A., Norris, M., O'Rourke, T., Murray, L.R., and Wood, D.J. (2005), Designing effective sand control systems to overcome problems in water injection wells, SPE 93564, pp. 1-11.
- Santarelli, F.J., Sanfilippo, F., Embry, J.M., and Turnbull, J. (2011), The sanding mechanisms of water injectors and their quantification in terms of sand production: example of the Buzzard field (UKCS), SPE 146551, PP. 1-13.
- Santarelli, F.J., Skomedal, E. Markestad, P., Berge, H.I., Nasvig, H. (1998), Sand production on water injectors: just how bad can It get?, SPE/ISRM 47329, pp. 107-115.
- Servant, G., Marchina, P., and Nauroy, J.F. (2007), Near-wellbore: sand production issues, SPE 109894.
- Skjaerstein A., Tronvoll, J., Santarelli, F.J., and Joranson, H. (1997), Effect of water breakthrough on sand production: experimental and field evidence, SPE 38806.
- Syed, A., Bertran, A., Donald, A., Sinha, B., Bose, S. (2011), Continuous statistical indicator of stress-induced dipole flexural wave anisotropy, 52th annual logging symposium, Colorado, USA.
- Vardoulakis, I., and Papamichos, E. (2003), A continuum theory for erosion in granular media, *Rivista Italiana Di Geotecnica*.
- Vardoulakis, I., Stavropoulou, M., and Papanastasiou, P. (1996), Hydro-mechanical aspects of the sand production problem, transport in porous media, Vol. 22, pp. 225-244.
- Vaziri, H., Nouri, A., Hovem, K., and Wang, X. (2007), Computation of sand production in water injectors, SPE 107695, pp. 1-9.
- Veeken, C.A.M., Davies, D.R., Kenter, C.J., and Kooijman, A.P. (1991), Sand production prediction review: developing an integrated approach, SPE 22792.
- Vermeer, P.A., and de Borst, R. (1984), Non-associated plasticity for soils, concrete and rocks, *Heron*, Vol. 29, No. 3, pp. 1-64.
- Wu, B., Tan, C.P., and Lu, N. (2005), Effect of water cut on sand production-an experimental study, SPE 92715.
- Zoback, M.D. (2007), *Reservoir geomechanics*, Cambridge University Press, USA.

CHAPTER 2

LITERATURE REVIEW

2.1 Introduction

The majority of the world's petroleum reservoirs are found in sandstone formations. During petroleum extraction, sand production in these reservoirs is of critical concern due to the adverse effects of sanding on production/injection well performance and equipment. Loosely consolidated sandstone reservoirs are more prone to sanding due to the loose bonds between sand particles, which are broken during plastic deformation. The sanding phenomenon normally occurs in two stages: a) complete mechanical degradation of the rock; and b) transport of the detached sand particles into the wellbore or perforations by fluid flow. This means that rock degradation is considered as a prerequisite for sanding. This research focuses on the first stage of sanding (i.e. degradation phase) due to monotonic and specially cyclic loads in (very) weakly consolidated sandstone reservoirs.

Rock around petroleum wells is subjected to cyclic loading due to repeated changes in the effective stresses in the rock. It may experience many loading cycles via injection start-up and shut-in cycles and injection/production rate fluctuations. Every cycle of unloading-reloading gives rise to energy dissipation and thus plastic deformation which leads to degradation of cementation bonds. A constitutive model is required to address stress-strain behaviour and mechanical degradation of soft sandstone in the course of cyclic loading.

This chapter initially reviews common failure criteria which are used in sanding analysis. Their strengths and weakness in reproducing behavior of sand/cemented sand also will discuss. Then different types of cyclic loading (which both can occur during well operation) and their differences will be discussed. The chapter will review famous elasto-plastic theories which are usually used for simulation of cyclic loading. Effectiveness of these theories in describing cyclic loading will be

discussed too. Then stress-strain and volumetric behaviour of sand and cemented sand will be discussed. Ultimately the chapter proposes a methodology to come up with a suitable constitutive model which can be used for describing cyclic behavior of cemented sands.

2.2 Numerical models of sanding

Some sanding models only predicts the onset of sand production and some assume sandstone initially has been fully degraded and only predict rate and mass of sanding. A comprehensive sanding model, however, not only predicts sanding potential (i.e. conditions for the onset of sand production) but it should also predict the rate and ultimate volume of sand production [Mathis 2003, Servant et. al. 2007, FJar et. al. 2008].

It is clear that a sanding model cannot take all influential factors of sanding into account. Thus, each model may emphasize on a number of these factors depending on the adopted sanding criteria and existing experimental observations which are used to validate the model [Rahmati et. al. 2013]. Numerical models of sanding are generally divided into three categories: a) continuum models b) discontinuum models c) hybrid models. Continuum approach is the most prevalent method in numerical modeling of sand production. When the rock becomes totally disintegrated and sand production starts, the rock is no longer a continuum. Hence, discontinuum models based on the discrete element method (DEM) should be used to simulate the discontinuous nature of sand production. In combined method (the so-called hybrid approach), both the continuum and discontinuum approaches are used such that the continuum approach is used for the far field region and the discontinuum approach is used for the near cavity (i.e. wellbore or perforation) region [Rahmati et. al. 2013]. Since the focus of the current research is on degradation phase of sand production and the constitutive modeling, only the continuum approach with emphasis on the common failure criteria in the sanding models will be discussed here.

Despite the simplicity of the elastic or perfectly plastic base constitutive models, they do not provide a realistic description of the mechanical behaviour of

cemented sand/weak sandstone. Hence, the use of an elasto-plastic constitutive model is more appropriate for describing the mechanical behaviour of sandstone [Veeken et. al. 1991]. Mohr-Coulomb yield criterion is the most popular yield criterion in geomechanics in general and in sanding analysis in particular. It is used either in the linear form, or in the bilinear form to better capture the curvature of the failure envelope [for example see Sulem et. al. 1999, Wang and Lu 2001, Nouri et. al. 2003]. This originates from its simplicity and applicability for a wide range of geomaterials including various types of soil and rock. It also provides asymmetric yield surface in the deviatoric plane (i.e. the principal stress space) or around hydrostatic axis in the conventional triaxial $q-p$ plane. This is in accordance with experimental observations which indicate that the material has smaller peak strength under extension loading in comparison with compression. The Mohr-Coulomb yield surface has six vertices in the deviatoric plane (i.e. an irregular hexagonal shape) which can cause numerical instabilities. These vertices are numerically problematic in calculating the unit normal to the yield surface [Chen 1994, Khong 2004]. The shortcomings of the Mohr-Coulomb yield criterion in describing the mechanical behaviour of geomaterials are as follows:

- a) Geomaterials generally do not follow a linear failure envelope. Therefore, the pore collapse failure (i.e. the compressional failure) which can occur in the case of highly porous sandstone cannot be captured using a linear failure envelope [Economides and Nolte 2000].
- b) Unlike the critical state base models, void ratio (density/porosity) is not included in the constitutive model which is a major deficiency for any sand model [Jefferies 1993]. Consequently, the infinite shearing under the constant volume, constant deviator stress, and constant mean stress (i.e. the critical state) cannot be replicated.
- c) Numerical singularities/instability due to the vertices on the yield surface [Minassian 2003, Gadde and Rusnak 2008].
- d) It assumes constant elastic moduli, while they are pressure sensitive.

The Drucker-Prager yield criterion is the second well-known commonly used yielding criterion in the sanding analysis [for example see Tronvoll et. al. 1992,

Morita and Fuh 1998, Younessi and Rasouli 2012]. It is a simple modification of the Von Mises yield criterion which includes the effect of the hydrostatic pressure on yielding. It is also one of the first yield criteria which incorporated the effect of the intermediate principal stress on the rock strength. The Drucker-Prager yield surface (also known as extended Von Mises criterion) also may be considered as a smooth approximation for the Mohr-Coulomb yield surface. Hence, it is numerically more stable than the Mohr-Coulomb yield criterion [Chen 1994, Minassian 2003, Gadde and Rusnak 2008]. The Drucker-Prager yield criterion can be obtained by either circumscribing or inscribing the Mohr-Coulomb yield surface in the deviatoric plane. In contrast to the Mohr-Coulomb yield surface, the Drucker-Prager yield surface contains cap portion. The cap yield surface can model inelastic behavior under hydrostatic loading [Grueschow 2005] where grain crushing is the dominant mechanism (i.e. failure by compaction or pore collapse) [Challa 2005]. Pore collapse is a volumetric yielding in which the rock volume is decreased due to drastic irreversible reduction in pore volume or porosity. Pore collapse usually occur at high mean stress and (very) low deviator stress [Hickman 2004]. Significant irrecoverable reduction in porosity occurs due to the increase in mean effective stress acting on the rock matrix as a result of oil and gas withdrawal. Sever compaction can cause sand production, wellbore instability, and reduce formation permeability [Abdulazeez 1994]. The main deficiency of the Drucker-Prager similar to other circular yield surfaces is that the yield locus gives rise to the symmetry of the yielding conditions in the deviatoric plane. Thus, the Drucker-Prager yield criterion does not provide a realistic representation of the failure condition for geomaterials where a Mohr-Coulomb type of failure criterion is more suitable. Moreover, the application of the isotropic hardening for circular yield surfaces leads to violation of the Bauschinger effect during cyclic loading. The introduction of the third invariant of the deviator stress in the definition of the modified version of Drucker-Prager yield criterion makes the shape of the yield surface relatively noncircular, but still very close to a full circular shape. The modified version causes the predictions to

be more realistic. However, it overestimates the rock strength [Colmenares and Zoback 2002, Gadde and Rusnak 2008].

Liu et. al. (2008) and Oluyemi and Oyemeyin (2010) used the Hoek and Brown failure criterion, which was initially developed for estimating the rock mass strength in excavation design [Zoback 2007], in their sanding model. Other failure criteria such as modified Lade criterion have been used uncommonly in geomechanics as well [Ewy 1998, Nawrocki 2010]. Few researchers have also used the critical state base constitutive model in their geomechanic models as well. For instance, Wang et. al. (2011) used a critical state base constitutive model, called Soft Rock Model, in their sanding analysis. De Souza et. al. (2012) used a critical-state constitutive model, known as the Chalk Model, in their reservoir geomechanic model. Roshan (2011) used Modified Cam Clay in wellbore stability analysis.

It should be noted that non-critical state constitutive models simulate sand behaviour under different initial conditions using different material parameters. That is, the same sand with different void ratios is treated as different material by assigning different material parameters. The setback stems from absence of density/void ratio in the constitutive model while in reality sand behavior changes with density/void ratio. Absence of void ratio in constitutive model is a major deficiency for any sand model [Jefferies 1993]. Similar to any other continuum elasto-plastic constitutive model, critical state models constitute of four major components which include elastic properties, yield function, plastic potential function, and hardening rule. Different definitions of these components results in different constitutive models. Critical state models, however, incorporate void ratio in their constitutive relationships. Therefore this framework is adopted during this research to investigate mechanical degradation of weakly cemented sand under monotonic and cyclic loading. Concept of critical state is briefly discussed here.

Critical state soil mechanics was initially introduced by Roscoe et. al. (1958), and Schofield and Wroth (1968). Soils and other granular materials under continuous shear straining ultimately reach a constant state since they can not compress or

dilate and strengthen and weaken indefinitely [Schofield and Wroth 1968, Atkinson 1993]. This constant state is termed critical state which reaches at large shear strains (say larger than 15% for soils). Critical state is associated with continuous shear deformation without any change in void ratio/volume, shear or normal stresses. This mathematically can be expressed by [Khong 2004]:

$$\frac{de}{d\varepsilon_q} = \frac{dq}{d\varepsilon_q} = \frac{dp}{d\varepsilon_q} = 0 \quad (2.1)$$

where ε_q is deviator strain, e is void ratio, q is deviator stress, and p is mean effective stress. Soils will flow as a frictional fluid at critical state [Schofield and Wroth 1968].

Critical states for any given soil make a line in the (e, q, p) space which is named as the critical state line (CSL). The CSL is defined either in (e, p) plane in which void ratio or specific volume is defined as a function of p or in (q, p) plane in which q and p are linearly related by the critical state stress ratio [Schofield and Wroth 1968, Atkinson 1993].

Incorporation of void ratio in original and Modified Cam Clay model still was not enough to correctly reproduce dense sand response [Jefferies 1993]. To overcome this deficiency, Jefferies (1993) proposed a hardening rule which depends on proximity to critical state line. This was in contrast to conventional critical state models which coupled yield surface size with plastic volumetric strain increment. Imam (1999) and Imam et. al. (2005) used the same procedure to propose their hardening rule. Dependency of hardening rule to proximity to critical state line in their model comes from its dependency to so-called state parameter. State parameter determines relative distance between current void ratio and critical state void ratio in any given p [Been and Jefferies 1985, Jefferies and Been 2000]. Therefore location of the CSL, which is not present in non-critical state base models, plays an important role in model predictions since it provides a critical state void ratio for any given stress state. Value of the state parameter in any given stress state determines proximity to the CSL in terms of absolute value and direction (i.e. positive or negative). Infinite shearing occurs without any energy dissipation when the state parameter remains zero under constant shear stress. If

CSL is considered ideally as ultimate condition of all distortional process, void ratio should migrate to CSL at large strains regardless of its initial value [Jefferies 1993]. A soil is said to be in dry/dense side of the CSL if its corresponding state parameter is negative otherwise it is said to be in wet/loose side of the critical state line. Soils which are in dry side and wet side of the CSL tend to dilate and compress, respectively [Jefferies 1993].

2.3 Slow cyclic loading vs. fast cyclic loading

Because we are interested in sand production due to cyclic loading, two types of cyclic loading which may occur in reservoir are discussed here.

Dynamic loading refers to propagation of stress waves within the medium. The dynamic equation of a moving homogenous solid is written as follows [Rascol 2009]:

$$F + \operatorname{div} \sigma = \rho \ddot{u}_d \quad (2.2)$$

in which F are external body forces, ρ is density, and \ddot{u}_d is acceleration.

Dynamic measurements usually measure wave speeds (at a given frequency) and induced deformation during imposed oscillations [Martinez 2014].

Quasi static loading refers to slow variations of material state. That is, quasi static loads are exerted to material in slowly varying ways, which implies that static conditions can be assumed [Kappos 2002]. Therefore the inertia term (right side of equation (2.2)) is negligible for quasi static loading [Rascol 2009].

Dynamic loading is a general term which includes various types of loads such as seismic or sonic waves loads, turbulent fluid flow vibrations induced loads, blasting shock waves loads, and so on [Mitchell and Soga 2005, Silva 2005]. The common denominator of dynamic loads is that they produce very high or high strain rates for instance strain rate in earthquake loads ranges from 0.001 sec^{-1} to larger than 0.1 sec^{-1} , and in blasting loads range from 100 sec^{-1} to 10000 sec^{-1} . However strain rate is small in quasi static loads ranging from 10^{-8} sec^{-1} to 10^{-5} sec^{-1} [Silva 2005]. Dynamic loads also have very high or high frequencies, for example frequency in seismic waves is normally in range of $10\text{--}50 \text{ Hz}$, in sonic logging is about $1\text{--}10 \text{ KHz}$, and in laboratory ultrasonic

measurements is about 1 *MHz* [Zoback 2007]. Clearly wave loads with smaller frequency affect larger area because they have larger wave length, and vice versa. Therefore dynamic mechanical measurements are affected by the frequency of loading/deformation, and strain amplitudes [Martinez 2014].

The following sets of equations are needed to be solved in dynamic loading [Pando 1995, Querol and Blázquez 2006]:

$$[M_d][\ddot{u}_d] + [C_d][\dot{u}_d] + [K_{st}][u_d] = [F(t)] \quad (2.3)$$

$[F(t)]$ is dynamic force vector which is time dependent, $[\dot{u}_d]$ is velocity vector, $[\ddot{u}_d]$ is acceleration vector, $[K_{st}]$ is stiffness matrix, $[C_d]$ is damping matrix, and $[M_d]$ is mass matrix. This equation is a second order differential equation which needs to be solved for the displacement $[u_d]$ [Kappos 2002].

Note that damping is a viscous effect which indicates the capacity of the material or system to hinder its own vibration by absorbing energy [Reilly and Brown 1991]. This ability increases with progress of time.

For quasi static loads, the last equation is reduced to the following equation:

$$[K_{st}]_{n \times n}[u_d]_{n \times 1} = [F]_{n \times 1} \quad (2.4)$$

where $[F]$ is force vector independent of time, and $[u_d]$ is displacement vector.

In summary, the rate of loading is important for dynamic cyclic loading unlike the slow cyclic loading for which the rate of loading is not a concern. This leads to the fact that the dynamic cyclic loading tests are conducted very fast (say every cycle in a second) in contrast to the slow cyclic loading in which the loading is applied very slowly with a constant velocity. The term "cyclic loading" in this research is an abbreviation for the slow cyclic loading unless otherwise is indicated.

Both types of (slow) cyclic and dynamic loadings can occur around injection or production wells. Cyclic loading can occur due to fluctuations in injection or production rates which results in increase or decrease in mean effective stress. These variations of injection and production rates usually occur slowly in the range of hours/days leading to slow cycle of unloading-reloading. Slow cyclic loading can also occur due to planned/controlled shut-in and start-up cycles.

Plastic deformation occurs in every cycle due to repeated changes of mean effective stress. This results in gradual degradation of rock strength around cavity, which itself is already under high amount of stress concentration. Full degradation of rock structure and sanding onset may occur due to accumulation of plastic strain during cyclic loading.

Injection/production stops may also be irregular (unplanned) during hydrocarbon extraction/fluid injection. The uncontrolled shut-ins take place in the case of an unpredictable incident such as loss of power or dramatic reduction in productivity or injectivity index. The so-called water hammer pressure pulses will be generated as a consequence of the rapid shut-ins. Water hammer waves cause turbulent flow vibrations induced loads which are applied to rock around injection/production wells. If weak sandstone is fully degraded by slow cycle of unloading and reloading, it can be liquefied by water hammer wave loads provided that its porosity/void ratio is high enough. In general, slow start-up and shut-in cycles and water hammer cyclic pressure waves can lead to severe rock degradation, possible liquefaction and massive sanding. Vaziri et. al. (2007) performed sanding analysis for different rocks under operational cyclic conditions (i.e. start-up and shut-in cycles in addition to water hammer pressure cycles). Cohesion was assumed to degrade with equivalent plastic strain. They found that sandstones with unconfined confining strength (UCS) of about 1.4 MPa do not experience sanding for a number of years without water hammer and even with water-hammer. In their study, every shut-in cycle was assumed to typically represent an operational life of about one month. Weak rocks with UCS smaller than 700 KPa, on the other hand, experienced sanding in very early cycles. They also found that for a given sandstone and injection pressure, there is a threshold amplitude below which water hammer likely do not have impact on degradation of rock structure. Effects of water hammer cyclic waves on injection wells and wellbore stability can be found in Choi and Huang (2011) and Han et. al. (2003).

Since we are interested in first phase of sand production here, only (slow) cycling loading is investigated in this research. Proposed constitutive model and approach which were used for modeling cyclic loading of uncemented/cemented sands will

be discussed later in chapter 3 and 5. Mechanical response of granular materials under cyclic loading will also be discussed in these chapters.

2.4 Cyclic loading modeling by classical plasticity framework

The traditional elasto-plastic models use a single yield surface to separate the domains of elastic and plastic states. These models provide good description for mechanical behavior of materials under monotonic loading. They, however, have some deficiencies in modeling cyclic loading [Yu 2006]. Overall, these models cannot reproduce complicated behavior observed under cyclic loading where stress reversal (i.e. change in the sign of the stress increment) takes place frequently [Chen 1994]. That is, they cannot describe the observed hysteretic behavior. One major source of these shortcomings is that traditional constitutive models predict purely elastic response for any stress state or stress path inside the yield surface. The inability of these models to capture non linearity of plastic modulus, accumulation of plastic strain and irrecoverable pore pressure generation during unloading and subsequent reloading is a direct consequence of this assumption [Yang et. al. 2011]. These setbacks resulted in extensive research from the 1960s to seek better elasto-plastic models that are more appropriate in simulating cyclic behavior [Yu 2006, Chen 1994, Reilly and Brown 1991].

Fig. 2-1 indicates an example that the classical models fail to predict hysteresis loop. Hysteresis refers to different stress paths in unloading and reloading due to energy dissipation and heterogeneous deformation during cycle of unloading-reloading. In general, however, it may be defined as dependency of a system not only to its current status but also on its past status because the system can be in more than one internal state [Mielke and Roubicek 2003]. For stress-strain curve, it implies that some parts of the material under unloading and reloading conditions still may remain on loading and unloading phases, respectively. The loading in the extension side of the stress-strain curve (i.e. $q < 0$) is referred to as reverse loading. Cyclic loading without reverse loading is referred to as

one-way cyclic loading. If it has reverse loading, it is referred to as two-way cyclic loading [Desai 2001].

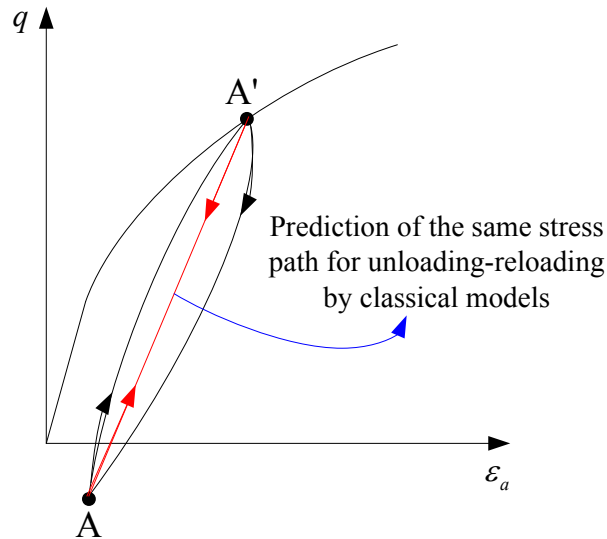


Fig. 2-1 Perfect hysteresis loop in a two-way cycle

Fig. 2-2 shows an example that illustrates that the conventional elasto-plastic theory fails to simulate cyclic response correctly. Cam Clay model predicts a stable response in which mean effective stress (p) remains unchanged during undrained cyclic loading as long as the stress path lies inside the current yield surface. The reason is that pure elastic response for stress paths within the yield surface is assumed in this conventional critical state model. It also predicts the same stress path for unloading and reloading in deviator stress-deviator strain ($q - \varepsilon_q$) and pore pressure-deviator strain ($p_w - \varepsilon_q$) planes.

It can be shown why in Cam Clay model a constant p response for unloading undrained conditions is predicted under assumption of elastic deformation for stress paths inside the yield locus. It is shown by knowing that no volume change occurs during undrained conditions.

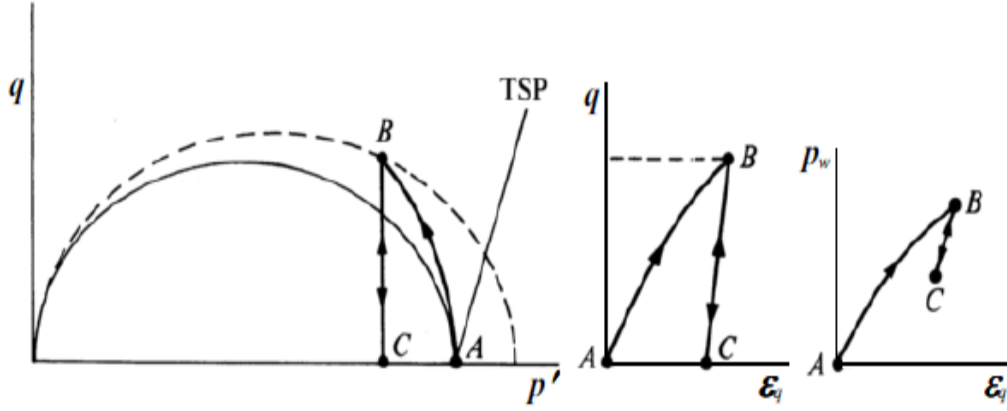


Fig. 2-2 Predicted response of a normally consolidated clay to undrained cyclic loading by Cam Clay [Wood 1990]

We know that change in the effective mean stress is supposed to induce elastic volume change only and no elastic volume change occurs due to change in the deviator stress. Hence,

$$\dot{\epsilon}_p^e = \frac{\dot{p}}{K} \quad (2.5)$$

$\dot{\epsilon}_p^e$ is elastic volumetric strain and K is the elastic bulk modulus.

Changes along unloading-reloading line in Cam Clay model are supposed to be purely elastic. Thus, the unloading-reloading line is represented using a straight line as follows:

$$v = v_k - k_{ur} \ln p \quad (2.6)$$

k_{ur} is slope of the unloading reloading line which is a material parameter for Cam Clay model. v_k is the specific volume associated with unit mean effective pressure, 1 kpa or 1 Mpa depends on unit of measurement. Therefore,

$$\dot{\epsilon}_p^e = -\frac{\dot{v}^e}{v} = \frac{k_{ur}\dot{p}}{vp} \quad (2.7)$$

Minus sign is used in formula since compression is assumed to be positive. The equations (2.5) and (2.7) imply that the bulk modulus of elasticity K changes directly with the mean effective stress in this model.

The plastic volumetric strain is formulated using the constant p loading during which no elastic volumetric strain occurs. Assume the current stress state is on

the isotropic consolidation line (point 1 in Fig. 2-3) in compression plane. Compressive plastic loading results in a reduction of void ratio and expansion of the yield surface. Having expanded the current yield surface, the stress path has to move along the corresponding unloading reloading line up to a point having the same mean effective stress than that for the inception of the loading. Thus [Wood 1990],

$$\dot{v} = \dot{v}^p = -(\lambda - k_{ur}) \ln \left(\frac{p_{c2}}{p_{c1}} \right) \quad (2.8)$$

Hence, $\dot{\varepsilon}_p^p = (\lambda - k_{ur}) \dot{p}_c / v p_c$ which results in the following formula:

$$\dot{p}_c = \frac{v p_c}{\lambda - k_{ur}} \dot{\varepsilon}_p^p \quad (2.9)$$

This is volumetric hardening law in conventional critical state theory. λ is the slope of the isotropic compression and critical state lines in Cam Clay model which is considered as a material parameter. Note that isotropic compression and critical state lines are assumed to be parallel in Cam Clay model.

For undrained condition, no volume change is allowed meaning the total volumetric strain increment is zero always. Therefore [Wood 1990],

$$\frac{k_{ur} \dot{p}}{v p} = -(\lambda - k_{ur}) \frac{\dot{p}_c}{v p_c} \quad (2.10)$$

This equation implies that the changes in p and p_c must always be of the converse sign. Because no plastic deformation is allowed inside the yield surface in Cam Clay model, effective preconsolidation pressure (p_c) does not change during a process whose stress path lies inside the yield locus. Thus the right hand side of equation (2.10) becomes zero for stress paths inside the yield locus. Therefore \dot{p} must be zero to satisfy equation (2.10) (i.e. no volume change condition) [Wood 1990].

In reality, however, the unloading and reloading paths are associated with plastic deformations which give rise to irrecoverable pore pressure accumulation during undrained cyclic loading. Normally consolidated clays or loose sands show unstable behavior with progressively increasing pore pressure which leads to

movement of the stress path towards lower values of the mean effective normal stress (see Fig. 2-4).

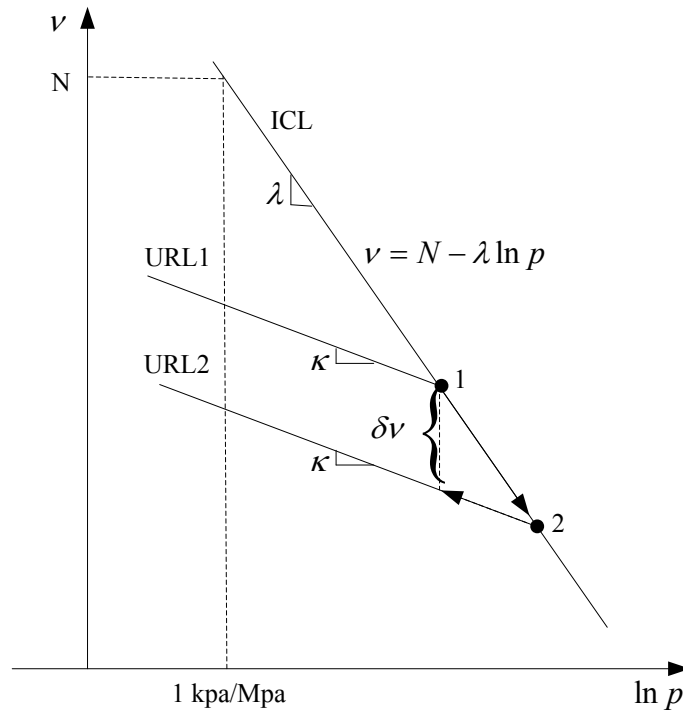


Fig. 2-3 Plastic loading under constant p stress path in compression plane for Cam Clay model. URL and ICL are abbreviations for unloading-reloading line and isotropic compression line

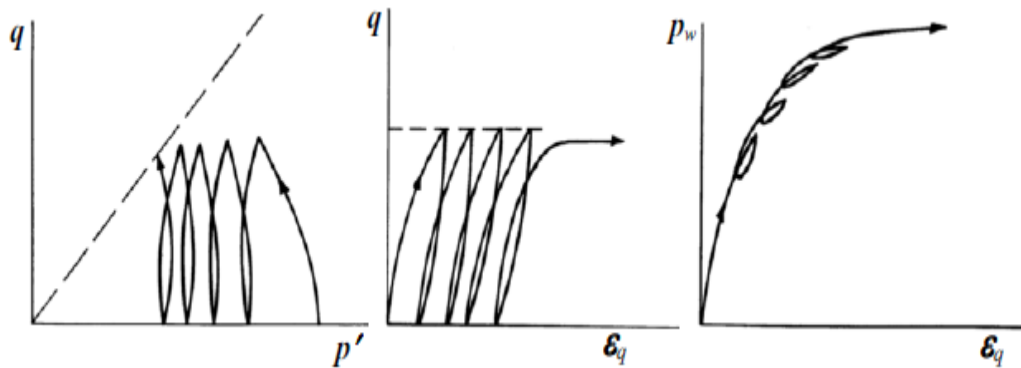


Fig. 2-4 Typical response of a normally consolidated clay/loose sand observed under undrained cyclic loading [Wood 1990]

2.5 Bounding surface plasticity concept

Bounding surface plasticity is one of the most common theories which is used to model cyclic loading. The most important motivation for using this theory is to model cyclic behavior. This theory is used throughout this research as the base framework to model sand/cemented sand behavior in response to cyclic loading. Concept of bounding surface plasticity theory and how it was originally proposed is discussed here.

The underlying foundation of the bounding surface plasticity theory can be visualized by trend of the plastic modulus, H , variations in a typical uniaxial stress-plastic strain curve shown in Fig. 2-5. In accordance with the classical elasto-plastic theory, the total strain increment is decomposed to plastic and elastic increments, $d\varepsilon = d\varepsilon^e + d\varepsilon^p$ in which $d\varepsilon = d\sigma/H^t$, $\varepsilon^e = d\sigma/H^e$, $d\varepsilon^p = d\sigma/H$, where $d\sigma$ is uniaxial stress increment and H^t , H^e , H are the tangent, the elastic and the plastic modulus, respectively. Therefore for uniaxial loading [Chen 1994]:

$$\frac{1}{H^t} = \frac{1}{H^e} + \frac{1}{H} \quad (2.11)$$

When only elastic deformation takes place $H^t = H^e$ implying that the initial values of H must be infinite. Immediately thereafter, at the initiation of plastic deformation after an elastic state, for smooth transition from elastic into elasto-plastic range, H is assumed to have a very high value and move on to reduce as plastic deformation continues [Dafalias and Popov 1975, Chen 1994].

Three distinct regions may be seen in Fig. 2-5. The first one (OB_0 or B_2A_2) is an elastic region where H has an infinite value. The second region (B_0B_1 or A_2A_1) occurs beyond the initial yield where H diminishes rapidly as a function of the plastic strain until it arrives at the third region (B_1B_2 or A_1A_0) in which H continues to take on an almost constant value, H_o , associated with the slope of the boundary line (XX' or YY'). According to uniaxial experiments, it can be assumed that the third portion of stress-plastic strain curve converges to the bounding lines which are often assumed to be straight lines at a fixed distance for simplicity.

These lines cannot be crossed, but can change position and size in the course of the loading process [Dafalias and Popov 1977, Chen 1994].

The smooth variations of the plastic modulus suggests that H is a function of δ , H_o and some other parameters. The following conditions, however, must be fulfilled [Vermeer and Borst 1984]:

$$1) H > H_o \quad 2) H = H_o \quad \text{if } \delta = 0 \quad 3) H = \infty \quad \text{if } \delta = \delta_o$$

By accounting these requirements, H_p may be defined as follows (this indicates why the plastic modulus in the bounding surface theory is normally decomposed into two segments, bounding surface and additive plastic modulus):

$$H = H_o + h\left(\frac{\delta}{\delta_o - \delta}\right) \quad (2.12)$$

where δ is distance between the current stress and the corresponding bounding line, δ_o is the distance between the initial yield point (B_o or A_2) and the corresponding bounding line (XX' or YY'), and h is a material parameter [Chen 1994]. That is, δ measures the distance of a particular stress state to the associated point on the corresponding bounding line. δ varies continuously during plastic loading [Dafalias and Popov 1977, Vermeer and Borst 1984].

In multi-axial conditions, the stress state is bounded by a surface, hence the name bounding surface. The bounding surface provides an exterior limit for the stress space and a reference state for cyclic loading. Fig. 2-6 illustrates a typical bounding surface model for a cohesionless soil.

During plastic flow, the bounding surface and loading surface can expand, contract, or move. The bounding surface, however, always surround the current stress state since a stress state outside the bounding surface has no physical meaning. The stress state lies on the bounding surface if $F = 0$. The stress state will not make F zero if the yield surface f lies inside the bounding surface F [Vermeer and Borst 1984]. The plastic strain, however, occurs inside the bounding surface when $f = 0$.

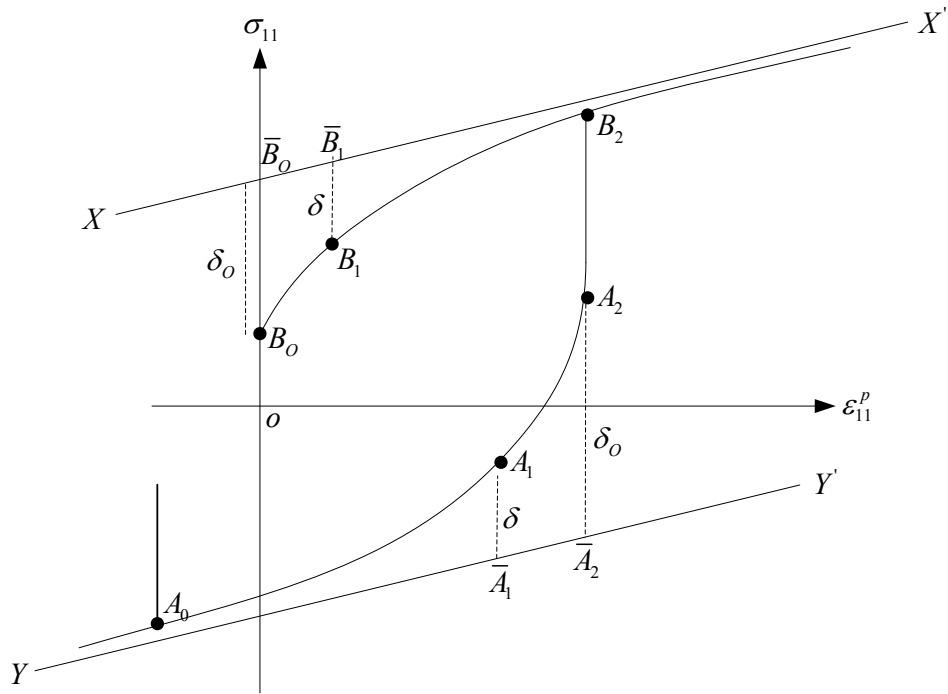


Fig. 2-5 Schematic illustration of the bounding lines in uniaial stress-plastic strain curve [modified after Dafalias and Popov 1977]

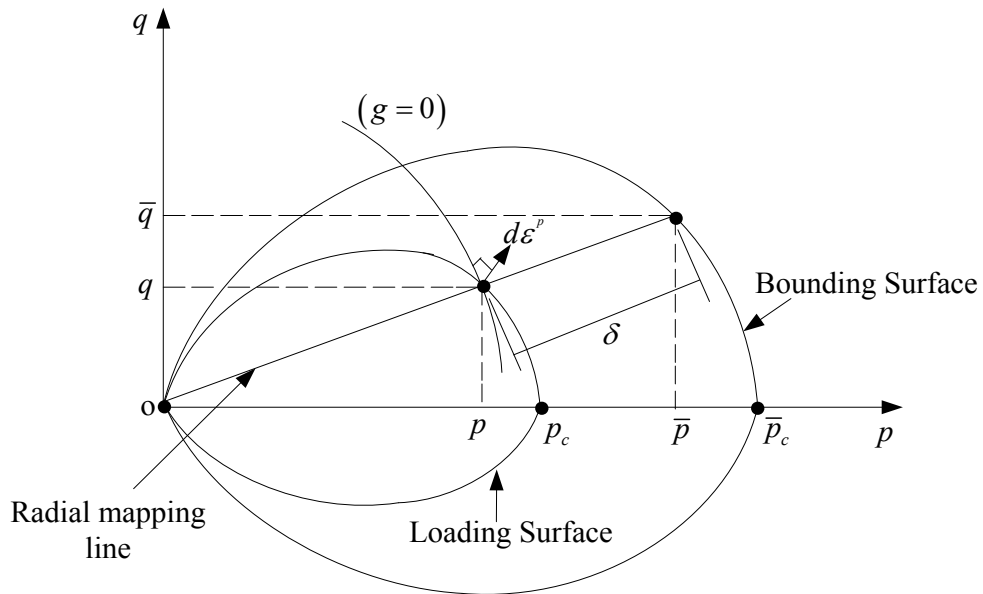


Fig. 2-6 A typical bounding surface model in conventional triaxial stress space for cohesionless sands

2.5.1 Mapping rule

In the bounding surface theory, plastic deformation is allowed to take place when the stress state lies on or within the bounding surface. This is obtained by a specific definition of the plastic modulus that controls the magnitude of the plastic strain within the bounding surface. The plastic modulus can be assumed to be a function of its value at the bounding surface and the distance between the current stress point and its corresponding point on the bounding surface [Chen 1994, Khong 2004]. This association is achieved in radial mapping by intersection of the bounding surface with a line passing through the projection center and the current stress point. The radial mapping formulation apparently was employed for the first time by Hashiguchi and Ueno (1977) without recognizing that they were presenting a bounding surface formulation [Dafalias 1986]. In deviatoric mapping, the association is achieved by intersection of the bounding surface with a vertical line passing through the current stress point and p axis. Crouch et. al. (1994) proposed a combined radial and deviatoric mapping rule by employing the deviatoric mapping for over-consolidated region and the radial mapping for normally consolidated region. This approach, however, did not find popularity. Due to similarity of the shape of the two surfaces, the image stress state (\bar{p}, \bar{q}) can be evaluated using the current stress state (p, q) in radial mapping as follows:

$$\frac{\bar{q}}{\bar{p}} = \frac{q}{p} = \frac{p_c}{\bar{p}_c} = b_p \quad 0 \leq b_p \leq 1 \quad (2.13)$$

Obviously b_p is 0 at the origin and it is equal to 1 at the image point when the loading surface and bounding surface coincide. The identity conditions ($p = \bar{p}$ and $q = \bar{q}$) ensure that two surfaces cannot intersect and hence, it imposes restrictions on their relative evolution [Dafalias 1986].

Changes in the locations of the projection center give rise to changes in the predicted values for \bar{p} and \bar{q} , the plastic modulus of the bounding surface, δ and hence, the plastic modulus of the loading surface. This affects elasto-plastic stiffness and the predicted values for plastic strain increments and thus, elastic strain increments. An interesting case is to consider the projection center at the

center of a kinematic elliptical loading surface in which the projection center evolves with plastic loading. Sensitivity analysis is required to determine if these changes result in better predictions for the model. Dafalias and Herrmann (1982) arrived in better calibration for a soil with large over consolidation ratio using a projection center different from the stress origin.

2.5.2 Plastic modulus at the image point

The plastic modulus at the image point is calculated by the condition that if the stress state lies on the bounding surface (the loading and the bounding surface coincide), a corresponding increment in value of the image stress will occur for any increment of the current stress. That is, the bounding surface undergoes hardening by changing position of the current stress due to plastic deformation (i.e. by hardening of the loading surface). Under this condition, the plastic strain increment is identical to that obtained from a conventional elastic-plastic model with the bounding surface as the yield surface. Thus, [Bardet 1986, Altaee 1992, Reilly and Brown 1991, Khong 2004, Yu 2006, Yu et. al. 2007]:

$$\dot{\varepsilon}_p^p = \frac{1}{\bar{H}} (f_{,p} \dot{p} + f_{,q} \dot{q}) g_{,p} = \frac{1}{\bar{H}} (F_{,\bar{p}} \dot{\bar{p}} + F_{,\bar{q}} \dot{\bar{q}}) g_{,\bar{p}} \quad (2.14)$$

$$\dot{\varepsilon}_q^p = \frac{1}{\bar{H}} (f_{,p} \dot{p} + f_{,q} \dot{q}) g_{,q} = \frac{1}{\bar{H}} (F_{,\bar{p}} \dot{\bar{p}} + F_{,\bar{q}} \dot{\bar{q}}) g_{,\bar{q}} \quad (2.15)$$

\bar{H} denotes the plastic modulus of the bounding surface, superimposed bar indicates variables of the bounding surface, g is plastic potential function, $\dot{\varepsilon}_p^p$ is plastic volumetric strain increment, $\dot{\varepsilon}_q^p$ is plastic deviator strain increment, and $f_{,p}$ stands for derivation of f with respect to p .

The bounding plastic modulus can be calculated by forcing the image stress state to remain on the bounding surface as it changes its size (i.e. consistency condition) as follows [Yu 2006]:

$$\bar{H} = -F_{,\varepsilon_p^p} g_{,\bar{p}} = -F_{,\bar{p}_c} \bar{p}_{c,\varepsilon_p^p} g_{,\bar{p}} \quad (2.16)$$

If the combined volumetric and deviator hardening law is used, the bounding plastic modulus similarly is calculated as follows:

$$\bar{H} = - \left(F_{,\bar{p}_c} \bar{p}_{c,\varepsilon_p^p} g_{,\bar{p}} + F_{,\bar{p}_c} \bar{p}_{c,\varepsilon_q^p} g_{,\bar{q}} \right) \quad (2.17)$$

2.5.3 Plastic modulus at the current stress point

As mentioned, the plastic modulus at the current stress point is assumed to be equal to the plastic modulus at image stress point in addition to another term which relates the dependency of the response to the relative distance between the current stress point and its associated image point (additive plastic modulus) using the following equations:

$$H = \bar{H} \quad \text{if } b_p = 1 \quad \quad H = +\infty \quad \text{if } b_p = 0 \quad (2.18)$$

The restrictions imposed by these equations guarantee that the response under loading/reloading is mainly elastic when the stress state is far away from the bounding surface and that the loading surface and bounding surface coincide when the current stress state lies on the bounding surface [Bardet 1986, Khalili et. al. 2005, Yu et. al. 2007, Suebsuk et. al. 2011].

A typical formula to calculate the plastic modulus of the loading surface is as follows [Dafalias 1986, Russel and Khalili 2004, Khalili et. al 2005, Yu 2006]:

$$H = \bar{H} + A \left(\frac{\delta}{\delta_o - \delta} \right) \quad \delta = \sqrt{(\bar{p} - p)^2 + (\bar{q} - q)^2} \quad (2.19)$$

where A is a (positive) model constant. δ_o is a reference distance such that $\delta_o - \delta \geq 0$.

The distance between the current stress and the corresponding image stress at the beginning of each loading/unloading process (i.e. stress reversal) is chosen as a measure of δ_o [Vermeer and Borst 1984].

Khong (2004) used the following formula for his model, CASM-c:

$$H = \bar{H} + \frac{h(1 - b_p)^s}{p b_p} \quad (2.20)$$

where h and s are two (positive) material parameters.

It is worthwhile to point out that the bounding surface is assumed to evolve with plastic deformation even if the stress point lies inside the surface. This evolution

is based on \bar{H} which is obtained using the consistency condition. It is possible, however, to assume a different scheme. One may hinder the evolution of the bounding surface, until the stress state reaches it, by considering only a portion of the increment in its hardening parameter [Dafalias 1986]. This means using a different value for the bounding plastic modulus, \bar{H}' . When the stress state is on the bounding surface, the entire increment in bounding hardening parameter is considered and hence, $\bar{H}' = \bar{H}$. Even when the stress does not lie on the bounding surface, the value of \bar{H} has to be utilized for calculating the plastic modulus for the loading surface [Dafalias 1986]. It guarantees a continuous change of H since it is always related to \bar{H} even though the abrupt change from \bar{H}' to \bar{H} implies a discontinuous hardening rate for the bounding surface [Dafalias 1986]. A special case is when $\bar{H}' = 0$, i.e. the initial bounding surface (for instance associated with the global maximum shear stress) is kept fixed until it is reached by the current stress, and then, it evolves according to \bar{H} . \bar{H} is used for calculating H even before the beginning of the evolution of the bounding surface. This approach, however, does not appear to be physically sound since it implies a bounding surface that remains fixed or evolves in a restricted way, while plastic deformation occurs within it [Dafalias 1986].

Bardet (1986) assumed that the critical state is reached when H and \bar{H} simultaneously become zero. That is, the two surfaces are supposed to coincide at the critical state. He also noted that the peak shear stress in his model is associated with zero H and non-zero (negative) \bar{H} which implies that two surfaces do not coincide at the peak state. This is because a non-zero (negative) \bar{H} can be cancelled out only by a non-zero positive additive plastic modulus, meaning non-zero δ .

An interesting situation arises when the bounding surface undergoes softening ($\bar{H} < 0$) but $H > 0$ for large values of δ . With the progress of loading and reduction of δ towards zero, H varies smoothly from positive to zero and then negative (while $\bar{H} < 0$) allowing simulation of an initially raising and then falling stress-strain curve [Dafalias 1986].

2.6 Cyclic plasticity theories

2.6.1 Single surface kinematic hardening theory

Kinematic (anisotropic) hardening describes the evolution of material anisotropy in the course of plastic deformation, stress induced anisotropy by virtue of the stress history. This is obtained by translating the yield surface in the stress space [Kavvadas and Amorosi 2000]. Pure kinematic hardening law assumes that the size and shape of the initial yield surface do not change while isotropic hardening assumes uniform expansion/contraction of the yield surface without any change in its location or shape. That is, the yield surface in isotropic hardening models expands/shrinks uniformly to accommodate stress states beyond the current yield surface. Alternatively this can be done by translating the yield surface without any change in its size, kinematic hardening [Reilly and Brown 1991]. Unlike isotropic hardening models in circular yield surfaces such as Von Mises and Drucker-Prager, kinematic hardening fulfills Bauschinger effect observed in the uniaxial tests.

If the initial center of the yield surface lies at the origin, isotropic hardening can be generally described by the following equation [Yu 2006]:

$$f(\sigma_{ij}) - R_y(N) = 0 \quad (2.21)$$

where R_y represents the size of the yield surface as a function of hardening parameter, N , which is a function of the plastic strain.

For pure kinematic hardening, however, yielding is assumed to be a function of the reduced stress tensor as follows:

$$f(\sigma_{ij} - k_{ij}) - R_{y0} = 0 \quad (2.22)$$

k_{ij} (back stress tensor) represents the coordinates of the center of the yield surface and R_{y0} denotes the size of the original yield surface. The evolution of the back stress tensor can be expressed as a function of the plastic strain, stress, back stress itself or a combination of them [Yu 2006].

Another well-known hardening rule is the mixed or combined isotropic-kinematic hardening. It assumes that the yield surface not only uniformly expands or contracts but also translates in the stress space in the course of plastic flow in order to accommodate new states of stress. It can be represented mathematically by the following equation:

$$f(\sigma_{ij} - k_{ij}) - R_y(N) = 0 \quad (2.23)$$

Schematic representation of isotropic hardening, kinematic hardening and mixed hardening is shown in the Figs. 2-7 to 2-9, correspondingly.

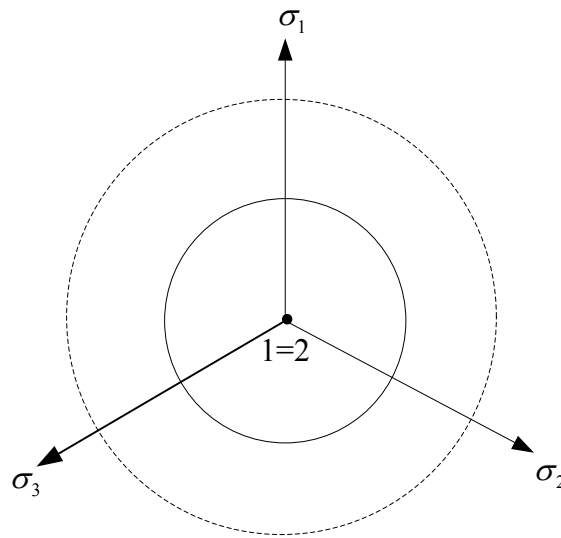


Fig. 2-7 Isotropic hardening for an assumed circular yield surface

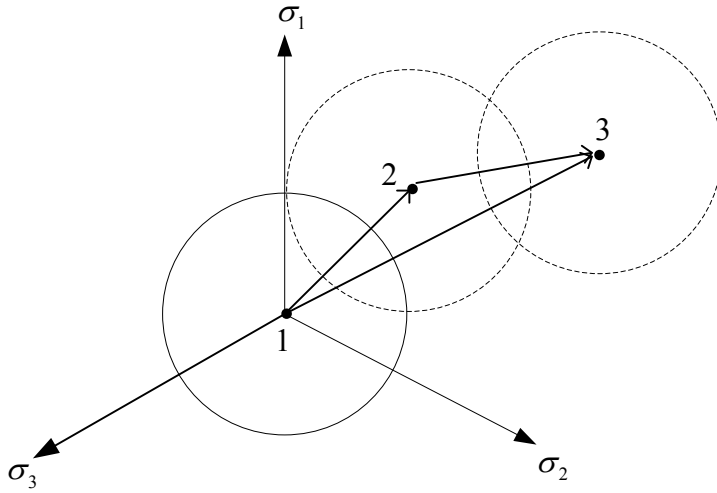


Fig. 2-8 Kinematic hardening for an assumed circular yield surface

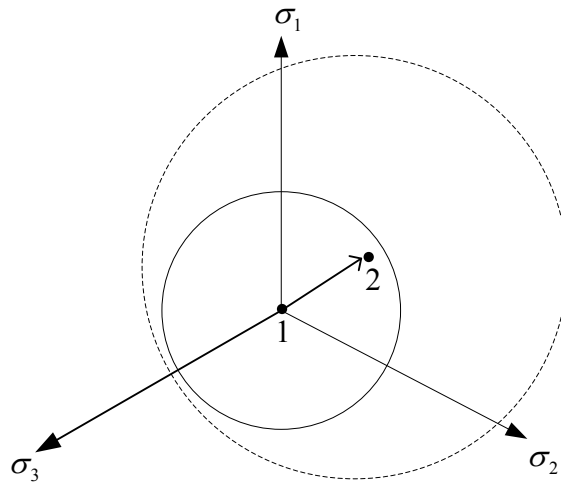


Fig. 2-9 Combined isotropic-kinematic hardening for an assumed circular yield surface

The first kinematic hardening rule was proposed by Prager (1955). He assumed that the yield surface translates in the direction of the plastic strain increment as follows [Chen 1994, Yu 2006]:

$$\dot{k}_{ij} = h_a \dot{\varepsilon}_{ij}^p \quad (2.24)$$

h_a is a material parameter. If an associated flow rule is adopted, the yield surface should translate in the direction of the unit normal to the yield surface according

to this translation rule. This linear evolution rule suggests no evolution of the yield locus within the elastic region.

The second famous kinematic hardening rule was proposed by Ziegler (1959) as follows [Chen 1994, Yu 2006]:

$$\dot{k}_{ij} = d\mu (\sigma_{ij} - k_{ij}) \quad (2.25)$$

where $d\mu$ is not a model constant since it is calculated based on the consistency condition in contrast to Prager's model constant which is chosen arbitrarily [Yu 2006]. This translation rule states that yield surface translates in the direction of $\sigma_{ij} - k_{ij}$.

Ziegler and Prager's rules represent linear kinematic hardening. They produce linear stress-strain response and cannot capture the curvature of the stress-strain response using a continuously varying plastic modulus under a pure kinematic hardening scheme. This renders the use of a nonlinear kinematic hardening rule necessary if one wants to capture the stress-strain behavior using a pure kinematic hardening law. Armstrong and Frederick's kinematic hardening rule is one of the most well-known non-linear kinematic hardening rules. It was initially proposed by Armstrong and Frederick (1966) for metals to account for the kinematic translation of the yield surface using a non-linear rule. It has broadly used in metal engineering in its original or modified forms. The mathematical definition of the original form of this non-linear kinematic hardening rule is expressed by:

$$\dot{k}_{ij} = \frac{2}{3} c_1 \dot{\varepsilon}_{ij}^p - c_2 k_{ij} \dot{z} \quad \dot{z} = \sqrt{\frac{2}{3} \dot{\varepsilon}_{ij}^p \dot{\varepsilon}_{ij}^p} \quad (2.26)$$

where c_1 and c_2 are Armstrong and Frederick's model constants and \dot{z} is the accumulative plastic strain increment.

Simulation of cyclic loading using a single surface kinematic hardening law can be performed based on changes of the stiffness observed during cyclic experiments. Stiffness is expected to decrease during virgin/first loading. It, however, shows a sudden increase immediately after the inception of unloading accompanied with decrease in its magnitude when material undergoes further

unloading. There will be dramatic boost again in the stiffness with the start of reloading accompanied with decline in the stiffness when the soil experiences further reloading [Reilly and Brown 1991]. In general, high stiffness occurs immediately after a change is imposed in the direction of effective stress/strain path [Khong 2004]. Fig. 2-10 illustrates the adopted approach for cyclic loading which is consistent with stiffness changes. Fig. 2-11 shows the assumed movement of a circular yield surface during cyclic loading.

The general formulation of traditional single surface kinematic hardening is almost the same as that for the isotropic hardening. The major difference stems from definition of the plastic modulus and the need for calculation of the back stress evolution in each stress/strain increment. Thus, the general formulation of combined isotropic and kinematic hardening for a strain controlled formulation can be written as:

$$\dot{\sigma}_{ij}^{EP} = (C_{ijmn}^E - C_{ijmn}^P)\dot{\varepsilon}_{mn} \quad C_{ijmn}^P = \frac{C_{ijkl}^E \frac{\partial g}{\partial \sigma_{kl}} \frac{\partial f}{\partial \sigma_{\alpha\beta}} C_{\alpha\beta mn}^E}{H} \quad (2.27)$$

in which:

$$H = -\frac{\partial f}{\partial N} \frac{\partial N}{\partial \varepsilon_{ij}^p} \frac{\partial g}{\partial \sigma_{ij}} + \frac{\partial f}{\partial \sigma_{ij}} C_{ijkl}^E \frac{\partial g}{\partial \sigma_{kl}} + \text{kinematic hardening term} \quad (2.28)$$

The kinematic hardening term depends on the type of selected kinematic hardening rule.

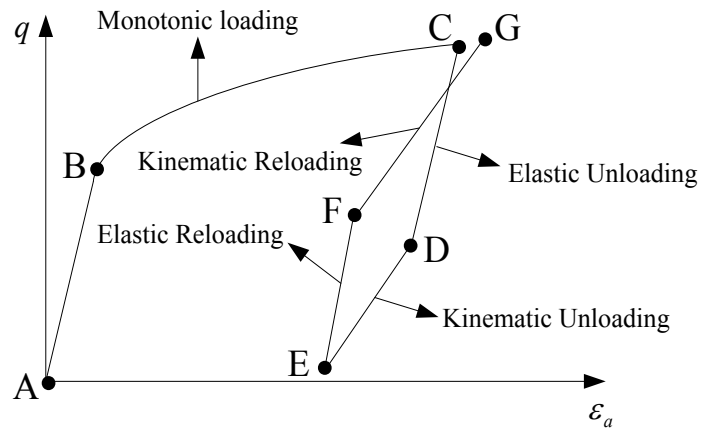


Fig. 2-10 Schematic representation of the approach used for single surface kinematic hardening

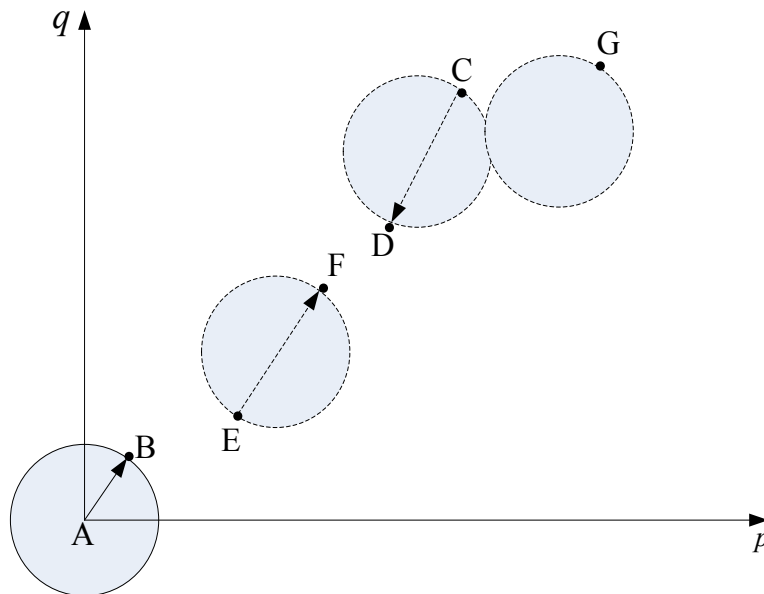


Fig. 2-11 Schematic representation of assumed movement of a circular yield locus during cyclic loading

2.6.2 Multi-surface plasticity theory

Multi-surface theory was introduced originally in the form of a collection of similar nested yield loci, concentric initially around a reference point, to approximate the non-linear stress-strain behavior using a piecewise linear approximation [Yu 2006]. The piecewise linear approximation is provided by a field of plastic moduli which constitutes n linear pieces of constant plastic

moduli. Every yield surface is associated with a constant plastic modulus. The innermost yield surface in this theory represents the domain of pure elastic behavior. The outermost yield surface is referred to as the bounding surface which builds a geometrical boundary in stress space outside which the inner yield loci cannot move. Incorporation of more linear segments (i.e. more yield surfaces) in the model leads to more accuracy in approximation of the nonlinear experimental curves [Prevost 1982, Elgamal et. al. 2003].

All yield loci which are reached by the stress point translate in stress space along a given stress path without any change in their shape or orientation. The activated yield loci sequentially touch and push each other [Yu 2006]. When the stress point reaches f_n , all inner yield surfaces (f_1, f_2, \dots, f_{n-1}) already have translated to become tangential to each other and to f_n at the point of their contact located on f_n . If a stress increment then is imposed, f_n and thus, other inner yield surfaces translate toward the next yield surface, f_{n+1} [Prevost 1982]. The major question is how the yield surfaces move in the stress space. Thus, a translation rule should be applied to govern the evolution of the yield surfaces intercepted by the stress point [Yu 2006]. Iwan (1967) assumed that translation of the current yield surface towards the next yield surface is in direction of the plastic strain increment. This translation rule may result in intersections between sub yield loci [Yu 2006]. Iwan's translation rule is similar to Prager's kinematic hardening rule for single surface plasticity. The model constant in evolution of the back stress tensor in Iwan's translation rule, however, is obtained by the consistency condition unlike that for Prager's rule which is picked up arbitrary. Mroz (1967) in return offered that the yield loci should continuously contact and push each other, but never intersect. Mroz's translation rule states that the current yield surface translates along a vector triggering from the current stress point and ends to a conjugate point on the next yield surface which has the same direction of outward unite normal as the current stress point. This translation rule guarantees that the yield loci never intersect since the yield loci are aligned gradually along the current stress path direction [Elgamal et. al. 2003, Yu 2006]. Mroz et. al (1978 and 1979) later extended the application of multi-surface model to cyclic loading. When

material undergoes unloading, the stress point first reaches the other side of the innermost yield surface, implying that the response is purely elastic before this happens without any translation of the yield surfaces. The stress point arrives at the other side of the outer yield surfaces with progress of unloading. Similar to loading conditions, the yield surfaces under unloading conditions continuously contact each other and become tangential to each other at contact point.

The outstanding feature of the multi-surface theory is that complete determination of the model parameters only demands identification of the initial positions, sizes and plastic moduli of the yield surfaces [Prevost 1982]. Evolution of hardening parameters with plastic strain also should be determined if mixed hardening is adopted. All the yield loci which are reached by the current stress state undergo both translation and uniform expansion/contraction under mixed hardening scheme. The remaining surfaces, however, only expand or contract uniformly.

Translation of the yield surfaces in multi-surface plasticity under pure kinematic hardening can be described using Fig. 2-12.

The two consequent yield surfaces can be mathematically expressed as follows [Yu 2006]:

$$f_i = f(\sigma_{ij} - k_{ij}^i) - R_y^i = 0 \quad f_{i+1} = f(\sigma_{ij} - k_{ij}^{i+1}) - R_y^{i+1} = 0 \quad (2.29)$$

where R_y^i and R_y^{i+1} represent the size of the yield surfaces f_i and f_{i+1} . k_{ij}^i and k_{ij}^{i+1} are the back stress tensors associated with f_i and f_{i+1} , correspondingly.

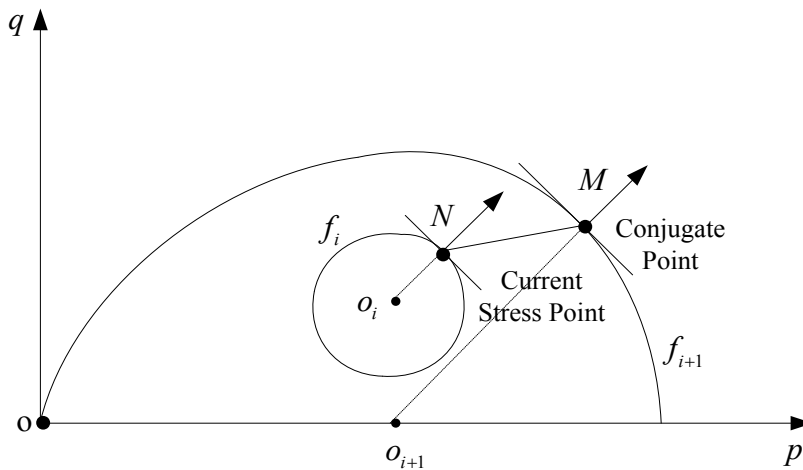


Fig. 2-12 Mroz's Translation rule

Assume the current stress state σ_{ij} (i.e. the point N) lies on the surface f_i . Mroz's translation rule suggests that f_i translates along NM , where M is the conjugate point on f_{i+1} having the same direction of outward normal as N . Based on the size of the (circular) yield surfaces:

$$\frac{R_y^i}{R_y^{i+1}} = \frac{\sigma_{ij}^N - k_{ij}^i}{\sigma_{ij}^M - k_{ij}^{i+1}} \quad (2.30)$$

The yield surface f_i is assumed to translate along NM . Thus,

$$\dot{k}_{ij}^i = h_a (\sigma_{ij}^M - \sigma_{ij}^N) \quad (2.31)$$

h_a is a positive constant. Substituting the expression for σ_{ij}^M from the last equation results in [Yu 2006]:

$$\dot{k}_{ij}^i = \frac{h_a}{R_y^i} [(R_y^{i+1} - R_y^i) \sigma_{ij}^N - (k_{ij}^i R_y^{i+1} - k_{ij}^{i+1} R_y^i)] \quad (2.32)$$

The only unknown for evolution of the back stress tensor of f_i is h_a which is determined by the consistency condition as follows:

$$df_i = \frac{\partial f_i}{\partial \sigma_{ij}} d\sigma_{ij} + \frac{\partial f_i}{\partial k_{ij}^i} dk_{ij}^i = 0 \quad (2.33)$$

Thus [Yu 2006]:

$$h_a = \frac{\frac{\partial f_i}{\partial \sigma_{ij}} d\sigma_{ij}}{\frac{\partial f_i}{\partial \sigma_{kl}} (\sigma_{kl}^M - \sigma_{kl}^N)} \quad (2.34)$$

h_a can be similarly calculated for mixed hardening as follows [Yu 2006]:

$$h_a = \frac{\frac{\partial f_i}{\partial \sigma_{ij}} d\sigma_{ij} + \frac{\partial f_i}{\partial R_y^i} \frac{\partial R_y^i}{\partial \varepsilon_{ij}^p} d\varepsilon_{ij}^p}{\frac{\partial f_i}{\partial \sigma_{kl}} (\sigma_{kl}^M - \sigma_{kl}^N)} \quad (2.35)$$

Application of this translation rule is difficult for non-circular or non-elliptical yield loci. For instance, Vermeer and Borst (1984) believe that this translation rule unlike metals is not proper for frictional materials because the normal to any

point of a Mohr-Coulomb type yield surface cannot correspond to the normal of any point of the next yield surface.

2.6.3 Bounding surface plasticity theory

Multi-surface plasticity models are complex due to the necessity of tracking the sizes and positions of all yield surfaces in the stress space. This excessive storage requirement is one of the most paramount deficiencies of multi-surface plasticity [Prevost 1982, Chen 1994, Suebsuk et. al. 2011, Yang et. al. 2011]. Bounding surface theory was introduced to overcome some of the numerical drawbacks of multi-surface models. For instance, yielding is assumed continuous within the bounding surface in the bounding surface plasticity theory. The inner and outer surfaces are called the loading surface and the bounding surface, respectively [Prevost 1982, Yu 2006]. The most important motivation for using the bounding surface theory is the same as that for using multi-surface theory, characterizing material behavior in response to cyclic loading [Chen 1994].

Bounding surface theory allows a progressive accumulation of plastic strain during loading/reloading and unloading. This means that plastic deformation can occur when the stress state lies on or within the bounding surface. It should be reminded that other names such as two-surface plasticity, limiting surface, distinct yield surface, failure surface, and memory surface have also been used in the literature rather than the bounding surface [Dafalias 1986]. The bounding surface is not necessary a failure surface, although it may be.

The specific feature of the bounding surface concept is that hardening of the loading surface and thus, the magnitude of the plastic strain depends on how near or how far the stress state approaches or leaves the bounding surface. That is, plastic deformation at any stress point inside the bounding surface is computed by defining the plastic modulus of the loading surface as a function of distance between the current stress point from its associated image point on the bounding surface.

Multi-surface plasticity may be considered as a special case of the bounding surface plasticity theory. It is sufficient to consider a piecewise continuous

projection rule and a piecewise change of the loading surface plastic modulus rather than continuous ones which is adopted in the bounding surface formulation [Dafalias 1986]. The relative position of the sub yield surfaces is an indirect measure of the distance of the current stress from the associated image stress and the mapping is achieved through the intermediate image stresses corresponding to conjugate points on temporary surfaces [Dafalias 1986]. Note that the dependency of the plastic modulus on the distance between the current stress point and its associated image stress point have not been introduced in the formulation of multi-surface plasticity theory [Dafalias 1986].

The bounding surface similar to the conventional yield locus has geometrical meaning implying that the stress point can exist on and within the bounding surface, but not outside of it. That is, it defines permissible areas of the current state and provides an exterior limit for the stress state [Khalili et. al. 2008]. It, however, suffers from having a physical meaning unlike the conventional yield surface implying the inception of energy dissipation (the elasto-plastic behavior) when stress state hits the yield surface [Hashiguchi 2009].

A brief historical account on the development of the bounding surface models can be stated as follows:

The bounding surface plasticity for the first time was proposed independently by Dafalias and Popov (1975, 1977) and Krieg (1975) for simulating cyclic response of metals.

Poorooshasb and Pietruszczak (1985) developed a time independent constitutive model using the bounding surface concept. They assumed that the material response is captured using two sets of surfaces with similar shapes, bounding and yield surfaces. The bounding surface is supposed to evolve until a limiting state (i.e. failure) is reached. Upon stress reversal, however, the behavior of the material is predominantly governed by the yield surface which is surrounded by the bounding surface. The model assumes that the principal stress axes are fixed to avoid uncertainties associated with the so called coaxiality condition (coincidence of the axes of the plastic strain increment and those of the total stress tensor) especially for non-associated flow rule. It also assumes non-associated

flow rule and kinematic hardening. However, the model has not been formulated within the critical state framework.

Dafalias and Herrmann (1982) and Dafalias (1986) developed a critical state bounding surface model for soils that employs an associated flow rule, a radial mapping rule and a distance dependent additive plastic modulus. To obtain a better description of the soil response and take into consideration the cohesion of the material, three-segment isotropic bounding surface (two ellipses and one hyperbola) rather than a single one is used. The model was validated only against monotonic experimental tests. It should be pointed out that checking model predictions on the intersection of the surfaces in the stress space is necessary for yield functions constituting two or more intersecting surfaces. These intersections are prone to mathematical singularity [Chen 1994].

Bardet (1986) extended application of the bounding surface plasticity theory to describe nonlinear behavior of sands. The model is based on radial mapping rule and isotropic hardening. He employed the characteristic state line associated with no volume change which defines the transition state between contractive and dilative behaviors. This definition is very similar to definition of the phase transformation line which was introduced initially by Tatsuoka and Ishihara (1974). Different critical state lines are assumed in this model for the same sand under different initial states (i.e. loose and dense sand). The use of an associative flow rule is a major deficiency in Bardet's model. This is in contrast to the behavior of sands since it does not follow the associated flow rule.

Al-Tabbaa (1987) developed a two-surface model which can be perceived as a kinematic extension of the Modified Cam Clay model by introducing a bubble surface inside the bounding surface [Yu 2006]. The bubble is a kinematic loading surface denoting domain of a purely elastic response [Khong 2004]. The model uses associated flow rule and does not take cohesion into account.

Stallebrass (1990) later introduced a third surface called the history surface into theory of the bounding surface plasticity theory. This is based on experimental observations which show the dependency of the stress-strain behavior of overconsolidated clays on both the current stress state and stress state on the

loading history. Another advantage for introducing the third surface is that it produce smoother variation of the plastic modulus [Yu 2006]. The Stallebrass's model is in fact an extension of Al-Tabbaa's model. Similar to Al-Tabbaa's model, it also uses associated flow rule and does not take cohesion into consideration. Further improvement of Stallebrass's model was later carried out by McDowell and Hau (2004) by applying a non-associated flow rule. The modified model, however, still is not suited for cohesive soils.

Crouch et. al. (1994) and Crouch and Wolf (1994) developed isotropic bounding surface for two and three dimensional stress space in the critical state framework. Use of a combined radial and deviatoric mapping, pure isotropic volumetric hardening law, non-associative flow rule and also use of bilinear critical state line in the compression plane ($e - \ln p$) are the main features of these two models.

Rahim (2002) applied the concepts of two-surface plasticity theory, without explicitly referring to the name of the theory, for Modified Cam Clay model. He assumed isotropic yield surface of the Modified Cam Clay model decreases its size to pass through every stress point under an unloading condition. Change in the size of the bounding surface is assumed to be a fraction of that for the loading surface using an extra model parameter. For reloading, however, he assumed the size of the bounding surface remains unchanged until the stress state reaches the bounding surface.

The model created more recently by Russel and Khalili (2004) and Khalili et. al. (2005, 2006) employs a bounding surface similar to the yield function which was introduced by Yu (1998) and a limiting isotropic compression line as a reference for the high pressure region. It was defined for sand as the locus of the loosest possible state the sand can reach. In order to capture grain crushing at high stresses, the critical state line in compression is expressed in three linear segments. Excluding Khalili et. al (2006) which uses kinematic hardening, isotropic hardening is used in two other models. All of them, however, have been proposed for cohesionless soils.

Khong (2004) developed a unified bounding surface model to capture cyclic response of both sand and clay. The original model proposed by Yu (1998) is

called CASM-a. It uses the state parameter concept and a non-associated flow rule. Later Khong (2004) developed a new model called CASM-b. CASM-b is based on radial mapping formulation of the bounding surface plasticity theory. That is, CASM-b is extended version of CASM-a allowing evaluation of the plastic deformation inside the bounding surface. However, CASM-b is proper for monotonic loading only since it was only formulated for loading conditions. Also a purely elastic response was assumed for unloading, meaning no plastic strain is anticipated under unloading conditions. The newest version of CASM was created by improving performance of CASM-b for modeling cyclic behavior. This model called CASM-c divides a general stress path into three distinct offshoots: virgin shear loading, unloading and reloading, then a different formula is applied to determine the plastic modulus in every offshoot [Khong 2004, Yu 2006, Yu et. al. 2007]. CASM-c was proposed for cyclic loading of cohesionless soils.

By incorporating the mobile projection center, Yang et. al. (2011) modified a bounding surface-generalized plasticity model which has already been created for structured soils. They assume that the projection center moves from its initial location to the inception point of the stress reversal. Isotropic hardening modulus for both unloading and reloading is unified using this concept. An associated flow rule was also adopted for the model.

2.7 Volume change and stress-strain behaviour of sand and cemented sand

Volume changes in sands are important since they cause changes in strength, deformation properties, and stiffness and therefore influence stability. Changes in volume can occur due to applied stresses, temperature, and so on. However, (hydrostatic and particularly shear) stress induced volume changes are the most important ones for most practical applications [Mitchell and Soga 2005]. Volume changes for sands during conventional drained triaxial monotonic tests is shown typically in terms of the void ratio vs. shear strain in Fig. 2-13.

Both loose and dense sands (under the same cell pressure) ultimately approaches nearly the same void ratio beyond which further shear strain will not lead to any

volume changes. This void ratio which may be considered as reference void ratio is referred to as the critical void ratio (e_{cr}) [Ranjan and Rao2005, Venkatramaiah 2006]. Sands with initial void ratio larger than the critical void ratio (i.e. loose sands) tend to decrease their volume continuously throughout shearing. However sands with initial void ratio less than the critical value (i.e. dense sand) tend to increase their volume after an initial reduction in volume. The reason is that sand particles prefer to move apart/dilate in dense sand and move close/contract in loose sand [Gulhati and Datta 2008]. That is, shear force on loose sands causes grains to fall into large voids existing between grains resulting on void ratio reduction, while for dense sands it causes grains to climb up adjacent grains leading to void ratio increase [Martinez 2003, Towhata 2008].

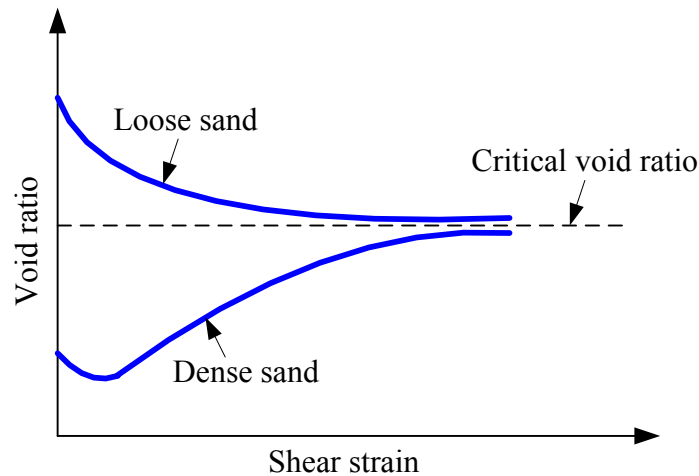


Fig. 2-13 Effect of initial void ratio on volume changes of sands during drained triaxial tests

Under triaxial undrained condition, pore pressure increases throughout shearing for loose sand while it decreases at large shear strains after an initial increase at small shear strains for dense sand (see Fig. 2-14) [Mitchell and Soga 2005, Venkatramaiah 2006] The reason is that volume change is prevented during undrained condition. Therefore tendency for compression and dilation is balanced by positive and negative pore pressure generation, respectively. Since no volume change occurs at the critical void ratio, no pore pressure increment occurs as well, meaning pore pressure remains constant at the critical void ratio. Therefore the critical void ratio provides a basis by which volume changes under drained

condition and pore pressure changes under undrained condition can be predicted [Ranjan and Rao2005]. These specific changes of void ratio/specific volume are salient feature of the critical state theory. Schofield and Wroth (1968) and Mitchell and Soga (2005) define the critical state as follows:

After a large shear induced volume change at a given effective confining pressure, a soil ultimately will reach a unique constant void ratio which is intrinsic to the soil (i.e. independent of its initial density, fabric, and so on). At this stage, interlocking already achieved due to densification or over consolidation is destroyed in the case of dense soils and for loose soils the metastable structure is lost and the soil is fully destructed. Once this occurs, the soil is said to have reached its critical state strength during which shear deformation occurs without any resistance. The critical state can be used as a reference state to explain the effect of void ratio/density and overconsolidation ratios, on strength properties of the soils.

Wan and Guo (2004) believe that the critical state void ratio is not unique for different sand specimens with a given initial void ratio and effective confining pressure if their initial fabric is not the same.

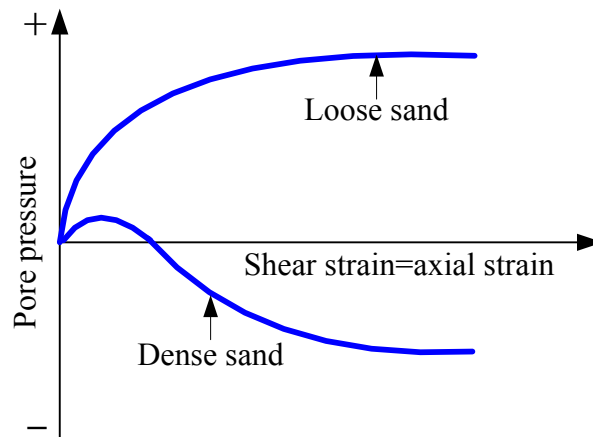


Fig. 2-14 Pore pressure generation during undrained triaxial tests on loose and dense sands

The critical void ratio can be determined experimentally. It is determined under a given set of initial conditions by plotting the volume change versus void ratio. The void ratio for which the volume change is zero is the critical void ratio [Venkatramaiah 2006]. If similar tests are conducted but under different cell

pressures and the critical void ratio associated with each cell pressure is determined similarly, we can obtain a formula which relates the critical void ratio to (mean effective) pressure. This is usually obtained in a semi-logarithm plot (i.e. e_{cr} vs. $\ln p$) (for example see Bardet 1986, Yu et. a. 2007). Imam (1999) and Lee et. al. (2004), however, used a third order polynomial equation to fit the experimental data of e_{cr} vs. p . The relationship between the critical void ratio and mean effective stress forms the critical state line in the compression plane.

As mentioned, sand samples at the same confining pressure but different initial void ratio have different volumetric response. However this does not mean sand samples with the same initial void ratio have necessarily the same volumetric behaviour since the critical void ratio depends on the cell pressure (i.e. confining pressure) [Venkatramaiah 2006]. That is, in addition to void ratio/porosity dependency, mechanical behaviour of sands is pressure sensitive similar to other geomaterials and unlike metal. It means the typical volumetric behaviour of sands can change with change in magnitude of (confining) pressure. Loose sands may dilate if the confining pressure is very low or dense sands may show tendency for progressive compression if the confining pressure is large enough [Ranjan and Rao2005]. Note that the effective mean pressure also acts as a frictional factor for geomaterials since an increase in p causes an increase in shear strength and stiffness (i.e. elastic modulus). At a given effective confining pressure, the shear strength of sands consists of two parts [Venkatramaiah 2006]: a) the internal frictional resistance between grains, and b) Interlocking (i.e. locking of one particle by the adjacent particles). Interlocking which resists deformation/particle sliding contributes a significant portion of the shearing strength in dense sands, while its contribution in shearing strength of loose sand is negligible. Its magnitude depends on shape of the grains and their initial packing arrangements. The internal friction angle is a measure of the resistance of sands against sliding. It is a very important factor in shearing strength of cohesionless sands [Venkatramaiah 2006].

In addition to volumetric behaviour, the stress-strain behaviour of sands also depends on the initial density/void ratio. The typical stress-strain behaviour for

loose and dense sands under drained and undrained conditions are shown in Figs. 2-15 to 2-16.

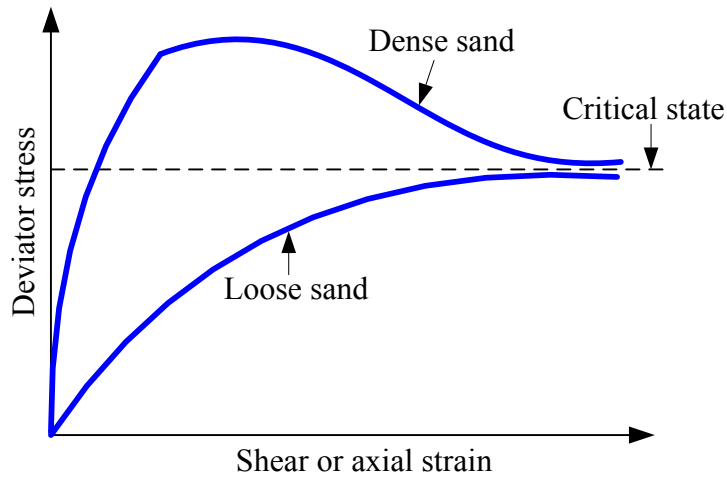


Fig. 2-15 Typical stress-strain curves for sands under drained triaxial tests

The deviator stress reaches a clear peak in dense sands and then falls in post peak region under drained shear, while it builds up gradually for loose sands until it reaches the critical state. Denser sands have larger strength and stiffness compared to looser sands which is expected. Behaviour of medium sand is intermediate to that of loose and dense sands. Therefore dense sands can tolerate higher amount of the deviator stress at low shear strains compared to loose sands since they are stronger. With increase in shear strain during drained shearing, however, the dense sands soften as their volume increase, while loose sands harden as their volume decrease without exhibiting any distinct peak strength. At very large shear strains, however, density of loose and dense sand samples become comparable and thus so do their strengths [Gulhati and Datta 2008]. These are typical stress-strain for sands under drained shear. If dense and loose sands undergo drained shear under high and low confining pressures, respectively, they may show ductile and brittle responses, accordingly. Note also that initial void ratio of in-situ sands tends to be denser than critical void ratio for most situations [Jefferies 1993].

Samples with the same initial void ratio and confining pressure can also show different stress-strain and volumetric behaviour also if their fabrics are not the

same since initial fabric (i.e. grain contact anisotropy) plays an important role in the subsequent deformation [Jefferies 1993, Mitchell and Soga 2005]. Chapter 6 elaborates the effects of fabric and intermediate principal stress on mechanical response of granular materials.

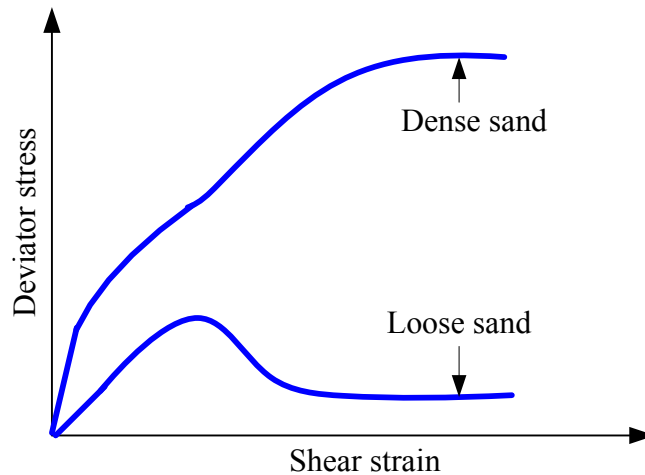


Fig. 2-16 Typical stress-strain curves for sands under undrained triaxial tests

Dense sands continuously harden under undrained shearing, while loose sands experience sudden loss of the strength after reaching the peak deviator stress. Medium sands are expected to undergo loss of the strength in post peak region as well. However the decrease in the strength is temporary (i.e. the quasi steady state behavior occurs) since they again harden with further straining until they reach to the critical state [Wan and Guo 2001b, Mitchell and Soga 2005]. Therefore in addition to initial density, confining pressure/mean effective stress, friction angle, interlocking, and fabric, the drainage condition (i.e. drained or undrained) affects the shear strength of granular materials. Clearly intensity of the cementation bonds between sand particles is a very important factor which affects the shear strength of granular materials too.

Shear resistance in cemented sands or sandstone in general constitutes of two major components: the cementation bonds between sand grains, and the frictional component which resists particle sliding [Clough et al. 1981]. The type and amount of cementing agent and the number of particle contacts are influential factors which affect the strength of cementation bonds and therefore the shear

strength of cemented sand/sandstone [Consoli et al. 2012]. With an increase in the degree of cementation, peak strength, tensile strength and stiffness of the material increase. Cementation also results in a more brittle and dilatant behaviour and is more significant than friction at low confining pressures [Clough et al. 1981]. The failure mode is usually brittle for cemented sand at lower confining pressures and ductile at higher pressures. At higher confining pressures, the frictional component is more dominant, resulting in a more ductile response. That is, the contribution of the cementation and friction in the shearing resistance may change depending on the confining pressure. However, cementation contributes significantly in cemented sand resistance for heavily cemented sand even at higher confining pressures [Clough et al. 1981]. Chapter 4 and 5 provide relatively comprehensive discussion on frictional resistance of cemented sands. Frictional characteristics of uncemented and cemented sands are also compared in these chapters. It should be pointed out that type of tests, mineralogy, grain size and grain shape (i.e. sorting), and grain size distribution also affect the shearing resistance of granular materials [Mitchell and Soga 2005].

Cyclic loading of sands usually causes densification [Mitchell and Soga 2005]. Void ratio decreases continuously in the case of loose sands until the cyclic liquefaction occurs. However for dense sands, the void ratio does not decrease continuously but fluctuates with cyclic loading [Pradhan 1989, Chung 2010]. That is, dense sand initially contracts during loading and unloading, however, when the stress path reaches the phase transformation line (i.e. when it reaches its maximum contraction under a given deviator and effective mean stress), the sand dilates. The sand response becomes compressive again when stress reversal occurs and it continues until the stress path reaches the phase transformation line again, where the void ratio increases again. These fluctuations between the contractive and dilative behaviour cause the dense sand to strengthen and weaken, respectively, with progress of cyclic loading [Elgamal et. al. 2003, Lenart 2008]. However, overall behaviour results in contraction (i.e. void ratio reduction) [Mitchell and Soga 2005]. Chapter 4 and 5 provide several examples of two-way and one-way cyclic loading on different uncemented and cemented sands.

2.8 Methodology

The critical state constitutive model with a capped yield surface seems to be a decent choice in simulating the behaviour of cohesionless and weakly cemented sands. This is because the density and pressure dependency of the sand behaviour can be captured by critical state constitutive models. Moreover the pore collapse failure (which occurs under high effective consolidation pressures and very small deviator stresses in highly porous geomaterials) can be captured by yield functions which have a distinct cap portion. A critical state constitutive model which was developed already by Imam (1999) is chosen as the base model for this purpose. The model uses a capped yield surface which is characterized by its size and shape. They are determined by the effective preconsolidation pressure, and the stress ratio at the peak of the undrained effective stress path, respectively. The capped yield surface is also a function of the stress ratio, confining pressure, and an indirect function of the state parameter and void ratio. Hardening in this model depends on proximity to the critical state line since components of the hardening rule, the failure mean effective stress and effective preconsolidation stress, are function of the state parameter in each stress or strain increment. The proposed model was validated against different directions and modes of shearing over a broad range of specific volumes and effective consolidation pressures (see Imam et. al. 2005).

To properly model the stress-strain and volumetric behaviour of cohesionless sands under cyclic loading, the bounding surface plasticity framework is used. This theory allows plastic deformation to occur throughout shearing including unloading and reloading when the stress path lies inside the yield locus. Some modifications also are carried out in formulation of the original model. The proposed modified model then is calibrated and validated against triaxial cyclic loading tests for selected sands. Predictive capability of the upgraded model is promising since it can capture the important characteristics of sand under cyclic loading (see chapter 3).

To predict mechanical response of cemented sands/soft sandstone, tensile strength and cohesion are integrated into the constitutive relationships. Major components

of the original model including the yield function, elastic properties, hardening rule, and plastic potential function are also modified to make the constitutive model more suitable for cemented granular sands. Having implemented these modifications, the radial mapping formulation of bounding surface plasticity theory is then incorporated in the model. Finally, performance of the proposed model is examined according to experimental observations of different cemented sands under monotonic loadings (see chapter 4).

To model cyclic behaviour of cemented sands or (very) weak sandstone, the proposed model still needs further modifications. Initially similar modifications which were performed to model cyclic response of uncemented sands are implemented in the constitutive model of cemented sands. To capture hysteresis loops, then elastic moduli during unloading conditions are modified using those of loading conditions. This improvement in model formulation causes prediction of initially stiffer response at commencement of unloading and then a softer response with progress of unloading. This is in accordance with experimental observations which suggest material stiffness increases immediately after stress reversal occurs and decreases with progress of unloading/reloading until the next stress reversal occurs [Reilly and Brown 1991]. The primary mechanism for mechanical degradation of cemented sand/weak sandstone in this bounding surface model is attributed to destruction of the cementation bonds by plastic deformation. Comparison between experimental observations and numerical predictions shows fair ability of the proposed model in predicting monotonic and cyclic behaviour of cemented sands/weak sandstone. Hysteresis loops in cyclic tests are also captured with fair accuracy (see chapter 5).

To extend application of the proposed constitutive model in capturing the intrinsic anisotropy, further improvements are required. This is performed by integrating fabric tensor which accounts for inherent or structural anisotropy and a scalar-valued state variable, which are indirectly incorporated into equation of the loading surface, and therefore in hardening rule, and dilatancy relationship. To capture effect of the intermediate principal stress on mechanical behaviour of the material, the b -parameter also is integrated into formulation of the model.

Ultimately, the model performance is assessed based on hollow cylinder tests (see chapter 6).

The proposed constitutive models in chapters 3-6 are implemented in FLAC 2D which is a commercial finite difference software developed by ITASCA. The implementation is written in FISH which is a programming language in FLAC. FLAC uses the proposed constitutive model as a user defined constitutive model to simulate stress-strain and volumetric behaviour of the material under a set of initial, boundary, and loading conditions. All simulations in the following chapters were performed using FLAC (except those in chapter 3) which have been modeled using single grid block/element. FLAC simulations show some oscillations in the prediction of pore pressure and hence mean effective stress for two-way undrained triaxial cyclic loading. Therefore predictions of 1D model (implemented in Excel) are used in chapter 3.

Note that general agreement between trend of experimental observations and model predictions is considered as a criterion for assessing the model performance in this work. The assessment is based on visual comparison between measured and predicted results.

2.9 Conclusion

A constitutive model is required to predict rock mechanical deformation during life of a production/injection well. Such predictions can be performed ideally before the well is put in production/injection line. They help operators to realize which production/injection rate, or pressure drawdown can be applied safely to avoid possible sanding. If they know that sanding is likelihood after for instance a certain number of cycles, preventive measure can be adopted to curb remarkable costs or damages which can be imposed by sand production.

The critical state constitutive framework accompanied with state parameter concept appears to be a good choice for sanding analysis. The advantage of critical state model is that it includes void ratio/porosity in its formulation which is in accordance with experimental observations which indicate void ratio/specific volume dependency of sand/cemented sand behavior. This is in contrast to

conventional non-critical state models which do not directly include void ratio in their formulation.

To investigate material behavior under cyclic loading, the critical state constitutive model should be integrated in a proper elasto-plastic theory. The bounding surface plasticity theory seems to be a suitable selection since it can capture elasto-plastic deformation in the course of unloading-reloading cycles. This is unlike classical plasticity which assumes pure elastic response for any stress path inside the yield surface. Even though small plastic deformation may occur when stress path is inside the yield surface under unloading-reloading conditions, it will accumulate during subsequent cycles. Therefore inaccurate results may be predicted by a model if plastic deformation is neglected under unloading and reloading conditions when material is subjected to many cycles.

2.10 References

Abdulazeez, A. (1994), Constitutive modeling of rocks and numerical simulation of oil reservoirs exhibiting pore collapse, Ph.D. thesis, The university of Oklahoma, Oklahoma, USA.

Alejano, L.R., and Alonso.E. (2005), Consideration of dilation angle and rock masses, *International Journal of Rock Mechanics & Mining Sciences*, Vol. 42, pp. 481–507.

Al-Tabbaa, A. (1987), Permeability and stress-strain response of Speswhite kaolin, Ph.D. thesis, The University of Cambridge, Cambridge, U.K.

Altaee, A.A. (1992), Finite element implementation validation and deep foundation application of a bounding surface plasticity model, Ph.D. thesis, The University of Ottawa, Ottawa, Canada.

Bardet, J.P. (1986), Bounding surface plasticity model for sands, *Journal of Engineering Mechanics*, Vol. 112, No. 11, pp. 1198-1217.

Been, K., and Jefferies, M. G. (1985), A state parameter for sands, *Géotechnique*, Vol. 35, No. 2, pp. 99-112.

Bellarby, J. (2009), *Well completion design*, Elsevier, Netherlands.

Challa, V. (2005), Influence of third invariant of deviatoric stress and intermediate principal stress on constitutive models and localization conditions for high porosity sandstone, Ph.D. thesis, Clarkson University, Potsdam, USA.

Chen, W.F. (1994), *Constitutive equations for engineering materials*, Elsevier, Netherlands.

Choi, S.K., and Huang, W.S. (2011), Impact of water hammer in deep sea water injection wells, SPE 146300, pp. 1-14.

Chung, A.B. (2010), *Unifies modeling for sand under generalized stress paths*, Ph.D. thesis, Columbia University, New York, USA.

Clough, G.W., Shafii Rad, N., Bachus, R.C., and Sitar, N. (1981), Cemented sands under static loading, *Journal of the geotechnical engineering division*, Vol. 107, No. 6, pp. 799-817.

Colmenares, L.B., and Zoback, M.D. (2002), A statistical evaluation of intact rock failure criteria constrained by polyaxial test data for five different rocks, *International Journal of Rock Mechanics and Mining Sciences*, Vol. 39, pp. 695-729.

Consoli, N.C., Cruz, R.C., Fonseca, A.V.D., and Coop, M.R. (2012), Influence of Cement-Voids Ratio on Stress-Dilatancy Behavior of Artificially Cemented Sand, *Journal of geotechnical and geoenvironmental engineering*, Vol. 138, No. 1, pp. 100-109.

Crouch, R.S., and Wolf, J.P. (1994), Unified 3D critical-state bounding-surface model for soils incorporating continuous plastic loading under cyclic paths. Part I: constitutive relations, *International journal for numerical and analytical methods in geomechanics*, Vol. 18, No. 11, pp. 735-758.

Crouch, R.S., Wolf, J.P., and Dafalias, Y.F. (1994), Unified critical-state bounding-surface plasticity model for soils, *Journal of Engineering Mechanics*, Vol. 120, No. 11, pp. 2251-2270.

Dafalias, Y.F. (1986), Bounding Surface Plasticity. I: Mathematical foundation and hypoplasticity, *Journal of Engineering Mechanics*, Vol. 112, No. 9, pp. 966-987.

Dafalias, Y.F., and Herrmann, L.R. (1982), Bounding surface formulation of soil plasticity, *Soil Mechanics-Transient and Cyclic Loads*, Wiley, pp. 253-282.

Dafalias, Y.F., and Popov, E.P. (1975), A model of nonlinearly hardening materials for complex loading, *Acta Mechanica*, Vol. 21, pp. 173-192.

Dafalias, Y.F., and Popov, E.P. (1977), Cyclic loading for materials with a vanishing elastic region, *Nuclear Energy and Design*, Vol. 41, pp. 293-302.

Desai, C. S. (2001), *Mechanics of materials and interfaces: The disturbed state concept*, CRC Press, USA.

De Souza, A.L.S., de Souza, J.A.B., Meurer, G.B., Naveira, V.P., and Chaves, R.A.P. (2012), Reservoir geomechanics study for deepwater field identifies ways

to maximize reservoir performance while reducing geomechanics risks, SPE 160329, pp. 1-19.

Economides, M.J., and Nolte, K.G (2000), Reservoir stimulation, Third edition, John Wiley and Sons, USA.

Elgamal, A., Yang, Z., Parra, E. and Regheb, A. (2003), Modeling of cyclic mobility in saturated cohesionless soils, International Journal of Plasticity, Vol. 19, pp. 883-905.

Ewy, R.T. (1998), Wellbore stability predictions using a modified lade criterion, SPE/ISRM 47251, PP. 247-254.

Fjar, E., Holt, R.M., Horsrud, P., Raaen, A.M., and Risnes, R. (2008), Petroleum related rock mechanics, Elsevier, UK.

Gadde, M.M., and Rusnak, J.A. (2008), Applicability of Drucker-Prager failure criterion to estimate polyaxial rock strength, ARMA 08-137.

Gulhati, S.K., and Datta, M. (2008), Geotechnical engineering, McGraw Hill company, India.

Grueschow, E. R. (2005), Yield cap constitutive models for predicting compaction localization in high porosity sandstone, Ph.D. thesis, Northwestern University, Chicago, USA.

Hashiguchi, K. (2009), Elastoplasticity theory, Springer-verlag, Germany.

Hashiguchi, K., and Ueno, M. (1977), Elasto-plastic constitutive laws of granular materials, 9th International Conference on Soil Mechanics and Foundation Engineering, Japan, pp. 73-82.

Han, G., Ioannidis, M., and Dusseault, M.B. (2003), Semi-analytical solutions for the effect of well shut-down on rock stability, Journal of Canadian Petroleum Technology, Vol. 42, No. 12, pp. 46-53.

Hickman, R.J. (2004), Formulation and implementation of a constitutive model for soft rock, Ph.D. thesis, Virginia Polytechnic Institute and State University, Virginia, USA.

Hoek E. (2007), Practical Rock Engineering, www.rocscience.com.

Imam, M.R., Chan, D.H., Robertson, P.K., and Morgenstern, N.R. (2002a), effect of anisotropic yielding on the flow liquefaction of loose sand, Soils sand Foundations, Vol. 42, No. 3, pp. 33-44.

Imam, M.R., Morgenstern, N.R., Robertson, P.K., and Chan, D.H. (2002b), Yielding and flow liquefaction of loose sand, Soils sand Foundations, Vol. 42, No.3, pp. 19-31.

- Iwan, W.D. (1967), On a class of models for the yielding behaviour of continuous and composite systems, *Journal of Applied Mechanics*, Vol. 34, pp. 612-617.
- Jardine, S.I., Johnson A.B., and Stibbs, W. (1993), Hard or soft shut-in: which is the best approach?, *SPE* 25712.
- Jefferies, M.G. (1993), Nor-Sand: a simple critical state model for sand, *Géotechnique*, Vol. 43, No. 1, pp. 91-103.
- Jefferies, M., and Been, K. (2000), Implications for critical state theory from isotropic compression of sand, *Geotechnique*, Vol. 50, No.4, pp. 419-429.
- Kappos, A. J. (2002), *Dynamic loading and design of structures*, Taylor & Francis Group, USA.
- Kavvadas, M., and Amorosi, A. (2000), A constitutive model for structured soils, *Géotechnique*, pp. 263 –273.
- Khalili, N., Habte, M. A., and Valliappan S. (2005), A bounding surface plasticity model for cyclic loading of granular soils, *International Journal For Numerical Methods In Engineering*, Vol. 63, pp. 1939–1960.
- Khalili, N., Habte, M. A., and Valliappan S. (2006), Monotonic and cyclic analysis of granular soils, *Computational Methods in Engineering and Science*, China, pp. 59-70.
- Khalili, N., and Liu, M.D. (2008), A bounding surface plasticity model for soils with stress increment direction dependent plastic potential, 12th international conference of international association for computer methods and advances in geomechanics, Goa, India.
- Khong, CD. (2004), Development and numerical evaluation of unified critical state models, PhD thesis, The University of Nottingham, Nottingham, U.K.
- Krieg, R.D. (1975), A practical two-surface plasticity theory, *Journal of Applied Mechanics*, Vol. 42, No. 3, pp. 641-646.
- Lenart S. (2008), The response of saturated soils to a dynamic load. *Acta Geotechnica Slovenica*, Vol. 5, No. 1, pp. 37-49.
- Liu, Y., Wan, R.G., and Jian, Z. (2008), Effects of foamy oil and geomechanics on cold production, *Journal of Canadian Petroleum Technology*, Vol. 47, No. 4, pp. 1-7.
- Martinez, B. N. (2003), Strength properties of granular materials, M.Sc. thesis, Louisiana State University, Louisiana, USA.
- Martinez, J.M. (2014), Elastic properties of sedimentary rocks, Ph.D. thesis, The university of Alberta, Edmonton, Canada.

- Mathis, S.P. (2003), Sand management: A review of approaches and concerns, SPE 82240, pp. 1-7.
- Mielke, A., and Roubicek, T. (2003). A rate-independent model for inelastic behavior of shape-memory alloys, *Multiscale Modeling and Simulation*, Vol. 1, No. 4, pp. 571-597.
- Michelis, P. (1987), True triaxial cyclic behavior of concrete and rock in compression, *International Journal of Plasticity*, Vol. 3, pp. 249-270.
- Minassian, G.H. (2003), Behavior of granular materials under cyclic and repeated loading, Ph.D. thesis, University of Alaska Fairbanks, Alaska, USA.
- Mitchell, J. K., and Soga, K. (2005), *Fundamentals of soil behavior*, Third edition, John Wiley & Sons, USA.
- Morita, N., and Fuh, G.F. (1998), Prediction of sand problems of a horizontal well from sand production histories of perforated cased wells, SPE 48975, pp. 113-119.
- Mroz, Z., (1967), On the description of anisotropic hardening, *Journal of the Mechanics and Physics of Solids*, Vol. 15, pp. 163-175.
- Mroz, Z., Norris, V. A. and Zienkiewicz, O.C. (1978), An anisotropic hardening model for soils and its application to cyclic loading, *International Journal for Numerical and Analytical methods in Geomechanics*, Vol. 2 ,pp. 203-221.
- Mroz, Z., Norris, V. A. and Zienkiewicz, O.C. (1979), Application of an anisotropic hardening model in the-analysis of elasto-plastic deformation of soils, *Géotechnique*, Vol. 29, No. 1, pp. 1-34.
- Nasr, M.S., and Edbieb, S.M. (2012), Effect of sand production on the productivity of oil wells in unconsolidated sandstone reservoirs in Sirte basin Libya (field case study), 19th Annual India Oil & Gas Review Summit & International Exhibition, Mumbai.
- Nawrocki, P.A. (2010), Critical wellbore pressures using different rock failure criteria, *ISRM International Symposium and 6th Asian Rock Mechanics Symposium*, New Delhi, India.
- Nouri, A., Kuru, E. and Vaziri, H. (2009), Elastoplastic modeling of sand production using fracture energy regularization method, *Journal of Canadian Petroleum Technology*, Vol. 48, No. 4, pp. 64-71.
- Nouri, A., Vaziri, H., Belhaj, H., and Islam, R.(2003), A comprehensive approach to modeling sanding during oil production, SPE 81032, pp. 1-7.
- Nouri, A., Vaziri, H., Kuru, E., and Islam, R. (2006), A comparison of two sanding criteria in physical and numerical modeling of sand production, *Journal of Petroleum Science and Engineering*, Vol. 50, pp. 55-70.

- Oluyemi, G.F., and Oyemeyin, M. B. (2010), Analytical critical drawdown (CDD) failure model for real time sanding potential prediction based on Hoek and Brown failure criterion, *Journal of Petroleum and Gas Engineering*, Vol. 1, No. 2, pp. 16-27.
- Pando, M. A. (1995), The effect of the degree of shear stress reversal on the liquefaction potential of saturated sands, M.Sc. thesis, The university of Alberta, Edmonton, Canada.
- Perkins, T.K., and Gonzalez, J.A. (1985), The effect of thermoelastic stresses on injection well fracturing, *SPE 11332-PA*, Vol. 25, No. 1, pp. 78-88.
- Poorooshab, H.B., and pietruszczak, S. (1985), On yielding and flow of sand; a generalized two-surface model, *Computers and Geotechnics*, Vol. 1, No. 1 , pp. 33-58.
- Pradhan, T. B. S. (1989), The behavior of sand subjected to monotonic and cyclic loadings, Ph.D. thesis, Kyoto University, Kyoto, Japan.
- Prager, W. (1955), The theory of plasticity-a survey of recent achievement, *Proceedings of the Institution of Mechanical Engineers*, London, pp. 3-19.
- Prevost, J.H. (1982), Two-surface versus multi-surface plasticity theories: A critical assessment, *International journal for numerical and analytical methods in geomechanics*, Vol. 6, pp. 323-338.
- Querol, S.L., and Blázquez, R. (2006), Liquefaction and cyclic mobility model for saturated granular media, *International Journal for Numerical and Analytical Methods in Geomechanics*, Vol. 30, pp. 413-439.
- Rahim, Amir (2002), Simple cyclic loading model based on Modified Cam Clay, CRISP company.
- Rahmati, H., Jafarpour, M., Azadbakht, S., Nouri, A., Vaziri, H., Chan, D., and Xiao, Y. (2013), Review of sand production prediction models, *Journal of Petroleum Engineering*, Review Article, pp. 1-16.
- Ranjan, G., and Rao A.S. (2005), *Basic and applied soil mechanics*, New age international publisher, India.
- Rascol, E. (2009), *Cyclic Properties of Sand: Dynamic behaviour for seismic applications*, Ph.D. thesis, University of EPFL, Lausanne, Switzerland.
- Reilly, M.P.O, and Brown, S.F. (1991), *Cyclic loading of soils: from theory to design*, Blackie and son limited, U.K.
- Roscoe, K. H., Schofield, A. N., and Wroth, C. P. (1958), On the yielding of soils, *Getechnique*, Vol. 8, No. 1, pp. 22-52.

- Roshan, H. (2011), Three dimensional non-linear anisotropic thermo-chemo-poro-elastoplastic modeling of borehole stability in chemically active rocks, Ph.D. thesis, University of New South Wales, Sydney, Australia.
- Russel, A., and Khalili N. (2004), A bounding surface plasticity model for sands exhibiting particle crushing, *Canadian Geotechnical Journal*, Vol. 41, No. 6, pp. 1179-1192.
- Saada, A.S., Liang, L., Figueroa, L., and Cope, C.T. (1999), Bifurcation and shear band propagation in sands, *Geotechnique*, Vol. 49, No. 3, pp. 367-385.
- Servant, G., Marchina, P., and Nauroy, J.F. (2007), Near-wellbore: sand production issues, SPE 109894.
- Schofield, A., and Wroth, P. (1968), *Critical state soil mechanics*, McGraw-Hill, U.K.
- Silva, C. W. (2005), *Vibration and shock handbook*, Taylor & Francis Group, USA.
- Stallebrass, S. E. (1990), Modeling the effect of recent stress history on the deformation of overconsolidated soils, Ph.D. thesis, The City University, London, U.K.
- Stavropoulou, M., Papanastasiou, P., and Vardoulakis (1998), Coupled wellbore erosion and stability analysis, *International Journal for numerical and analytical Methods in Geomechanics*, Vol. 22, No. 9, pp. 749-769.
- Suebsuk, J., Horpibulsuk, S., and Liu, M.D. (2011), A critical state model for overconsolidated structured clays, *Computers and Geotechnics*, Vol. 38, No. 5, pp. 648-658.
- Sulem, J., and Ouffroukh, H. (2005), Shear banding in drained and undrained triaxial tests on a saturated sandstone: porosity and permeability evolution, *International Journal of Rock Mechanics & Mining Science*, Vol. 43, pp. 292-310.
- Sulem, J., Vardoulakis, I., Papamichos, E., Oulahna, A. and Tronvoll, J. (1999), Elasto-plastic modelling of red wildmoor sandstone, *Journal of Mechanics of Cohesive-Frictional Materials*, Vol. 4, No. 3, pp. 215-245.
- Tatsuoka, F., and Ishihara, K. (1974), Drained deformation of sand under cyclic stresses reversing direction, *Soils and Foundations*, Vol. 14, No. 3, pp. 51-65.
- Towhata, I. (2008), *Geotechnical Earthquake Engineering*, Springer, Germany.
- Tronvoll, J., Morita, N., and Santarelli, F.J. (1992), Perforation Cavity Stability: comprehensive laboratory experiments and numerical analysis, SPE 24799, PP. 339-349.

- Vaziri, H., Nouri, A., Hovem, K., and Wang, X. (2007), Computation of sand production in water injectors, SPE 107695, pp. 1-9.
- Veeken, C.A.M., Davies, D.R., Kenter, C.J., and Kooijman, A.P. (1991), Sand production prediction review: developing an integrated approach, SPE 22792.
- Venkatramaiah, C. (2006), Geotechnical engineering, New age international publishers, India.
- Vermeer, P.A., and de Borst, R. (1984), Non-associated plasticity for soils, concrete and rocks, Heron, Vol. 29, No. 3, pp. 1-64.
- Wan, R.G., Guo, P.J. (2001b), Effect of microstructure on undrained behaviour of sands, Canadian Geotechnical Journal, Vol. 38, No. 1, pp. 16-28.
- Wang, Y., and Lu, B. (2001), A Coupled reservoir-geomechanics model and applications to wellbore stability and sand prediction, SPE 69718, pp. 1-14.
- Wang, J., Yale, D., and Dasari, G. (2011), Numerical modeling of massive sand production, SPE 147110, pp. 1-14.
- Wood, D.M. (1990), Soil behavior and critical state soil mechanics, The Cambridge University Press, USA.
- Yang, C., Huang, M.S., and Cui, Y.J. (2011), Constitutive model of unsaturated structured soils under cyclic loading, Taylor & Francis group, pp. 987-992.
- Younessi, A. and Rasouli, V. (2012), Numerical simulations of sanding under different stress regimes, ARMA 12-373.
- Yu, H.S. (1998), CASM: A unified state parameter model for clay and sand, International Journal of Numerical and Analytical Methods in Geomechanics, Vol. 22, pp. 621-653.
- Yu, H.S. (2006), Plasticity and geotechnics, Springer, USA.
- Yu, H.S., Khong, C., and Wang J. (2007), A unified plasticity model for cyclic behaviour of clay and sand, Mechanics Research Communications, Vol. 34, No. 2, pp. 97-114.
- Ziegler, H. (1959), A modification of Prager's hardening rule, Quarterly of Applied Mathematics, Vol 17, pp. 55-65.
- Zoback, M.D. (2007), Reservoir geomechanics, Cambridge University Press, USA.

CHAPTER 3

CONSTITUTIVE MODEL FOR CYCLIC BEHAVIOUR OF COHESIONLESS SAND

3.1 Introduction

Classical plasticity is based on the concept of a single yield surface which is used to separate the elastic and plastic domains. Traditional plasticity provides a good description for the overall stress-strain behaviour of monotonic loading when no unloading occurs. However, it has some major drawbacks with regard to the simulation of cyclic loading. The most critical deficiency is that it provides a purely elastic response within the yield surface [Yu 2006]. The idealized stress-strain curve of Fig. 3-1 implies that large plastic strains are predicted by the model during primary loading, but during the subsequent unload-reload, only purely elastic strains within the yield surface are predicted. Additional plastic strain can occur only upon reloading to a stress state beyond the inception point of the stress reversal, point A' , and when the subsequent behaviour is identical to the case that would have occurred as if there was no unloading [Chen and Han 2007]. This is not suitable for modeling the behaviour of soil under cyclic loading because in reality, all unload-reload cycles give rise to a gradual stockpile of plastic strain and energy dissipation [Khong 2004, Yu et al. 2007].

Therefore, classical plasticity cannot replicate the non-linearity of the modulus, accumulation of plastic strain nor irrecoverable pore pressure generation during unloading and consequent reloading [Habte 2006, Yu 2006, Yang et al. 2011]. That is, it fails to duplicate complicated behaviour observed under cyclic loading conditions in the elasto-plastic range (i.e. cyclic plasticity), where stress reversal takes place frequently. This shortcoming of the traditional models was a turning point for the plasticity theory, which finally led to the development of alternative plasticity models [Reilly and Brown 1991, Chen 1994, Yu 2006].

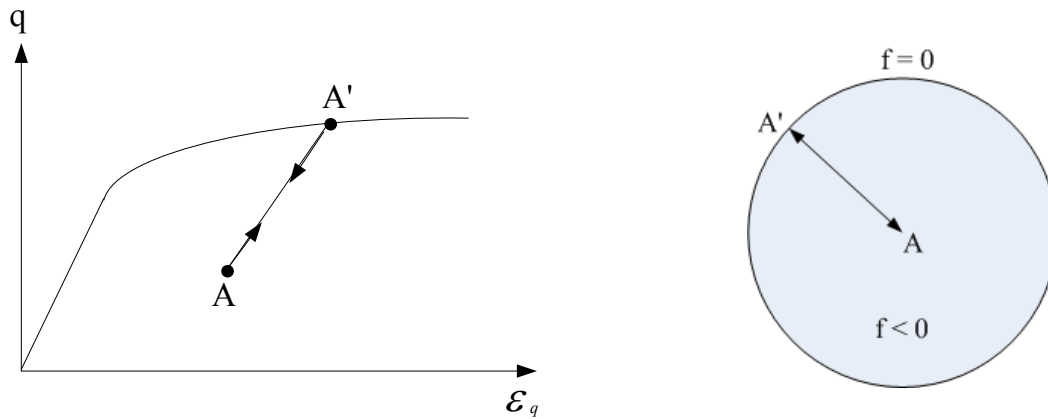


Fig. 3-1 Unloading and reloading from an elasto-plastic state: idealized stress-strain curve using traditional plasticity

Multi-surface and bounding surface plasticity are two mainstream approaches for modeling soil behaviour in response to cyclic loading (Reilly and Brown 1991, Habte 2006, Yu et al. 2007, Suebsuk et al. 2011, Yang et al. 2011]. The theory of multi-surface or nested plasticity originally was introduced by Mroz (1967) and Iwan (1967) for metals, but immediately found applications in the modeling of geomaterials [Yu 2006, Suebsuk et al. 2011]. In general, however, multi-surface plasticity models are complicated due to the use of many sub-yield surfaces and the need to track the position and size of all yield surfaces in the stress space [Chen 1994]. This demands a considerable amount of computational resources for the configuration of sub-yield and stress reversal surfaces. There are substantial challenges with increasing the number of yield surfaces in a model, making the model computationally very demanding and numerically more unstable [Chen 1994, Suebsuk et al. 2011, Yang et al. 2011]. Bounding surface plasticity was introduced to address some of the numerical shortcomings of multi-surface plasticity. For example, there is no need to track the locations and sizes of all the active yield surfaces in the bounding surface theory since yielding is assumed to be continuous inside the bounding surface. Hence, the location of the two surfaces effectively describes the distribution of all intermediate loading surfaces, thus references to them are not essential [Yu 2006]. Dafalias and Popov (1975, 1977) and Krieg (1975) independently proposed the bounding surface plasticity concept for the first time using kinematic hardening. Many similar models have been

introduced later specially for clays [Mroz et al. 1979, Pastor et al. 1985, Zienkiewicz et al. 1985, Al-Tabbaa 1987, McDowell and Hau 2004]. Dafalias and Herrmann (1982) and Dafalias (1986) originally introduced the radial mapping formulation of the bounding surface theory. The radial mapping scheme has been adopted in many models that were later proposed within the bounding surface plasticity framework [Bardet 1986, Crouch et al. 1994, Khong 2004, Russel and Khalili 2004, Yu et al. 2007, Suebsuk et al. 2011]. This chapter presents a specific version of the bounding surface plasticity, which does not incorporate the radial mapping formulation. That is, unlike conventional bounding surface plasticity in which the plastic modulus is expressed as the summation of the additive and bounding surface plastic moduli, the plastic modulus is stated only as a function of that of the loading surface. This is similar to Imam and Chan's (2008) approach for modelling cyclic loading.

3.2 Brief overview of the original model

The detained formulation of the original model can be reviewed in Imam (1999) and Imam et al. (2005). A brief overview is provided here.

The yield function is expressed as:

$$f = (\eta - \alpha)^2 - M_\alpha^2 \left(1 - \sqrt{\frac{p}{p_c}} \right) = 0 \quad (3.1)$$

$$M_\alpha^2 = (5M_p - \alpha)(M_p - \alpha) \quad (3.2)$$

where η is the stress ratio, M_p is the stress ratio at the peak of the undrained effective stress path (UESP), p is the mean effective stress, α is a scalar constant whose magnitude is non-zero only for anisotropically consolidated sands and p_c is the effective preconsolidation stress which controls the size of the yield surface.

Note the parameter M_p determines the stress conditions at which the cap and the front portion of the yield surface are separated from each other. It is also used to evaluate the stress ratio at the peak of the yield surface. This is consistent with early claims that in loose sands, the stress ratio at the peak of the yield surface is

very close to the stress ratio at the peak of UESP [Imam 1999]. M_p is evaluated for compression and extension, respectively, as follows:

$$M_{p,c} = \frac{6\sin\varphi_{p,c}}{3 - \sin\varphi_{p,c}} \quad (3.3)$$

$$M_{p,e} = \frac{6\sin\varphi_{p,e}}{3 + \sin\varphi_{p,e}} \quad (3.4)$$

in which $\varphi_{p,c}$ and $\varphi_{p,e}$ are the friction angles at the point of peak shear stress in the triaxial compression and triaxial extension tests, respectively. They can be calculated by:

$$\sin\varphi_{p,c} = \sin\varphi_\mu - k_p\psi_p \quad (3.5)$$

$$\sin\varphi_{p,e} = \sin\varphi_\mu - k_p\psi_p - a_p \quad (3.6)$$

where $\psi_p = e - e_p$ is the state parameter at the peak in which e is void ratio, and e_p is the critical state void ratio which is evaluated at mean effective stress corresponding to M_p (i.e. at $p = p_p$), φ_μ is the friction angle associated with $\psi_p = 0$ in triaxial compression and is close to the interparticle friction angle and k_p and a_p are model parameters. Experimental observations which support dependency of M_p to void ratio and the state parameter at the peak can be found in Imam et. al. (2002).

When the stress path is at the peak of UESP, it is found from equation (3.1) that $p_p = 0.64 p_c$ for isotropically consolidated sands regardless of void ratio and confining pressure at consolidation. This relationship is similar to Ishihara (1993) relationship, who observed that the ratio of mean normal stress at the peak of UESP to that at consolidation is constant. By conducting undrained tests on sands consolidated to different mean normal stresses and void ratios, the ratios of 0.61 and 0.63 were obtained for a clean and silty sand, respectively [Imam et. al. 2005].

Isotropic nonlinear elasticity is assumed for the model. The shear and bulk moduli are calculated from the following equations:

$$G = G_a \frac{(2.973 - e)^2}{1 + e} \left(\frac{p}{p_{atm}} \right)^n \quad (3.7)$$

$$K = K_a \frac{(2.973 - e)^2}{1 + e} \left(\frac{p}{p_{atm}} \right)^n \quad (3.8)$$

in which G_a and K_a are reference elastic moduli accounted as material parameters and p_{atm} is the atmospheric pressure. A value of 0.5-0.55 is usually used for n , depending on the type of sand.

Following the work of Wood (1990) and Manzari and Dafalias (1997), the stress-dilatancy relationship is defined as:

$$D = A(M_{PT} - \eta) \quad (3.9)$$

$$A_c = \frac{9}{9 + 3M_{PT,c} - 2M_{PT,c}\eta} \quad (3.10)$$

$$A_e = \frac{9}{9 - 3M_{PT,e} - 2M_{PT,e}\eta} \quad (3.11)$$

where

$$\sin\varphi_{PT,c} = \sin\varphi_{CS} + k_{PT}\psi_s \quad (3.12)$$

$$\sin\varphi_{PT,e} = \sin\varphi_{CS} + k_{PT}\psi_s + a_{PT} \quad (3.13)$$

in which M_{PT} is the phase transformation stress ratio, φ_{CS} is the critical state friction angle, $\psi_s = e - e_{CS}$ is the state parameter [Been and Jefferies 1985, Jefferies 1993], e_{CS} is the critical void ratio and k_{PT} and a_{PT} are both model parameters. Similar to how M_p is calculated using $\sin\varphi_p$ under triaxial compression and extension conditions, M_{PT} under compression and extension conditions is obtained from $\sin\varphi_{PT}$. Equation (3.12) and (3.13) are similar to the Manzari and Dafalias (1997) relationship [Imam et. al. 2005]. Note that the phase transformation concept was originally introduced by Tatsuoka and Ishihara (1974).

Hardening in this model depends on the proximity to the critical state, in contrast to conventional critical state models which relate the size of the yield surface to void ratio [Jefferies 1993]. Pure size shear hardening law is stated as:

$$\frac{\partial p_c}{\partial \varepsilon_q^p} = \frac{hG_{ini}}{(p_f - p_c)_{ini}} (p_f - p_c) \quad (3.14)$$

in which h is a material parameter, p_f is the failure mean effective stress and $(p_f - p_c)_{ini}$ is the initial value of $(p_f - p_c)$ at the end of consolidation and prior to shearing. Calculation of M_f is based on $\sin\varphi_f$ which itself is obtained by:

$$\sin\varphi_f = \sin\varphi_{cs} - k_f\psi_s \quad (3.15)$$

where k_f is a material parameter.

3.3 A bounding surface model for the cyclic response of sand

The major components of the proposed two-surface model are elasticity, stress-dilatancy relationship, loading surface and bounding surface, stress-strain relationships and loading criterion. They are briefly discussed here.

3.3.1 Elasticity

Isotropic nonlinear elasticity adopted for the original model is retained for simplicity.

3.3.2 Stress-dilatancy relationship

The absolute value of the stress ratio $|\eta|$ is applied in the formula of the stress-dilatancy of the original model rather than the stress ratio η .

3.3.3 Loading surface and bounding surface

The loading surface is expressed as:

$$f = \left(\frac{q - q_a}{p - p_a} - \alpha \right)^2 - M_a^2 \left(1 - \sqrt{\frac{p - p_a}{p_c}} \right) = 0 \quad (3.16)$$

where p_a and q_a are components of kinematic hardening tensor which evolves with plastic deformation. This definition of the loading surface suggests that p_a must always be smaller than p .

The loading surface during the first loading time is supposed to be identical to that of the original model, meaning the kinematic hardening tensor originally lies at the origin of the coordinate system.

The bounding surface is supposed to have the same shape as the loading surface for simplicity. Thus, the bounding surface is expressed as:

$$F = \left(\frac{\bar{q} - \bar{q}_a}{\bar{p} - \bar{p}_a} - \alpha \right)^2 - M_\alpha^2 \left(1 - \sqrt{\frac{\bar{p} - \bar{p}_a}{\bar{p}_c}} \right) = 0 \quad (3.17)$$

The superimposed bar denotes variables for the bounding surface. The size of the bounding surface is determined by \bar{p}_c .

The bounding surface provides an exterior limit for stress space since a stress state outside the bounding surface has no physical meaning. The bounding surface always encircles the loading surface, may touch it tangentially at a point or even becomes identical with it, but never intersects it [Chen 1994, Vermeer and Borst 1984, Chen and Han 2007]. Therefore, to ensure that the current stress state will not cross the bounding surface, the initial ratio of size of the two surfaces ($\bar{p}_c/p_c > 1$) is kept constant during the shearing process. The initial size of the loading and bounding surfaces at the start of shearing is considered to be equal to the hydrostatic pressure and failure mean effective pressure, respectively. It is also assumed that the components of the kinematic hardening tensor always coincide for the two surfaces, i.e. $(\bar{p}_a, \bar{q}_a) = (p_a, q_a)$. Fig. 3-2 illustrates change in position and size of the loading surface and bounding surface during shearing process.

The conventional assumption that the current stress state always lies on the loading surface is adopted in this model. This implies that the plastic deformation takes place as soon as loading embarks in the stress space. This is true especially for sand since the elastic shear deformation of sand is negligible. This assumption also made it possible to capture plastic deformation under unloading/reloading conditions when the stress path was inside the bounding surface. This is a remarkable feature of the bounding surface plasticity theory which captures

plastic deformation not only when a stress state lies on the bounding surface, but also within.

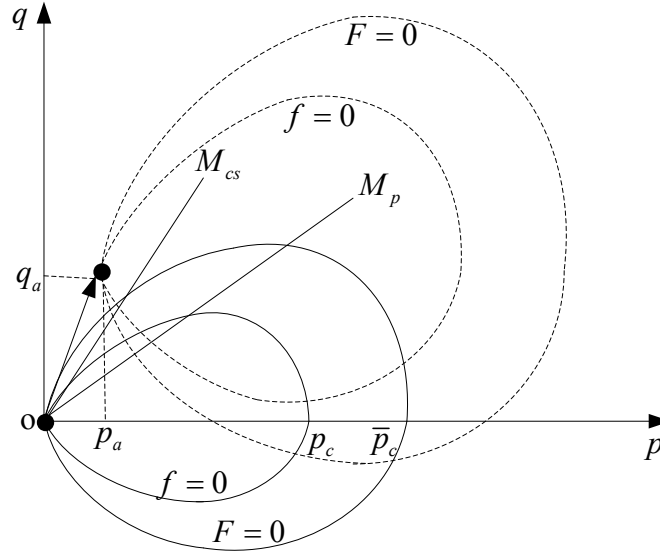


Fig. 3-2 Schematic representation of change in position and size of the loading surface and bounding surface during elasto-plastic deformation

Armstrong and Frederick's (1966) nonlinear kinematic hardening law is adopted to govern the evolution of the loading surface. For triaxial conditions, it is expressed as follows:

$$\dot{p}_\alpha = \frac{2}{3} c_1 \frac{\dot{\varepsilon}_p^p}{3} - c_2 p_\alpha \dot{z} \quad (3.18)$$

$$\dot{q}_\alpha = c_1 \dot{\varepsilon}_q^p - c_2 q_\alpha \dot{z} \quad (3.19)$$

where c_1 and c_2 are model constants, $\dot{\varepsilon}_p^p$ and $\dot{\varepsilon}_q^p$ are plastic volumetric and deviator strain increments and \dot{z} is the accumulative plastic strain increment which is defined as:

$$\dot{z} = \sqrt{\frac{2}{3} \dot{\varepsilon}_{ij}^p \dot{\varepsilon}_{ij}^p} \quad (3.20)$$

p_α and q_α are components of the kinematic hardening tensor which are defined as:

$$p_\alpha = \frac{\alpha_{11} + 2\alpha_{33}}{3} \quad (3.21)$$

$$q_\alpha = \alpha_{11} - \alpha_{33} \quad (3.22)$$

Note that the second term on the right side of equations (3.18) and (3.19) represents a nonlinear term for the proposed kinematic hardening model, while the first part is similar to Prager's linear kinematic hardening rule.

3.3.4 Stress-strain relationships

Constitutive relationships are governed by the following equations in accordance with standard incrementally linear stress-strain relationships:

$$\dot{p} = K \left(\dot{\varepsilon}_p - LD \text{sign}(m_p) \right) \quad (3.23)$$

$$\dot{q} = 3G \left(\dot{\varepsilon}_q - \sqrt{2/3} L \text{sign}(m_q) \right) \quad (3.24)$$

where K and G are bulk and shear elastic moduli, D is the dilatancy rate, L is the normalized plasticity multiplier and m_p and m_q are components of the unit normal to the plastic potential surface which can be obtained using the dilatancy relationship.

The parameter L is determined from the following relationship:

$$L = \frac{KR\dot{\varepsilon}_p + \sqrt{6}G\dot{\varepsilon}_q}{H_n + KR D + 2G} \quad (3.25)$$

$$R = \sqrt{\frac{2}{3} \frac{\frac{\partial f}{\partial p}}{\frac{\partial f}{\partial q}}} \quad (3.26)$$

$$\frac{\partial f}{\partial p} = \frac{-2}{p - p_a} \left[\left(\frac{q - q_a}{p - p_a} \right)^2 - \alpha \left(\frac{q - q_a}{p - p_a} \right) \right] + \frac{M_\alpha^2}{2\sqrt{p_c(p - p_a)}} \quad (3.27)$$

$$\frac{\partial f}{\partial q} = \frac{2}{p - p_a} \left(\frac{q - q_a}{p - p_a} - \alpha \right) \quad (3.28)$$

$$m_q = \frac{1}{\sqrt{1 + D^2}} \quad (3.29)$$

$$m_p = \begin{cases} \frac{tD}{\sqrt{1 + D^2}} & D \geq 0 \\ -\frac{tD}{\sqrt{1 + D^2}} & D < 0 \end{cases} \quad (3.30)$$

where $t = 1$ for compressive loading and $t = -1$ for extensive loading. The definition of m_p based on the sign of the dilatancy rate for a given loading direction enables the proposed model to capture phase transformation under undrained cyclic loading. Also, different signs of m_p for compression and extension under a given dilatancy rate enables the model to capture the prevalent volumetric contraction observed during the cyclic loading of loose sands.

Components of the unit vector to the plastic potential surface for unloading are assumed to be related to those defined already as follows:

$$m_{p,u} = -m_p \quad (3.31)$$

$$m_{q,u} = m_q \quad (3.32)$$

Applying consistency condition for a combined isotropic shear and kinematic hardening law and ignoring shape hardening, the normalized plastic modulus can be calculated for triaxial condition using:

$$H_n = -\sqrt{\frac{2}{3}} \frac{1}{\left|\frac{\partial f}{\partial q}\right|} \frac{\partial f}{\partial p_c} \frac{\partial p_c}{\partial \varepsilon_q^p} + H_n^{kinematic} \quad (3.33)$$

$$H_n^{kinematic} = R \left(\frac{2}{9} c_1 D - c_2 p_\alpha \sqrt{\frac{2}{9} D^2 + 1} \right) + c_1 - c_2 u_Q q_\alpha \sqrt{\frac{2}{9} D^2 + 1} \quad (3.34)$$

in which

$$\frac{\partial f}{\partial p_c} = \frac{-M_\alpha^2}{2p_c} \sqrt{\frac{p - p_a}{p_c}} \quad (3.35)$$

$$u_Q = \frac{\frac{\partial f}{\partial q}}{\left|\frac{\partial f}{\partial q}\right|} \quad (3.36)$$

H_n for unloading is supposed to be related to loading as follows:

$$\frac{H_{n,u}}{H_n} = R_u \sqrt{\frac{p}{0.01 p_{atm}} |\eta|} \quad (3.37)$$

The application of the stress ratio in the definition of the unloading plastic modulus results in a gradual decrease in the value of $H_{n,u}$ due to a decreasing trend in the stress ratio with progress in unloading. This implies that more plastic deformation occurs with the advancement of unloading, which is in line with experimental observations.

R_u is a positive value greater than one. This implies that the unloading-induced plastic strain increment is smaller than the loading induced plastic strain increment because a larger plastic modulus leads to a smaller plasticity multiplier and ultimately a smaller plastic strain increment.

A simple analysis of the definition of the plastic deviator strain increment reveals that the total, elastic and plastic deviator strain increments always have the same sign. They are all positive under compressive loading or extensive unloading. However, negative values are predicted for all of them under compressive unloading or extensive loading. Note that the sign of the normalized plasticity multiplier (L) is positive under compressive loading or extensive unloading. It, however, is negative for compressive unloading or extensive loading. In general, L is positive when the total deviator strain increment is positive and vice versa.

3.3.5 Loading criterion and loading direction

$$\dot{f} = \frac{\partial f}{\partial p} \dot{p} + \frac{\partial f}{\partial q} \dot{q} \quad (3.38)$$

Positive values for \dot{f} signify loading, and negative values denote unloading.

The direction of loading can be determined either by the sign of the deviator stress or deviator part of the unit normal to the loading surface. Values for q and n_q are positive for compressive loading and negative for extensive loading.

3.4 Performance of the proposed bounding surface model

The proposed model was used to predict the behaviour of several two-way drained and undrained cyclic triaxial tests on cohesionless sands. The test data

were gathered from the literature. Material parameters and their assigned values are presented in Table 3-1.

Table 3-1 Material parameters used for calibration of Fuji River sand, Toyoura sand and Niigata sand

Parameter	Fuji River sand	Toyoura sand	Niigata sand
k_p	1.5	1	1.5
φ_μ	24	21	21
a_p	0.15	0.15	0.15
φ_{cs}	31	31	28
k_{pT}	1.25	0.25	1.25
a_{pT}	0.10	0.15	0.10
G_a	5e6	5e6	5e6
K_a	8e6	8.5e6	8.5e6
h	1	1	1
k_f	0.75	0.75	0.75
c_1	5e6	0.5e6	5e6
c_2	500	500	500
R_u	5	5	5

3.4.1 Drained cyclic loading test on Fuji River sand

Fig. 3-3 shows the predictions of the proposed bounding surface model for drained cyclic tests conducted by Tatsuoka and Ishihara (1974) on Fuji River sand. The test was performed on a medium dense sample of Fuji River sand with an initial void ratio and constant confining pressure equal to 0.74 and 200 *KPa*, respectively. The test was carried out using cyclic axial loads with increasing stress amplitude in successive cycles. Progressive contraction of sand with cyclic loading was captured by the model. Fig. 3-3 shows that the continuous increases of shear strain and stress ratio with the continuation of cyclic loading were reproduced in both the compression and extension sides. The model predicted the first clear dilative response in the extension side of the fourth cycle at a point, which has almost the same stress ratio, but slightly higher volumetric strain compared to those of the measured values. Dilative response, however, was anticipated on the compression side for the last cycle, while experimental

observations suggest that it first occurs on the extension side. This implies that the predicted compressive phase transformation stress ratio for the last cycle is smaller than the actual one during the physical experiment.

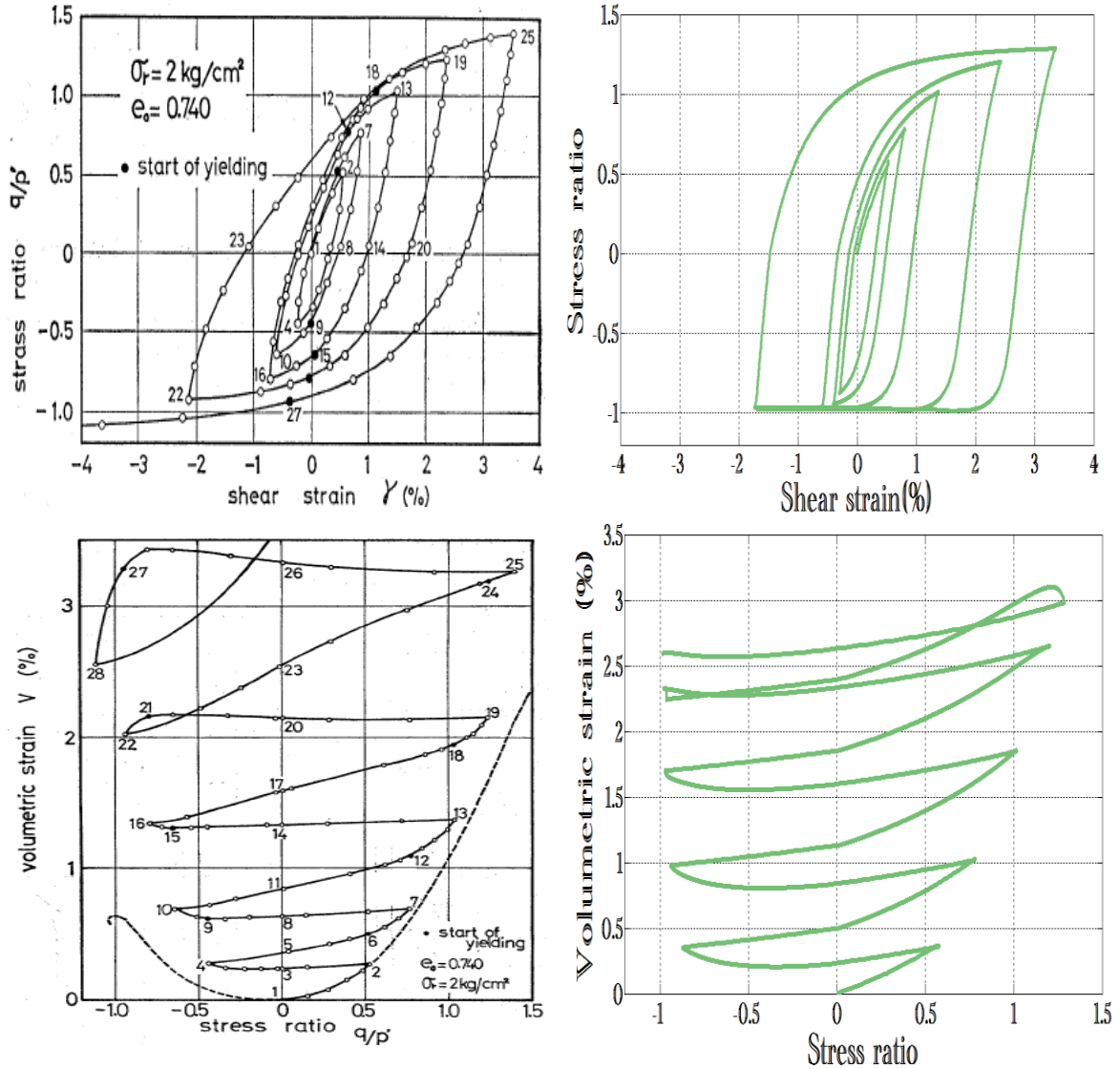


Fig. 3-3 Measured and predicted response of Fuji River sand during drained cyclic loading

3.4.2 Drained and undrained cyclic loading tests on Toyoura sand

Several two-way cyclic tests were conducted by Pradhan et al. (1989) on Toyoura sand. The sample used in Pradhan et al. (1989) consisted of quartz with angular to sub-angular particles [Ling and Yang 2006]. Drained cyclic tests on Toyoura sand were carried out under a constant p stress path. This stress path can be modeled by imposing a zero elastic volumetric strain increment, making the total

volumetric strain equal to plastic volumetric strain. Figs. 3-4 to 3-6 show the results of the cyclic tests on Toyoura sand.

A reasonable agreement between the predicted and measured values of increasing amplitude of the stress ratio and shear strain during successive cycles can be found in Fig. 3-4. The successive softening and stiffening of the sample in the course of loading and unloading stages of cyclic loading are captured as well. However, the stronger dilative behaviour in the compressive side of the third cycle is predicted compared to the measured one.

Fig. 3-5 shows the constant p stress path during which the amplitude of shear strain decreases with the number of loading cycles and tends to approach a steady value. As observed, the trend and values of the shear strain and also the stress ratio have been captured by the model. The initial compression accompanied by subsequent expansion is captured by the model as well. However, the predicted tendency of the soil for dilation in compressive side of the successive cycles is stronger than the measured behaviour. This implies that the phase transformation surface is placed in a smaller q for a given p in the numerical model in comparison with the physical experiment. Thus, the predicted stress path reaches the phase transformation surface sooner than the experiment.

Fig. 3-6 displays triaxial undrained cyclic test on a saturated loose sample of Toyoura sand. The model predictions capture the stress-shear strain and the associated stress path during the constant deviator stress amplitude cycles ($q = \pm 25 \text{ KPa}$) very well. In particular, the model captures the progressive reduction in the mean effective stress, the ultimate deviator stress and also occurrence of the phase transformation in the extension side with reasonable accuracy. However, the stress path after the occurrence of the phase transformation (i.e. cyclic liquefaction) is not in very good agreement with the measured stress path. That is, the smaller reduction of the mean effective stress was predicted due to underestimation of excess pore pressure, which itself is directly linked to the magnitude of the volumetric strain increment. As it will be discussed later, accurate prediction of pore pressure generation after failure of the

soil caused by cyclic liquefaction requires new formulation due to the dynamic nature of the hydromechanical process.

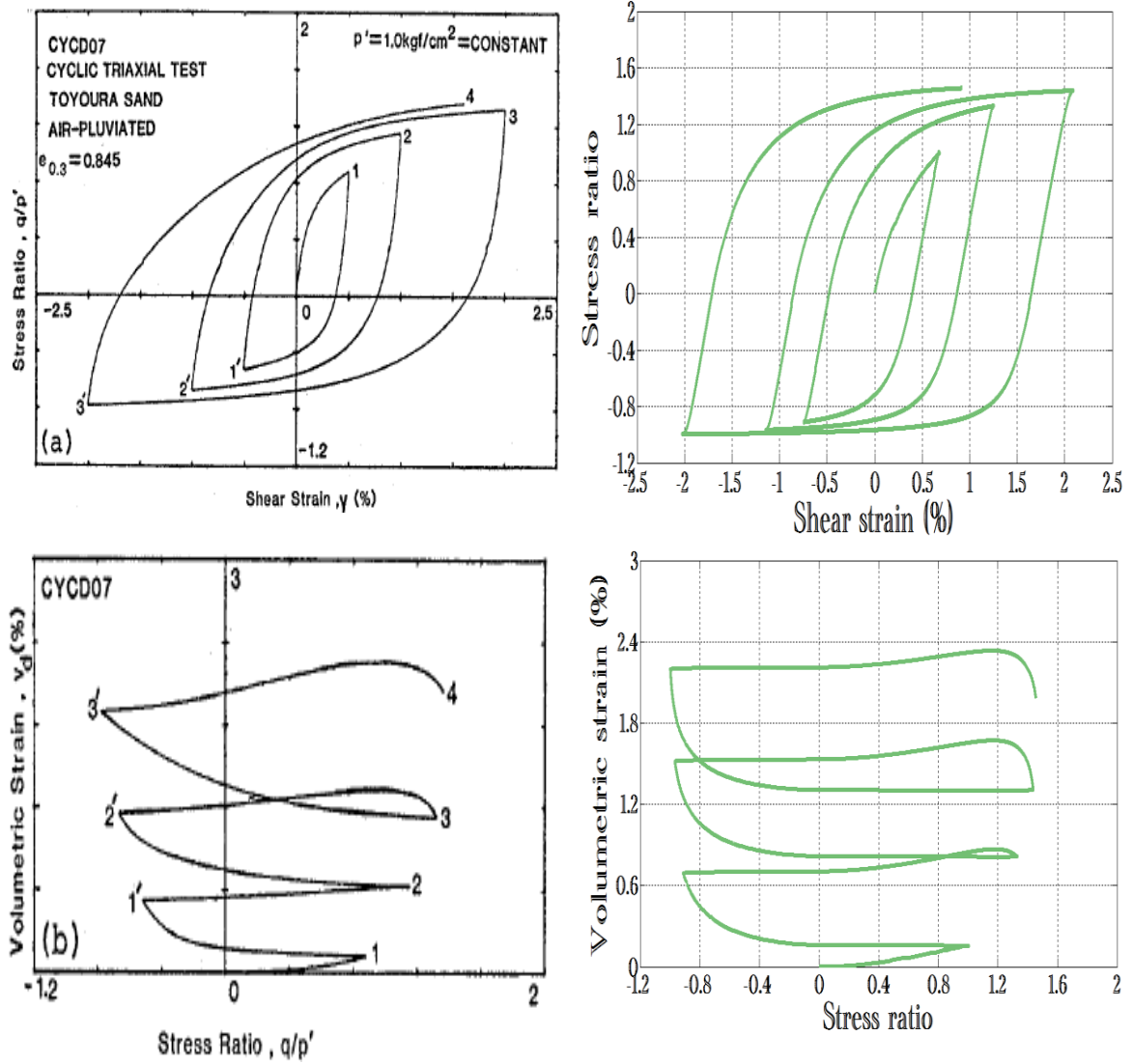


Fig. 3-4 Measured and predicted response of Toyoura sand during drained cyclic loading with an initial void ratio of 0.845 and confining pressure of 98 KPa

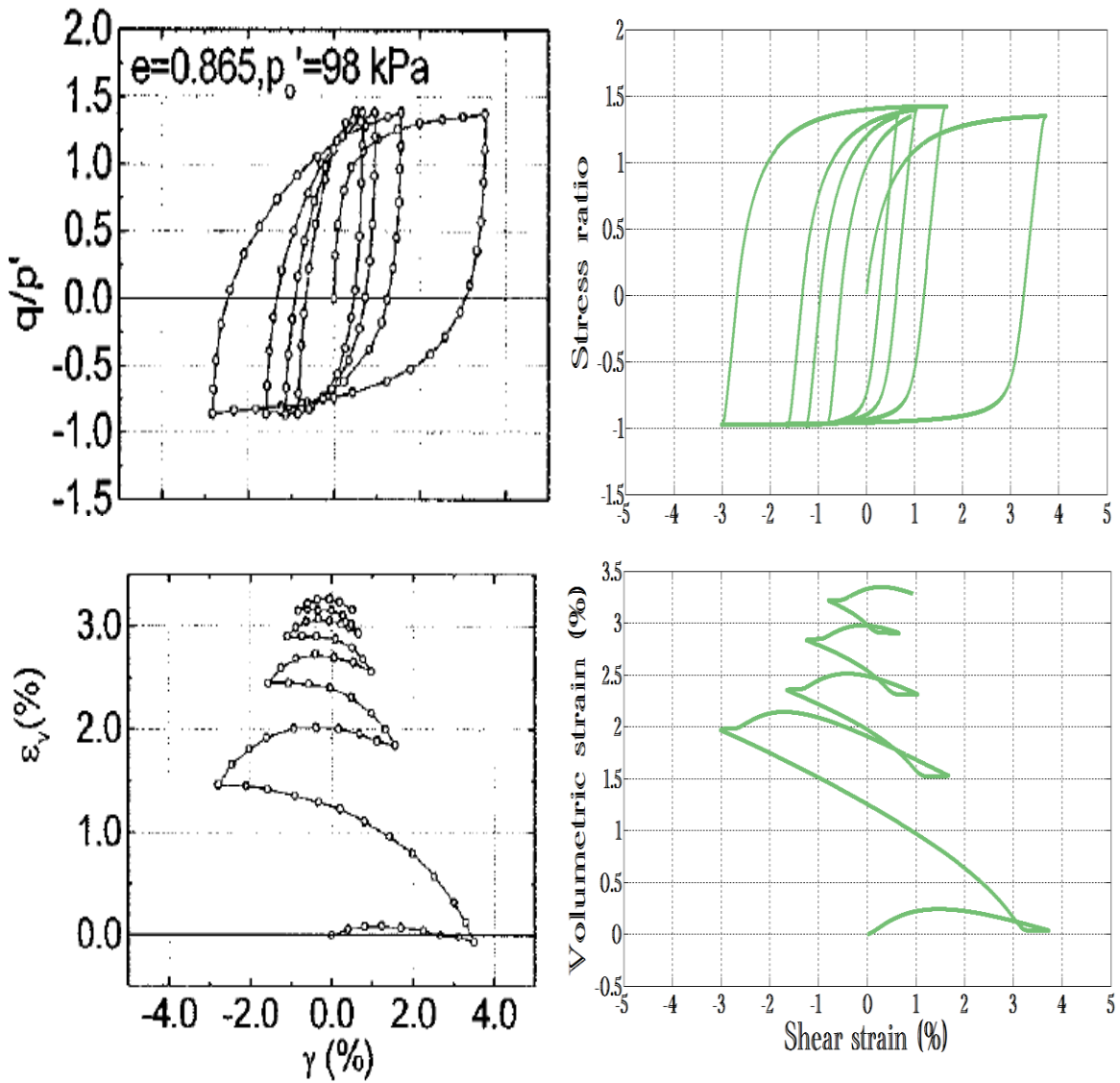


Fig. 3-5 Measured and predicted behaviour of Toyoura sand during drained cyclic loading with an initial void ratio of 0.865 and confining pressure of 98 KPa

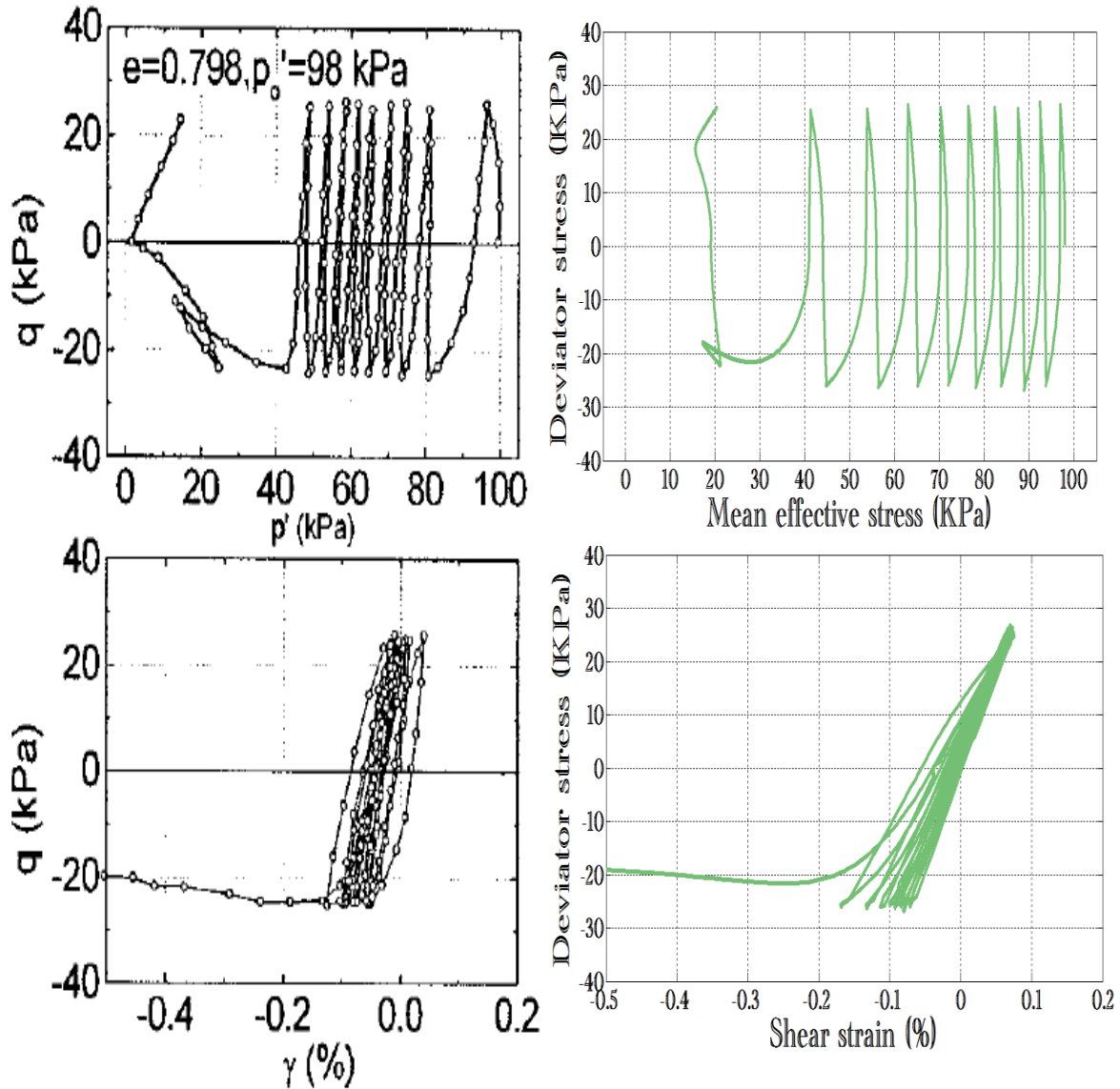


Fig. 3-6 Measured and predicted response of Toyoura sand during undrained cyclic loading with an initial void ratio of 0.798 and confining pressure of 98 kPa

3.4.3 Undrained cyclic loading test on Niigata sand

Fig. 3-7 plots the results of triaxial undrained stress-controlled cyclic loading test conducted by Ishihara et. al. (1975) on a saturated sample of Niigata sand. During the initial cycles, the deviator stress-shear strain loops are almost vertical since very small shear strains/axial strains are developed. When the stress path reaches the phase transformation surface (i.e. cyclic liquefaction), the soil experiences a temporary constant volume phase by remaining on the phase transformation surface for a short time. This behaviour is accompanied by a constant q stress path

and large amounts of deformation. Decrease in p and large deformation without considerable increase in shear stress are common features of cyclic liquefaction and cyclic mobility [Lenart 2008]. Temporary steady-state behaviour ends as the stress path leaves the phase transformation surface resulting in dilative behaviour. Consequently, negative pore pressure develops and the mean effective stress increases. The contractive behaviour and positive pore pressure develops once more with stress reversal leading to decrease in the mean effective stress. The stress path hits the phase transformation surface in the compression side causing dilative behaviour and negative pore pressure development resulting in an increase in the mean effective stress. These fluctuations between the contractive and dilative behaviour cause the sand to continuously weaken (liquefy) and strengthen (densify) which indicates strong dilative response after the soil liquefies [Li and Ming 2000, Elgamal et. al. 2003, Querol and Blázquez 2006, Lenart 2008, Orense and Pender 2012].

The proposed model captures the nearly vertical stress-strain behaviour and continuous reduction in mean effective stress in the initial constant deviatoric stress amplitude cycles ($q = \pm 75 \text{ KPa}$) fairly well. It also predicts cyclic liquefaction with reasonable accuracy at a stress point which has almost the same deviatoric stress and mean effective stress compared to those of the experiment. However, smaller shear deformations (i.e. stiffer response) were predicted by the model after the phase transformation, which has been shown by stress path 22-23. Also the reduction in the mean effective stress for stress path 23-24 is underestimated by the model because of the underestimation of the excess pore pressure. Consequently, the stress path reaches the phase transformation surface in the compression side at a stress point with greater deviatoric stress and the mean effective stress compared to the measured values. These discrepancies in matching the flowing behaviour continue during stress path 25-28, which has not been shown. The source of these differences originates from the fact that post-liquefaction behaviour is associated with very quick changes in pore pressure and plastic deformation [Yu et. al. 2007]. Calculation of pore pressure development during the post-liquefaction phase needs special

considerations. The rapid and large changes of the hydro-mechanical properties by cyclic liquefaction/cyclic mobility can be captured by models which have been formulated for the earthquake type loading [Querol and Blázquez 2006, Yu et. al. 2007, Lenart 2008].

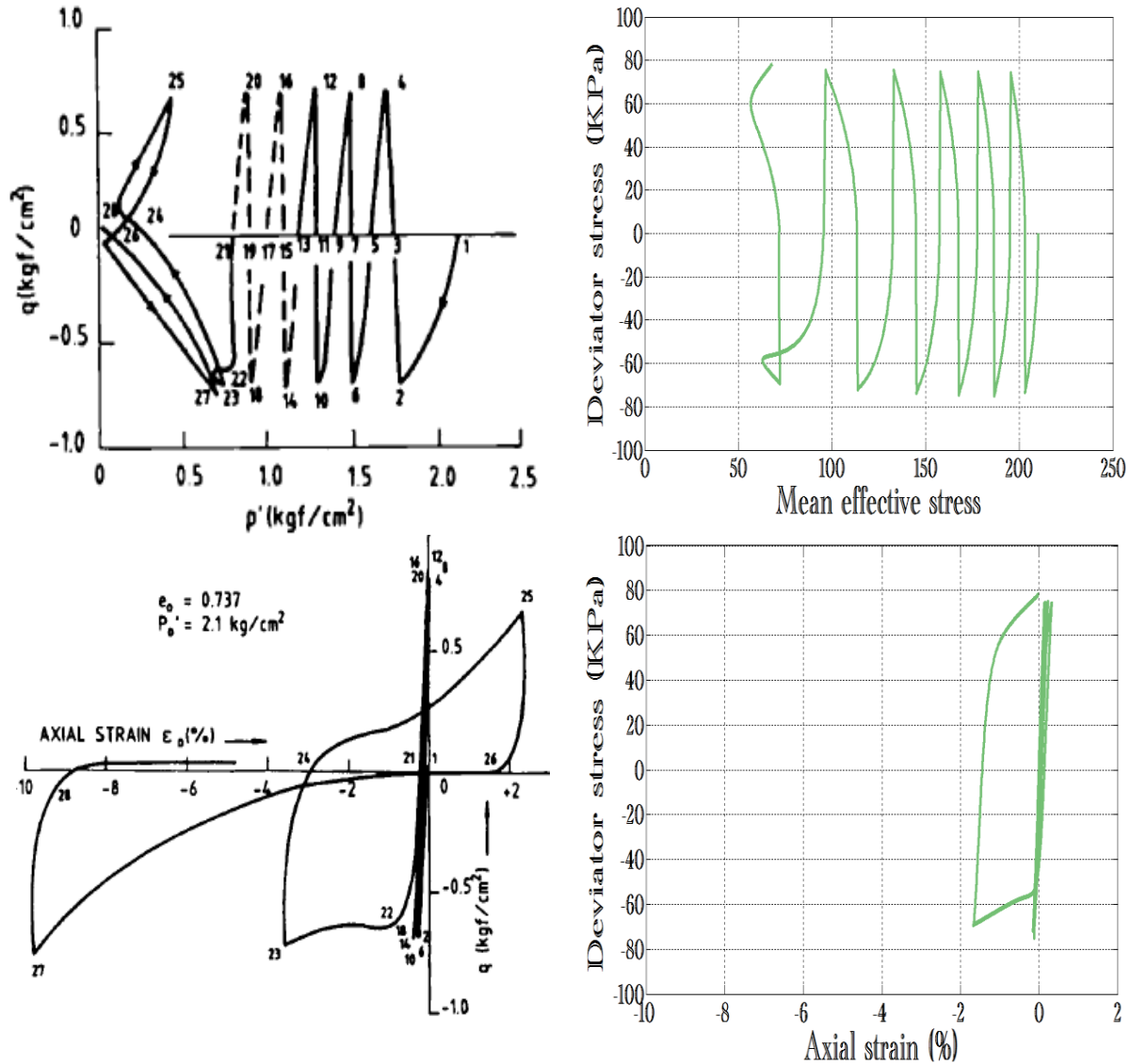


Fig. 3-7 Measured and predicted response of Niigata sand during undrained cyclic loading

3.5 Conclusion

A critical state constitutive model has been presented for cohesionless sands under cyclic loading within the framework of the bounding surface plasticity theory. Predictions of the proposed model for cyclic loading are in reasonable agreement with experimental measured data. The main characteristics of sand behaviour in

response to cyclic loading have been captured fairly well. It, however, appears that if the definition of the pore pressure generation and plastic modulus change upon liquefaction, movement of the stress path towards zero mean effective stress may be better replicated. In line with this suggestion, a smaller plastic modulus will provide a softer response, which has been observed experimentally. However, introduction of a new method in predicting pore pressure generation for the post-liquefaction phase requires special attention to dynamic loads.

3.6 References

Al-Tabbaa, A. (1987), Permeability and stress-strain response of Speswhite kaolin, Ph.D. thesis, The University of Cambridge, Cambridge, U.K.

Armstrong, P.J. and Frederick, C.O. (1966), A mathematical representation of the multiaxial Bauschinger effect, CEGB Report, RD/B/N731, Berkeley Nuclear Laboratories.

Been, K., and Jefferies, M. G. (1985), A state parameter for sands, *Géotechnique*, Vol. 35, No. 2, pp. 99-112.

Bardet, J.P. (1986), Bounding surface plasticity model for sands, *Journal of Engineering Mechanics*, Vol. 112, No. 11, pp. 1198-1217.

Chen, W.F. (1994), *Constitutive equations for engineering materials*, Elsevier, Netherlands.

Chen, W.F. and Han D.J. (2007), *Plasticity for structural engineers*, John Ross Publishing, USA.

Crouch, R.S., Wolf, J.P., and Dafalias, Y.F. (1994), Unified critical-state bounding-surface plasticity model for soils, *Journal of Engineering Mechanics*, Vol. 120, No. 11, pp. 2251-2270.

Dafalias, Y.F. (1986), Bounding surface plasticity. I: mathematical foundation and hypoplasticity, *Journal of Engineering Mechanics*, Vol. 112, No. 9, pp. 966-987.

Dafalias, Y.F., and Herrmann, L.R. (1982), Bounding surface formulation of soil plasticity, *Soil Mechanics-Transient and Cyclic Loads*, Wiley, pp. 253-282.

Dafalias, Y.F., and Popov, E.P. (1975), A model of nonlinearly hardening materials for complex loading, *Acta Mechanica*, Vol. 21, pp. 173-192.

Dafalias, Y.F., and Popov, E.P. (1977), Cyclic loading for materials with a vanishing elastic region, *Nuclear Energy and Design*, Vol. 41, pp. 293-302.

- Elgamal, A., Yang, Z., Parra, E. and Regheb, A. (2003), Modeling of cyclic mobility in saturated cohesionless soils, *International Journal of Plasticity*, Vol. 19, pp. 883-905.
- Habte, M.A. (2006), Numerical and constitutive modelling of monotonic and cyclic loading in variably saturated soils, Ph.D. thesis, The University of New South Wales, Sydney, Australia.
- Imam, M.R. (1999), Modeling the constitutive behavior of sand for the analysis of static liquefaction, Ph.D. thesis, The University of Alberta, Edmonton, Canada.
- Imam, M.R., and Chan, D.H. (2008), Application of a critical state model for the cyclic loading of sands, In *Proceedings from GeoEdmonton: 61st Canadian Geotechnical Conference*, Edmonton, pp. 127-134.
- Imam, M.R., Morgenstern, N.R., Robertson, P.K., and Chan, D.H. (2002), Yielding and flow liquefaction of loose sand, *Soils and Foundations*. Vol. 42, No. 3, pp. 19-31.
- Imam, S.M.R., Morgenstern N.R., Robertson P.K., and Chan, D.H. (2005), A critical-state constitutive model for liquefiable sand, *Canadian Geotechnical Journal*, Vol. 42, No. 3, pp. 830-855.
- Ishihara, K. (1993) Liquefaction and flow failure during earthquake. *Géotechnique*, Vol. 43, No. 3, pp. 351-415.
- Ishihara, K., Tatsuoka, F., and Yasuda, S. (1975), Undrained deformation and liquefaction of sand under cyclic stresses, *Soils and Foundation*, Vol. 15. No. 1, pp. 29-44.
- Iwan, W.D. (1967), On a class of models for the yielding behaviour of continuous and composite systems, *Journal of Applied Mechanics*, Vol. 34, pp. 612-617.
- Jefferies, M.G. (1993), Nor-Sand: a simple critical state model for sand, *Géotechnique*, Vol. 43, No. 1, pp. 91-103.
- Khong, CD. (2004), Development and numerical evaluation of unified critical state models, Ph.D. thesis, The University of Nottingham, Nottingham, U.K.
- Krieg, R.D. (1975), A practical two-surface plasticity theory, *Journal of Applied Mechanics*, Vol. 42, No. 3, pp. 641-646
- Lenart, S. (2008), The response of saturated soils to a dynamic load, *Acta Geotechnica Slovenica*, Vol. 5, No. 1, pp. 37-49.
- Li, X.S., Ming, H.Y.(2000), Unified modeling of flow liquefaction and cyclic mobility, *Soil Dynamics and Earthquake Engineering*, Vol. 19, pp. 363-369.

- Ling, H.I., and Yang, Y. (2006), Unified sand model based on the critical state and generalized plasticity, *Journal of Engineering Mechanics*, Vol. 132, No. 12, pp. 1380-1391.
- Manzari, M.T., and Dafalias, Y. F. (1997), A critical state two-surface plasticity model for sands, *Géotechnique*, Vol. 47, No. 2, pp. 255-272.
- McDowell G.R., and Hau K.W. (2004), A generalised Modified Cam Clay model for clay and sand incorporating kinematic hardening and bounding surface plasticity, *Granular Matter*, Vol. 6, No. 1, pp. 11-16.
- Mroz, Z., (1967), On the description of anisotropic hardening, *Journal of the Mechanics and Physics of Solids*, Vol. 15, pp. 163-175.
- Mroz, Z., Norris, V. A. and Zienkiewicz, O.C. (1979), Application of an anisotropic hardening model in the analysis of elasto-plastic deformation of soils, *Géotechnique*, Vol. 29, No. 1, pp. 1-34.
- Orense, R., and Pender M. (2012), Liquefaction characteristics of pumice sands, EQC project 10/589, The University of Auckland, Auckland, New Zealand.
- Pastor, M., Zienkiewicz, O.C., and Leung, K.K. (1985), Simple model for transient soil loading in models for sands earthquake analysis. II. Non-associated models for sands, *International Journal for Numerical and Analytical Methods in Geomechanics*, Vol. 9, pp. 477-498.
- Pradhan, T. B. S. (1989), The behavior of sand subjected to monotonic and cyclic loadings, PhD thesis, Kyoto University.
- Pradhan, T.B.S., Tatsuoka, F., and Sato, Y. (1989), Experimental stress-dilatancy relations of sand subjected to cyclic loading, *Soils and Foundations*, Vol. 29, pp. 45-64.
- Querol, S.L., and Blázquez, R. (2006), Liquefaction and cyclic mobility model for saturated granular media, *International Journal for Numerical and Analytical Methods in Geomechanics*, Vol.30, pp. 413-439.
- Reilly, M.P.O, and Brown, S.F. (1991), *Cyclic loading of soils: from theory to design*, Blackie and son limited, U.K.
- Russel, A., and Khalili N. (2004), A bounding surface plasticity model for sands exhibiting particle crushing, *Canadian Geotechnical Journal*, Vol. 41, No. 6, pp. 1179-1192.
- Suebsuk, J., Horpibulsuk, S., and Liu, M.D. (2011), A critical state model for overconsolidated structured clays, *Computers and Geotechnics*, Vol. 38, No. 5, pp. 648-658.
- Tatsuoka, F., and Ishihara, K. (1974), Drained deformation of sand under cyclic stresses reversing direction, *Soils and Foundations*, Vol. 14, No. 3, pp. 51-65.

Vermeer, P.A., and de Borst, R. (1984), Non-associated plasticity for soils, concrete and rocks, *Heron*, Vol. 29, No. 3, pp. 1-64.

Wood, D.M. (1990), *Soil behavior and critical state soil mechanics*, Cambridge University Press, USA.

Yang, C., Huang, M.S., and Cui, Y.J. (2011), Constitutive model of unsaturated structured soils under cyclic loading, Taylor & Francis group, pp. 987-992.

Yu, H.S. (2006), *Plasticity and Geotechnics*, Springer, USA.

Yu, H.S., Khong, C., and Wang J. (2007), A unified plasticity model for cyclic behaviour of clay and sand, *Mechanics Research Communications*, Vol. 34, No. 2, pp. 97-114.

Zienkiewicz, O.C., Leung, K.K., and Pastor, M. (1985), Simple model for transient soil loading in earthquake analysis. I. basic model and its application, *International Journal for Numerical and Analytical Methods in Geomechanics*, Vol. 9, pp. 453-476.

CHAPTER 4

A BOUNDING SURFACE CONSTITUTIVE MODEL FOR CEMENTED SAND UNDER MONOTONIC LOADING

4.1 Introduction

Imam (1999) developed a critical state constitutive model capable of capturing the response of cohesionless sands. The proposed model was successfully validated against different directions and modes of shearing, including triaxial compression and extension conditions.

In order to model artificially or naturally cemented sand, the model requires some modifications because the response of cemented soils is different from cohesionless soils. Cemented soils have a structure which causes major effects on their mechanical response. It was found that the compression curve for most natural soils lie above the corresponding intrinsic compression line, making them more brittle [Yu et al. 2007]. The structure in natural soils is believed to be a combination of fabric (orientation or arrangement of soil particles), and bonding (cementation between soil particles) which can be destroyed due to plastic deformation. This degradation of the structure under applied loads not only can change the size and shape of the yield surface, but also diminish the stiffness of the soil [Yu et al. 2007, Yang et al. 2011].

Geologically, the structure depends on the type of deposition and post depositional diagenesis. Diagenesis produces the formation of interparticle bonding similar to artificially cement-treated soils which are made by adding cementing agents such as Portland cement [Yu et al. 2007]. This enhances the mechanical properties of soil by boosting its stiffness and strength. Bonding, presumed to be the main factor for the increase in strength, in a general sense includes all types of cohesive forces at the interparticle contacts by cementing

agents. From a macroscopic standpoint, the existence of bonds between sand particles is reflected by the occurrence of a non-zero tensile strength [Lee et al. 2004].

It is natural to expect that, in addition to the maximum past pressure, the degree of cementation (strength of bonds between soil particles) affects the size of the initial elastic domain. Because bonding between soil particles gives rise to an increase in stiffness and strength, the initial yield surface is expected to enlarge. Experimental observations support this idea. In fact, regardless of different originating mechanisms, the engineering effects of all factors due to cementation are similar since they all result in increased stiffness and development of cohesion and tensile strength [Lee et al. 2004]. This is why all newly created models for bonded geomaterials assume a larger yield surface compared to the corresponding unbonded counterparts [Gens and Nova 1993, Nova et al. 2003, Nova 2006, Navarro et al. 2010]. Most of these models employ a modified Cam-Clay model as the base constitutive model. This makes them unsuitable for bonded sands because sand does not have a unique normal consolidation line, which is required in the Cam-Clay framework [Jefferies 1993, Yu et al. 2007].

In this development, cementation is first implemented into the original model by incorporating tensile strength and cohesion into the formulation of the constitutive relationships. Definitions of the yield function, elastic moduli, plastic hardening modulus, flow rule and other components of the model are rectified accordingly to achieve this goal. Having incorporated tensile strength and cohesion into the model, the modified model is integrated into the framework of bounding surface plasticity [Dafalias 1986, Dafalias and Herman 1986].

Bounding surface plasticity was proposed for the first time for metal by Dafalias and Popov (1975) due to the trend of the plastic modulus variations and position of the stress state in typical uniaxial stress-plastic strain curves. In this theory, stress states are presumed to be bounded always by a surface which is called the bounding surface. Hence, the bounding surface provides an exterior limit for the stress space. It is also presumed that the stress states always lie in another surface called the loading surface. During plastic flow, the bounding surface and loading

surface can uniformly expand/contract, move or even rotate. The bounding surface, however, always surrounds the current stress state since a stress state outside the bounding surface has no physical meaning. That is, regardless of the size of the loading surface, the bounding surface always encircles the loading surface, may touch it tangentially at a point or even becomes identical with it, but never intersects it. The elastic nucleus is another surface in which the plastic modulus gets an infinite value rather than an explicit value. However, for simplicity, it is usually assumed that the elastic domain dwindles into a single point, meaning the plastic deformation takes place as soon as the loading embarks in the stress space. The remarkable feature of the bounding surface concept is that the hardening of the loading surface and the resulting magnitude of the plastic deformation depend on the proximity of the stress state to the bounding surface. In fact, plastic deformation at any stress point inside the bounding surface is computed by dividing the plastic modulus of the loading surface into two segments: the bounding and additive plastic moduli. Then, radial mapping is utilized to evaluate the corresponding unique image stress point on the bounding surface needed to calculate these two moduli [Reilly and Brown 1991].

Bardet (1986) extended the application of the bounding surface plasticity theory to describe nonlinear behavior of cohesionless sands. The model is based on radial mapping rule and isotropic hardening. He employed the characteristic state line associated with no volume change which defines the transition state between contractive and dilative behaviors. The use of an associative flow rule for sand is a major deficiency in Bardet (1986)'s model.

Al-Tabbaa (1987) developed a bounding surface model for clay which can be considered as an extension of the Modified Cam Clay model by introducing a bubble surface inside the bounding surface [Yu 2006]. The model uses associated flow rule and does not take cohesion into account.

Crouch et. al. (1994) and Crouch and Wolf (1994) developed isotropic bounding surface for two and three dimensional stress space in the critical state framework. Use of a combined radial and deviatoric mapping, pure volumetric hardening law, non-associative flow rule and also use of bilinear critical state line in the

$e - \ln p$ plane are the main features of these two models. Discontinuity between the two mapping regions and the large number of material parameters are some of the deficiencies of these models.

The model created recently by Russel and Khalili (2004) and Khalili et. al. (2005) employs a bounding surface similar to the yield function which was introduced by Yu (1998) and a limiting isotropic compression line as a reference for the high pressure region. In order to capture grain crushing at high stresses, the critical state line in compression is expressed in three linear segments. Russel and Khalili (2004)'s model, which was proposed for monotonic behavior of cohesionless sands, uses the radial mapping rule with a fixed projection center. However, Khalili et. al. (2005)'s model, which was proposed for cyclic behavior of cohesionless sands, uses the radial mapping rule with a mobile projection center. That is, the projection center is assumed to move from its initial location to the inception point of stress reversal. Yang et. al. (2011) also uses the mapping rule with the mobile projection center in their bounding surface-generalized plasticity model. To remove excessive memory and storage requirement due to complex mapping rule adopted in Khalili et. al. (2005), Kan et. al. (2014) more recently introduced a single stress-point mapping rule which is simpler for application in complex loading-unloading paths.

In this chapter, the radial mapping formulation of the bounding surface plasticity theory with a fixed mapping center is used to model monotonic behavior of cemented sands. This is in contrast to most of the previous bounding surface plasticity models which were introduced to model the stress-strain behaviour of cohesionless soils.

4.2 Brief description of the original model

The theory and detailed formulation of the original model can be found in Imam et al. (2005). A brief overview is given here.

Adopting the stress ratio at the peak of the undrained effective stress path, M_p , is a main feature of the model. This is consistent with early claims that in loose sand, the stress ratio at the peak of the yield surface is very close to the stress ratio at

the peak of the undrained effective stress path. Shear strains associated with the peak of the undrained effective stress path are usually relatively small. This results in a more accurate evaluation of the peak of the yield surface because in the early stages of undrained tests, straining is more uniform and less affected by localization. As a result, the shape of the yield surface depends on M_p [Imam and Chan 2008]. Similar to other critical state models, the soil state at large strains where the soil structure is fully destroyed is represented by the critical state line. The model employs a single set of model constants (nine for compressive and two for extensive loading in its most general form) to predict sand response over a wide range of void ratios and confining pressures.

The yield function is expressed as:

$$f = (\eta - \alpha)^2 - M_\alpha^2 \left(1 - \sqrt{\frac{p}{p_c}} \right) = 0 \quad (4.1)$$

$$M_\alpha^2 = (5M_p - \alpha)(M_p - \alpha) \quad (4.2)$$

where η is the stress ratio, p is the mean effective stress, α is a scalar constant whose magnitude is zero for isotropically consolidated sands, and p_c is the effective preconsolidation pressure which is a hardening parameter controlling the size of the yield surface.

M_p is evaluated for compression and extension, respectively, with the following equations:

$$M_{p,c} = \frac{6 \sin \varphi_{p,c}}{3 - \sin \varphi_{p,c}} \quad (4.3)$$

$$M_{p,e} = \frac{6 \sin \varphi_{p,e}}{3 + \sin \varphi_{p,e}} \quad (4.4)$$

in which $\varphi_{p,c}$ and $\varphi_{p,e}$ are the friction angles at the point of peak shear stress in triaxial compression and triaxial extension, respectively. They are calculated by:

$$\sin \varphi_{p,c} = \sin \varphi_\mu - k_p \psi_p \quad (4.5)$$

$$\sin \varphi_{p,e} = \sin \varphi_\mu - k_p \psi_p - a_p \quad (4.6)$$

where $\psi_p = e - e_p$ in which e is void ratio, and e_p is the critical state void ratio which is evaluated at mean normal pressure corresponding to the peak point of shear stress (i.e. at $p = p_p$), φ_μ is the friction angle associated with $\psi_p = 0$ in triaxial compression and is usually close to the interparticle friction angle and k_p and a_p are model parameters.

Similar to conventional plasticity, isotropic elasticity is represented by two elastic parameters: the bulk and shear moduli. They are expressed as a direct function of the mean effective stress and inverse function of void ratio as follows:

$$G = G_a \frac{(2.973 - e)^2}{1 + e} \left(\frac{p}{p_{atm}} \right)^n \quad (4.7)$$

$$K = K_a \frac{(2.973 - e)^2}{1 + e} \left(\frac{p}{p_{atm}} \right)^n \quad (4.8)$$

where G_a and K_a are reference elastic moduli which are considered as material parameters, and p_a is atmospheric pressure. A value of 0.5-0.6 is usually used for n , depending on the type of sand.

Following the work of Wood (1990) and Manzari and Dafalias (1997), the stress-dilatancy relationship is defined as:

$$D = A(M_{PT} - \eta) \quad (4.9)$$

$$A_c = \frac{9}{9 + 3M_{PT,c} - 2M_{PT,c}\eta} \quad (4.10)$$

$$A_e = \frac{9}{9 - 3M_{PT,e} - 2M_{PT,e}\eta} \quad (4.11)$$

where

$$\sin\varphi_{PT,c} = \sin\varphi_{cs} + k_{PT}\psi_s \quad (4.12)$$

$$\sin\varphi_{PT,e} = \sin\varphi_{cs} + k_{PT}\psi_s + a_{PT} \quad (4.13)$$

in which M_{PT} is the phase transformation stress ratio reached under undrained conditions when volumetric-plastic strain (and as a result dilatancy) changes its sign, resulting in a change in the sign of \dot{p} , φ_{cs} is the critical state friction angle (a

model parameter), $\psi_s = e - e_{cs}$ is the state parameter which is the difference between the current void ratio and the critical state void ratio at the current mean normal stress [Been and Jefferies 1985, Jefferies 1993], and k_{pT} and a_{pT} are both material parameters. M_{pT} for compression and extension is obtained based on $\sin\varphi_{pT}$ similarly as for $M_{p,c}$ and $M_{p,e}$. Due to the dependency of M_{pT} on the state parameter, the effect of void ratio and mean effective pressure is indirectly included in the flow rule.

Hardening in this model depends on the proximity to the critical state in contrast to conventional critical state models which couple the size of the yield surface to void ratio and obtain hardening law based on plastic volumetric strain using a constant p stress path [Schofield 1993, Wood 1990, Bardet 1986, Yu 2006, Yu et al. 2007, Suebsuk et al. 2010 and 2011]. This is similar to Jefferies's approach (1993) which formulated size hardening as a function of the difference between the current maximum hardness and the current size of the yield surface. The reason for deviating from the classical method is that there are infinite numbers of normal consolidation lines for sand by virtue of its ability to repack. Thus, direct coupling between void ratio and the yield surface size is not feasible in sand since there is no unique reference on the compression plane ($e - \ln p$) from which one can project the current stress point into the $q - p$ plane to obtain the effective preconsolidation pressure [Jefferies 1993].

Pure size shear hardening law is expressed as:

$$\frac{\partial p_c}{\partial \varepsilon_q^p} = \frac{hG_{ini}}{(p_f - p_c)_{ini}} (p_f - p_c) \quad (4.14)$$

in which h is a model parameter, p_f is the failure mean effective stress, which is obtained by substituting the failure stress ratio (M_f) for η in the yield function equation, and $(p_f - p_c)_{ini}$ is the initial value of $(p_f - p_c)$ at the end of consolidation and prior to shearing. M_f is calculated based on $\sin\varphi_f$, which itself is obtained by adopting a Mohr-Coulomb type failure criterion as follows:

$$\sin\varphi_f = \sin\varphi_{cs} - k_f\psi_s \quad (4.15)$$

where k_f is a model parameter. Note that M_f is the maximum attainable stress ratio at the current stress state.

Note that shape hardening can also occur during shearing due to changes in M_p or $\sin\phi_p$ with plastic (deviator) strain. Equations (4.5) and (4.6) defines a linear relationship between $\sin\phi_p$ and ψ_p . Changes in ψ_p come from changes in the void ratio or the mean pressure at the peak of the undrained effective stress path. Application of the model has shown that use of the initial value of M_p or $\sin\phi_p$ at the start of shearing and neglecting the subsequent shape hardening during shearing does not lead to considerable lack of accuracy (Imam et. al. 2005).

4.3 A critical state framework for bonded sand

Modification of the original model is carried out based on experimental observations showing the differences between the response of cemented and equivalent uncemented soils. Fig. 4-1 schematically represents the effect of bonding on the isotropic compression curve. It can be recognized that bonded geomaterials exist at a higher void ratio for the same mean normal pressure, leading to broader admissible states compared to unbonded materials. Differences in the void ratios of bonded and equivalent unbonded materials at their loosest possible state under a specific mean pressure can signify the degree of bonding. Significant differences in the values denote higher degrees of bonding and higher initial yield stresses. As shown in Fig. 4-1, the degree of bonding also may be taken into account as the difference between the mean normal stresses at the loosest possible state for the bonded and unbonded material under the same void ratio. This implies that cemented soil can carry a higher stress at a given void ratio or can carry a given stress at a higher void ratio [Vatsala et al. 2001].

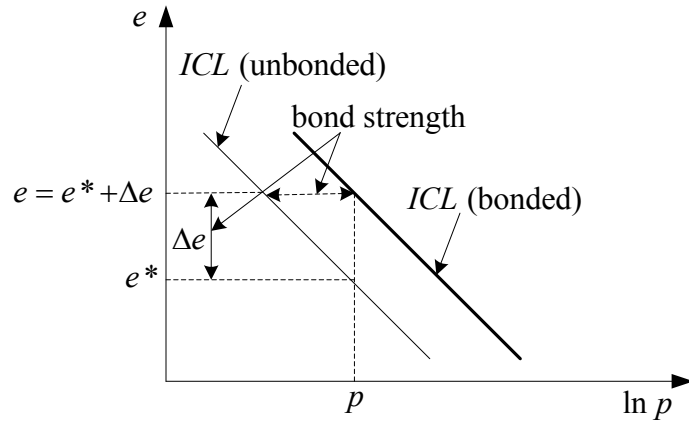


Fig. 4-1 Idealized representation of compression response for bonded soil

Fig. 4-2, obtained by experimentation, exemplifies that the yield stress increases with an increase in cement content, implying a larger size for the initial yield surface. The initial yield is considered as the point at which breakage of the cement bonds commences and is regarded as a state where the compression plane and stress-strain curves deviate from the initial linear response.

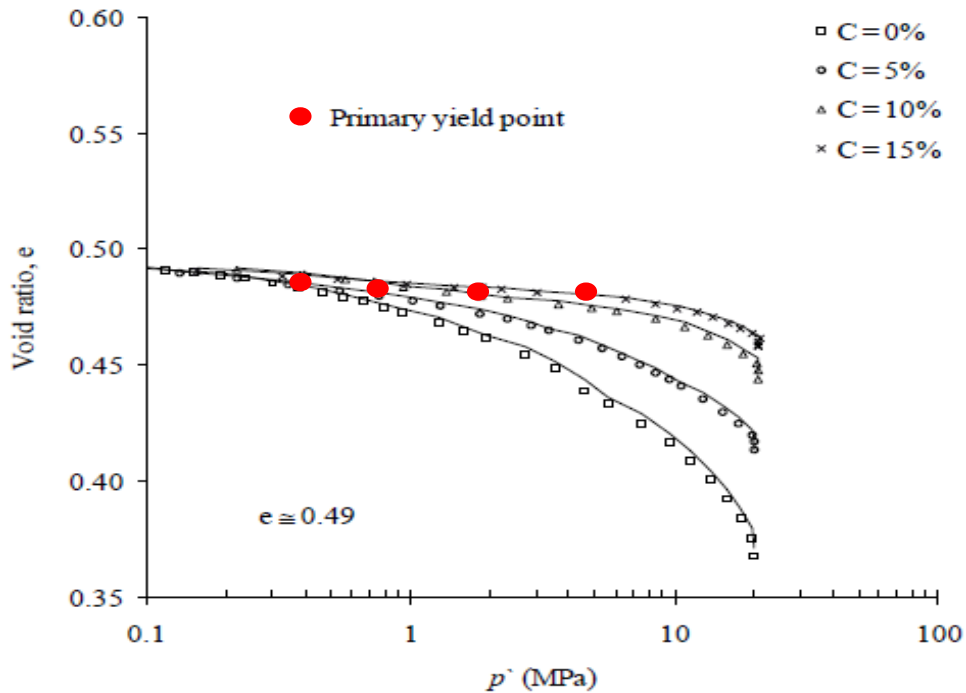


Fig. 4-2 Effect of cement content on the initial yield point of cement treated Portaway sand [modified after Marri 2010]

Fig. 4-3 suggests that by increasing the cement content, there is an increase in the normalized initial yield stress (and peak stress). The position of the yield point also shifts towards the left, implying a stiffer response with an increase in the cement content. It is clear that the tendency for a brittle response for the same confining stress increases with cement content. For an ideal case, the shear stress-strain curve for structured soils will ultimately be identical to that for remoulded soils at a critical state where all cemented bonds will be destroyed. This, however, does not always materialize because some bonds may not be broken even after an appreciable amount of shearing well beyond the initial yield point [Lee et al. 2004]. That is, cemented soil may arrive at the ultimate void ratio after a large amount of shearing rather than at the critical state void ratio, which is associated with constant volume and is independent of the initial state. This is one of the existing challenges in applying the critical state theory in cemented soil and especially in cemented sand. Many researchers (for instance Leeson and Campbell 1983, Ferreira and Bica 2006, and Marri 2010) have also argued that in reality the CSL is an ultimate state line rather than the critical state line because volumetric change often remains inconstant for cemented sand. Thus, one may expect CSL to depend on the initial void ratio for cemented sand as observed experimentally by Marri (2010). It was concluded that critical state lines for cemented sands locate to the right and above the CSL of equivalent uncemented sands. Higher cement content give rise to larger critical state void ratios for a given confining stress as well. Uncertainty in the application of a unique critical state line for cemented sand at large is more than that for uncemented sand since deformation under constant volume occurs uncommonly for cemented sand. Note that the application of a non-unique CSL has been reported for cohesionless sand as well. For example, in Bardet's work (1986) different critical state lines are used to calibrate the response of loose and dense Sacramento River Sand.

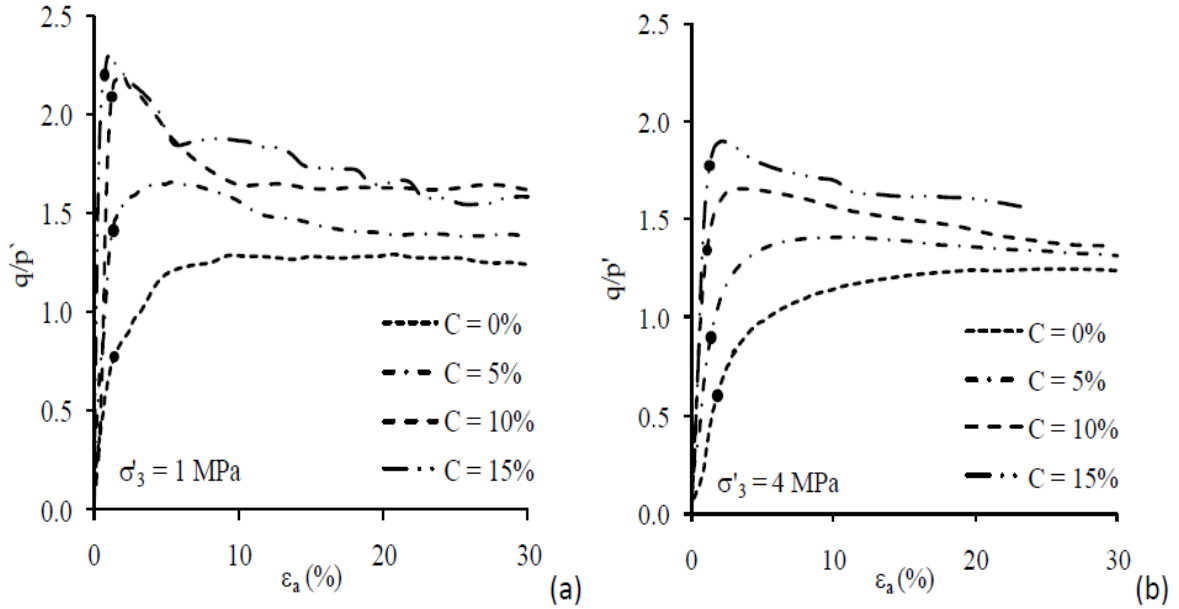


Fig. 4-3 Effect of cement content on the location of the initial yield point (small bold circles): a) triaxial tests with confining pressure of 1 MPa b) triaxial tests with confining pressure of 4 MPa [Marri 2010]

As mentioned earlier, bonding provides tensile strength, cohesion and additional strength to the material. In considering the additional strength, the yield surface for the unbonded geomaterials must be enlarged towards the right. It must also be expanded towards the left to account for the tensile strength. Thus, more bonding results in larger expansion of the yield surface towards both the right and left.

Fig.4-4 illustrates the schematic representation of the modified yield surface. For simplicity, the original shape of the yield function is preserved. Expansion towards the right and left are indicated by p_o and p_t , respectively, p_b controls yielding of the bonded material in isotropic compression, which determines the size of the enlarged yield surface, and p_o controls the growth in size of the initial elastic domain. The degree of bonding may be expressed as p_o/p_c .

The yield function, flow rule, hardening modulus and elastic properties are modified in order to create a new constitutive model suitable for cemented sand. A brief discussion of the modifications for the new constitutive model is presented herein.

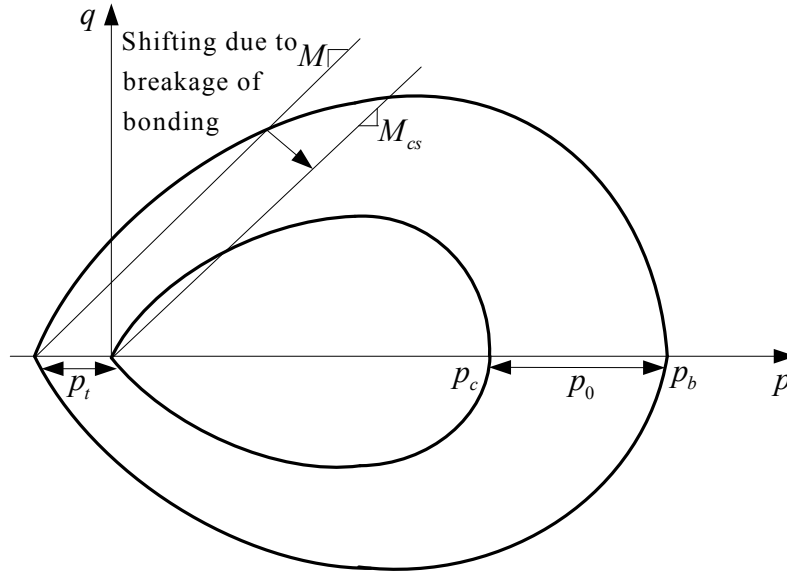


Fig. 4-4 Schematic representation of the modified yield surface

4.3.1 Elasticity

In line with experimental observations that indicate bonded geomaterials have higher stiffness values compared to their reconstituted counterparts [Marri 2010, Yu 2006], the definition of the elastic properties are modified similar to the approach adopted by Yu et al. (2007) as follows:

$$G = G_a \frac{(2.973 - e)^2}{1 + e} \left(\frac{p}{p_{atm}} \left(1 + \sqrt{\frac{p_0}{p}} \right) \right)^n \quad (4.16)$$

$$K = K_a \frac{(2.973 - e)^2}{1 + e} \left(\frac{p}{p_{atm}} \left(1 + \sqrt{\frac{p_0}{p}} \right) \right)^n \quad (4.17)$$

This definition provides three important features of the bonded geomaterials [Yu et al. 2007]: a) extra initial elastic stiffness due to bonding; b) a decline in the initial increase of elastic stiffness by an increase in the initial mean normal stress at the start of shearing; and c) the progressive reduction of moduli due to breakage of bonding during plastic straining.

4.3.2 Yield function

The new yield function is defined as follows:

$$f = \left(\frac{q}{p + p_t} - \alpha \right)^2 - M_\alpha^2 \left(1 - \sqrt{\frac{p + p_t}{p_b}} \right) = 0 \quad (4.18)$$

$$p_b = p_t + p_c + p_o \quad (4.19)$$

where α and M_α^2 are defined similar to the definitions given in the original model. For triaxial conditions, $\alpha = 0$ and $M_\alpha^2 = 5M_p^2$. Note that the original yield function has been modified according to Gens and Nova (1993). Similar assumptions have also been considered for the relationships between additional strengths and p_c .

$$\frac{p_o}{p_c} = b_1 \quad (4.20)$$

$$\frac{p_t}{p_c} = \beta b_1 \quad (4.21)$$

These assumptions suggest a direct relationship between two additional strengths as follows:

$$p_t = \beta p_o \quad (4.22)$$

This direct relationship enables p_t and p_o to simultaneously reduce to zero.

Hence, p_b which controls the size of the yield surface for bonded sand consists of two components:

$$p_b = p_c + (1 + \beta)p_o \quad (4.23)$$

where p_c plays the same role as the effective preconsolidation pressure for uncemented soil.

Destructuration of bonds between sand particles due to plastic deformation (as a damage parameter) is supposed to only change the size of the bonded yield surface. The shape of the bonded yield surface, however, is supposed to remain unchanged. When considering bond destructuration, the following simple linear relationship is assumed:

$$dp_o = -\gamma p_o d|\varepsilon_q^p| \quad (4.24)$$

The adopted rule for the degradation of p_o implies that the number of bonds that breaks with plastic deformation is proportional to the total number of bonds [Nova 2005].

4.3.3 Flow rule

Rowe (1962) derived the stress dilatancy relationship for soils using the minimum energy consideration for particle sliding [cited in Imam 1999] as follows:

$$R = KD \quad \text{for } TC \quad (4.25)$$

$$R = \frac{K}{D} \quad \text{for } TE \quad (4.26)$$

where R is the ratio of major principal stress to minor principal stress, K is a material parameter, TC stands for triaxial compression, TE stands for triaxial extension, and D is the dilatancy parameter written based on increments of volumetric and major principal strains. The constant K is based on the assumption that the ratio of work done by the driving stress to the work done by the driven stress in any strain increment should be a constant. Driving and driven stresses for triaxial compression, respectively, are axial and radial stresses. That is, for triaxial compression [Wood 1990]:

$$\frac{\sigma_a \dot{\varepsilon}_a}{-2\sigma_r \dot{\varepsilon}_r} = K = \frac{1 + \sin\varphi_f}{1 - \sin\varphi_f} \quad (4.27)$$

R , K , and D mathematically are expressed as follows [Imam 1999]:

$$R = \frac{\sigma_1}{\sigma_3} \quad (4.28)$$

$$K = \tan^2 \left(45 + \frac{\varphi_f}{2} \right) \quad \varphi_\mu < \varphi_f < \varphi_{cv} \quad (4.29)$$

$$D = 1 - \frac{d\varepsilon_v}{d\varepsilon_1} \quad (4.30)$$

Incorporation of varying φ_f in the constitutive model is difficult [Imam 1999], as φ_f varies between interparticle and critical state friction angles. This is why usually a constant value is assumed for φ_f . With assuming a constant value for φ_f (which means a constant volume or critical state friction angle) and neglecting elastic strains, Wood formulated Rowe's stress-dilatancy relationship for the compression and extension of soils, respectively, as follows [Wood 1990]:

$$D = \frac{\dot{\epsilon}_p^p}{\dot{\epsilon}_q^p} = \frac{9(M_{cs,c} - \eta)}{9 + 3M_{cs,c} - 2M_{cs,c}\eta} \quad (4.31)$$

$$D = \frac{\dot{\epsilon}_p^p}{\dot{\epsilon}_q^p} = \frac{9(M_{cs,e} - \eta)}{9 - 3M_{cs,e} - 2M_{cs,e}\eta} \quad (4.32)$$

Rowe's relationship, however, does not capture the stress-dilatancy behaviour of cemented sand. The deviation of predictions from observed volumetric behaviour in some cases become very pronounced, although one may arrive at better predictions for the shear stress-strain curve. The change in volumetric behaviour in the cemented soil mainly depends on the cementation and breakage of particle bonding [Lee et al. 2004]. Laboratory test results have suggested that dilatancy is not only affected by the friction angle φ_f , but also by interparticle cohesion. Also, it is believed that the total work performed by the stresses is dissipated partly through friction and partly through destroying the structure. Thus, it is logical to incorporate cohesion into the dilatancy relationship. One approach is by changing the parameter K as follows [Yu et al. 2007]:

$$K = \tan^2 \left(45 + \frac{\varphi_f}{2} \right) + \frac{2c}{\sigma_3} \tan \left(45 + \frac{\varphi_f}{2} \right) \quad (4.33)$$

Normalizing cohesion with respect to the minor principal stress implies that cohesion decreases with an increase in the minor principal stress. This is compatible with experimental observations where the response of bonded materials under triaxial compression change from brittle to ductile with an increase in the confining stress [Yu et al. 2007]. Crushing of the particles may be one reason for this shift. Even though some experimental evidence suggests the suppression of dilatancy by cohesion [Yu et al. 2007], counter observations regarding the impact of bonding on stress-dilatancy have been reported as well. For instance, Clough et al. (1981), Asghari et al. (2003) and Marri (2010) found that an increase in the cement content had a tendency of inducing dilatancy and subsequently reduced compression. According to Fernandez and Santamarina (2000), cemented sand seems to be more dilative than its reconstituted counterpart. Higher dilation under undrained conditions implies that lower excess pore water pressure is produced by shear, and sand is also less prone to

liquefaction. This suggests that bonding enhances the liquefaction resistance of sand [Gao and Zhao 2012]. What is clear, however, is that dilatancy is influenced by bonding. The stress-dilatancy relationship, by incorporating cohesion for compression, may be calculated by [Yu et al. 2007]:

$$D = \frac{9(M_{cs} - \eta) + 6\frac{c}{p}\sqrt{(2M_{cs} + 3)(-M_{cs} + 3)}}{9 + 3M_{cs} - 2M_{cs}\eta + 4\frac{c}{p}\sqrt{(2M_{cs} + 3)(-M_{cs} + 3)}} \quad (4.34)$$

Cohesion is assumed to decrease with plastic shear strain as follows:

$$dc = ce^{-\xi d|\varepsilon_q^p|} \quad (4.35)$$

It is clear that when cohesion is zero, Rowe's stress-dilatancy relationship for unbonded soils will be recovered.

Compatible with Imam's approach [Imam et al. 2005], the dilatancy relationship is written in terms of the variable phase transformation stress ratio rather than the constant critical state stress ratio. This makes the dilatancy relationship closer to the original formula which was proposed by Rowe (1962). For triaxial compression conditions:

$$D = \sqrt{\frac{2}{3}} \left(A(M_{pt} - \eta) + \frac{6B}{C} \right) \quad (4.36)$$

$$A = \frac{9}{C} \quad (4.37)$$

$$C = 9 + 3M_{pt,c} - 2M_{pt,c}\eta + 4B \quad (4.38)$$

$$B = \frac{c}{p}\sqrt{(2M_{pt} + 3)(-M_{pt} + 3)} \quad (4.39)$$

4.3.4 Hardening modulus

A pure size shear hardening law is adopted for the modified model. Variation of p_c with respect to shear strain is assumed to be exactly the same as that for the unbonded model. Also similar to the original model, shape hardening due to variations of M_p is neglected for the modified model. After some manipulation and ensuring the state of stress remains on the modified yield surface, the

following formula is derived for the normalized hardening modulus under triaxial conditions:

$$H_n = -\sqrt{\frac{2}{3}} \frac{1}{\left|\frac{\partial f}{\partial q}\right|} \frac{\partial f}{\partial p_b} \frac{\partial p_b}{\partial \varepsilon_q^p} \quad (4.40)$$

where,

$$\frac{\partial f}{\partial p_b} = -\frac{M_\alpha^2}{2p_b} \sqrt{\frac{p+p_t}{p_b}} \quad (4.41)$$

$$\frac{\partial f}{\partial q} = \frac{2}{p+p_t} \left(\frac{q}{p+p_t} - \alpha \right) \quad (4.42)$$

$$\frac{\partial p_b}{\partial \varepsilon_q^p} = \frac{\partial p_c}{\partial \varepsilon_q^p} + (1+\beta) \frac{\partial p_o}{\partial \varepsilon_q^p} = \frac{hG_{ini}}{(p_f - p_c)_{ini}} (p_f - p_c) - (1+\beta)\gamma p_o \quad (4.43)$$

$$\frac{\partial f}{\partial p} = \frac{-2q}{(p+p_t)^2} \left(\frac{q}{p+p_t} - \alpha \right) + \frac{1}{2} M_\alpha^2 \frac{1}{\sqrt{p_b(p+p_t)}} \quad (4.44)$$

$$p_f = \frac{p}{\left(1 - \frac{(M_f - \alpha)^2}{M_\alpha^2} \right)^2} \quad (4.45)$$

Consistent with Gens and Nova (1993), the plastic hardening modulus is stated by two competing terms. That is, the change of the bonded yield surface is controlled by two different mechanisms: a) an unbounded hardening law, hardening or softening the unbonded yield surface due to void ratio reduction or augmentation; and b) bond degradation, shrinking the bonded yield surface by virtue of plastic deformation. Thus, softening occurs when the resultant sign of the plastic modulus becomes negative.

4.3.5 Material parameters

Five additional model parameters were introduced in the bonded model:

1. Initial value of p_o
2. Initial value of tensile strength to evaluate β
3. Decay parameter of bond strength (γ)
4. Cohesion (c)

5. Rate of degradation of cohesion (ξ)

The initial value of p_o is equal to the difference between the initial values of p_b and p_c . The initial value of p_c for the triaxial test is taken as the maximum mean normal stress characterizing the initial elastic domain for uncemented soil. The initial value of p_b can be evaluated by conducting an isotropic compression test on cemented sand to determine the initial yield value of p_b [Nova 2005].

The parameter β , which controls the size of the tensile strength surface, is obtained when the initial value of the tensile strength is evaluated using results from a tensile test. If there is no data regarding the tensile strength, the unconfined compressive strength may be considered as an approximation for the tensile strength (tensile strength is in order of 5% to 20% of the unconfined compressive strength); otherwise, a typical value in the range of 0.05-0.25 may be selected as a value for β .

The parameter γ controls the rate at which bonds are broken. The higher value of γ , the faster the bonded yield surface becomes identical to the unbonded yield surface.

The parameter c can be evaluated using the Mohr-Coulomb failure envelope.

The parameter ξ can be evaluated by fitting predicted volumetric behaviour to measured experimental data.

It should be noted that if a zero value is assigned for all five additional material parameters, the original constitutive model will be recovered.

4.4 A bounding surface model for cemented sand

4.4.1 Elasticity and flow rule

For simplicity, all assumptions made for the elasticity and flow rule of the modified bonded model are retained unchanged.

4.4.2 Bounding and loading surfaces

The bounding surface is assumed to have the same shape as the yield surface of the modified bonded model. This assumption not only makes calculations simpler, but it is also useful to support a typical assumption made in the bounding surface

plasticity regarding the direction of the plastic strain increment. This assumption will result in a formula for the plastic modulus of the bounding surface. It can be shown that if an associated flow rule is adopted, the unit outward normal at the current stress state is always equal to that of the image point as long as the two surfaces have the same shape.

Thus, the cemented bounding and loading surfaces in terms of conventional triaxial variables are written as follows:

$$F_{CBS} = \left(\frac{\bar{q}}{\bar{p} + p_t} - \alpha \right)^2 - M_\alpha^2 \left(1 - \sqrt{\frac{\bar{p} + p_t}{\bar{p}_b}} \right) = 0 \quad (4.46)$$

$$f_{CLS} = \left(\frac{q}{p + p_t} - \alpha \right)^2 - M_\alpha^2 \left(1 - \sqrt{\frac{p + p_t}{p_b}} \right) = 0 \quad (4.47)$$

in which,

$$\bar{p}_b = p_t + \bar{p}_c + \bar{p}_o \quad (4.48)$$

$$p_t = \bar{\beta} \bar{p}_o = \beta p_o \quad (4.49)$$

The superimposed bar signifies variables of the bounding surface.

The relationship of the tensile strength suggests that $\bar{\beta}$ and \bar{p}_o cannot be chosen arbitrarily simultaneously because they must result in the same tensile strength as that obtained by β and p_o . This means only one of them, for instance \bar{p}_o , can be chosen as a material parameter. To avoid having more model parameters, \bar{p}_o may be obliged to obtain an initial value which produces the same initial bonding for the cemented bounding surface than that for the cemented loading surface. Based on this simplifying assumption, it can be shown that:

$$\bar{\beta} = \frac{\beta p_o}{\left(\frac{p_o}{p_c}\right) \bar{p}_c} = \frac{\beta p_c}{\bar{p}_c} \quad (4.50)$$

Thus,

$$\bar{p}_b = \bar{p}_c + \beta \left(1 + \frac{1}{\bar{\beta}} \right) p_o \quad (4.51)$$

The initial values of p_c and \bar{p}_c are evaluated from the confining pressure and failure mean normal pressure at the commencement of shearing, respectively. Fig. 4-5 illustrates the proposed bounding surface model. LS, CLS, BS and CBS respectively stand for loading surface, cemented loading surface, bounding surface (which is associated with loading surface) and cemented bounding surface (which is associated with cemented loading surface).

For simplicity, the size ratio between the cemented loading and cemented bounding surfaces is assumed to remain fixed in the course of plastic loading. This assumption assures that the loading surface never intersects the bounding surface and that the stress state always lies inside the bounding surface. The application of a fixed size ratio between the loading and bounding surfaces already has been practiced by several researchers [Al-Tabbaa 1987, Hau 2003, McDowell and Hau 2004].

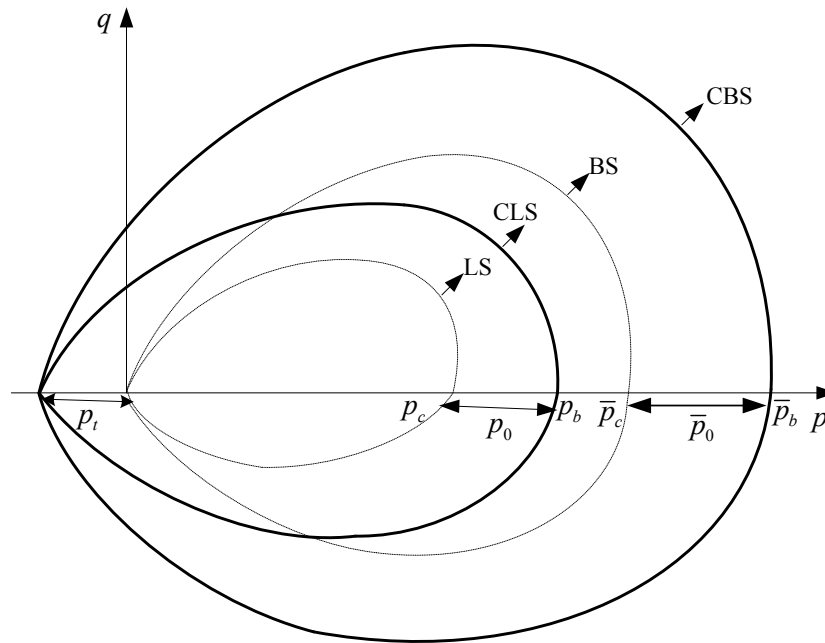


Fig. 4-5 Schematic representation of the proposed bounding surface model within a conventional triaxial (p, q) space

4.4.3 Projection rule

The radial mapping rule is employed to associate any current stress point with a corresponding unique image point. This is achieved by the intersection of the cemented bounding surface with a line passing through the projection center and the current stress point (see Fig. 4-6). Because of the similarity in shape and radial symmetry of the surfaces, the unique image stresses (\bar{p}, \bar{q}) can be evaluated using the current stresses (p, q) as follows:

$$\frac{\bar{p} + p_t}{p + p_t} = \frac{\bar{q}}{q} = \frac{\bar{p}_b}{p_b} = b_p \quad 1 \leq b_p \leq \infty \quad (4.52)$$

Because the projection center is not at the origin of the coordinate system, stress ratios at the current stress point and the corresponding image point are not the same. However, they are equal when all structures have been destroyed.

Note that the mapping rule is not invertible (i.e. while a unique image stress exists on the bounding surface for a given current stress on the loading surface, a given image stress may correspond to many stress states [Dafalias 1986]).

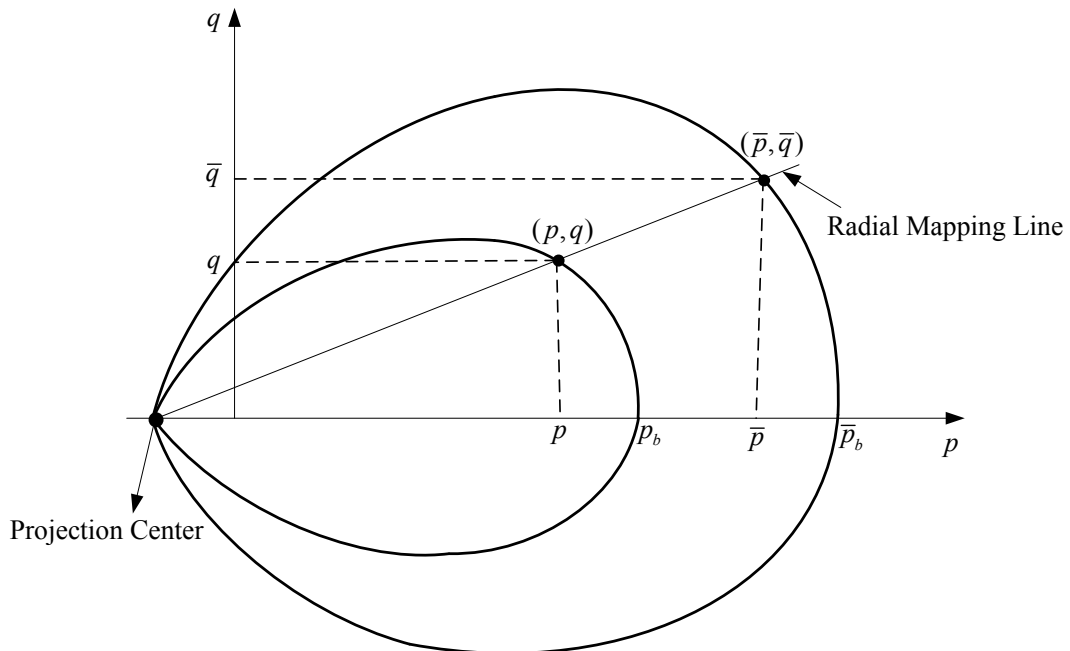


Fig. 4-6 Radial mapping rule for a conventional triaxial (p, q) space

4.4.4 Hardening modulus

In line with the mainstream approach for the bounding surface plasticity, the plastic hardening modulus is divided into two parts: the bounding surface modulus and additive plastic modulus.

$$H_n = \bar{H}_n + H_f \quad (4.53)$$

The additive plastic modulus indicates a dependency of the response on the relative distance between the current stress point and corresponding image point. The dependency of the plastic response on the distance between the current stress and its image point stemmed from experimental observations where uniaxial stress strain curves asymptotically approached fixed or variable bounds in the stress space under complex loading histories [Chen 1994, Chen and Han 2007]. The following formula is proposed for the additive plastic modulus:

$$H_f = \frac{\Gamma \cdot p \cdot \delta}{(\delta_o - \delta)^2} \quad (4.54)$$

The parameter Γ signifies the dependency of the response to the type of material. Also, δ is the distance between the current stress point and the corresponding image point:

$$\delta = \sqrt{(\bar{p} - p)^2 + (\bar{q} - q)^2} \quad (4.55)$$

where δ_o is the initial value of δ .

This definition guarantees that H_f is always positive and has an infinite value at the start of shearing. H_f reduces to zero when the loading surface and bounding surface for the cementation coincide. These are prerequisite for the additive plastic modulus definition [Vermeer and Borst 1984].

The value of \bar{H}_n is calculated by coercing the state of stress to remain on the bounding surface for a special case when two surfaces coincide. Under triaxial conditions, it can be shown that:

$$\bar{H}_n = -\sqrt{\frac{2}{3}} \frac{1}{\left| \frac{\partial F}{\partial \bar{q}} \right|} \frac{\partial F}{\partial \bar{p}_b} \frac{\partial \bar{p}_b}{\partial \varepsilon_q^p} \quad (4.56)$$

in which:

$$\frac{\partial F}{\partial \bar{p}_b} = -\frac{M_\alpha^2}{2\bar{p}_b} \sqrt{\frac{\bar{p} + p_t}{\bar{p}_b}} \quad (4.57)$$

$$\frac{\partial F}{\partial \bar{q}} = \frac{2}{\bar{p} + p_t} \left(\frac{\bar{q}}{\bar{p} + p_t} - \alpha \right) \quad (4.58)$$

$$\frac{\partial \bar{p}_b}{\partial \varepsilon_q^p} = \frac{\partial \bar{p}_c}{\partial \varepsilon_q^p} + \beta \left(1 + \frac{1}{\bar{\beta}} \right) \frac{\partial p_o}{\partial \varepsilon_q^p} \quad (4.59)$$

$$\frac{\partial \bar{p}_c}{\partial \varepsilon_q^p} = \frac{hG_{ini}}{(\bar{p}_f - \bar{p}_c)_{ini}} (\bar{p}_f - \bar{p}_c) \quad (4.60)$$

It is assumed that linear destruction of the structure by plastic shear deformation gives rise to changes in the size of the cemented loading surface. Its shape, however, is supposed to remain unchanged due to this destruction. That is,

$$\frac{\partial p_o}{\partial \varepsilon_q^p} = -\gamma p_o \quad (4.61)$$

4.5 Assessment of the proposed bounding surface model

The proposed bounding surface model is evaluated against the triaxial compression tests of two artificially cemented sands under different void ratios and confining pressures. The first set of experimental observations comes from the observed behaviour of artificially cemented Ottawa sand [Wang and Leung 2008]. Figs. 4-7 to 4-9 compare the simulated and measured response of cemented Ottawa sand for different cement contents in terms of shear stress-strain, void ratio-axial strain and volumetric strain-axial strain plots. Table 4-1 lists the model parameters and their allocated values for the simulation of Ottawa cemented sand with 1% cement content. The same material parameters are utilized also for prediction of behaviour of 2% and 3% cement content samples excluding critical state friction angle, critical state line and cohesion. Experimentally measured cohesion and critical state friction angles of 11.5 *kPa* and 30.9 degrees were used

for 2% cement content samples, and values of 44 *kPa* and 31.1 degrees were used for 3% cement content samples.

Table 4-1 Material parameters used for the calibration of cemented Ottawa sand (1%),
 $p^* = p + p_t$

Parameter name	Ottawa cemented sand (1%)
k_p	1.5
φ_μ	20
φ_{cs}	28.8
k_{PT}	1.4
G_a	6e6
K_a	8e6
h	1
k_f	0.75
e_{cs}	$-0.0063477p^{*3} + 0.0367p^{*2} - 0.11991p^* + 0.760$ (p^* in MPa)
p_o	0.12e6
γ	10
β	0.107
c	0.0075e6
ξ	0.08
Γ	1

It is believed that after a large shear-induced volume change, cohesionless sand ultimately arrives at a unique void ratio which is independent of its initial state. This unique void ratio is associated with full destructure of the soil structure and infinite amount of shearing. Fig. 4-8, however, reveals a noteworthy point for the ultimate state of the same cemented sand with different cement content under a given confining pressure. It is clear that samples with different cement content arrive at different ultimate void ratios after an appreciable amount of shearing. This implies that there is no unparallel critical state line that forms the ultimate state for all distortional processes. That is, CSL depends on cement content. It also can be inferred that the CSL for higher cement contents lies at a high position in the compression plane ($e - \ln p$) because it gives rise to a higher ultimate void ratio at a given confining pressure. The following ultimate state lines were adopted for 2% and 3% cement content samples:

$$e_{cs}(2\%) = -0.0063477p^{*3} + 0.0367p^{*2} - 0.11991p^* + 0.790 \quad (p^* \text{ in MPa})$$

$$e_{cs}(3\%) = -0.0063477p^{*3} + 0.0367p^{*2} - 0.11991p^* + 0.8725 \quad (p^* \text{ in MPa})$$

As seen in Figs. 4-8 to 4-9, the predicted and measured volumetric behaviours are in good agreement. The change of response from contractive to dilative, which is associated with strain softening, is seen in all tests. This change of behaviour is predicted numerically by a change of dilatancy rate sign from positive to negative. This causes immediate change in the sign of the plastic volumetric strain increment. The sign of the total volumetric strain increment also varies due to this change after a short time. It is also clear from Figs. 4-7 to 4-9 that samples with the higher cement content show stronger dilative and brittle behaviour. It should be noted that there is small discrepancy in the predicted and observed stress-strain behaviour of the test with 3% cement content. That is, the model has predicted the weaker softening response for the post peak region of the test with 3% cement content.

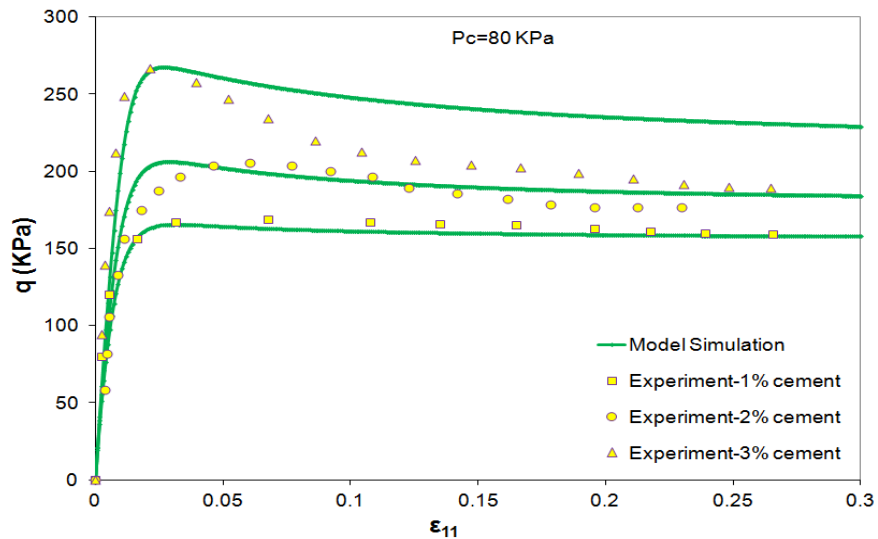


Fig. 4-7 Measured and predicted response of cemented Ottawa sand for deviator stress vs. axial strain curve under different cement contents

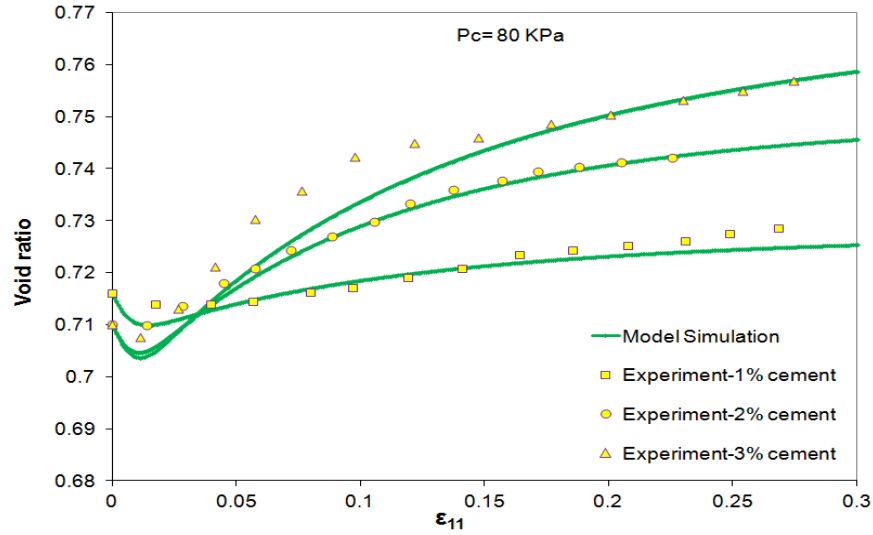


Fig. 4-8 Measured and predicted response of cemented Ottawa sand for void ratio vs. axial strain curve under different cement contents

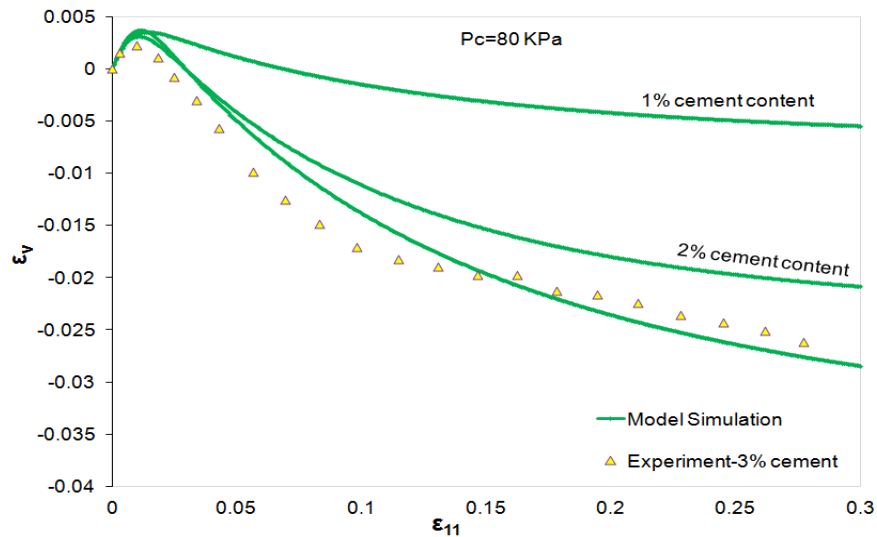


Fig. 4-9 Measured and predicted response of cemented Ottawa sand for volumetric strain vs. axial strain curve under different cement contents

The second set of experimental data was obtained from the observed responses of artificially cemented Portaway sand [Marri 2010]. Figs. 4-10 to 4-11 show the simulated and measured behaviour of cemented Portaway sand under different cement contents for deviatoric stress-strain and volumetric strain-axial strain curves. Fig. 4-12 exhibits the predicted response for the void ratio-axial strain

curve. Material parameters and their assigned values for these simulations are presented in Table 4-2.

For the 10% cement content samples, measured cohesion of 3.18 *MPa* and critical state friction angle of 36 degrees were used. The other remaining material parameters for the 10% cement content samples were the same as those utilized for the 5% cement content samples. For the 0% cement content samples, values of zero were allocated for all five additional material parameters relevant to cementation. Except the critical state line, the other material parameters for the 0% cement content samples were the same as the unbounded material parameters for the 5% cement content samples. The following ultimate state lines were adopted based on experimental observations:

$$e_{cs}(10\%) = 0.60 - 0.0097 \ln(p^*) \quad (p^* \text{ in } MPa)$$

$$e_{cs}(0\%) = 0.402 - 0.0086 \ln(p^*) \quad (p^* \text{ in } MPa)$$

Table 4-2 Material parameters used for calibration of artificially cemented Portaway sand (5%)

Parameter name	Portaway cemented sand (5%)
k_p	1
φ_μ	32
φ_{cs}	34
k_{pT}	1.25
G_a	10e6
K_a	28e6
h	1
k_f	0.75
e_{cs}	$0.49 - 0.00925 \ln(p + p_t)$ (p & p_t in <i>MPa</i>)
p_o	8e6
γ	5
β	0.10
c	1.08e6
ξ	2
Γ	1

Figs. 4-10 to 4-11 show that the proposed model has captured the progressive compressive and ductile behaviour of 0% and 5% cement content samples well.

Sign of the dilatancy rate and volumetric strain increment remains unchanged throughout shearing for tests with purely ductile behaviour. Though 5% cement content sample shows compressive response, the tendency for compression is less compared to that of 0% cement content sample. This decreasing trend in tendency for compression is seen in 10% cement content sample as well such that change of compressive to dilative behaviour is observed clearly for the sample with 10% cement content. The model has not captured the strain softening for 10% cement content well. The weaker drop in the peak deviator stress has been predicted by the model for the post peak region. The selection of an alternative flow rule can improve prediction of the brittle response. However, defining a reliable stress-dilatancy relationship is a challenging task for cemented soil in general and cemented sand in particular because it is difficult to simultaneously match both observed volumetric and shear behaviours perfectly for the samples with brittle response. The use of an additional destruction law, which can account for additional material degradation in post peak region, may also leads to better predictions for the strain softening. A potential source of the discrepancy in predicting the strain softening may also come from assumption of a uniform state of stress and strain within the samples. The non-uniformities and localized deformations might develop in the real samples during experimental tests. This possible development of localized zones of greater strains might result in stronger softening compared to predictions of the model which are based on average behaviour of different nodes.

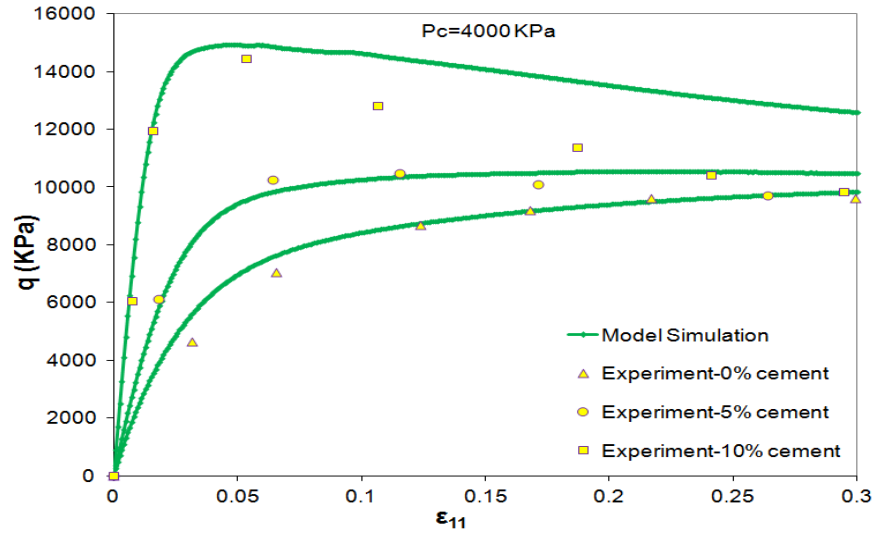


Fig. 4-10 Measured and predicted response of cemented Portaway sand for deviator stress vs. axial strain curve under different cement contents

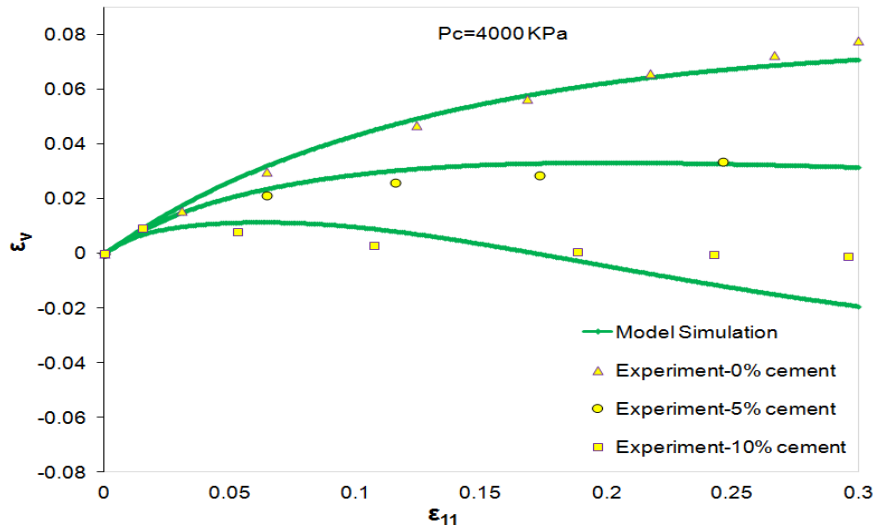


Fig. 4-11 Measured and predicted response of cemented Portaway sand for volumetric strain vs. axial strain curve under different cement contents

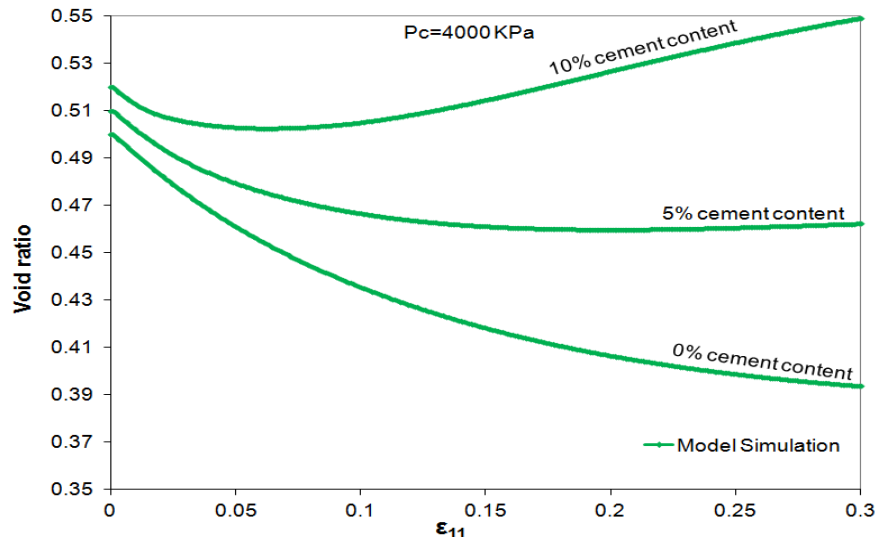


Fig. 4-12 Predicted response of cemented Portaway sand for void ratio vs. axial strain curve under different cement contents

4.6 Conclusion

A bounding surface model for monotonic loading of cemented sands was presented in this chapter. Two sets of triaxial compression tests on artificially cemented sands with different cement contents, void ratios and confining pressures were chosen to assess the effectiveness of the proposed modified model. Comparison of the simulated and observed behaviours showed an encouraging predictive capability of the proposed bounding surface model for cemented sand despite some simplifying assumptions. Moreover, because the proposed model was an extended version of the original model, the advantages of the original model were retained. A major drawback of the model was the prediction of the softening response for high cement contents. The application of an alternative flow rule, instead of the original or modified stress-dilatancy relationship, can result in better predictions by the model. Therefore the proposed model can capture the mechanical behaviour of cemented sands with low cement content. Although it can be used for cemented sand with high cement content, it shows some deficiencies in modeling the post peak responses.

4.7 References

Al-Tabbaa, A. (1987), Permeability and stress-strain response of speswhite kaolin, Ph.D. thesis, The University of Cambridge, Cambridge, U.K.

Asghari, E., Toll, D.G., and Haeri, S.M. (2003), Triaxial behaviour of a cemented gravely sand, Tehran alluvium, Geotechnical and Geological engineering, Vol. 21, No. 1, pp. 1-28.

Been, K., and Jefferies, M. G. (1985), A state parameter for sands, Géotechnique, Vol. 35, No. 2, pp. 99-112.

Bardet, J.P. (1986), Bounding surface plasticity model for sands, Journal of Engineering Mechanics, Vol. 112, No. 11, pp. 1198-1217.

Chen, W.F. (1994), Constitutive equations for engineering materials, Elsevier, Netherlands.

Chen, W.F., and Han D.J. (2007), Plasticity for structural engineers, John Ross Publishing, USA.

Clough, G.W., Shafii Rad, N., Bachus, R.C., and Sitar, N. (1981), Cemented sands under static loading, Journal of the Geotechnical Engineering Division, Vol. 107, No. 6, pp. 799-817.

Crouch, R.S., and Wolf, J.P. (1994), Unified 3D critical-state bounding-surface model for soils incorporating continuous plastic loading under cyclic paths. Part I: constitutive relations, International journal for numerical and analytical methods in geomechanics, Vol. 18, No. 11, pp. 735-758.

Crouch, R.S., Wolf, J.P., and Dafalias, Y.F. (1994), Unified critical-state bounding-surface plasticity model for soil, Journal of Engineering Mechanics, Vol. 120, No. 11, pp. 2251-2270.

Dafalias, Y.F. (1986), Bounding surface plasticity. I: mathematical foundation and hypoplasticity, Journal of Engineering Mechanics, Vol. 112, No. 9, pp. 966-987.

Dafalias, Y.F., and Herrmann, L.R. (1986), Bounding surface plasticity. II: application to isotropic cohesive soils, Journal of Engineering Mechanics, Vol. 112, No. 12, pp. 1263-1291.

Dafalias, Y.F., and Popov, E.P. (1975), A model of nonlinearly hardening materials for complex loading, Acta Mechanica, Vol. 21, pp. 173-192.

Fernandez, A.L., and Santamarina, J.C. (2000), Effect of cementation on the small-strain parameters of sands, Canadian Geotechnical Journal, Vol. 38, No. 1, pp. 191-199.

- Ferreira, P., and Bica, A. (2006), Problems in identifying the effects of structure and critical state in a soil with a transitional behaviour, *Géotechnique*, Vol. 56, No. 7, pp. 445-454.
- Gao, Z., and Zhao, J. (2012), Constitutive modeling of artificially cemented sand by considering fabric anisotropy, *Computers and Geotechnics*, Vol. 41, pp. 57-69.
- Gens, A., and Nova, R. (1993), Conceptual bases for a constitutive model for bonded soils and weak rocks, *Geotechnical engineering of hard soils-soft rocks*, pp. 485-494.
- Hau, K.W. (2003), Application of a three surface kinematic hardening model to the repeated loading and thinly surfaced pavements, Ph.D. thesis, The University of Nottingham, Nottingham, U.K.
- Imam, M.R. (1999), Modeling the constitutive behavior of sand for the analysis of static liquefaction, Ph.D. thesis, The University of Alberta, Edmonton, Canada.
- Imam, M.R., and Dave Chan. (2008), Application of a critical state model for the cyclic loading of sands, In *Proceedings from GeoEdmonton: 61st Canadian Geotechnical Conference*, Edmonton, pp. 127-134.
- Imam, S.M.R., Morgenstern N.R., Robertson P.K., and Chan, D.H. (2005), A critical-state constitutive model for liquefiable sand, *Canadian Geotechnical Journal*, Vol. 42, No. 3, pp. 830-855.
- Jefferies, M.G. (1993), Nor-Sand: a simple critical state model for sand, *Géotechnique*, Vol. 43, No. 1, pp. 91-103.
- Kan, M. E, Taiebat, H.A., and Khalili, N. (2014), Simplified mapping rule for bounding surface simulation of complex loading paths in granular materials, *International journal of Geomechanics*, Vol. 14, No. 2, pp. 239-253.
- Khalili, N., Habte, M. A., and Valliappan S. (2005), A bounding surface plasticity model for cyclic loading of granular soils, *International journal for numerical methods In engineering*, Vol. 63, pp. 1939–1960.
- Lee, K.H., Chan, D.H., and Lam, K.C. (2004), Constitutive model for cement treated clay in a critical state framework, *Soils and Foundations*, Vol. 44, No. 3, pp. 69-77.
- Leeson, J., and Campbell, D. (1983), The variation of soil critical state parameters with water-content and its relevance to the compaction of two agricultural soils, *Journal of Soil Science*, Vol. 34, No. 1, pp. 33-44.
- McDowell G.R., and Hau K.W. (2004), A generalised Modified Cam Clay model for clay and sand incorporating kinematic hardening and bounding surface plasticity, *Granular Matter*, Vol. 6, No. 1, pp. 11-16.

- Manzari, M.T., and Dafalias, Y. F. (1997), A critical state two-surface plasticity model for sands, *Géotechnique*, Vol. 47, No. 2, pp. 255-272.
- Marri, A. (2010), The mechanical behaviour of cemented granular materials at high pressures, Ph.D. thesis, The University of Nottingham, Nottingham, U.K.
- Navarro, V., Alonso, J., Calvo, B., and Sanchez, J. (2010), A constitutive model for porous rock including effects of bond strength degradation and partial saturation, *International Journal of Rock Mechanics & Mining Sciences*, Vol. 47, No. 8, pp. 1330–1338.
- Nova, R. (2005), A simple elastoplastic model for soils and soft rocks, In *Soil Constitutive Models: Evaluation, Selection, and Calibration*, ASCE pp. 380-399.
- Nova, R. (2006), Modelling of bonded soils with unstable structure, *Springer Proceedings in Physics, Modern Trends in Geomechanics*, Vol. 106, pp. 129-141.
- Nova, R., Castellanza, R., and Tamagnini, C. (2003), A constitutive model for bonded geomaterials subject to mechanical and/or chemical degradation, *International Journal for Numerical and Analytical Methods in Geomechanics*, Vol. 27, No. 9, pp. 705–732.
- Reilly, M.P.O, and Brown, S.F. (1991), *Cyclic loading of soils: from theory to design*, U.K.: Blackie and son limited.
- Rowe, P.W. (1962), The stress-dilatancy relation for static equilibrium of an assembly of particles in contact, *Proceedings of Royal. Society, London*, Vol. 269, pp. 500-527.
- Russel, A., and Khalili N. (2004), A bounding surface plasticity model for sands exhibiting particle crushing, *Canadian Geotechnical Journal*, Vol. 41, No. 6, pp. 1179-1192.
- Schofield, A.N. (1993), *Original Cam-Clay*, International Conference on Soft Soil Engineering, Guangzhou, China.
- Suebsuk, J., Horpibulsuk, S., and Liu, M.D. (2011), A critical state model for overconsolidated structured clays, *Computers and Geotechnics*, Vol. 38, No. 5, pp. 648-658.
- Suebsuk, J., Horpibulsuk, S., and Liu, M.D. (2010), Modified structured cam clay: a generalised critical state model for destructured, naturally structured and artificially structured clays, *Computers and Geotechnics*, Vol. 37, No. 7-8, pp. 956, 968.
- Vatsala, A., Nova, R., and Murthy, B.R.S. (2001), Elastoplastic model for cemented soils, *Journal of Geotechnical and Geoenvironmental Engineering*, Vol. 127, No. 8, pp. 679-687.

Vermeer, P.A., and de Borst, R. (1984), Non-associated plasticity for soils, concrete and rocks, *Heron*, Vol. 29, No. 3, pp. 1-64.

Wang., Y.H., and Leung, S.C. (2008), Characterization of cemented sand by experimental and numerical investigations, *Journal of Geotechnical & Geoenvironmental Engineering.*, Vol. 134, No. 7, pp. 992-1004.

Wood, D.M. (1990), *Soil behavior and critical state soil mechanics*, Cambridge University Press, USA.

Yang. C., Huang, M.S., and Cui, Y.J. (2011), Constitutive model of unsaturated structured soils under cyclic loading, *Taylor and Francis group*, pp. 987-992.

Yu, H.S. (1998), CASM: A unified state parameter model for clay and sand, *International Journal of Numerical and Analytical Methods in Geomechanics*, Vol. 22, No. 8, pp. 621-653.

YU, H.S. (2006), *Plasticity and Geotechnics*, Springer, USA.

Yu, H.S., Tan, S.M., and Schnaid, F. (2007), A critical state framework for modeling bonded geomaterials, *Geomechanics and Geoengineering*, Vol. 2, No. 1, pp. 61-74

CHAPTER 5

CONSTITUTIVE MODEL FOR MONOTONIC AND CYCLIC RESPONSE OF LOOSELY CEMENTED SAND FORMATIONS

5.1 Introduction

This chapter focuses on the constitutive behaviour and degradation of cemented sand/soft sandstone under monotonic and cyclic loadings. The two main approaches for the study of weak sandstone degradation caused by repeated loading include laboratory testing by conducting cyclic loading tests and the development of cyclic plasticity theories. The majority of the studies in the area of cyclic loading of sandstone or cemented sand are limited to earthquake (dynamic) type of loading. A few studies have characterized the deformation properties of sandstone under slow cyclic loading both theoretically and experimentally. In general, the behaviour of geomaterials under cyclic loading is remarkably complex. This may be due to the dependence of the constitutive relationship on pressure and void ratio as well as the non-linear behaviour of the sand matrix [Russel and Khalili 2004, Khalili et al. 2006]. Even the most sophisticated models cannot provide accurate predictions under general cyclic loading conditions [Reilly and Brown 1991]. Therefore the development of a reliable model to capture the cyclic behaviour of geomaterials has become one of the most demanding tasks in constitutive modeling [Vermeer and Borst 1984].

Most models for slow cyclic loading have been proposed for cohesionless soils. Thus a model that could capture soft sandstone response under slow cyclic loading would be a significant advancement as few studies have been conducted on sandstone behaviour in response to slow cyclic loading. In particular difficulty in the integration of the critical state concept in cyclic modeling is noted in the

literature [Imam and Chan 2008]. In this chapter, a critical state constitutive model is presented for slow cyclic loadings for soft sandstone.

The traditional plasticity theory appears to be unsuitable for modelling cyclic loading since it predicts a purely elastic response during unloading and reloading within the yield surface. That is, no plastic deformation is predicted for unloading and reloading unless the stress path reaches the yield surface again [Chen and Han 2007]. This is not suitable for modelling cyclic loading because, in reality, all unload-reload cycles result in the gradual accumulation of plastic strain and energy dissipation [Khong 2004, Lenart 2008] as shown schematically in Fig. 5-1. In other words the response in Fig. 5-1 suggests that loading and unloading stress paths are not the same. This is known as hysteresis, and it shows that the material fails to recover all the energy it receives in the loading-unloading cycle [Reilly and Brown 1991]. This is attributed to energy dissipation due to plastic deformation [Lenart 2008]. Hysteresis is the result of non-uniform deformation of the material in which different parts of the material are undergoing different stages of loading and unloading.

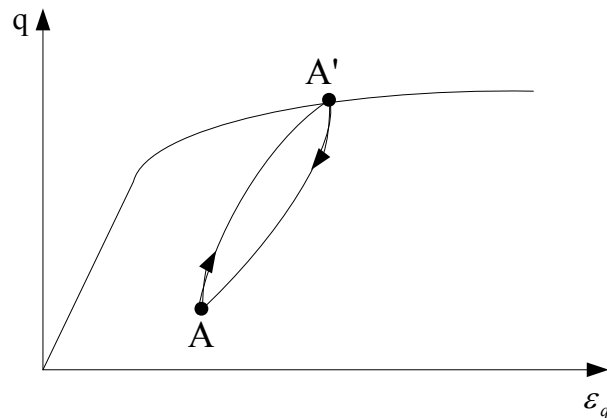


Fig. 5-1 Unloading and reloading from an elasto-plastic state: perfect hysteresis loop in a complete cycle

The effect of non-uniform deformation with different stages of loading and unloading can be illustrated using a friction block model. Uniform deformation is analogous to a single block as shown in Fig. 5-2. In this case, there is only one displacement in the system, which is represented by u . There is no slipping until the horizontal force (T) reaches the maximum frictional force (F_k) when the block

starts to move. At some displacement (u_1), if T decreases below F_k , movement will cease immediately and the force will vary between zero and F_k . There is no movement until T reaches F_k again and the displacement will continue from u_1 . There is no hysteresis effect, and there is no work done during the unloading and reloading cycle at u_1 .

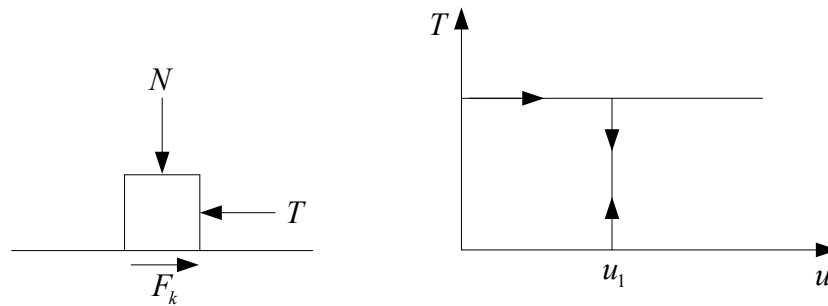


Fig. 5-2 Single frictional block on a flat surface and corresponding force displacement response

Non-uniform deformation in a material can be conceptually represented by a series of blocks as shown in Fig. 5-3¹. In this case, four blocks are connected by three springs with stiffness (K), and each block also is subjected to a normal force (N). The horizontal force (T) is slowly increased until the first block on the right, block 4, starts to move. There is no force applied on the other blocks until the spring between blocks 4 and 3 starts to compress. The force that will transmit to block 3 will be equal to the difference between T and F_k where F_k is the frictional resistance at the base of each block. Again, there is no force applied on block 2 until the force in the spring between blocks 4 and 3 exceeds F_k in block 3. The process continues until all of the blocks start to move when T is equal to or exceeds $4F_k$. Since the movement of all the blocks is in the direction of T , F_k will be acting in the opposite direction (Fig. 5-3a).

If T decreases below $4F_k$ after some movement of the blocks, the frictional force on block 4 will start to decrease until the direction is reversed as shown in Fig. 5-3b. There is no movement of block 4 until T decreases below $2F_k$. In this case, the force in the spring between blocks 4 and 3 will also decrease until the

¹ Dave Chan (2013), personal communication

direction of the frictional force under block 3 reverses its direction. In this case, T will become zero, representing a fully unloaded state as shown in Fig. 5-3c.

If T increases again, there is no movement in block 4 until its frictional force changes its direction and the value of T is equal to $2F_k$ as shown in Fig. 5-3d. This represents the reloading stage after T has been fully unloaded. It is clear that the reloading path is different than the unloading path since the mobilization of the friction force under the blocks is different, unlike the case of a single block. Movement of block 4 occurs when T increases above $2F_k$. When T is equal to $4F_k$, the frictional forces under all of the blocks point in the same direction and movement will continue in the direction of T . Fig. 5-4¹ shows force-displacement response of block 4.

As demonstrated in this simple system of blocks, the hysteresis effect is a result of non-uniform mobilization of frictional forces under the blocks since they are connected by deformable springs. If the blocks are connected by rigid springs, the hysteresis effect will disappear. In the case of a real material, since the stresses and strains in the material are generally non-uniform at the mesoscopic scale, it will give rise to the hysteresis effect much like the series of blocks connected by deformable springs. Therefore, energy dissipation occurs during the unloading and reloading process below the latest yield point.

¹ Dave Chan (2013), personal communication

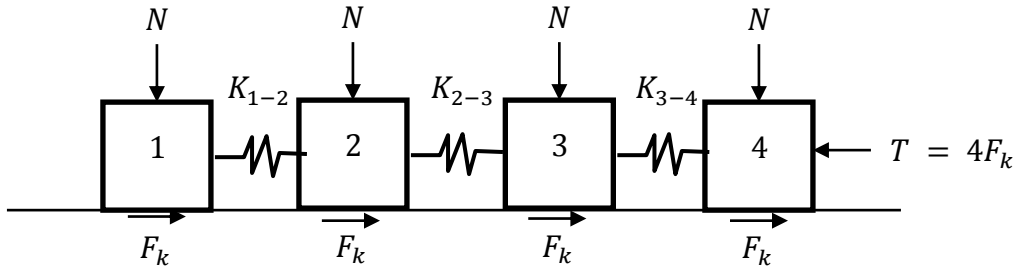


Fig. 5-3a Four blocks in series where T is increased until movement occurs in all of the blocks

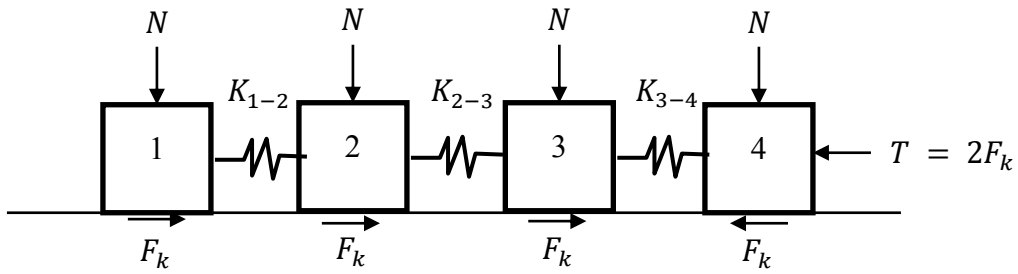


Fig. 5-3b T is decreased until the block 4 starts to move to the right

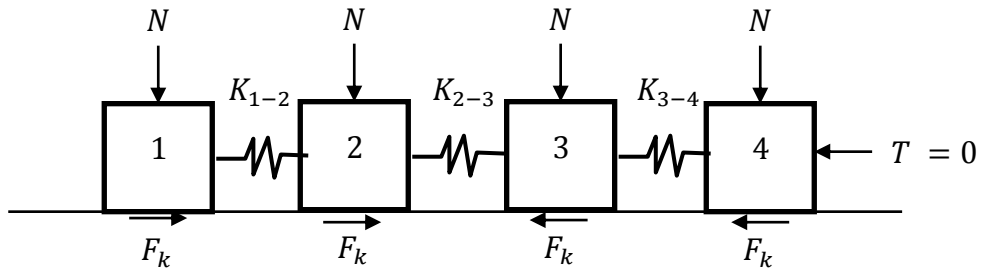


Fig. 5-3c T decreases to zero during unloading

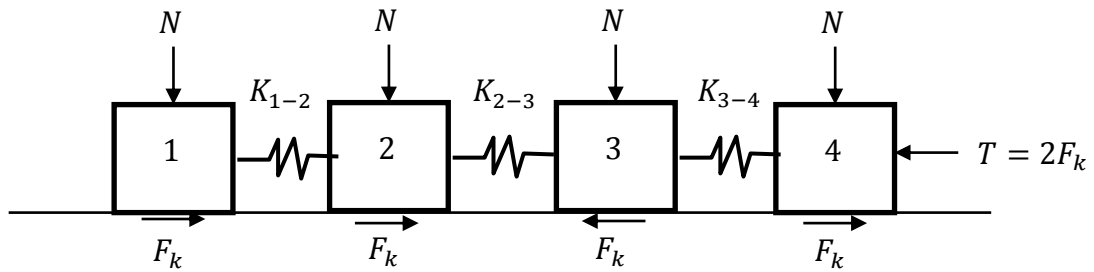


Fig. 5-3d T increases during reloading

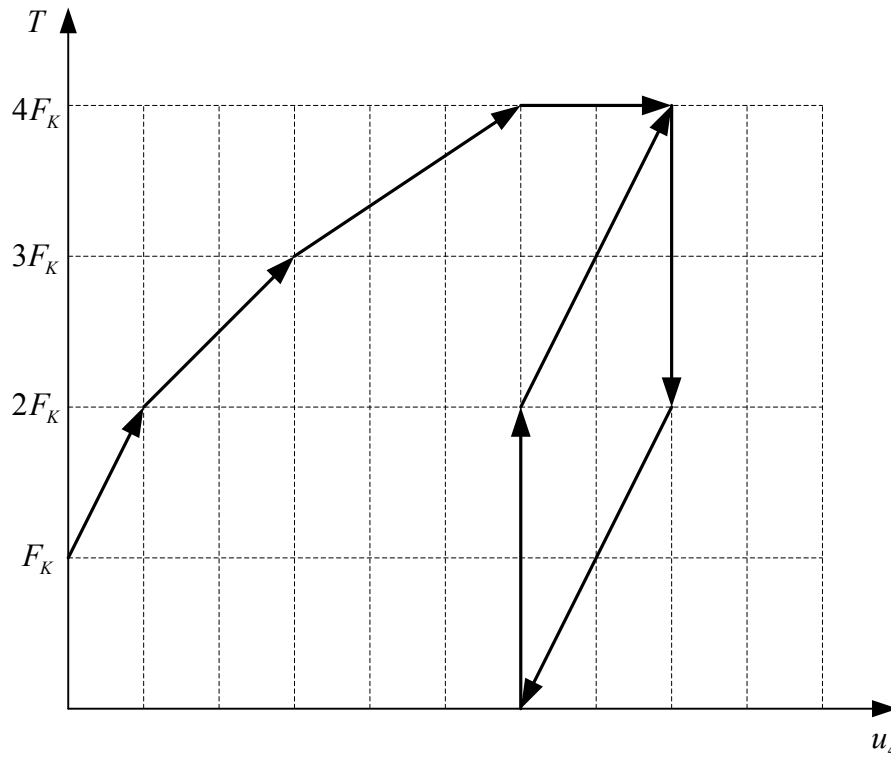


Fig. 5-4 Force displacement response of block 4 in the four-block system connected by springs

The shortcomings of the classical plasticity theory led to extensive research, beginning in the 1960s, in developing more sophisticated plasticity models to capture the cyclic behavior of geomaterials [Yu 2006]. Advanced constitutive models that have been introduced within the plasticity framework include multi-surface plasticity [for example see Iwan 1967, Mroz 1967, Mroz et al. 1978, 1979], bounding surface plasticity [for example see Dafalias and Popov 1975, Krieg 1975, Dafalias and Herrmann 1982, Bardet 1986, Dafalias 1986, Khong 2004, Khalili et al. 2005, Yang et al. 2011], generalized plasticity [for example see Zienkiewicz et al. 1985, Pastor et al. 1985, 1990, Ling and Yang 2006, Chung 2010] and subloading surface plasticity [for example see Hashiguchi 1989, Hashiguchi and Chen 1998].

The main aim of this chapter is to present a continuum elasto-plastic constitutive model within the bounding surface plasticity framework to model monotonic and cyclic loading of frictional and cohesive material. A critical state constitutive model proposed by Imam (1999) and Imam et al. (2005) is chosen to be the base

model. This model was developed for simulating the behaviour of cohesionless sands, under monotonic loading. Thus, modifications are incorporated into the model to include the behaviour of cemented sand/soft sandstone under monotonic loading. To predict cyclic behaviour using the bounding surface plasticity theory, normalized plastic modulus and elastic moduli are modified under unloading conditions without using the mapping rule. Although the projection rule is not incorporated, concepts of the bounding surface plasticity theory are used in the sense that plastic deformation is recorded for both loading and unloading conditions. This implies that the loading surface always passes through the current stress state regardless of the position of the stress path or the type of loading. Also by assuming a fixed size ratio between the bounding surface and the loading surface throughout the shearing process, the current stress always lies inside the bounding surface. However, unlike classical bounding surface plasticity in which the plastic modulus is expressed as the summation of the additive and bounding surface plastic moduli, the plastic modulus is stated only as a function of that of the loading surface. This is similar to Imam and Chan's (2008) approach for modeling the behaviour of cohesionless sand under cyclic loading. The proposed modified model ultimately is implemented in Flac 2D.

5.2 Cemented sand

Cemented soils and weak rocks constitute an intermediate class of geomaterials from a mechanical standpoint and are classified between a soil and a rock. They are often considered as non-textbook materials [Schnaid et al. 2001]. Their mechanical behaviour under various conditions is not as well understood as those of hard rocks or soils. It is known, for example, that their strength and deformation characteristics show strong non-linearity. The non-linear behaviour in the elastic range for soft rocks is known. Therefore, non-linear elasticity models are more appropriate than linear elasticity for soft rocks [Yoshinaka et al. 1998].

Cementation in natural cemented sand originates from the precipitation of cementing agents like silica, carbonate minerals (especially calcite), clay minerals

and iron oxides onto the surface of sand particles [Clough et al. 1981, Fjaer et al. 2008]. This cementation is produced during the diagenesis process which occurs normally under lower pressures and temperatures compared to metamorphism which happens under extremely high pressures and temperatures. Physical changes such as compaction due to the added weight of the younger sediments and chemical processes due to the interaction between sand grains and pore fluid are the main mechanisms responsible for cementation during the diagenesis process. Consequently, the degree of cementation is expected to increase with the depth of burial. This trend, however, may not always be the case particularly due to the possible presence of very low permeable clay minerals and overpressure in deeper layers, which can retard the diagenetic processes. Movement of the pore fluid through the sediments plays an important role in the diagenesis process as well. Lower cohesive strengths occur if circulation of the pore fluid through the reservoir rock is prevented [Fjaer et al. 2008].

Cementation in artificially cemented sand comes from an externally added cementing agent such as Portland cement. The amount of cementing agent and the number of particle contacts are the most important factors that affect the strength of artificially cemented sand [Consoli et al. 2012]. With an increase in the degree of cementation, peak strength, cohesion, tensile strength and stiffness of the material increase, while strain at peak strength decreases. Although a rise in the friction angle due to the addition of cementation has been reported, there is no general agreement on the effect of cementation on the peak friction angle of the material. Some researchers believe that cementation causes no change to the friction angle. A list of different researchers which concluded different results on the effect of cementation on peak friction angle can be found in Abdulla and Kioussis (1997) and Schnaid et al. (2001). Cementation also gives rise to a more brittle response ([Clough et al. 1981] and is more important than friction at low confining pressures. The failure mode is believed to be brittle for weakly cemented sand at lower confining pressures and ductile at higher pressures. Therefore, cemented sand shows a brittle response due to brittle failure of cementation bonds. At higher confining pressures, the frictional component is

more dominant, resulting in a more ductile response. However, for strongly cemented sand, cementation provides noticeable resistance even at higher confining pressures [Clough et al. 1981]. Note that artificially cemented sands are usually considered as the better choice for conducting triaxial tests for constitutive model development because of their uniformity, homogeneity and reproducibility. The cost of obtaining undisturbed natural samples and the variability inside the samples make it difficult to use natural cemented sands for the validation of constitutive relationships [Mohsin 2008].

It is believed that the shear stress-strain curve for (artificially or naturally) cemented sand will eventually approach that for uncemented sand at a critical state which is associated with zero dilatancy rate. This, however, does not always occur since cementation may not be completely broken even after large amounts of shearing far beyond the initial yield point [Lee et al. 2004]. That is, cemented sand after large amounts of shearing may arrive at the ultimate void ratio instead of the critical state void ratio which is associated with constant volume and is independent of the initial state. This implies that the concept of a unique critical state line does not apply for (artificially or naturally) cemented sand because it depends on the initial condition and especially on the cement content. This is one of the most crucial challenges in applying the critical state theory to cemented sand. Experimental determination of the critical state line (CSL) for cemented sand is also difficult due to its brittle behaviour and strain localization under high cement content or low confining pressure [Marri 2010].

5.3 Brief review of the original model

The detailed description of the original model can be found in Imam (1999) and Imam et al. (2005). A brief description is provided here.

The CSL in many proposed constitutive models for sand is used as a reference state to which various states of the soil are compared. Difficulty in determining the CSL position and the uncertainty of its position when the soil is loaded in different directions of shearing are major setbacks for this approach [Imam 1999, Imam et al. 2005]. The proposed constitutive model also relies on the CSL

position to determine the soil state at large strain. However, the impact of the uncertainties in the CSL location on soil properties at smaller strains is compensated by measuring the important properties under different directions of shearing from the experiment and correlating these properties to the CSL [Imam 1999]. The stress ratio at the peak of UESP is one of these properties by which the stress ratio at the peak of the yield surface is predicted [Imam et. al. 2002]. Shear strains associated with the peak of the UESP are relatively small, implying that the measurement of this property is more reliable because strain in the early stages of the undrained tests is more uniform and less affected by localization [Imam 1999, Imam et al. 2005]. Fig. 5-5 illustrates typical UESP in monotonic triaxial compressive loading on loose sands. The deviator stress initially increases until it reaches a peak at (p_p, q_{peak}) , where stress ratio M_p is mobilized. The deviator stress then decreases (strain softening) until UESP reaches the CSL [Imam et al. 2005].

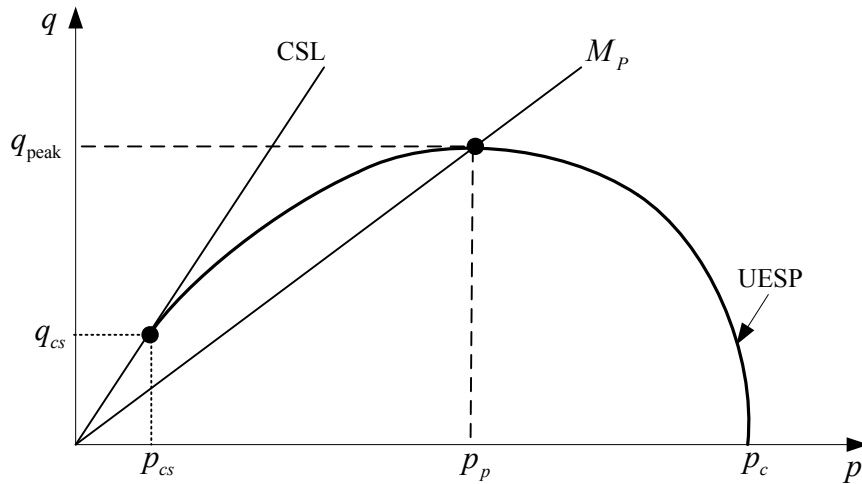


Fig. 5-5 Typical UESP in monotonic triaxial compressive loading on loose sands

The yield function of the original model is expressed as:

$$f = (\eta - \alpha)^2 - M_\alpha^2 \left(1 - \sqrt{\frac{p}{p_c}} \right) = 0 \quad (5.1)$$

$$M_\alpha^2 = (5M_p - \alpha)(M_p - \alpha) \quad (5.2)$$

where η is the stress ratio, M_p is the stress ratio at the peak of UESP, p is the mean effective stress, α is a scalar which represents anisotropic consolidation and its magnitude is zero for isotropic consolidation and p_c is the effective preconsolidation pressure which is considered as hardening parameter.

M_p is calculated for compressive and extensive loading, respectively, as follows:

$$M_{p,c} = \frac{6\sin\varphi_{p,c}}{3 - \sin\varphi_{p,c}} \quad (5.3)$$

$$M_{p,e} = \frac{6\sin\varphi_{p,e}}{3 + \sin\varphi_{p,e}} \quad (5.4)$$

in which $\varphi_{p,c}$ and $\varphi_{p,e}$ are the friction angles at the peak of UESP in triaxial compression and triaxial extension, respectively. They are evaluated by:

$$\sin\varphi_{p,c} = \sin\varphi_\mu - k_p\psi_p \quad (5.5)$$

$$\sin\varphi_{p,e} = \sin\varphi_\mu - k_p\psi_p - a_p \quad (5.6)$$

where $\psi_p = e - e_p$ is the state parameter at the peak in which e is void ratio, and e_p is the critical state void ratio which is evaluated at mean effective stress corresponding to M_p (i.e. at $p = p_p$), φ_μ is the friction angle associated with $\psi_p = 0$ in triaxial compression and is close to the interparticle friction angle and k_p and a_p are model parameters. Experimental observations which support dependency of M_p to void ratio and the state parameter at the peak can be found in Imam et. al. (2002).

Isotropic nonlinear elasticity is adopted in the model as:

$$G = G_a \frac{(2.973 - e)^2}{1 + e} \left(\frac{p}{p_{atm}}\right)^{0.5} \quad (5.7)$$

$$K = K_a \frac{(2.973 - e)^2}{1 + e} \left(\frac{p}{p_{atm}}\right)^{0.5} \quad (5.8)$$

where K and G are the bulk and shear elastic moduli, respectively, G_a and K_a are the respective reference moduli associated with the reference pressure p_{atm} , the atmospheric pressure.

Following the work of Wood (1990) and Manzari and Dafalias (1997), the stress-dilatancy relationship is defined as:

$$D = A(M_{PT} - \eta) \quad (5.9)$$

$$A_c = \frac{9}{9 + 3M_{PT,c} - 2M_{PT,c}\eta} \quad (5.10)$$

$$A_e = \frac{9}{9 - 3M_{PT,e} - 2M_{PT,e}\eta} \quad (5.11)$$

where

$$\sin\varphi_{PT,c} = \sin\varphi_{CS} + k_{PT}\psi_s \quad (5.12)$$

$$\sin\varphi_{PT,e} = \sin\varphi_{CS} + k_{PT}\psi_s + a_{PT} \quad (5.13)$$

in which M_{PT} is the phase transformation stress ratio, φ_{CS} is the critical state friction angle, $\psi_s = e - e_{CS}$ is the state parameter [Been and Jefferies 1985, Jefferies 1993], e_{CS} is the critical void ratio and k_{PT} and a_{PT} are both model parameters. Similar to how M_p is calculated using $\sin\varphi_p$ under triaxial compression and extension conditions, M_{PT} under compression and extension conditions is obtained from $\sin\varphi_{PT}$. Note that equation (5.12) and (5.13) are similar to the Manzari and Dafalias (1997) relationship.

Hardening in this model depends on the proximity to the critical state, in contrast to conventional critical state models which relate the size of the yield surface to void ratio [Jefferies 1993]. Shear hardening law is expressed as:

$$\frac{\partial p_c}{\partial \varepsilon_q^p} = \frac{hG_{ini}}{(p_f - p_c)_{ini}} (p_f - p_c) \quad (5.14)$$

in which h is a material parameter, p_f is the failure mean effective stress, $(p_f - p_c)_{ini}$ and G_{ini} are the initial value of $(p_f - p_c)$ and the shear elastic modulus, respectively, at the end of consolidation and prior to shearing. Calculation of M_f is based on $\sin\varphi_f$ which itself is obtained from the following equation:

$$\sin\varphi_f = \sin\varphi_{CS} - k_f\psi_s \quad (5.15)$$

where k_f is a material parameter.

5.4 A two-surface model for cemented sand

In line with the general tendencies to use as many simplifying assumptions as possible and to predict the stress-strain relationships using the simplest possible approach [Chen 1994], a relatively simple constitutive model is presented. For modeling the mechanical behavior of cemented sands, the base model is modified similar to the simplifying assumptions made by Gens and Nova (1993). Gens and Nova (1993) and Nova (2005) suggest that a yield surface which has been originally proposed for cohesionless soils can be used for cemented soils after some modifications are implemented in original yield function. They suggest that bonding (cementation between soil particles) provides tensile strength (p_t) and additional strength (p_o) to the material. In considering the additional strength, they suggested that the yield surface for the unbonded geomaterials must be enlarged towards the right. They also suggested that the yield surface must also be expanded towards the left to account for the tensile strength. Thus, more bonding leads to larger expansion of the yield surface towards both the right and left. Fig. 5-6 illustrates the schematic representation of the modified yield surface/loading surface. p_b controls yielding of the bonded material in isotropic compression, which determines the size of the enlarged yield surface, and p_o controls the increase in size of the initial elastic domain. The degree of bonding may be expressed as p_o/p_c [Gens and Nova 1993].

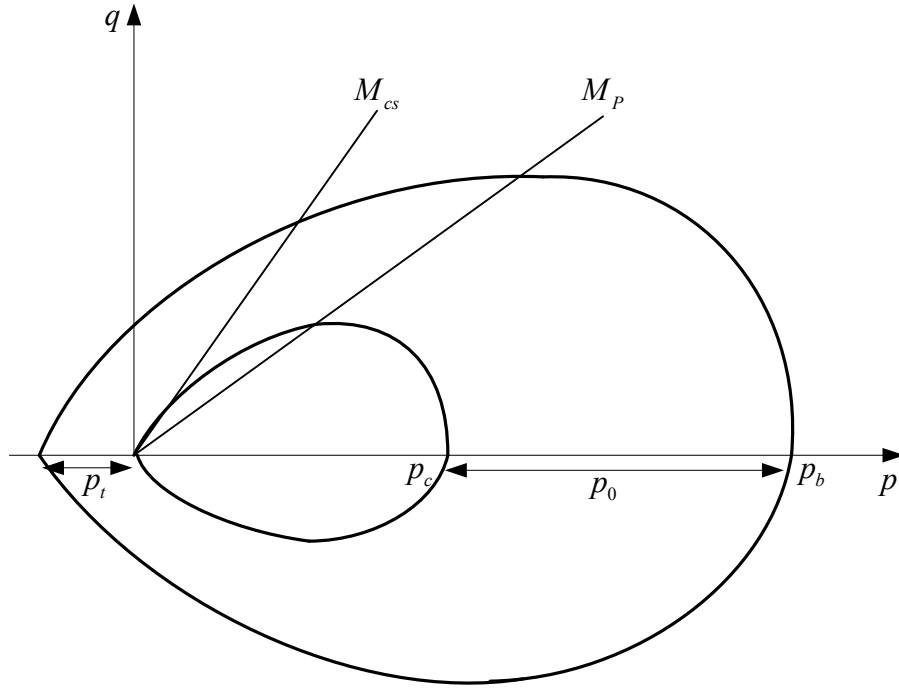


Fig. 5- 6 Schematic representation of the modified yield surface

To account for non-uniform deformation during cyclic loading, kinematic or anisotropic hardening parameters (i.e. p_a and q_a) are also integrated into formula of the modified loading surface. Bounding and loading surfaces, elastic properties, flow rule, and stress-strain relationships are major components of the modified model which are discussed here.

5.4.1 Bounding and loading surfaces

The bounding surface and loading surface are assumed to have the same shape for simplicity. In terms of the conventional triaxial parameters, the bounding surface (F) and loading surface (f) can be written respectively as (Fig. 5-7):

$$F = \left(\frac{\bar{q} - \bar{q}_a}{\bar{p} - \bar{p}_a + p_t} - \alpha \right)^2 - M_\alpha^2 \left(1 - \sqrt{\frac{\bar{p} - \bar{p}_a + p_t}{\bar{p}_b}} \right) = 0 \quad (5.16)$$

$$f = \left(\frac{q - q_a}{p - p_a + p_t} - \alpha \right)^2 - M_\alpha^2 \left(1 - \sqrt{\frac{p - p_a + p_t}{p_b}} \right) = 0 \quad (5.17)$$

$$M_a^2 = (5M_p - \alpha)(M_p - \alpha) \quad (5.18)$$

where q is the deviator stress, and p_a and q_a are components of the kinematic hardening tensor evolving with plastic strain. The kinematic hardening tensor is assumed to lie initially at the origin of the stress space, meaning for the first time loading: $(p_a, q_a) = (0,0)$.

The superimposed bar denotes variables of the bounding surface.

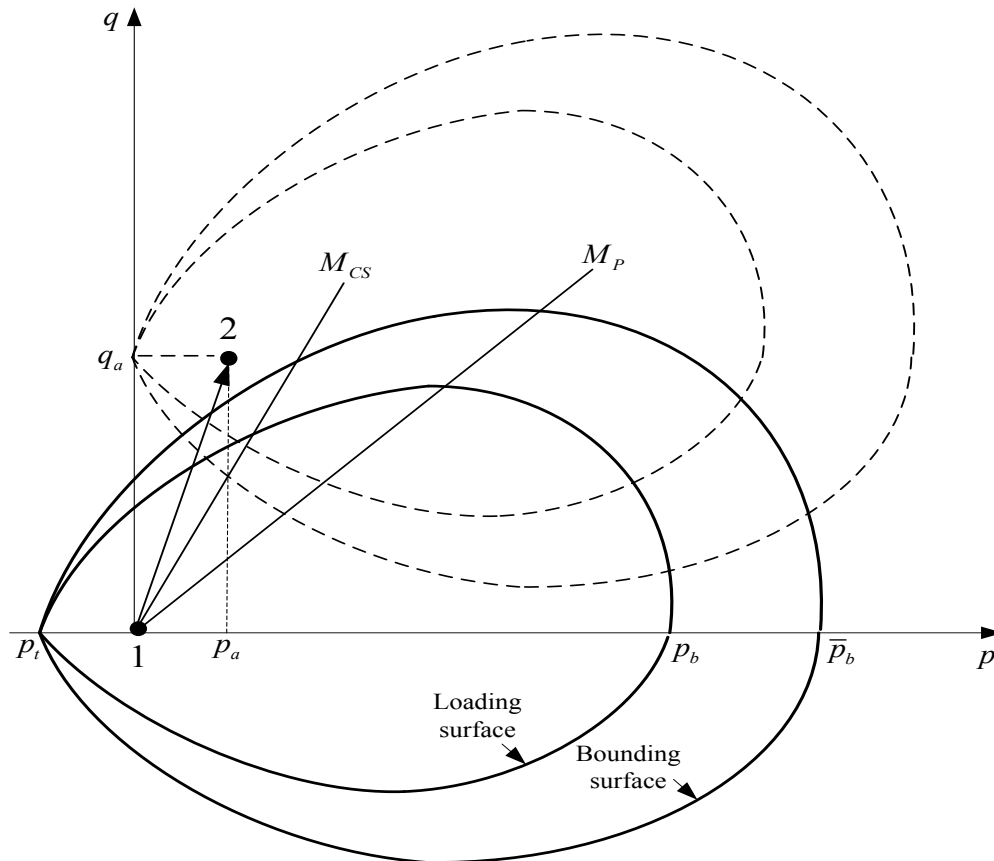


Fig. 5-7 Schematic representation of the loading and bounding surfaces at the start of loading (solid surfaces) and immediately after plastic loading starts (dashed surfaces). In addition to change of position, size of two surfaces also changes with further plastic loading (isotropic hardening). Kinematic hardening has been significantly magnified for better illustration

To ensure that the current stress state will not cross the bounding surface, it is assumed that the initial ratio of size of the two surfaces remain constant during the

shearing process. It is also assumed that the components of the kinematic hardening tensor always coincide for the two surfaces, i.e. $(p_a, q_a) = (\bar{p}_a, \bar{q}_a)$.

p_b and p_t are direct measures of the size of the loading surface and the tensile strength respectively which are defined using the following relationships:

$$p_b = p_c + (1 + \beta)p_o \quad (5.19)$$

$$p_t = \beta p_o \quad (5.20)$$

p_o is a measure of the increase in size of the uncemented yield surface due to strength increase by cementation, β is defined as the ratio between the tensile strength and p_o , and p_c plays the same role as the effective preconsolidation pressure for uncemented sand.

Destruction of the bonds between sand grains due to plastic deformation is assumed to lead to only changes in the size of the loading and bounding surfaces. Their shapes, however, are supposed to remain unchanged. To consider this destruction, the following simple linear relationship is assumed:

$$dp_o = -\gamma p_o d|\varepsilon_q^p| \quad (5.21)$$

where γ is a decay parameter which determines the rate of bond breakage, and dp_o indicates change in p_o due to change in plastic shear strain.

Note that the origin of plastic deformation of sand under low shear stresses mainly comes from grain crushing at the particle contact. Gross slippage at the particle contact, however, is responsible for plastic deformation under high shear stresses because the mobilized shear stresses are sufficient to overcome the resistance of the contact [Imam 1999].

Armstrong and Frederick's (1966) non-linear kinematic hardening law is adopted to control the evolution of the loading surface. For triaxial conditions, it is expressed as:

$$\dot{p}_\alpha = \frac{2}{3} c_1 \frac{\dot{\varepsilon}_p^p}{3} - c_2 p_\alpha \dot{z} \quad (5.22)$$

$$\dot{q}_\alpha = c_1 \dot{\varepsilon}_q^p - c_2 q_\alpha \dot{z} \quad (5.23)$$

where c_1 and c_2 are model constants, $\dot{\varepsilon}_q^p$ and $\dot{\varepsilon}_p^p$ are plastic deviator and volumetric strain increments, respectively, and \dot{z} is the accumulative plastic strain increment defined as:

$$\dot{z} = \sqrt{\frac{2}{3} \dot{\varepsilon}_{ij}^p \dot{\varepsilon}_{ij}^p} \quad (5.24)$$

p_α and q_α are the components of the kinematic hardening tensor, which are defined for triaxial conditions as:

$$p_\alpha = \frac{\alpha_{11} + 2\alpha_{33}}{3} \quad (5.25)$$

$$q_\alpha = \alpha_{11} - \alpha_{33} \quad (5.26)$$

5.4.2 Elastic properties

The definition of the elastic moduli in the original model is modified similar to Yu et al.'s (2007) approach as follows:

$$G = G_a \frac{(2.973 - e)^2}{1 + e} \left(\frac{p}{p_{atm}} \left(1 + \sqrt{\frac{p_o}{p}} \right) \right)^{0.5} \quad (5.27)$$

$$K = K_a \frac{(2.973 - e)^2}{1 + e} \left(\frac{p}{p_{atm}} \left(1 + \sqrt{\frac{p_o}{p}} \right) \right)^{0.5} \quad (5.28)$$

The elastic properties for unloading conditions are given as:

$$G = |\eta| G_a \frac{(2.973 - e)^2}{1 + e} \left(\frac{p}{p_{atm}} \left(1 + \sqrt{\frac{p_o}{p}} \right) \right)^{0.5} \quad (5.29)$$

$$K = |\eta| K_a \frac{(2.973 - e)^2}{1 + e} \left(\frac{p}{p_{atm}} \left(1 + \sqrt{\frac{p_o}{p}} \right) \right)^{0.5} \quad (5.30)$$

where $|\eta|$ denotes the absolute value of the stress ratio. Incorporation of η in the expression for the elastic moduli results in the prediction of a stiffer response at

the commencement of unloading and then a softer response when the stress ratio approaches the smaller deviator stresses. The decreasing trend is particularly more pronounced when the deviator stress is very small.

Suggestion of these expressions for the unloading elastic moduli comes from experimental observations. That is, the stiffness shows a sudden increase immediately after the inception of unloading accompanied with a relatively slow decrease when soil undergoes further unloading [Reilly and Brown 1991]. The elastic moduli for reloading conditions, however, are assumed to remain the same as those of the original loading. Although assuming that the elastic properties of the reloading conditions are in the same form as those for unloading conditions leads to better predictions of the hysteresis loops (see Fig. 5-12), it results in numerical instabilities in this case in Flac 2D model.

5.4.3 Flow rule

Experimental observations suggest that dilatancy is affected by the degree of cementation between sand particles. Most of studies have shown that an increase in the cement content gives rise to an increase in dilatancy and subsequent decrease in compression [Clough et al. 1981, Marri 2010]. Therefore, the original Rowe's stress-dilatancy relationship proposed for cohesionless sands cannot provide a good description for calculating the rate of dilation of cemented sands/weak sandstone.

By incorporating cohesion for compression, Rowe's stress-dilatancy relationship can be calculated by [Yu et al. 2007]:

$$D = \frac{9(M_{cs} - \eta) + 6\frac{c}{p}\sqrt{(2M_{cs} + 3)(-M_{cs} + 3)}}{9 + 3M_{cs} - 2M_{cs}\eta + 4\frac{c}{p}\sqrt{(2M_{cs} + 3)(-M_{cs} + 3)}} \quad (5.31)$$

where η is the stress ratio, and D is the dilatancy rate, c is cohesion, and M_{cs} is the critical state stress ratio. Cohesion is assumed to degrade with the total plastic strain increment as follows:

$$dc = ce^{-\xi\sqrt{(\dot{\epsilon}_q^p)^2 + (\dot{\epsilon}_p^p)^2}} \quad (5.32)$$

where ξ determines rate of cohesion degradation.

Clearly, when cohesion approaches zero, the original Rowe's stress-dilatancy relationship for cohesionless soils is recovered. The plastic potential function (g) associated with the dilatancy relationship in equation (5.31) takes the form [Yu et al. 2007]:

$$g = 3M_{cs} \ln\left(\frac{p + p_t - k_g}{\varphi_g}\right) + (2M_{cs} + 3) \ln\left(\frac{2(q - h_g)}{p + p_t - k_g} + 3\right) + (M_{cs} - 3) \ln\left(3 - \frac{q - h_g}{p + p_t - k_g}\right) = 0 \quad (5.33a)$$

$$k_g = \frac{\sqrt{(3 + 2M_{cs})(3 - M_{cs})} (36 - 12M_{cs})c}{18M_{cs}^2 - 27M_{cs} - 81} \quad (5.33b)$$

$$h_g = \frac{\sqrt{(3 + 2M_{cs})(3 - M_{cs})} (-54 + 18M_{cs})c}{18M_{cs}^2 - 27M_{cs} - 81} \quad (5.33c)$$

in which φ_g can be determined for any given stress state (p, q) by solving equation (5.33a) [Yu 2006].

Consistent with Imam (1999) and Imam et al. (2005), the flow rule is expressed based on a variable phase transformation stress ratio instead of a constant critical state stress ratio. Thus, for triaxial compression conditions:

$$D = \sqrt{\frac{2}{3}} \left(A(M_{pt} - |\eta|) + \frac{6B}{C} \right) \quad (5.34)$$

$$A = \frac{9}{C} \quad (5.35)$$

$$C = 9 + 3M_{pt} - 2M_{pt}|\eta| + 4B \quad (5.36)$$

$$B = \frac{c}{p} \sqrt{(2M_{pt} + 3)(-M_{pt} + 3)} \quad (5.37)$$

where M_{pt} is the phase transformation stress ratio.

5.4.4 Stress-strain relationships

Constitutive equations are governed by the following equations in line with incrementally linear stress-strain relationships:

$$\dot{p} = K \left(\dot{\varepsilon}_p - LD \text{sign}(m_p) \right) \quad (5.38)$$

$$\dot{q} = 3G(\dot{\epsilon}_q - \sqrt{2/3} L \text{sign}(m_q)) \quad (5.39)$$

m_p and m_q are components of the unit normal to the plastic potential surface which are obtained using the dilatancy relationship. L is determined from the following relationship:

$$L = \frac{KR\dot{\epsilon}_p + \sqrt{6} G \dot{\epsilon}_q}{H_n + KR D + 2G} \quad (5.40)$$

$$R = \sqrt{\frac{2}{3}} \frac{\frac{\partial f}{\partial p}}{\left| \frac{\partial f}{\partial q} \right|} \quad (5.41)$$

$$\begin{aligned} \frac{\partial f}{\partial p} &= \frac{-2}{p - p_a + p_t} \left(\left(\frac{q - q_a}{p - p_a + p_t} \right)^2 - \alpha \left(\frac{q - q_a}{p - p_a + p_t} \right) \right) + \frac{M_\alpha^2}{2\sqrt{p_b(p - p_a + p_t)}} \\ &= - \frac{\partial f}{\partial p_a} \end{aligned} \quad (5.42)$$

$$\frac{\partial f}{\partial q} = \frac{2}{p - p_a + p_t} \left(\frac{q - q_a}{p - p_a + p_t} - \alpha \right) = - \frac{\partial f}{\partial q_a} \quad (5.43)$$

$$m_q = \frac{1}{\sqrt{1 + D^2}} \quad (5.44)$$

$$m_p = \begin{cases} \frac{tD}{\sqrt{1 + D^2}} & D \geq 0 \\ \frac{-tD}{\sqrt{1 + D^2}} & D < 0 \end{cases} \quad (5.45)$$

where $t = 1$ for compressive loading and $t = -1$ for extensive loading.

For unloading, the components of the unit vector to the plastic potential surface are obtained by those defined already:

$$m_{p,u} = -m_p \quad (5.46)$$

$$m_{q,u} = m_q \quad (5.47)$$

H_n is the normalized plastic modulus which is obtained from the following equation:

$$H_n = -\sqrt{\frac{2}{3}} \frac{1}{\left|\frac{\partial f}{\partial q}\right|} \frac{\partial f}{\partial p_b} \frac{\partial p_b}{\partial \varepsilon_q^p} + H_n^{kinematic} \quad (5.48)$$

$$H_n^{kinematic} = R \left(\frac{2}{9} c_1 D - c_2 p_\alpha \sqrt{\frac{2}{9} D^2 + 1} \right) + c_1 - c_2 u_Q q_\alpha \sqrt{\frac{2}{9} D^2 + 1} \quad (5.49)$$

$$\frac{\partial f}{\partial p_b} = -\frac{M_\alpha^2}{2p_b} \sqrt{\frac{p - p_a + p_t}{p_b}} \quad (5.50)$$

$$\frac{\partial p_b}{\partial \varepsilon_q^p} = \frac{\partial p_c}{\partial \varepsilon_q^p} + (1 + \beta) \frac{\partial p_o}{\partial \varepsilon_q^p} = \frac{hG_{ini}}{(p_f - p_c)_{ini}} (p_f - p_c) - (1 + \beta) \gamma p_o \quad (5.51)$$

p_f is the failure mean normal stress which is calculated using an iterative method from the following equation:

$$p_f = \frac{p - p_a}{\left(1 - \frac{\left(\frac{M_f p_f - q_a}{p_f - p_a} - \alpha \right)^2}{M_\alpha^2} \right)^2} \quad (5.52)$$

H_n for unloading is assumed to be related to loading as follows:

$$\frac{H_{n,u}}{H_n} = R_u \sqrt{\frac{p}{p_{atm}}} |\eta| \quad (5.53)$$

where R_u is a model constant.

Due to the decrease in the stress ratio, higher plastic strains are predicted for a given total strain increment with advancement of unloading during one-way cyclic loading, which is in accordance with experimental observations.

5.4.5 Material parameters

k_p , φ_μ , φ_{CS} , k_{PT} , G_a , K_a , h , k_f , and CSL are material parameters of the original model [Imam 1999]. Methods of determination of these parameters have been given in Imam et al. (2005). The following material parameters were introduced in the upgraded model:

1. Initial value of p_o
2. Initial value of tensile strength to evaluate β
3. Decay parameter of bond strength (γ)
4. Cohesion (c)
5. Rate of degradation of cohesion (ξ)
6. Anisotropic hardening parameters (c_1, c_2)
7. Ratio of unloading plastic modulus to that of loading (R_u)

The initial value of p_o is equal to the difference between the initial values of p_b and p_c . The initial value of p_c is obtained from the maximum mean normal stress characterizing the initial elastic domain for unbonded soil. The initial value of p_b can be evaluated by conducting an isotropic compression test on cemented sand to determine the initial yield value of p_b [Nova 2005].

The parameter β is obtained using the initial value of the tensile strength. If there is no data regarding the tensile strength, the unconfined compressive strength can be used for an approximation of the tensile strength (tensile strength is in order of 5% to 20% of the unconfined compressive strength).

The parameter γ controls the rate at which bonds are broken. The higher value of γ , the faster the compression curve will become identical to that for uncemented material [Nova 2005].

The parameter c can be evaluated using the peak Mohr-Coulomb yield envelope.

The parameter ξ can be evaluated by fitting theoretical results of the volumetric behaviour to those of experimental observations.

The anisotropic hardening parameters c_1 and c_2 determine contribution of anisotropic/kinematic hardening in the combined isotropic-kinematic/mixed hardening rule. Larger difference between c_1 and c_2 causes the larger contribution of kinematic hardening to overall hardening. The constants c_1 and c_2 may be determined from stress-strain curve of uniaxial tests [Araujo 2002, Dunne and Petrinic 2006].

The parameter R_u is determined by fitting model predictions to unloading experimental data. A larger value of R_u results in a stiffer unloading response and a smaller unloading-induced plastic strain increment and vice versa.

5.4.6 Model performance

The performance of the proposed model is examined first against two sets of triaxial monotonic loading tests. Then, it is assessed against two triaxial one-way cyclic loading tests. Fig. 5-8 shows the calculated and observed behaviour of an artificially cemented gravelly sand under triaxial compression monotonic tests. Hydrated lime is used as the cementing agent for these samples [Asghari et al. 2003]. Table 5-1 lists the material parameters used for these analyses. Due to the lack of data, some of the material parameters such as the CSL, and critical state friction angle are selected based on the best match using one set of values for these parameters under a given cement content. Isotropic hardening is assumed for monotonic loading. Thus, a zero value is allocated for kinematic hardening related constants.

As seen in Fig. 5-8, the predicted and measured volumetric behaviours are in good agreement. The change of behaviour from contractive to dilative is observed in all tests. This is predicted numerically in the proposed model by a change of dilatancy rate sign from positive to negative. Fig. 5-8 also indicates less dilation at higher confining pressures, which is expected. Unlike volumetric behaviour, however, there is small discrepancy in the predicted and observed stress-strain behaviours. Using one critical state friction angle has led to slight underestimation of the peak deviator strength especially for the test with the confining pressure of 110 *kpa*, demonstrating the difficulty in applying the critical state theory for cemented soil. This difficulty has been observed experimentally as well. For instance, Lee et al. (2004) experimentally measured a larger critical state stress ratio and thus a greater critical state friction angle at lower confining pressures for a given cemented soil with a given cement percentage.

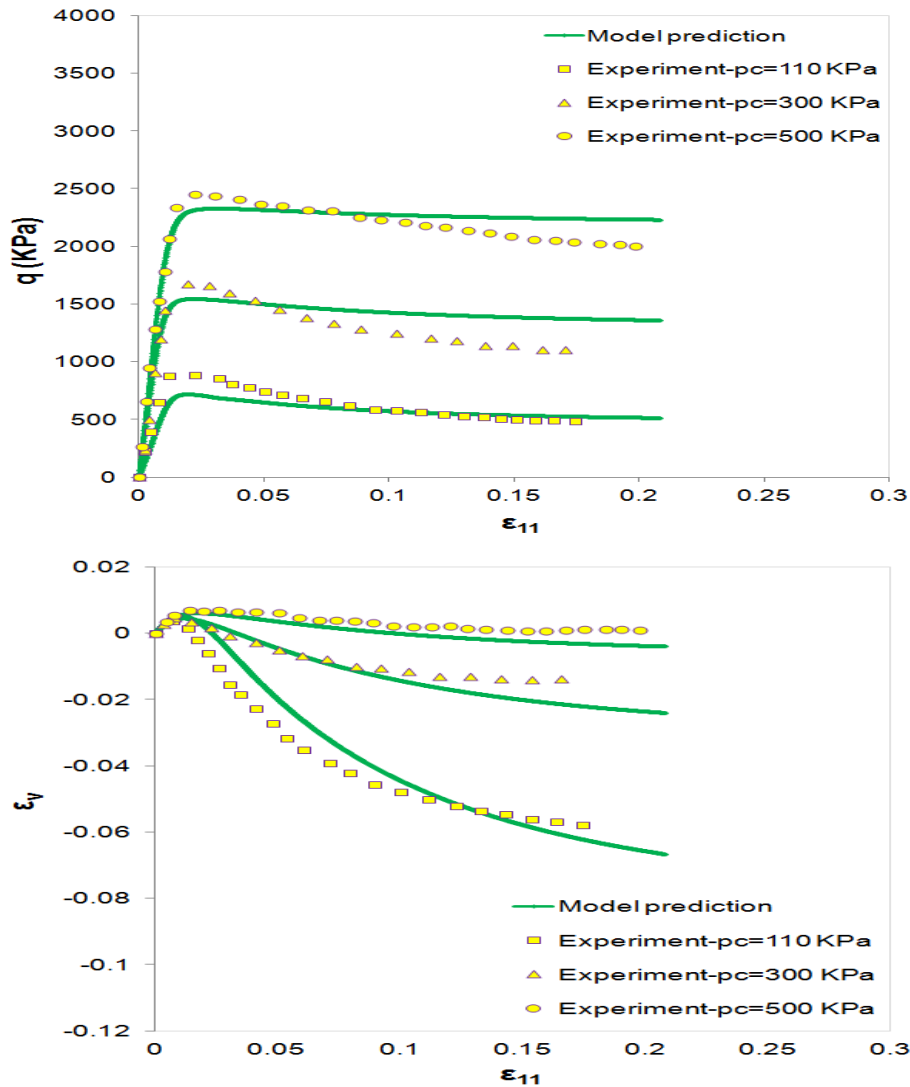


Fig. 5-8 Measured and predicted response of Tehran Alluvium cemented sand for samples with 3% cement content

Fig. 5-9 shows the predicted and observed behaviour of a slightly weathered rock obtained from the site of a pumped storage power station [Fu et al. 2013]. A unique CSL is chosen based on the best match for the rock behaviour under various confining stresses due to lack of data. Isotropic hardening is assumed for the material behaviour under monotonic loading. The material parameters used in Fig. 5-9 are listed in Table 5-1.

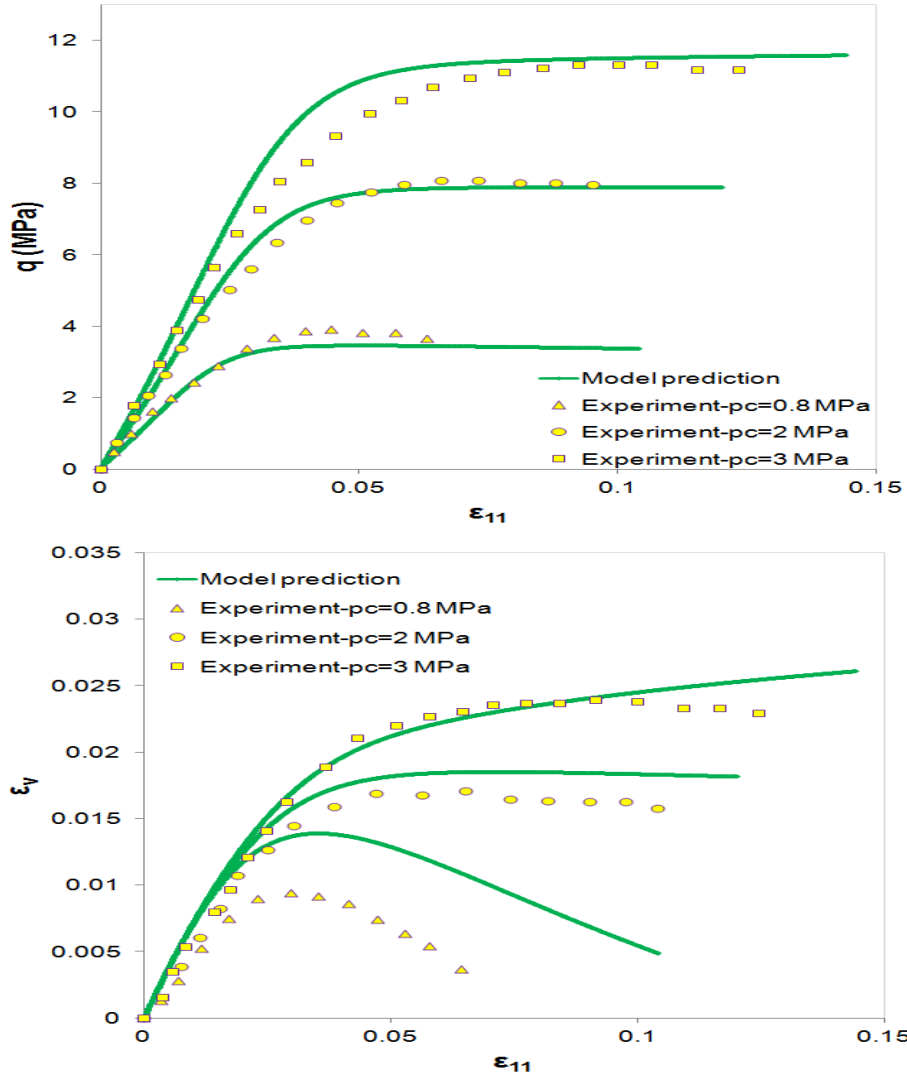


Fig. 5-9 Measured and predicted response of a slightly weathered rock under monotonic loading

The model was next examined against cyclic triaxial data [Mohsin 2008] for a cemented carbonate sand with 20% gypsum content (gypsum was used as the cementing agent) and an initial dry unit weight of 13 KN/m^3 (see Fig. 5-10). The model is able to predict the narrow hysteresis loops, but the loops may not be shown clearly in Fig. 5-10. Table 2 lists the material parameters used for the calibration of the triaxial cyclic and monotonic compression tests shown in Figs. 5-10 to 5-12.

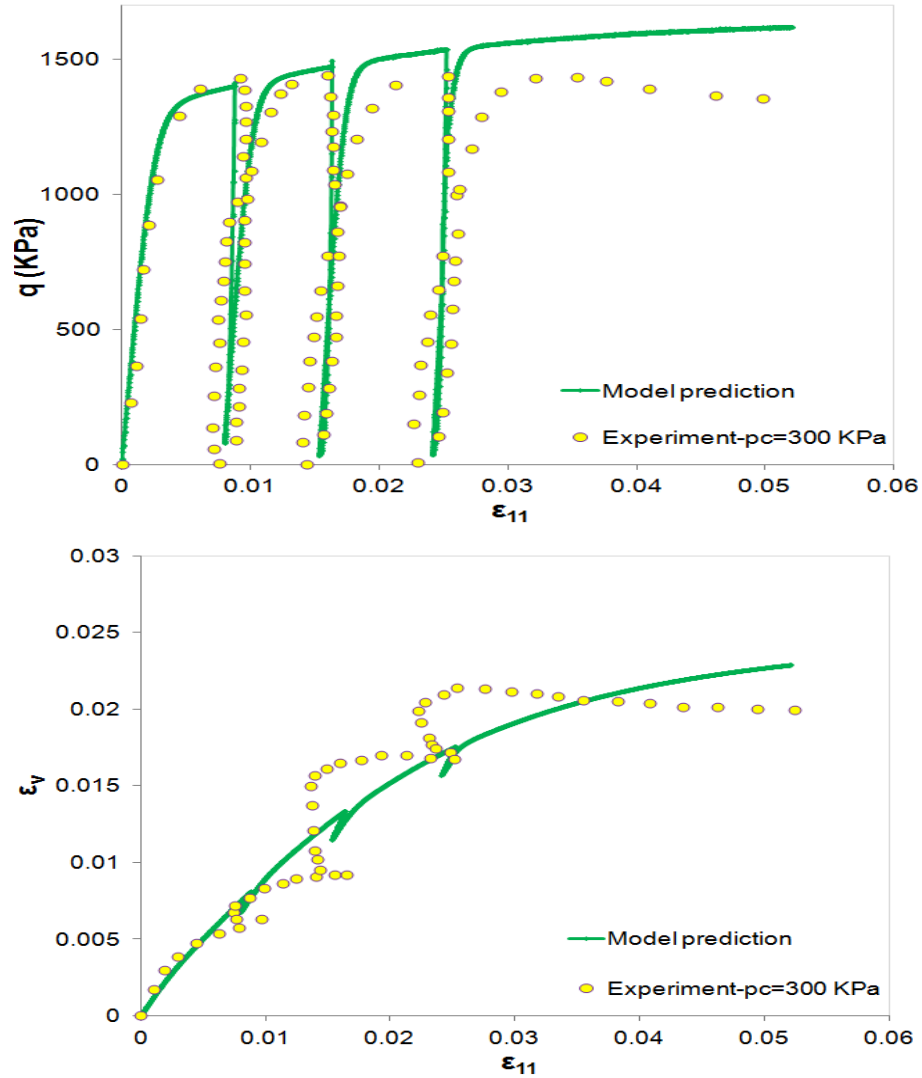


Fig. 5-10 Measured and predicted response of a cemented carbonate sand in a triaxial drained cyclic compression test

The model was then assessed against cyclic triaxial data of the rufous sandstone, which is a slightly weathered rock [Fu et al. 2013]. As can be seen from Fig. 5-11, the Flac 2D model is reasonably capable of capturing the observed shear and volumetric cyclic behaviour of the rufous sandstone. However there is discrepancy between the measured and predicted volume change during unloading. Experimental observations show that the material contracts during unloading while the model predictions suggest that it undergoes expansion. However, in general, the measured and predicted volumetric behaviour are in relatively good agreement.

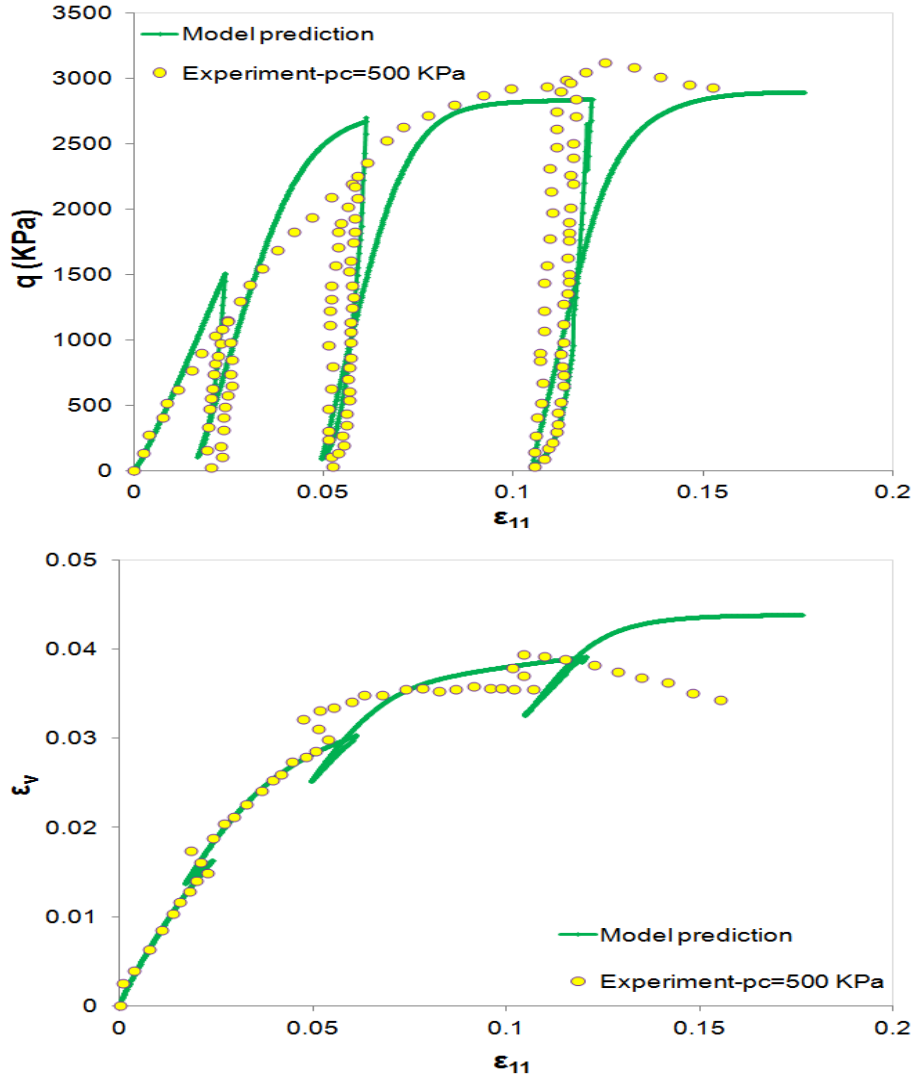


Fig. 5-11 Measured and predicted response of rufous sandstone under a triaxial drained cyclic compression test

Fig. 5-12 shows model predictions using 1D model (i.e. the constitutive equations are solved for one node) for the same initial conditions and material parameters as those of Fig. 5-11, when reloading elastic moduli are assumed similar to the unloading elastic moduli (equations (5.29) and (5.30)). As observed, the hysteresis loops are captured better in this case using 1D model. However, discrepancy in the measured and predicted volumetric response exists similar to Fig. 5-11. Note that numerical instabilities were encountered in the Flac 2D model when the reloading moduli were defined using equations (5.29) and (5.30) rather than equations (5.27) and (5.28). Therefore to avoid the instability, the reloading

elastic moduli were chosen to be the same as the loading elastic moduli (equations (5.27) and (5.28)) in Flac simulations.

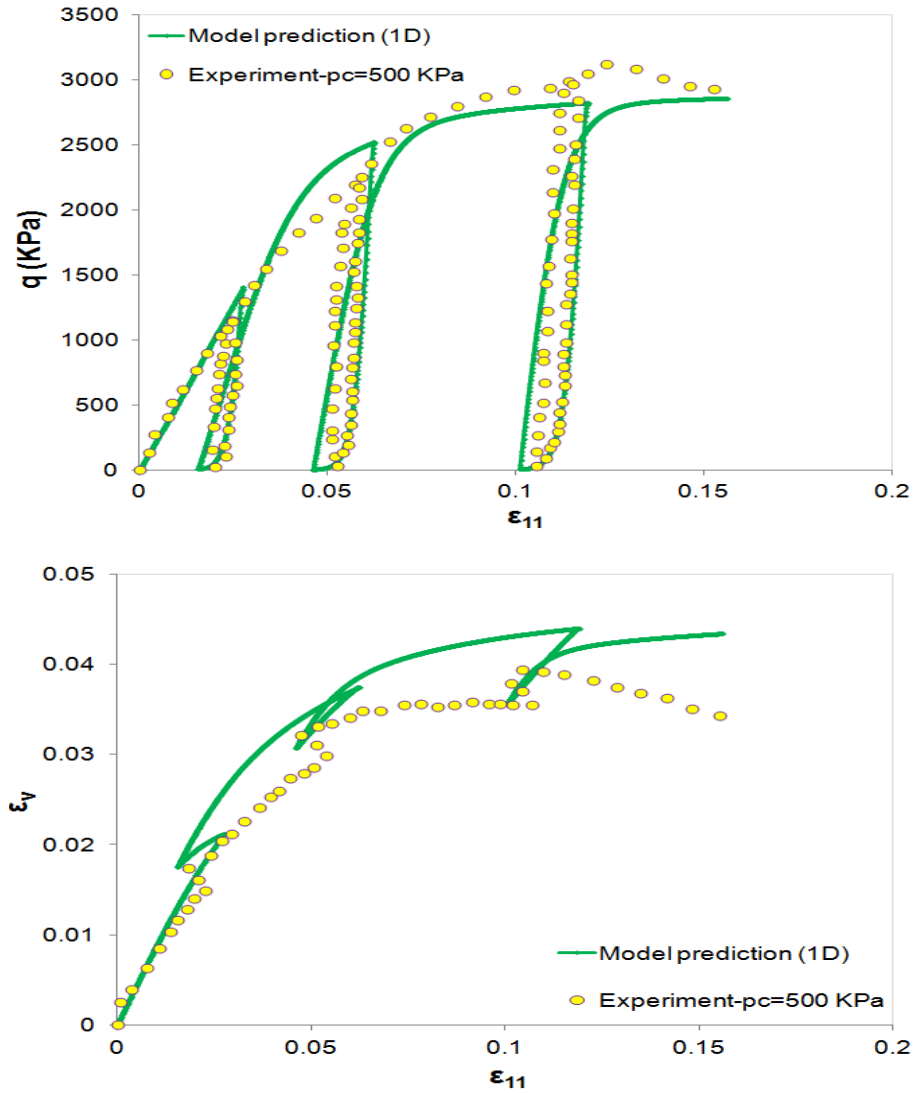


Fig. 5-12 Prediction of rufous sandstone behaviour using 1D model (reloading elastic moduli are defined similar to those of unloading conditions)

Table 5-1 Material parameters used for calibration in Figs. 8-9, $p^* = p + p_t$

Parameter name	Cemented gravely sand (Fig. 8)	Weathered rock (Fig. 9)
k_p	1.5	1
φ_μ	35	35
φ_{cs}	43.5	41.5
k_{pT}	1	1
G_a	2e7	9e6
K_a	3e7	15e6
h	1	1
k_f	0.75	0.75
e_{cs}	$0.47 - 0.02 \ln(p^*)$ (p^* in MPa)	$0.24 - 0.04 \ln(p^*)$ (p^* in MPa)
p_o (at highest p_c)	1.25e6	9e6
γ	25	15
c	2e5	1e6
ξ	25	15
β	0.2	0.1

Table 5-2 Material parameters used for calibration in Figs. 10-12, $p^* = p + p_t$

Parameter name	Cemented carbonate sand (Fig. 10)	Rufous sandstone (Figs. 11-12)
k_p	1	1.25
φ_μ	42	39
φ_{cs}	47	47
k_{pT}	1	1.25
G_a	2e8	4.5e6
K_a	5e7	7.5e6
h	1	1
k_f	0.75	0.75
e_{cs}	$2.29 - 0.44 \log(p^*)$ (p^* in KPa)	$-0.0063477p^{*3} + 0.0367p^{*2}$ $-0.11991p^* + 0.35$ (p^* in MPa)
p_o	9e5	25e5
γ	15	20
c	2e6	4e6
ξ	25	150
β	0.2	0.3
c_1	1e7	5e7
c_2	500	500
R_u	15	5

5.5 Conclusion

A continuum elasto-plastic constitutive model has been presented in this chapter to investigate the constitutive behavior of weak artificially and naturally cemented sand under monotonic and one-way cyclic loading. Destructuration of bonds between sand particles due to plastic deformation has been considered as the reason for mechanical degradation under applied loads. Several triaxial monotonic and cyclic compression tests on both artificially and naturally cemented sands have been chosen to assess the model performance. A comparison between the predicted and observed behaviour shows reasonably fair agreement. Hysteresis loops have been captured with reasonable accuracy too.

5.6 References

Abdulla A.A., and Kioussis P.D. (1997), Behaviour of cemented sands- I. testing, *International Journal for Numerical and Analytical Methods in Geomechanics*, Vol. 21, No. 8, pp. 533-547.

Araujo, M.C. (2002), Non-linear kinematic hardening model for multiaxial cyclic plasticity, M.Sc. thesis, Louisiana State University, Louisiana, USA.

Armstrong, P.J. and Frederick, C.O. (1966), A mathematical representation of the multiaxial Bauschinger effect, CEGB Report, RD/B/N731, Berkeley Nuclear Laboratories.

Asghari, E., Toll, D.G., and Haeri, S.M. (2003), Triaxial behaviour of a cemented gravely sand, Tehran alluvium, *Geotechnical and Geological Engineering*, Vol. 21, No. 1, pp. 1-28.

Bardet, J.P. (1986), Bounding surface plasticity model for sands, *Journal of Engineering Mechanics*, Vol. 112, No. 11, pp. 1198-1217.

Chen, W.F. (1994), *Constitutive equations for engineering materials*, Elsevier, Netherlands.

Chen, W.F. and Han D.J. (2007), *Plasticity for Structural Engineers*, John Ross Publishing, USA.

Chung, A.B. (2010), Unified modelling for sand under generalized stress paths, Ph.D. thesis, Columbia University, New York, USA.

Clough, G.W., Shafii Rad, N., Bachus, R.C., and Sitar, N. (1981), Cemented sands under static loading, *Journal of the Geotechnical Engineering Division*, Vol. 107, No. 6, pp. 799-817.

- Consoli, N.C., Cruz, R.C., Fonseca, A.V.D., and Coop, M.R. (2012), Influence of cement-voids ratio on stress-dilatancy behaviour of artificially cemented sand, *Journal of Geotechnical and Geoenvironmental Engineering*, Vol. 138, No. 1, pp. 100-109.
- Dafalias, Y.F. (1986), Bounding surface plasticity. I: Mathematical foundation and hypoplasticity, *Journal of Engineering Mechanics*, Vol. 112, No. 9, pp. 966-987.
- Dafalias, Y.F., and Herrmann, L.R. (1982), Bounding surface formulation of soil plasticity, *Soil Mechanics-Transient and Cyclic Loads*, Wiley, pp. 253-282.
- Dafalias, Y.F., and Popov, E.P. (1975), A model of nonlinearly hardening materials for complex loading, *Acta Mechanica*, Vol. 21, pp. 173-192.
- Dunne, F., and Petrinic, N. (2006), *Introduction to computational plasticity*, Oxford University Press, USA.
- Fjar, E., Holt, R.M., Horsrud, P., Raaen, A.M., and Risnes, R. (2008), *Petroleum related rock mechanics*, Elsevier, Netherlands.
- Fu, Z., Chen, S., and Peng, C. (2013), Modeling the cyclic behaviour of rockfill materials within the framework of generalized plasticity, *International Journal of Geomechanics*, ASCE.
- Gens, A., and Nova, R. (1993), Conceptual bases for a constitutive model for bonded soils and weak rocks, *Geotechnical Engineering of Hard Soils-Soft Rocks*, pp. 485-494.
- Hashiguchi K. (1989), Subloading surface model in unconventional plasticity, *International Journal of Solids and Structures*, Vol. 25, No. 8, pp. 917-945.
- Hashiguchi K., and Chen Z. P. (1998), Elastoplastic constitutive equations of soils with the subloading surface and the rotational hardening, *International Journal for Numerical and Analytical Methods in Geomechanics*, Vol. 22, No. 3, pp. 197-227.
- Imam, M.R. (1999), Modeling the constitutive behaviour of sand for the analysis of static liquefaction, Ph.D. thesis, The University of Alberta, Edmonton, Canada.
- Imam, M.R., and Chan, D.H. (2008), Application of a critical state model for the cyclic loading of sands, In *Proceedings from GeoEdmonton: 61st Canadian Geotechnical Conference*, Edmonton, pp. 127-134.
- Imam, M.R., Morgenstern, N.R., Robertson, P.K., and Chan, D.H. (2002), Yielding and flow liquefaction of loose sand. *Soils sand Foundations*, Vol. 42, No. 3, pp. 19-31.
- Imam, S.M.R., Morgenstern N.R., Robertson P.K., and Chan, D.H. (2005), A critical-state constitutive model for liquefiable sand, *Canadian Geotechnical Journal*, Vol. 42, No. 3, pp. 830-855.

Iwan, W.D. (1967), On a class of models for the yielding behaviour of continuous and composite systems, *Journal of Applied Mechanics*, Vol. 34, pp. 612-617.

Jefferies, M.G. (1993), Nor-Sand: a simple critical state model for sand, *Géotechnique*, Vol. 43, No. 1, pp. 91-103.

Khalili, N., Habte, M. A., and Valliappan S. (2005), A bounding surface plasticity model for cyclic loading of granular soils, *International Journal for numerical methods in engineering*, Vol. 63, pp. 1939–1960.

Khalili, N., Habte, M. A., and Valliappan S. (2006), Monotonic and Cyclic analysis of Granular Soils, *Computational Methods in Engineering And Science: Proceedings of Enhancement and Promotion of Computational Methods in Engineering and Science, China*, pp. 59-70.

Khong, CD. (2004), Development and numerical evaluation of unified critical state models, Ph.D. thesis, The University of Nottingham, Nottingham, U.K.

Krieg, R.D. (1975), A practical two-surface plasticity theory, *Journal of Applied Mechanics*, Vol. 42, No. 3, pp. 641-646.

Lee, K.H., Chan, D.H., and Lam, K.C. (2004), Constitutive model for cement treated clay in a critical state framework, *Soils and Foundations*, Vol. 44, No. 3, pp. 69-77.

Lenart, S. (2008), The response of saturated soils to a dynamic load, *Acta Geotechnica Slovenica*, Vol. 5, No. 1, pp. 37-49.

Ling, H.I., and Yang, Y. (2006), Unified sand model based on the critical state and generalized plasticity, *Journal of Engineering Mechanics*, Vol. 132, No. 12, pp. 1380-1391.

Manzari, M.T. , and Dafalias, Y. F. (1997), A critical state two-surface plasticity model for sands, *Géotechnique*, Vol. 47, No. 2, pp. 255-272.

Marri, A. (2010), The mechanical behaviour of cemented granular materials at high pressures, Ph.D. thesis, The University of Nottingham, Nottingham, U.K.

Mohsin, A.K.M. (2008), Automated Gmax measurement to explore degradation of artificially cemented carbonate sand, Ph.D. thesis, The University of Sydney, Sydney, Australia.

Mroz, Z., (1967), On the description of anisotropic hardening, *Journal of the Mechanics and Physics of Solids*, Vol. 15, pp. 163-175.

Mroz, Z., Norris, V. A. and Zienkiewicz, O.C. (1978), An anisotropic hardening model for soils and its application to cyclic loading, *International Journal for Numerical and Analytical methods in Geomechanics*, Vol. 2, pp. 203-221.

- Mroz, Z., Norris, V. A. and Zienkiewicz, O.C. (1979), Application of an anisotropic hardening model in the analysis of elasto-plastic deformation of soils, *Géotechnique*, Vol. 29, No. 1, pp. 1-34.
- Nova, R. (2005), A simple elastoplastic model for soils and soft rocks, ASCE, Geotechnical special publication, Vo. 128, pp. 380-399.
- Pastor, M., Zienkiewicz, O.C., and Chan A.H.C. (1990), Generalized Plasticity and the Modelling of Soil Behaviour, *International journal for numerical and analytical methods in geomechanics*, Vol. 14, pp. 151-190.
- Pastor, M., Zienkiewicz, O.C., and Leung, K.K. (1985), Simple model for transient soil loading in models for sands earthquake analysis. II. Non-associated models for sands, *International Journal for Numerical and Analytical Methods in Geomechanics*, Vol. 9, pp. 477-498.
- Reilly, M.P.O, and Brown, S.F. (1991), *Cyclic loading of soils: from theory to design*, Blackie and Son Limited, U.K.
- Russel, A., and Khalili N. (2004), A bounding surface plasticity model for sands exhibiting particle crushing, *Canadian Geotechnical Journal*, Vol. 41, No. 6, pp. 1179-1192.
- Schnaid, F., Prietto, P.D.M., and Consoli, N.C. (2001), Characterization of cemented sand in triaxial compression, *Journal of Geotechnical and Geoenvironmental Engineering*, Vol. 127, No. 10, pp. 857-868.
- Vermeer, P.A., and de Borst, R. (1984), Non-associated plasticity for soils, concrete and rocks, *Heron*, Vol. 29, No. 3, pp. 1-64.
- Wood, D.M. (1990), *Soil Behavior and Critical State Soil Mechanics*, Cambridge University Press, USA.
- Yang. C., Huang, M.S., and Cui, Y.J. (2011), Constitutive model of unsaturated structured soils under cyclic loading, In *proceedings of the fifth international conference on unsaturated soils*, Barcelona, pp. 987-992.
- Yoshinaka, R., Tran, T.V., and Osada M. (1998), Non-linear, stress and strain dependent behaviour of soft rocks under cyclic triaxial conditions, *International Journal of Rock Mechanics and Mining Sciences*, Vol. 35, No. 7, pp. 941-955.
- YU, H.S. (2006), *Plasticity and Geotechnics*, Springer, USA.
- Yu, H.S., Tan, S.M., and Schnaid, F. (2007), A critical state framework for modeling bonded geomaterials, *Geomechanics and Geoengineering*, Vol. 2, No. 1, pp. 61-74.
- Zienkiewicz, O.C., Leung, K.K., and Pastor, M. (1985), Simple model for transient soil loading in earthquake analysis. I. basic model and its application, *International Journal for Numerical and Analytical Methods in Geomechanics*, Vol. 9, pp. 453-476.

CHAPTER 6

INHERENT FABRIC ANISOTROPY

6.1 Introduction

As mentioned in chapter 4, the structure in natural soils is a combination of bonding and fabric. Therefore the overall behaviour of cemented sand depends not only on the degree of cementation between sand particles, but also on fabric in sand. Fabric reflects particle orientation, and particle contact arrangements. It describes the geometrical arrangement/packing of particles in general [Wan and Guo 2001a, Wan and Guo 2004]. During deposition process under earth gravity, sand particles usually deposit anisotropically and form fabric structure with cross-anisotropy (or transverse-isotropy). Cross-anisotropy as an inherent anisotropy is featured by one direction with distinctive anisotropy perpendicular to a bedding planes where it is almost isotropic. The perpendicular direction is the direction of deposition and is referred to as the axis of anisotropy [Gao and Zhao 2012]. Similar to uncemented sand, fabric is expected to affect cemented sand behaviour namely its stiffness, strength and dilatancy (the contractive or dilative tendency upon shearing) [Wan and Guo 2004, Gao and Zhao 2012]. Most constitutive models, however, are not formulated with considering the effect of bonding and fabric anisotropy simultaneously [Jefferies 1993, Li 2005, Gao and Zhao 2012]. That is, some constitutive models capture the influence of void ratio/mean stress on sand behaviour but neglect the effect of fabric. However, there is little doubt that sand fabric is an influential parameter in the constitutive behaviour of sand [Jefferies 1993].

Investigations at the microscopic level have shown that orientation of sand particles changes slightly even after large shear deformation. In other words, the inherent (structural/intrinsic) fabric anisotropy may be assumed constant during shearing process [Li and Dafalias 2002].

In this chapter, soil fabric is incorporated into the model using a symmetric fabric tensor F_{ij} which is kept constant to account for material inherent anisotropy and a scalar-valued state variable A which can represent the material anisotropic state. Modification of the constitutive model is carried out using a procedure which is similar to those of Li and Dafalias (2002) and Rasouli (2010).

6.2 Fabric tensor

The orientation of a non-spherical particle in a sand deposit can be represented using a second order fabric tensor as follows [Li and Dafalias 2002]:

$$F_{ij} = \frac{1}{2N} \sum_{k=1}^{2N} n_i^k n_j^k \quad (6.1)$$

where N is number of particles in a representative volume, and n is unit vector along major axis of elongation of the particle.

The magnitude of components of F_{ij} represents the net portion of particles which are statistically oriented towards a specific direction. F_{ij} is clearly symmetric and thus, it can be represented by three principal values of F_1, F_2 , and F_3 (not necessarily implying that $F_1 \geq F_2 \geq F_3$), and three corresponding principal directions. If we assume that the principal axes of the soil fabric coincide with a reference coordinate system (x'_1, x'_2, x'_3) , where the $x'_2 - x'_3$ plane defines the isotropic plane of the fabric (i.e. bedding plane), and the x'_1 axis shows the direction of deposition (i.e. perpendicular to the bedding plane), the fabric tensor can be defined as follows [Li and Dafalias 2002]:

$$F'_{ij} = \begin{pmatrix} F_1 & 0 & 0 \\ 0 & F_2 & 0 \\ 0 & 0 & F_3 \end{pmatrix} \quad (6.2)$$

In which $F_2 = F_3$ due to transverse-isotropy. It can be shown that F_{ij} has a unit trace which implies that $F_1 = 1 - F_2 - F_3 = 1 - 2F_3$. Therefore for a transversely isotropic soil with a given deposition direction (usually in the vertical direction), only one scalar quantity is required to define the fabric tensor. Oda and Nakayama (1989) proposed the following symmetric second order fabric tensor [Li and Dafalias 2002, Li 2005, Gao and Zhao 2012]:

$$F'_{ij} = \frac{1}{3 + \Delta} \begin{pmatrix} 1 - \Delta & 0 & 0 \\ 0 & 1 + \Delta & 0 \\ 0 & 0 & 1 + \Delta \end{pmatrix} \quad (6.3)$$

where Δ is a scalar that characterizes the magnitude of the cross-anisotropy. Δ is a material parameter which ranges from zero in the case of complete isotropy ($F'_{ij} = I/3 = \delta_{ij}/3$) to unity in the case of maximum anisotropy when the major axis of all particles are distributed in $x'_2 - x'_3$ plane (i.e. when the fabric is strongest in the bedding plane). Thus the fabric tensor F'_{ij} characterizes both the intensity and orientation of the inherent material anisotropy for a specific sand deposit.

If the sample has rotated and/or the reference frame has changed, the components of the fabric tensor will be subjected to orthogonal transformation as follows:

$$F_{kl} = a_{ki} a_{lj} F'_{ij} \quad (6.4)$$

where $a_{mn} = e_m \cdot e'_n$ is the direction cosine of the angle between e_m , the m th unit vector of the deformed coordinate system and e'_n , the n th unit vector of the original coordinate system.

6.3 Anisotropic state variable

The introduction of fabric tensor into a constitutive model which includes other tensor variables such as the stress tensor requires special considerations. This may lead to complex mathematical relationships. Li and Dafalias (2002) proposed a simple approach which accounts for the effect of the relative orientation of the stress and fabric tensors. This is done by the proper definition of a scalar-valued state variable A which is a function of both F_{ij} and σ_{ij} .

The tensor T_{ij} which is a function of both the fabric and stress tensors are defined as follows [Li and Dafalias 2002, Rasouli 2010]:

$$T_{ij} = \frac{1}{6} (\sigma_{im} F_{mj}^{-1} + F_{in}^{-1} \sigma_{nj}) \quad (6.5)$$

where F_{in}^{-1} is inverse of the fabric tensor F_{in} .

T_{ij} reflects the influence of the material fabric and its relative orientation with respect to stress. It is affected by the magnitude of the stress. Thus it is not suitable for direct use in describing the anisotropic stress states of a material. For

example if a material is isotropic (i.e. $T_{ij} = \sigma_{ij}$), a scalar-valued index derived from T_{ij} changes with the magnitude of σ_{ij} instead of having a unique value which is characteristics of the isotropic state. Hence some sorts of normalization relative to stress seem to be necessary [Li and Dafalias 2002].

We start with decomposition of the stress tensor into a deviatoric stress tensor and a hydrostatic stress tensor as follows:

$$\sigma_{ij} = s_{ij} + p\delta_{ij} = p(\eta_{ij} + \delta_{ij}) \quad (6.6)$$

where δ_{ij} is Kronecker delta, and the stress ratio η_{ij} is defined as:

$$\eta_{ij} = \frac{s_{ij}}{p} \quad (6.7)$$

Stress ratio R_f and the load angle θ are defined based on η_{ij} as follows [Li and Dafalias 2002]:

$$R_f = \sqrt{\frac{3}{2}\eta_{ij}\eta_{ij}} \quad (6.8)$$

$$\theta = -\frac{1}{3} \sin^{-1} \left(\frac{9}{2} \frac{\eta_{ij}\eta_{jk}\eta_{ki}}{R_f^3} \right) \quad (6.9)$$

A critical state failure surface in stress space is defined using R_f and θ as follows [Li and Dafalias 2002]:

$$R_f - M_c g(\theta) = 0 \quad (6.10)$$

where M_c is the critical stress ratio under triaxial compression, and

$$g(\theta) = \frac{\sqrt{(1+c^2)^2 + 4c(1-c^2)\sin 3\theta} - (1+c^2)}{2(1-c)\sin 3\theta} \quad (6.11)$$

Which is an interpolation function that interpolates R_f on the critical state failure surface based on θ such that $g(-30) = 1$, $g(0) = (c+c^2)/(1+c^2)$, and $g(30) = c$ [Li and Dafalias 2002]. c is a model constant which defines that ratio of the critical state ratio under triaxial extension over that of triaxial compression. Not all values of c result in $g(-30) = 1$ and $g(30) = c$. For example $c \leq 0.41$ does not lead to $g(-30) = 1$. However all typical values of c (say $0.6 < c < 1$) satisfy the above conditions.

Note that the critical state failure surface defined by equation (6.10) is independent of the material anisotropy. This is justified by the fact that the critical stress ratio is mainly controlled by the frictional coefficient between sand particles which is an intrinsic property and independent of the fabric [Li and Dafalias 2002].

As mentioned the effect of the fabric anisotropy must only depends on the orientation, and not the magnitude of the stress tensor. A stress $\hat{\sigma}_{ij}$ normalized with respect to mean effective stress and with deviatoric directions identical to those of σ_{ij} can be defined as follows [Li and Dafalias 2002]:

$$\hat{\sigma}_{ij} = \left(\sqrt{\frac{2}{3}} M_c g(\theta) \right) l_{ij} + \delta_{ij} = \hat{\eta}_{ij} + \delta_{ij} \quad (6.12)$$

where

$$l_{ij} = \frac{\eta_{ij}}{|\eta_{mn}|} = \sqrt{\frac{3}{2}} \frac{\eta_{ij}}{R_f} \quad (6.13)$$

is a unit tensor which represents the direction of the stress ratio tensor η_{ij} .

$\hat{\sigma}_{ij}$ clearly includes information on the stress orientation by l_{ij} . If we use $\hat{\sigma}_{ij}$ instead of σ_{ij} in equation (6.5), a normalized stress tensor can be defined as follows [Li and Dafalias 2002]:

$$\tilde{T}_{ij} = \frac{1}{6} (\hat{\sigma}_{im} F_{mj}^{-1} + F_{in}^{-1} \hat{\sigma}_{nj}) \quad (6.14)$$

\tilde{T}_{ij} can be decomposed into a deviatoric stress ratio tensor $\tilde{\eta}_{ij}$ and a hydrostatic part $\tilde{p} = \tilde{T}_{jj}/3$, as follows:

$$\tilde{T}_{ij} = \tilde{p}(\tilde{\eta}_{ij} + \delta_{ij}) \quad (6.15)$$

Similar to equations (6.8) and (6.9), \tilde{R}_f and $\tilde{\theta}$ are defined as follows [Li and Dafalias 2002]:

$$\tilde{R}_f = \sqrt{\frac{3}{2} \tilde{\eta}_{ij} \tilde{\eta}_{ij}} \quad (6.16)$$

$$\tilde{\theta} = -\frac{1}{3} \sin^{-1} \left(\frac{9}{2} \frac{\tilde{\eta}_{ij} \tilde{\eta}_{jk} \tilde{\eta}_{ki}}{\tilde{R}_f^3} \right) = -\frac{1}{3} \sin^{-1} \left(\frac{9}{2} \frac{\text{tr } \tilde{\eta}^3}{\tilde{R}_f^3} \right) \quad (6.17)$$

After some calculations, $\tilde{\eta}_{ij}$ and \tilde{R}_f can be expressed in terms of $\hat{\sigma}_{ij}$ and F_{ij}^{-1} as follows [Li and Dafalias 2002]:

$$\underline{\tilde{\eta}} = \frac{3}{2} tr^{-1}(\underline{\hat{\sigma}} \underline{F}^{-1})(\underline{\hat{\sigma}} \underline{F}^{-1} + \underline{F}^{-1} \underline{\hat{\sigma}}) - I \quad (6.18)$$

$$\tilde{R}_f = \sqrt{\frac{3}{2} tr \underline{\tilde{\eta}}^2} = \sqrt{\frac{27}{4} tr^{-2}(\underline{\hat{\sigma}} \underline{F}^{-1})(tr(\underline{\hat{\sigma}}^2 \underline{F}^{-2}) + tr(\underline{\hat{\sigma}} \underline{F}^{-1} \underline{\hat{\sigma}} \underline{F}^{-1})) - \frac{9}{2}} \quad (6.19)$$

$$tr \underline{\tilde{\eta}}^3 = \frac{27}{8} tr^{-3}(\underline{\hat{\sigma}} \underline{F}^{-1}) \left(2 tr(\underline{\hat{\sigma}} \underline{F}^{-1})^3 + 3 tr(\underline{\hat{\sigma}} \underline{F}^{-2} \underline{\hat{\sigma}}^2 \underline{F}^{-1}) + 3 tr(\underline{\hat{\sigma}} \underline{F}^{-1} \underline{\hat{\sigma}}^2 \underline{F}^{-2}) \right) - \frac{27}{2} tr^{-2}(\underline{\hat{\sigma}} \underline{F}^{-1}) \left(tr(\underline{\hat{\sigma}} \underline{F}^{-1})^2 + tr(\underline{\hat{\sigma}}^2 \underline{F}^{-2}) \right) + 6 \quad (6.20)$$

The symbol tr denotes the trace of a tensor, and underbar sign indicates a tensorial quantity.

Equation (6.19) and (6.20) show that the magnitude of $\underline{\hat{\sigma}}$ does not affect the values of \tilde{R}_f and $\tilde{\theta}$. Hence, any stress tensor rather than $\underline{\hat{\sigma}}$ can be used as long as it has the same stress ratio direction [Li and Dafalias 2002].

Li and Dafalias (2002) ultimately defined the fabric parameter as a function of \tilde{R}_f and $\tilde{\theta}$ using equation (6.10) as follows:

$$A = \frac{\tilde{R}_f}{M_c g(\tilde{\theta})} - 1 \quad (6.21)$$

Anisotropic parameter A can be used as a parameter for describing the sand fabric effect on constitutive behaviour. It can be shown that for isotropic material $A = 0$ while for anisotropic materials it can be either positive or negative, depending on the orientation of the stress relative to that of the soil fabric and to a weaker degree on the fabric intensity [Li and Dafalias 2002].

Variations of anisotropic parameter A with α and b is shown in Fig. 6-1 for chosen values of $\Delta = 0.2$, $M_c = 1.25$, and $c = 0.75$. α is the angle between the direction of the major principal stress and direction of deposition (usually vertical direction). b is b -parameter which is used to investigate effect of the intermediate principal stress and is defined as follows:

$$b = \frac{\sigma_2 - \sigma_3}{\sigma_1 - \sigma_3} \quad (6.22)$$

Triaxial compression (TC) and triaxial extension (TE) are two extreme modes of shearing which are associated with $b = 0, \alpha = 0$ and $b = 1, \alpha = 90$. The hollow cylinder (HC) test can provide tests with constant $0 < \alpha < 90$ and constant $0 < b < 1$ which are other modes of shearing between two extreme modes of TC and TE. The HC apparatus permits independent control on the magnitude and direction of the three principal stresses (i.e. rotation of the major-minor principal stress axes). Thus HC apparatus can be used for studies of inherent anisotropy, intermediate principal stress, and rotation of major/minor principal stress direction [Cai 2010].

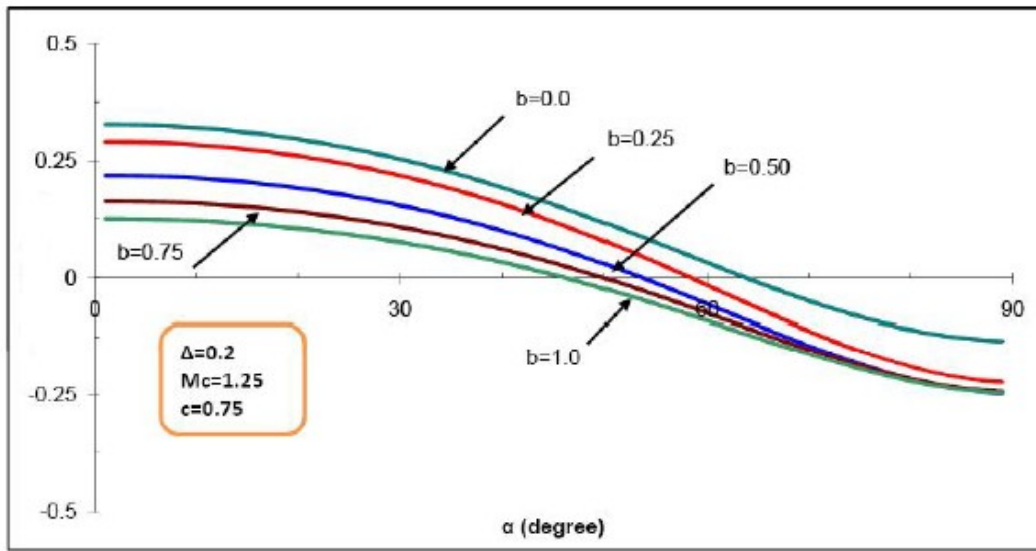


Fig. 6-1 Variations of anisotropic parameter A (vertical axis) with α and b (Rasouli 2010)

A schematic representation of the HC apparatus is shown in Fig. 6-2. During HC tests, the axis of σ_1 and σ_3 rotate by α around the fixed axis of $\sigma_2 = \sigma_{rr}$. This means one direction always remains principal direction during HC tests. Also directions of σ_{zz} , σ_{rr} , and $\sigma_{\theta\theta}$ correspond to those of F'_{11} , F'_{22} , and F'_{33} in equation (6.3). Any HC element is subjected to an axial load, F_v , torque, T , internal pressure, p_i , and external pressure, p_o . During shearing, the torque T develops shear stresses, $\tau_{\theta z}$ and $\tau_{z\theta}$ which are equal. The axial load causes a vertical stress, σ_{zz} , and p_i and p_o determine σ_{rr} and $\sigma_{\theta\theta}$ [Imam 1999, Li and Dafalias 2002, Cai 2010]. During HC test, there may or may not be pressure applied in the inner hole. If the inner pressure is zero, the inner wall will fail under the confining stresses.

However spalling will continue around the inner wall until the arching develops. Arching will reduce the stress on the wall until it is low enough leading to instability of inner wall.

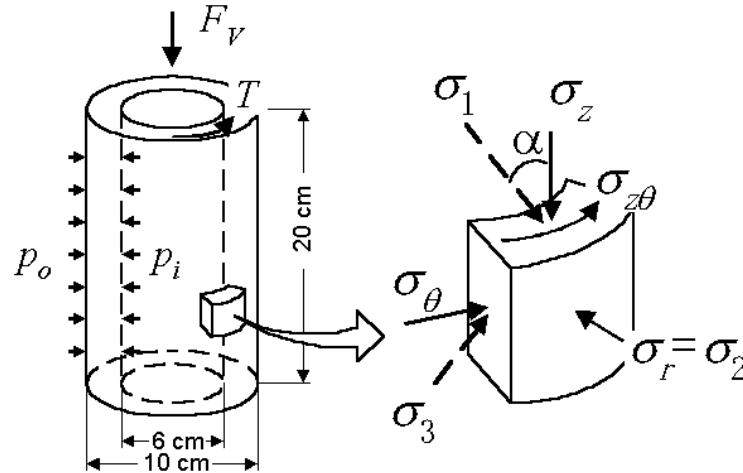


Fig. 6-2 Schematic representation of hollow cylinder apparatus (Yoshimine et. al. 1998)

6.4 Modification of the constitutive model using anisotropic state variable

Incorporation of anisotropic parameter A into the constitutive model is done similar to Rasouli (2010). He incorporated A by modifying the definition of M_p in the constitutive equations. Some important features of the model such as the plastic modulus, the yielding stresses, and consequently the stress-dilatancy relationship are affected by this stress ratio because the loading function includes M_p . These features will be a function of anisotropic state parameter if M_p is made a function of A . However, other features of the model like the failure stress ratio and critical state are not influenced by M_p . Thus, they are considered to remain unchanged by inherent anisotropy as in Manzari and Dafalias (1997) and Li and Dafalias (2002).

Definition of M_p initially is modified in order to include parameter b for different modes of shearing as follows (Imam 1999, Imam and Rasouli 2010):

$$M_p = \frac{6(1 - b + b^2)^{1/2} \sin \phi_p}{3 + (2b - 1) \sin \phi_p} \quad (6.23)$$

For $b = 0$ and $b = 1$, the formula will reduce to those of $M_{p,c}$ and $M_{p,e}$, respectively, in which subscript c stands for compression and subscript e denotes extension.

In order to account for the effects of inherent anisotropy and all modes of shearing including triaxial compression and triaxial extension, $\sin\varphi_p$ is defined using the following formula [Rasouli 2010]:

$$\sin\varphi_p = \sin\varphi_\mu - k_p\psi_p - a_p(A) \quad (6.24)$$

in which

$$a_p(A) = \frac{A_c - A}{A_c - A_e} \cdot a_p \quad (6.25)$$

where a_p is the material parameter in the original model, A is anisotropic state variable defined in equation (6.21), A_c and A_e are the anisotropic parameters in triaxial compression and triaxial extension, respectively, whose values depend on other inherent anisotropy related material parameters including Δ , c , and M_c . A_c and A_e can be located in Fig. 6-1 as far upper left side and far lower right side, respectively. For triaxial compression $A = A_c$ and $a_p(A) = 0$, and for triaxial extension $A = A_e$ and $a_p(A) = a_p$.

6.5 Model performance

Performance of the model is examined against hollow cylinder tests on Toyoura sand. These tests have been conducted under different values of α and b . All specimens in these undrained tests were consolidated isotropically to 100 kpa before they being sheared. They have chosen from Rasouli (2010). However they originally come from Yoshimine et. al. (1998). Note that some combinations of α and b were not tested during these HC tests because of uncontrolled non-uniformities and instabilities. In general, conducting HC tests with high values of b (say $b \geq 0.75$) is difficult since it is difficult to perform such tests due to non-uniformity of straining developed during these tests [Rasouli 2010].

The angle α changes in HC tests with change of the major principal stress relative to the vertical direction which is the deposition direction. However, it is assumed

here that it varies with change of the deposition direction (which is perpendicular to the bedding plane) relative to the vertical direction which is direction of the major principal stress. This is similar to the procedure which was adopted by Imam (1999) and Rasouli (2010). Axisymmetric mode is also used in order to resemble a cylindrical sample. Thus virtually triaxial tests are modelled, but under different deposition directions. Moreover, we already have included the effect of inherent anisotropy and different modes of shearing with incorporation of inherent anisotropy parameter A and b -parameter in formulation of the constitutive model. All of the following tests on Toyoura sand were modelled by one unique set of material parameters which are listed in table 6-1. Inherent anisotropy parameters were selected according to Li and Dafalias (2002). Assigned values for Δ, c and M_c result in $A_c = 0.328$ and $A_e = -0.25$. If other values are allocated for these parameters, A_c and A_e will have different values. Note that Δ, c and M_c are used to estimate a value for A under different combinations of α and b . It should be noted that in these calibrations for $b > 0.5$, it was assumed that: $a_p(A) = 0.67 a_p(A)$.

Measured and predicted behaviour of Toyoura sand under undrained HC tests with different values of α and b have been shown in Figs. 6-3 to 6-12. They are in relatively good agreement in general even though there are discrepancies in some cases. It was possible to capture better matches for those cases if a non-unique set of material parameters were used. However, the aim was to capture the experimental observations using one single set of material parameters. This aim resulted in similar inaccuracies in calibration of the HC tests in Li and Dafalias (2002) and Rasouli (2010) as well. Note that the reduced extension test was modelled for the test with $b = 1$ rather than the standard extension test because of Flac instability in simulating increasing radial strain/stress (i.e. decreasing axial strain/stress was modelled).

Table 6-1 Material parameters used for calibration of undrained HC tests on Toyoura sand

Parameter type	Name	Toyourea sand
Peak state	k_p	1.2
	φ_μ	21
	a_p	0.45
Stress-dilatancy	φ_{cs}	31
	k_{PT}	0.75
	a_{PT}	0.01
Elasticity	G_a	8e6
	K_a	8.5e6
Plastic stiffness	h	1
Failure	k_f	0.75
Critical state line	e_{cs}	$-0.0063477p^3 + 0.0367p^2 - 0.11991p + 0.92548$ (p in Mpa)
Inherent anisotropy	Δ	0.2
	M_c	1.25
	c	0.75

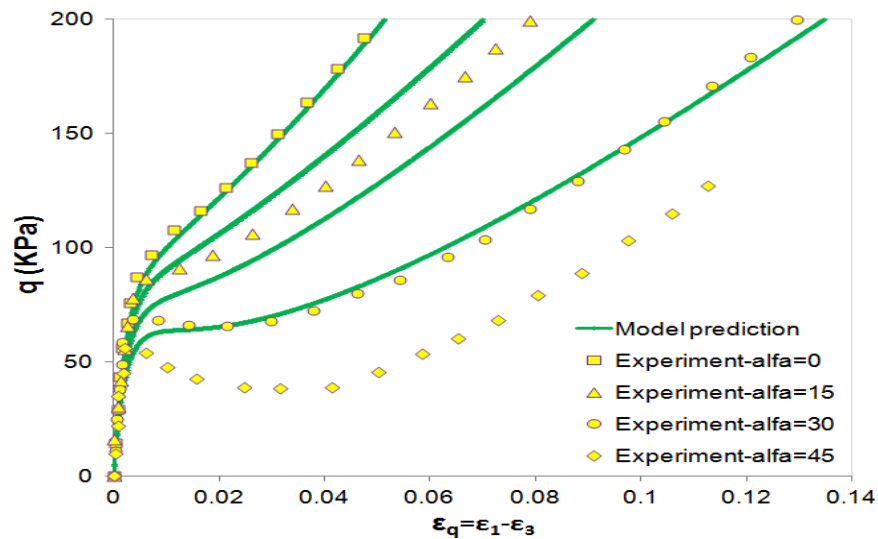


Fig. 6-3 Observed and predicted undrained response for deviator stress vs. shear strain curve under $b = 0$ and $\alpha = 0^\circ$ to 45°

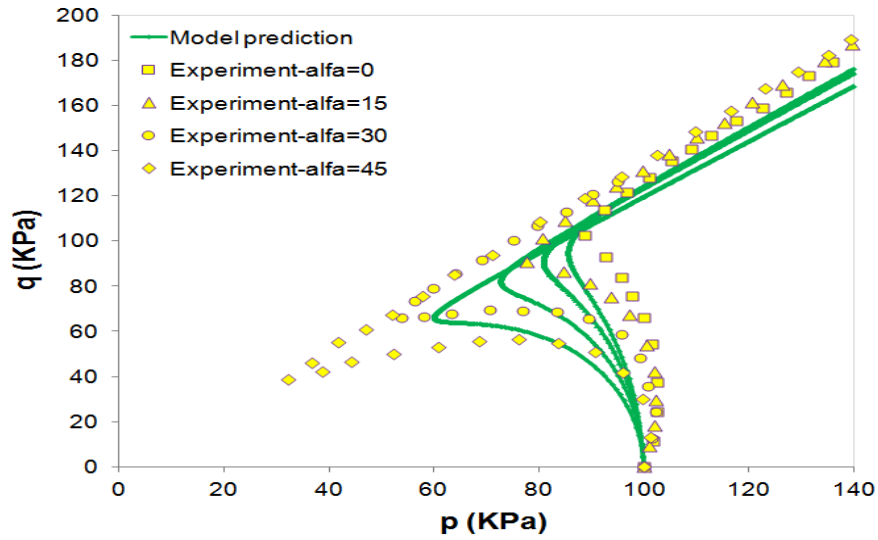


Fig. 6-4 Observed and predicted undrained response for deviator stress vs. mean effective stress curve under $b = 0$ and $\alpha = 0^\circ$ to 45°

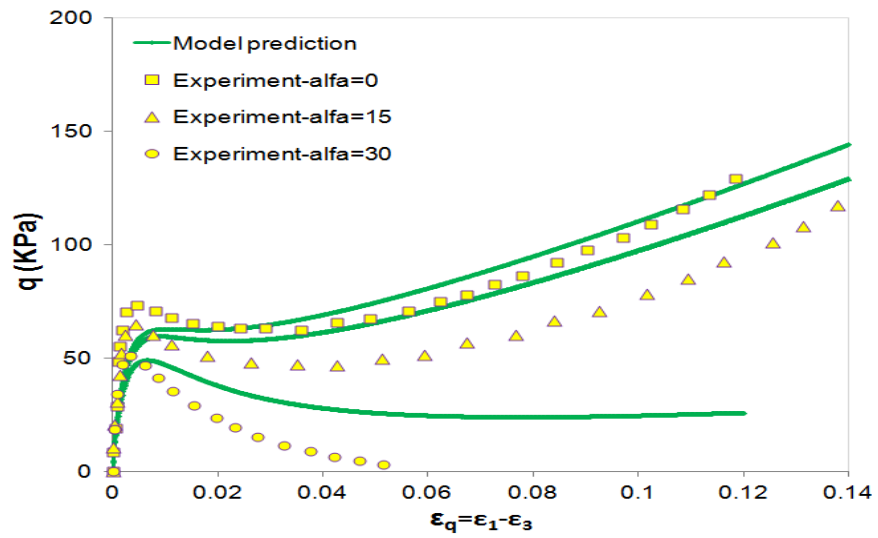


Fig. 6-5 Observed and predicted undrained response for deviator stress vs. shear strain curve under $b = 0.25$ and $\alpha = 0^\circ$ to 30°

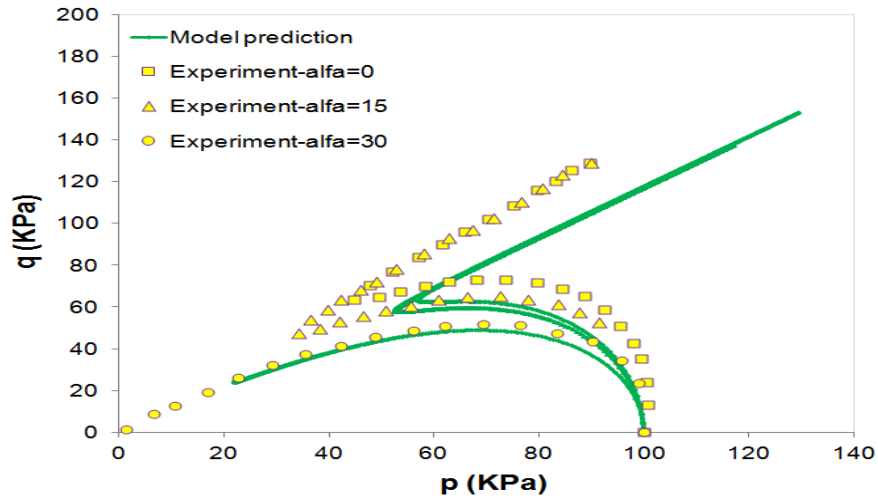


Fig. 6-6 Observed and predicted undrained response for deviator stress vs. mean effective stress curve under $b = 0.25$ and $\alpha = 0^{\circ}$ to 30°

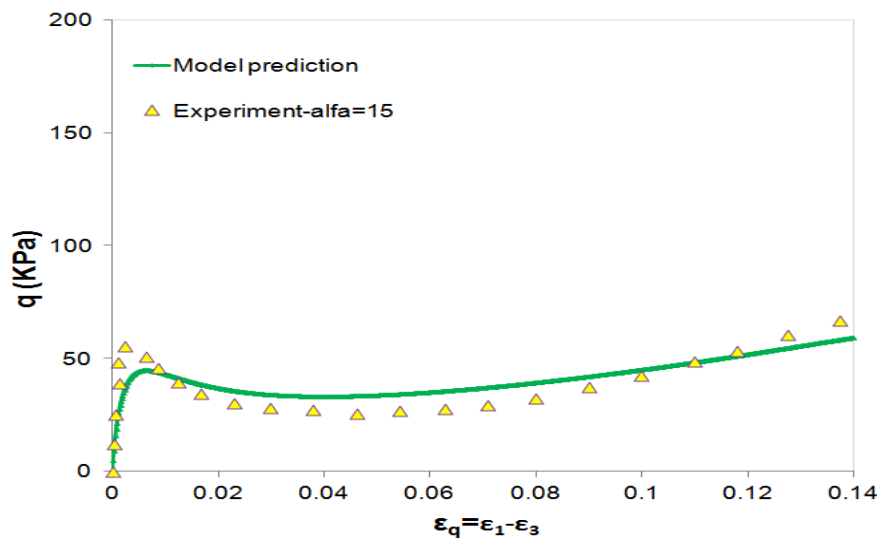


Fig. 6-7 Observed and predicted undrained response for deviator stress vs. shear strain curve under $b = 0.5$ and $\alpha = 15^{\circ}$

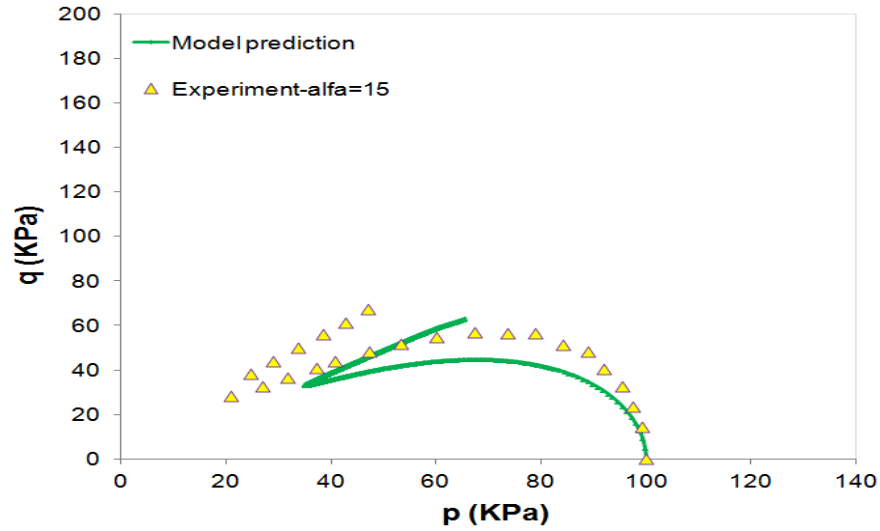


Fig. 6-8 Observed and predicted undrained response for deviator stress vs. mean effective stress curve under $b = 0.5$ and $\alpha = 15^\circ$

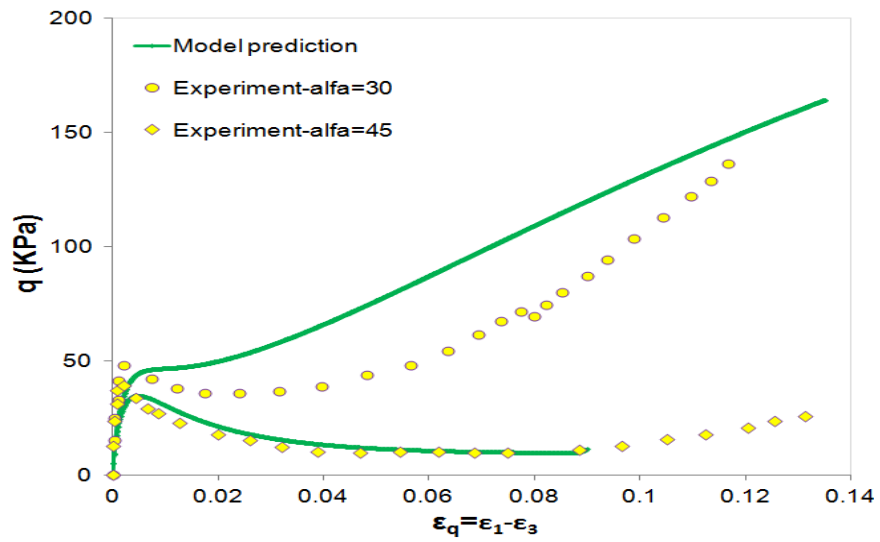


Fig. 6-9 Observed and predicted undrained response for deviator stress vs. shear strain curve under $b = 0.75$ and $\alpha = 30^\circ$ to 45°

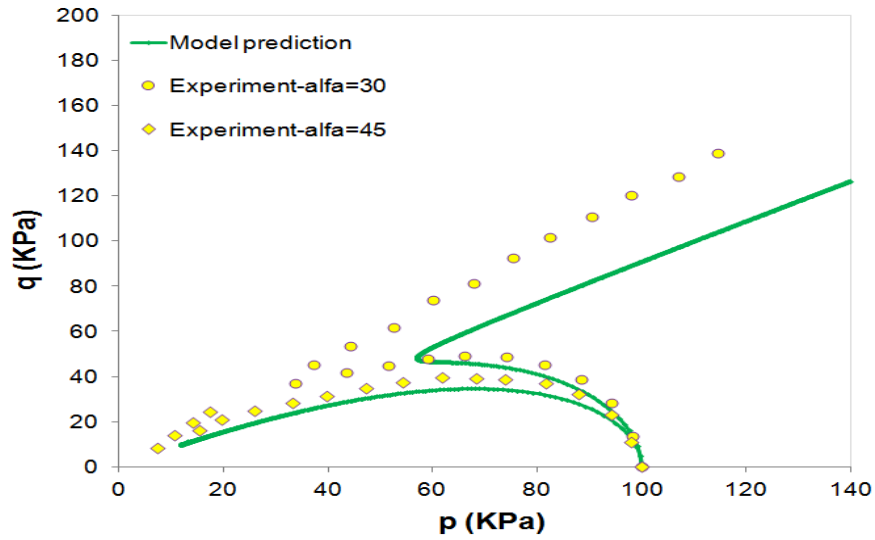


Fig. 6-10 Observed and predicted undrained response for deviator stress vs. mean effective stress curve under $b = 0.75$ and $\alpha = 30^\circ$ to 45°

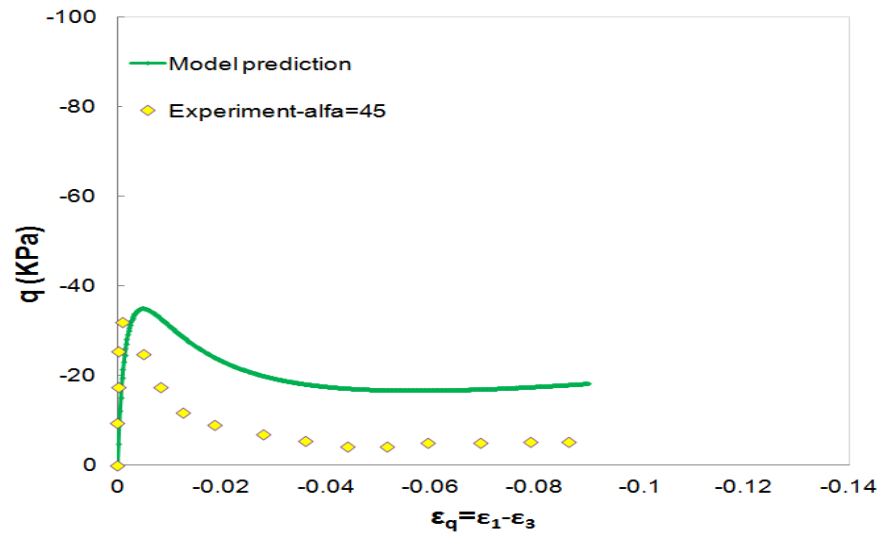


Fig. 6-11 Observed and predicted undrained response for deviator stress vs. shear strain curve under $b = 1.0$ and $\alpha = 45^\circ$

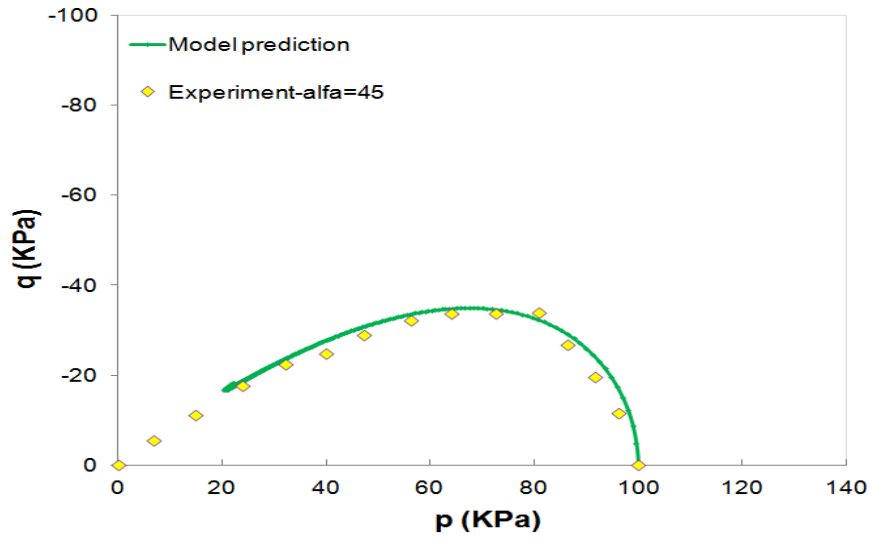


Fig. 6-12 Observed and predicted undrained response for deviator stress vs. mean effective stress curve under $b = 1.0$ and $\alpha = 45^\circ$

Figs. 6-13 to 6-22 show predicted behaviour of Toyoura sand using the same material parameters and the same conditions of the above HC tests, but under drained condition.

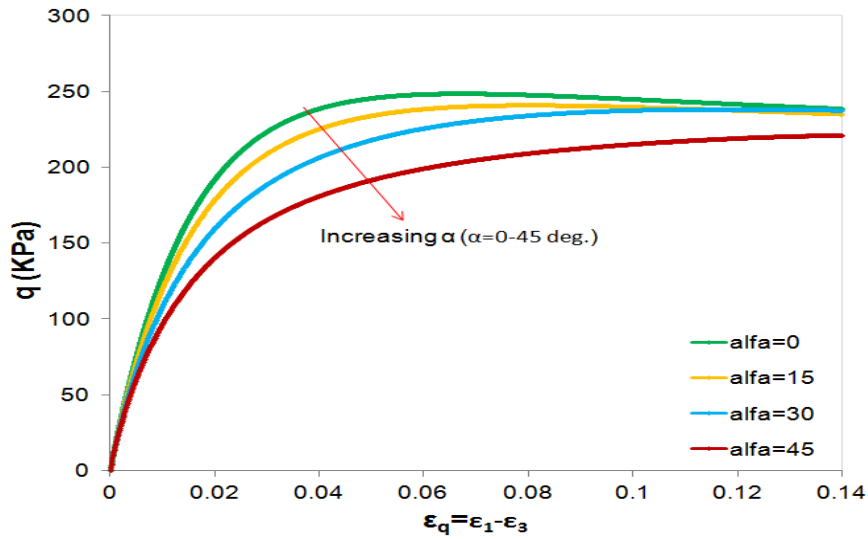


Fig. 6-13 Predicted drained behaviour for deviator stress vs. shear strain curve under $b = 0$ and $\alpha = 0^\circ$ to 45°

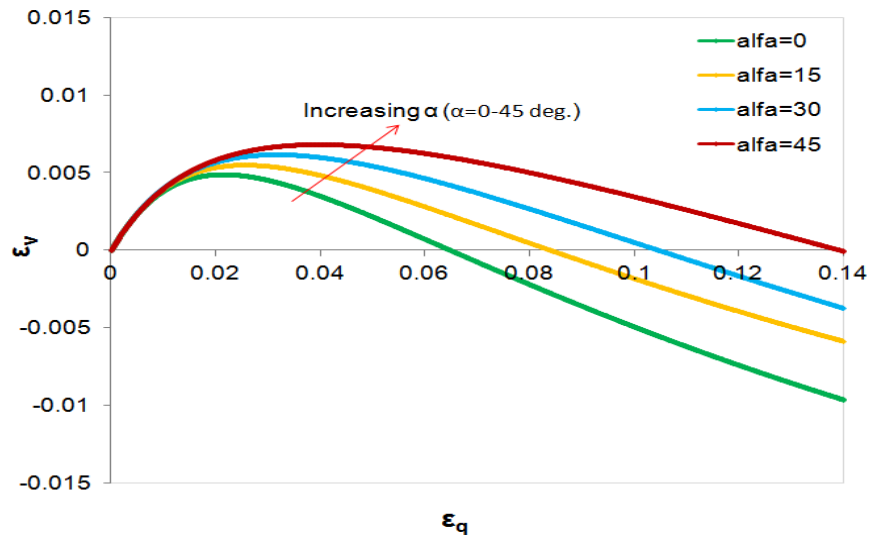


Fig. 6-14 Predicted drained behaviour for volumetric strain vs. shear strain curve under $b = 0$ and $\alpha = 0^{\circ}$ to 45°

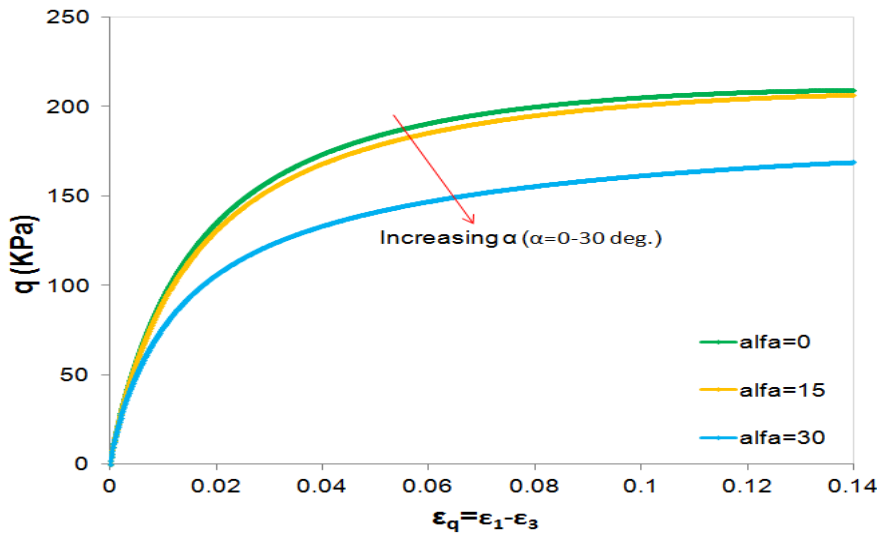


Fig. 6-15 Predicted drained behaviour for deviator stress vs. shear strain curve under $b = 0.25$ and $\alpha = 0^{\circ}$ to 30°

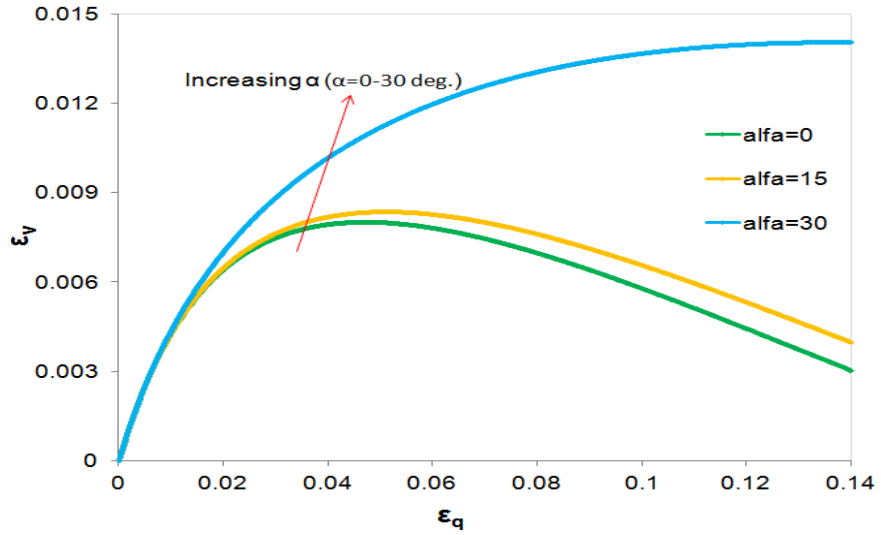


Fig. 6-16 Predicted drained behaviour for volumetric strain vs. shear strain curve under $b = 0.25$ and $\alpha = 0^{\circ}$ to 30°

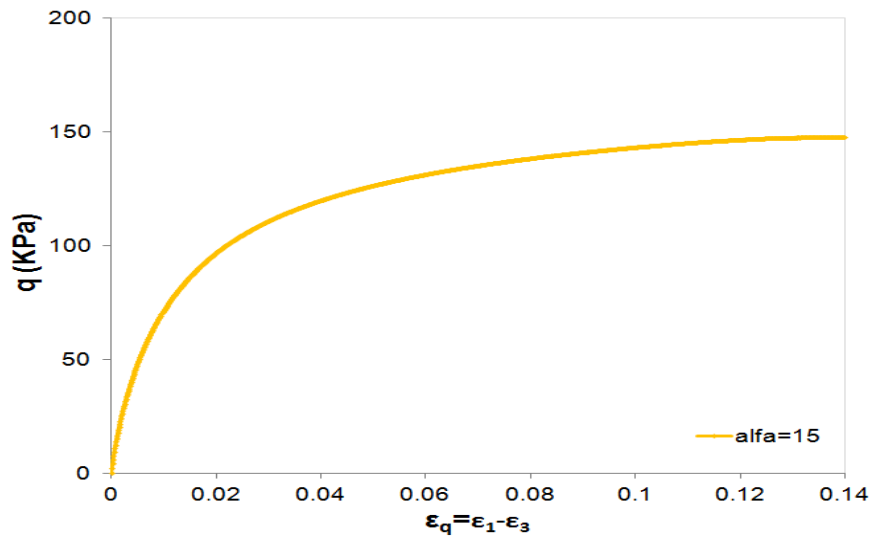


Fig. 6-17 Predicted drained behaviour for deviator stress vs. shear strain curve under $b = 0.5$ and $\alpha = 15^{\circ}$

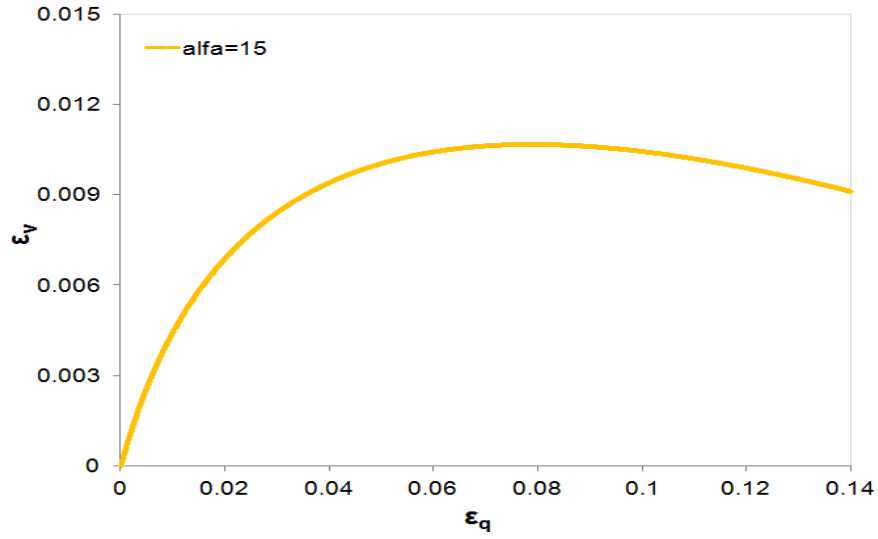


Fig. 6-18 Predicted drained behaviour for volumetric strain vs. shear strain curve under $b = 0.5$ and $\alpha = 15^\circ$

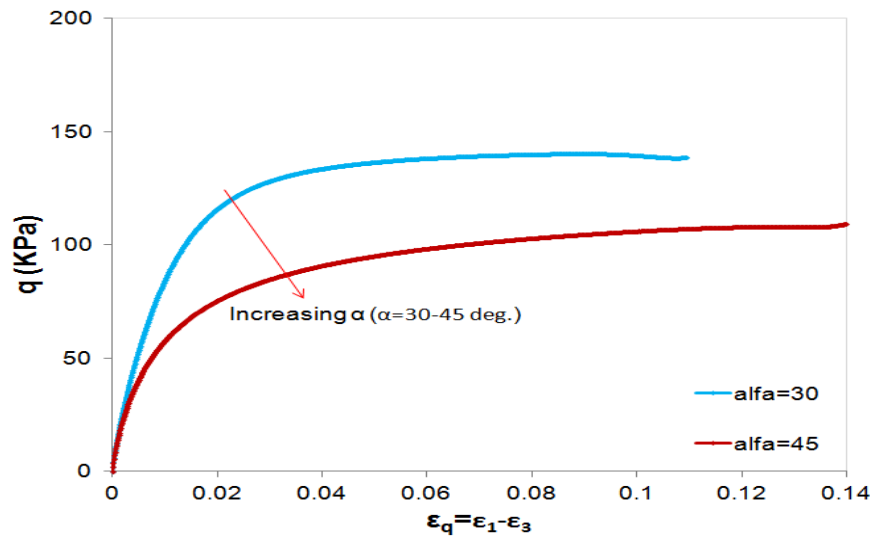


Fig. 6-19 Predicted drained behaviour for deviator stress vs. shear strain curve under $b = 0.75$ and $\alpha = 30^\circ$ to 45°

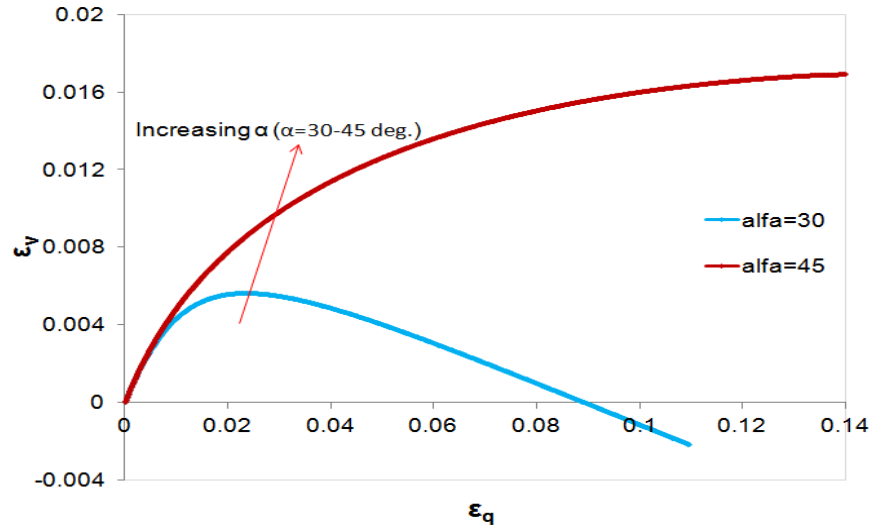


Fig. 6-20 Predicted drained behaviour for volumetric strain vs. shear strain curve under $b = 0.75$ and $\alpha = 30^\circ$ to 45°

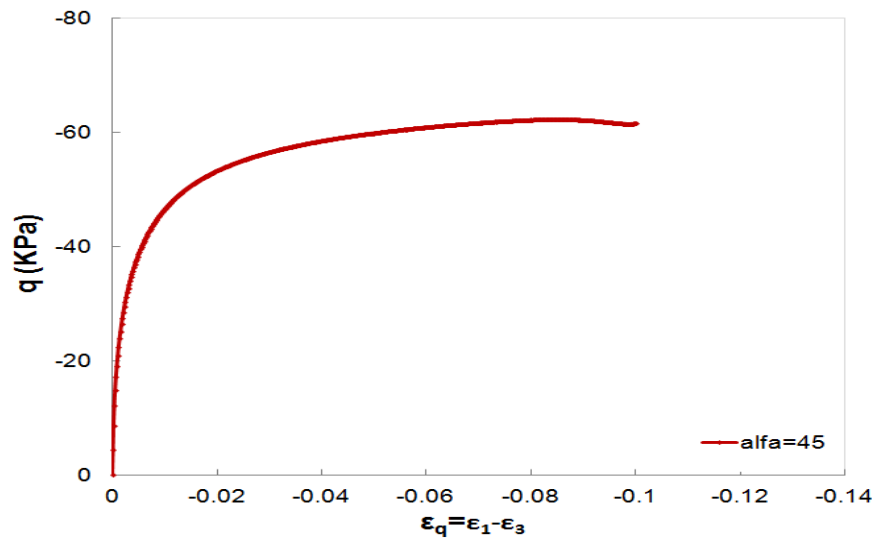


Fig. 6-21 Predicted drained behaviour for deviator stress vs. shear strain curve under $b = 1.0$ and $\alpha = 45^\circ$

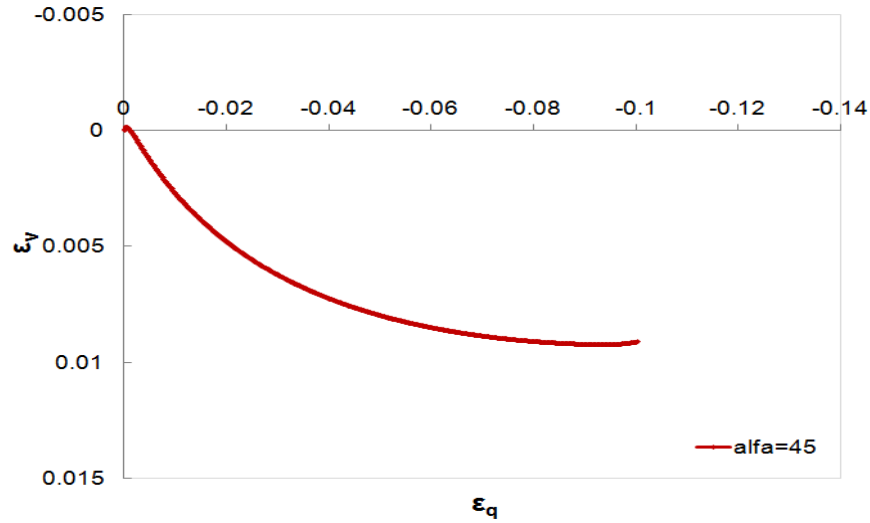


Fig. 6-22 Predicted drained behaviour for volumetric strain vs. shear strain curve under $b = 1.0$ and $\alpha = 45^\circ$

Figs. 6-23 to 6-24 show model predictions for drained HC tests on a hypothetical cemented sand. These tests have been modelled using one set of material parameters which are listed in table 6-2. Intrinsic anisotropy parameters were chosen similar to those in table 1. It was assumed also that all specimens were consolidated isotropically to pressure equals to 200 *kpa* and void ratio equals to 0.74 before they being sheared.

Table 6-2 Material parameters used for calibration of hypothetical drained HC tests on cemented sand in Figs. 6-23 to 6-24

Parameter type	Parameter name	Cemented sand
Original model	k_p	1.5
	φ_μ	29
	a_p	0.15
	φ_{cs}	31
	k_{PT}	1.25
	a_{PT}	0.10
	G_a	5e6
	K_a	8e6
	h	1
	k_f	0.75
	e_{cs}	$-0.0063477p^3 + 0.0367p^2 - 0.11991p + 0.76$ (p in Mpa)
Bonding (cementation)	p_o	2e5
	γ	15
	β	0.1
	c	5e3
	ξ	5

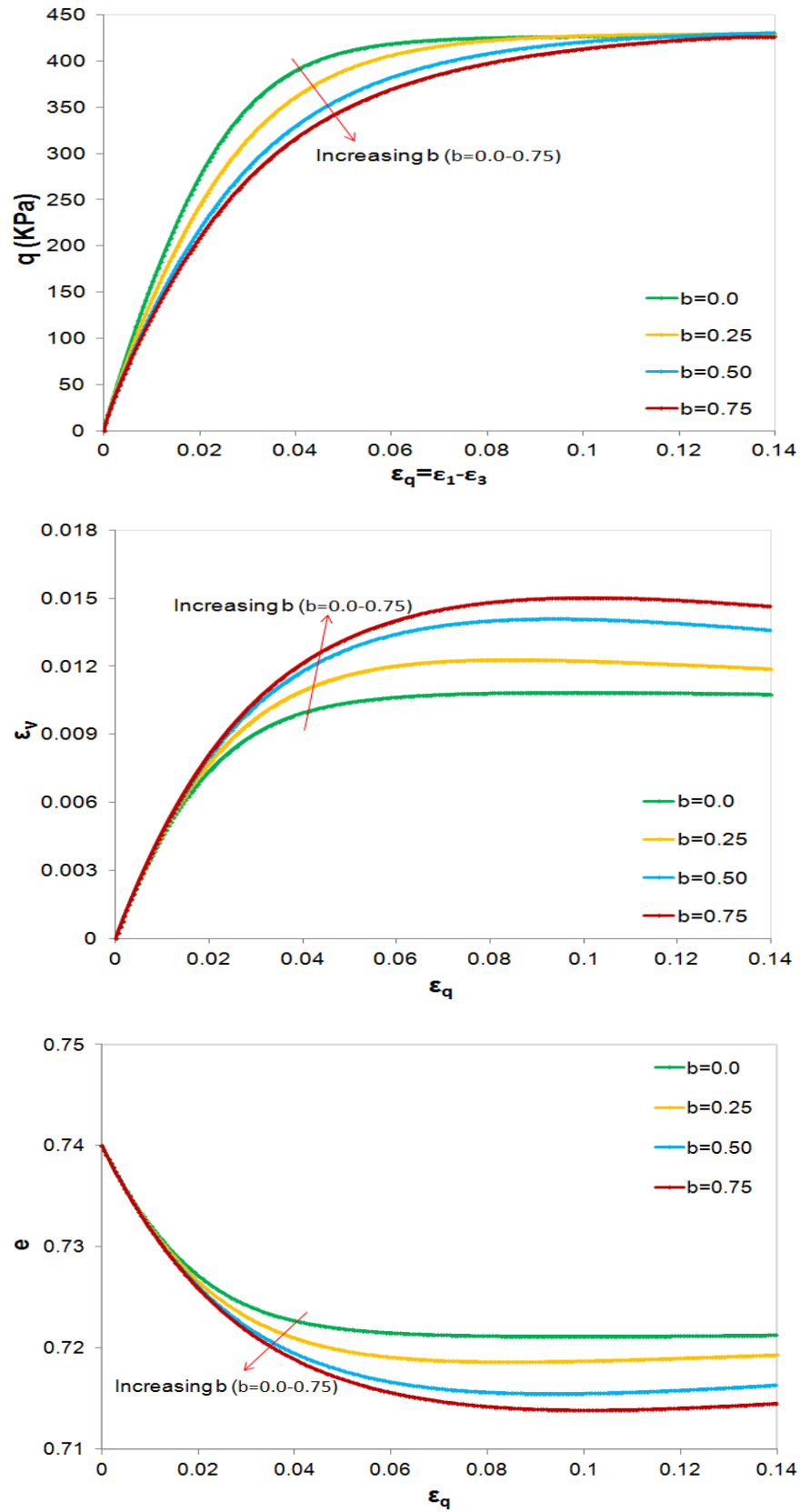


Fig. 6-23 Sensitivity analysis for a cemented sand under HC tests with $\alpha = 0^0$

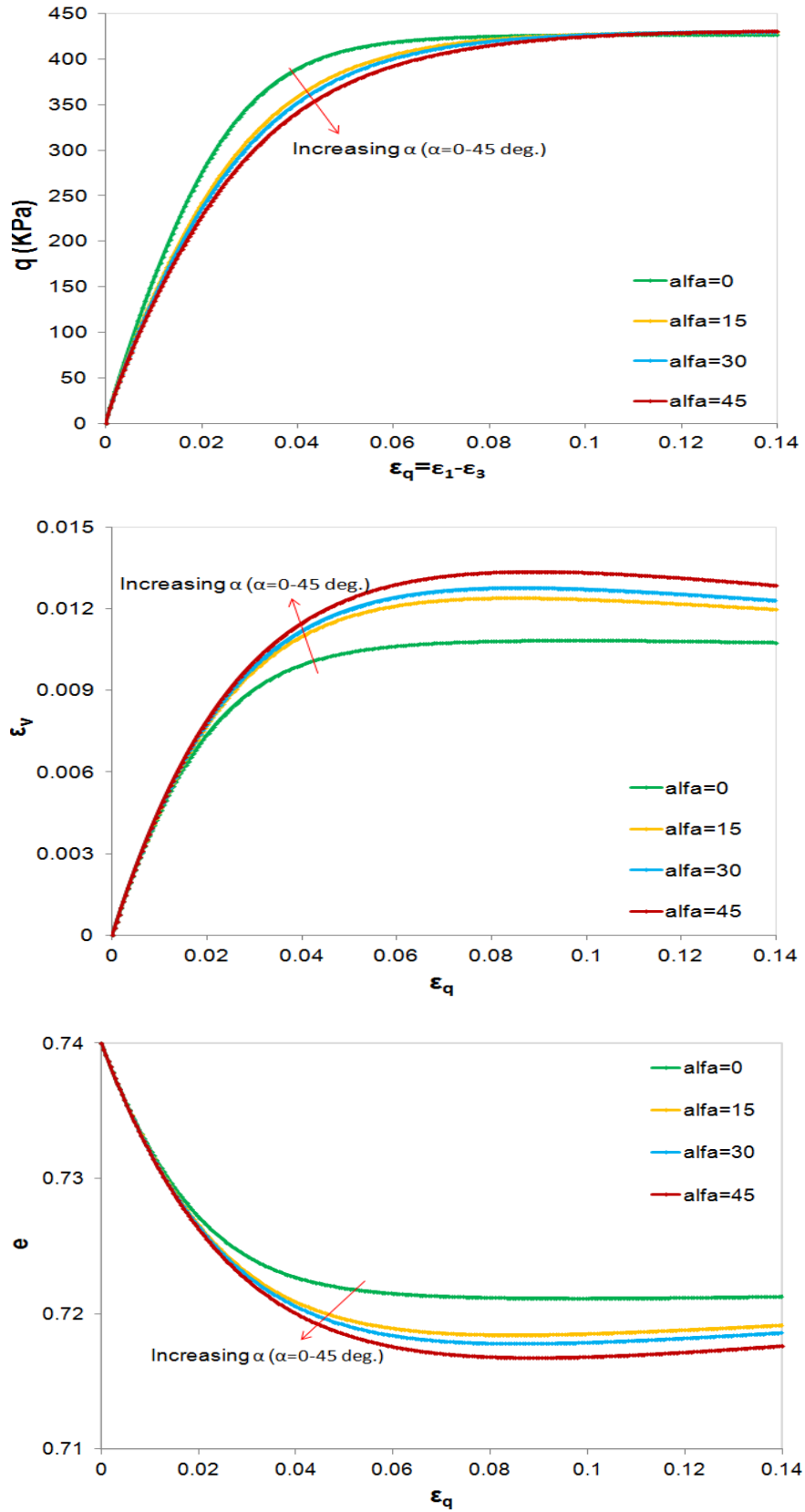


Fig. 6-24 Sensitivity analysis for a cemented sand under HC tests with $b = 0.25$

Results of sensitivity analysis in Fig. 6-23 reveal that the stiffness of cemented sand decreases with increasing the value of b , implying that TC and TE have the greatest and the lowest stiffness, respectively. Unlike stiffness, the tendency for contraction increases with increasing value of b which means TC and TE have the lowest and the highest tendency for contraction. This implies that the greater positive pore pressure will develop under undrained conditions for higher values of b leading to smaller resistant against liquefaction. These conclusions suggest that TC and TE, two extreme modes of shearing, are the strongest and the weakest modes of shearing, correspondingly, for identical conditions. This is in line with the literature [Imam 1999, Li and Dafalias 2002, Wan and Guo 2004, Gao and Zhao 2012].

Sensitivity analysis results in Fig. 6-24 show that the stiffness of weakly cemented sand in a given value of b decreases with increasing the value of α . Unlike stiffness, the tendency for contraction increases with increasing value of α . This implies that the greater positive pore pressure will develop under undrained conditions for higher values of α which result in smaller resistant against liquefaction. This is in accordance with the literature [Wan and Guo 2001b, Gao and Zhao 2012]. That is, most contact normals are oriented in the vertical direction when the bedding plane is horizontal (i.e. deposition direction is vertical) which causes the specimen to be strong. However when the bedding plane is vertical (i.e. deposition direction is horizontal), most contact normals are oriented horizontally which causes the specimen to be weak in vertical direction [Wan and Guo 2001b, Wan and Guo 2004].

Figs. 6-25 to 6-26 show model predictions for hypothetical cyclic HC tests on the same weakly cemented sand. In addition to material parameters listed in Table 6-2, cyclic loading related material parameters were chosen in this sensitivity analysis as follows:

$$c_1 = 5e6, c_2 = 500, R_u = 3$$

It was also assumed that the specimens were consolidated isotropically to pressure equals to 200 kpa and void ratio equals to 0.74 before they being sheared similar to monotonic HC tests on the same weakly cemented sand.

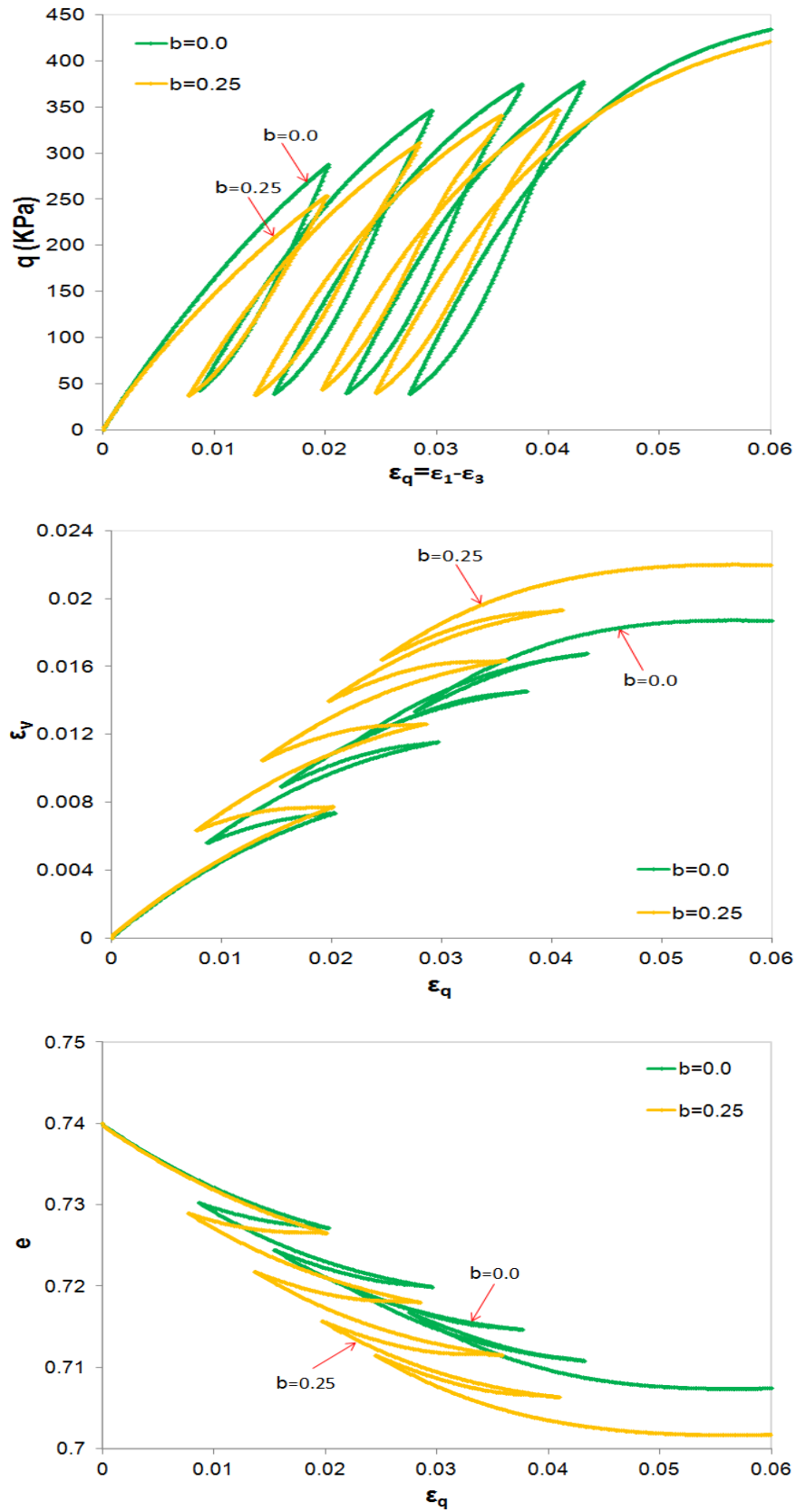


Fig. 6-25 Sensitivity analysis for cyclic HC tests with $\alpha = 0$ and $b = 0$ & 0.25

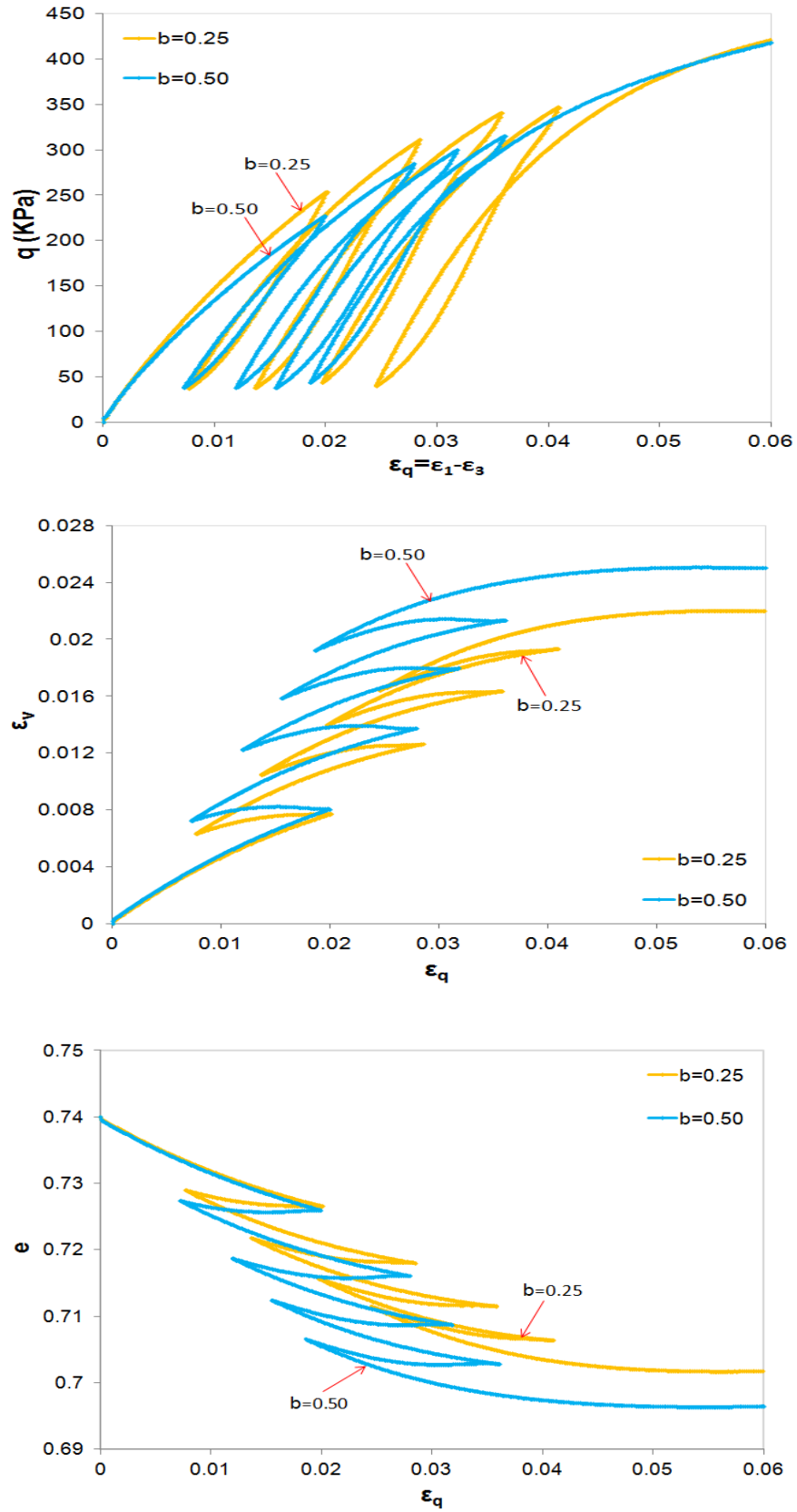


Fig. 6-26 Sensitivity analysis for cyclic HC tests with $\alpha = 0$ and $b = 0.25$ & 0.5

Fig. 6-27 shows cohesion degradation during hypothetical cyclic HC test with $b = 0$ in Fig. 6-25. About 50% of total degradation (i.e. about 2000 Pa) occurs during cycle of unloading-reloading. This means if conventional plasticity is used, cohesion degradation will be underestimated by about 50% since no plastic deformation is calculated by classical plasticity during cycle of unloading-reloading. Cohesion degradation during unloading-reloading cycle depends profoundly on unloading plastic modulus in the proposed constitutive model. Thus for other cases where $R_u > 3$, say $R_u = 15$, contribution of unloading-reloading cycles in total cohesion degradation is significantly much smaller than this case. However even small cohesion degradation during unloading-reloading will affect predicted outcomes because it will accumulate during successive cycles. Therefore it is required to record plastic deformation for stress paths inside the yield surface during cycles of unloading-reloading.

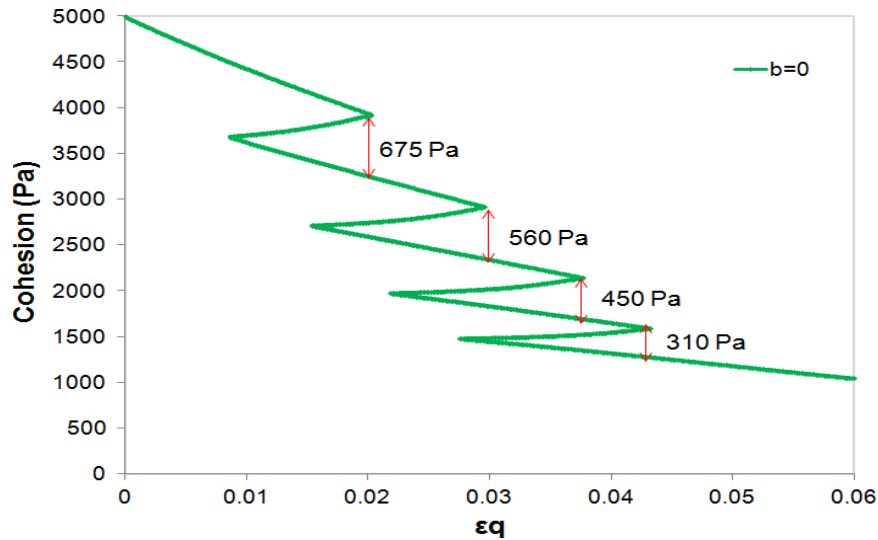


Fig. 6-27 Cohesion degradation during cyclic HC test with $\alpha = 0$ and $b = 0$

6.6 Conclusion

The overall response of cemented sand depends not only on the cementation bonds between sand particles, but also on fabric which reflect particle orientation and particle contact arrangements. Therefore the fabric as an influential parameter should be incorporated into constitutive model in order to accurately capture mechanical behavior of sand/cemented sand under various shearing/deformation

conditions. Thus fabric was incorporated into the model using a fabric tensor which represents material inherent anisotropy and a scalar-valued state variable which describe the material anisotropic state. To account for different modes of shearing, b -parameter was also integrated into formulation of the model. Performance of the modified model was examined against HC monotonic tests on Toyoura sand. Model predictions are in reasonable agreements with experimental observations. The model was also used to predict behaviour of a weakly cemented sand under cyclic HC tests with different values of b and α . Model predictions show that stiffness of cemented sand decreases and tendency for contraction increases with increasing value of b under a given α or with increasing value of α under a given value of b . These observations suggest that TC ($b = 0, \alpha = 0$) and TE ($b = 1, \alpha = 90$), two extreme modes of shearing, are the strongest and the weakest modes of shearing, respectively.

6.7 References

- Cai, Y. (2010), An experimental study of non-coaxial soil behaviour using hollow cylinder testing, Ph.D. thesis, The University of Nottingham, Nottingham, U.K.
- Gao, Z., and Zhao, J. (2012), Constitutive modeling of artificially cemented sand by considering fabric anisotropy, *Computers and Geotechnics*, Vol. 41, pp. 57-69.
- Jefferies, M.G. (1993), Nor-Sand: a simple critical state model for sand, *Géotechnique*, Vol. 43, No. 1, pp. 91-103.
- Imam, M.R. (1999), Modeling the constitutive behaviour of sand for the analysis of static liquefaction, Ph.D. thesis, The University of Alberta, Edmonton, Canada.
- Imam, R., Rasouli, R. (2010), Introduction of inherent anisotropy into a critical-state constitutive model for sands, proceedings of the 63rd Canadian Geotechnical Conference, Calgary, Canada. pp. 168-175.
- Li, X.S. (2005), Calibration of an anisotropic sand model, In Proceedings from GeoFrontiers: Calibration of Constitutive Models, ASCE, Austin, pp. 1-12.
- Li, X.S., and Dafalias, Y.F. (2002), Constitutive modeling of inherently anisotropic sand behaviour, *Journal of Geotechnical and GeoEnvironmental Engineering*, Vol. 128, No. 10, pp. 868-880.
- Manzari, M.T., and Dafalias, Y. F. (1997), A critical state two-surface plasticity model for sands, *Géotechnique*, Vol. 47, No. 2, pp. 255-272.

Oda, M. and Nakayama, H. (1989), Yield function for soil with anisotropic fabric, *Journal of Engineering Mechanics*, Vol. 115, No. 1, pp. 89-104.

Rasouli, R. (2010), Modelling of anisotropic behaviour of sands, M.Sc. thesis, Amir Kabir University of technology, Tehran, Iran.

Wan, R.G., and Guo, P.J. (2001a), Drained cyclic behavior of sand with fabric dependence, *Journal of Engineering Mechanics*, Vol. 127, No. 11, pp. 1106-1116.

Wan, R.G., and Guo, P.J. (2001b), Effect of microstructure on undrained behaviour of sands, *Canadian Geotechnical Journal*, Vol. 38, No. 1, pp. 16-28.

Wan, R.G., and Guo, P.J. (2004), Stress dilatancy and fabric dependencies on sand behavior, *Journal of Engineering Mechanics*, Vol. 130, No. 6, pp. 635-645.

Yoshimine, M., Ishihara, K., and Vargas, W. (1998), Effects of principal stress direction and intermediate principal stress on undrained shear behaviour of sand, *Soils and Foundations*, Vol. 38, No. 3, pp. 179–188.

CHAPTER 7

CONCLUSIONS

7.1 Summary and conclusions

1-D analysis has been chosen as the first step for embarking this research. Familiarity with elasto-plastic constitutive modelling has been the goal. The classical constitutive model has been implemented first for monotonic loading using Drucker-Prager and Mohr-Coulomb yield functions. Perfectly plastic and isotropic hardening have been applied for both associated and non-associated flow rule. Results of the model also have been verified against closed form solution (see appendix A.1). Then, pure kinematic hardening has been implemented using Prager and Ziegler's linear kinematic hardening laws and Armstrong and Frederick's non linear kinematic hardening law. Armstrong and Frederick's kinematic hardening rule has been utilized to calibrate cyclic triaxial compression tests under a pure kinematic hardening scheme. Reasonable agreements between predicted outcomes and experimental observations have been obtained (see appendix A.2).

In the next stage, a critical state constitutive model developed in the University of Alberta has been chosen as the base model. The model originally was created for cohesionless sands. The original model has been initially formulated within the two-surface plasticity theory for cohesionless sand under cyclic loading. The proposed two-surface model has been successfully calibrated and validated against triaxial cyclic compression tests using single set of model parameters for samples of identical sand type. The main features of sand behavior under cyclic loading have been captured relatively good. The greatest difficulty in two-way cyclic modeling arises as the first phase transformation occurs (i.e. the cyclic liquefaction in loose sands). The pore pressure increment has been underestimated in the post liquefaction phase. Therefore, some modifications in

the constitutive modeling of the post liquefaction phase are needed. The pore pressure and plastic hardening modulus are two potential candidates in this regard, for instance, a smaller plastic hardening modulus will produce a softer behavior and thus, the greater plastic deformation. An additional term can also be considered for the pore pressure increment in the post liquefaction phase to compensate the underestimation of the pore pressure. This term can be obtained by conducting the experimental observations.

To model the mechanical behaviour of cemented sands, the original constitutive model has been modified by change in the yield function, elastic moduli, the plastic hardening modulus, and flow rule. Then, it has been formulated according to the radial mapping formulation of the bounding surface plasticity theory. The proposed model has been examined against triaxial tests of two various artificially cemented sands under different void ratios and confining pressures. A notable deficiency of the model was the prediction of the strain softening. It was found that change of the flow rule not only affects the volumetric response, but it also affects the deviator stress-strain response. That is, more acceptable agreements for the deviator stress-strain curves were attained with incorporation of the flow rule of the original model. However, this decision led to significant deviation of the predicted volumetric behavior from that of the experiment. Therefore the application of an alternative flow rule, instead of the original or modified stress-dilatancy relationship, can result in better predictions by the model.

To model degradation of weakly cemented sandstone under (slow) cyclic loading, the proposed model for soft sandstone has been further modified by changing unloading plastic and elastic moduli. The proposed mixed bounding surface model has been assessed against triaxial monotonic and cyclic tests with fair accuracy. The hysteresis loops have been replicated qualitatively fair as well.

To simulate non-conventional triaxial tests, inherent fabric anisotropy and b -parameter have been incorporated into formulation of the constitutive model. This has been done by changing the formula of M_p and $\sin \varphi_p$. The modified model has been calibrated and validated against undrained HC tests on Toyoura sand.

Sensitivity analysis has been carried out under monotonic and cyclic HC tests on a poorly cemented sand as well.

The introduced model, ultimately, has been generalized into general stress space (see appendix B).

In summary, the proposed critical state bounding surface model implements simultaneously the concept of critical state, state parameter, kinematic hardening, material cohesion, non-associated flow rule, and inherent fabric anisotropy. This is a distinctive feature of this constitutive model compared to other similar models based on the bounding surface plasticity theory.

7.2 Recommendations

In accordance with the current research, the following future works are recommended:

- Incorporation of a new stress-dilatancy relationship for the cemented sand is the most pioneer need for the proposed constitutive model. This is important because modification of the flow rule affects not only the volumetric behavior, but also strain softening. The current stress-dilatancy relationship may not provide good predictions for volumetric behavior in some situations. The introduction of a new stress-dilatancy relationship appropriate for cemented sand/soft sandstone, however, requires extensive stress-dilatancy database for different cemented sands or soft sandstone.
- Further application of the proposed model requires the model to be calibrated against two-way cyclic loading tests of cemented sand (which are rare in the literature if they exist at all). Modification of the unloading elastic moduli may be needed so that the model can be used for two-way cyclic loading tests of cemented sand too.
- Modification of the elasticity laws to incorporate anisotropic elasticity. The presence of the bedding leads to different elastic moduli in the horizontal and vertical directions. Five elastic parameters are required to describe elastic behavior of a material with transverse isotropy.

- It is known for sand that there is linear relationship between the peak of UESP and the maximum consolidation pressure. It is assumed here that this is correct for cemented sand too. To evaluate this assumption, conducting undrained triaxial tests is recommended for cemented sand.
- Incorporation of the thermal strain-stress in the constitutive relationship results in more realistic predictions of the rock degradation under operational conditions. This can be especially influential in the case of a cold or very hot fluid injection into the reservoir which changes the geothermal gradient of the reservoir.
- Incorporation of the weakening effect of injected fluid (especially water) on the soft rock strength. This can be done by making the cementation destruction as a function of both the plastic strain and the chemical reactions due to incompatibility of the injected and reservoir fluids. The chemical reaction related parameter may be chosen as a function of the water saturation or water cut. Conducting experimental compressive tests under different water saturations or water contents is recommended in this regard.
- Extension of the current work to a coupled flow-deformation analysis. In most general case, a thermal-hydro-chemical-mechanical model can be created to incorporate influential factors in all geomechanics problems.
- To resemble changes of the deviator stress and strength of soft sandstone under cyclic conditions, an experimental study is recommended. During the tests, water pressure at the center of the specimen should be cycled slowly, for instance between anticipated maximum and minimum values. After a certain number of cycles, the specimen can be put under monotonic compression test to estimate strength change due to repeated changes of the mean effective stress. Conducting conventional and true triaxial cyclic compression and extension tests on soft sandstone by cycling the axial stress/strain and confining stress/strain is also recommended. Cyclic compression and extension tests under constant p or constant q stress path can be useful as well.

APPENDIX A

1D ANALYSIS OF CLASSICAL ELASTO-PLASTIC CONSTITUTIVE MODEL

If uniform/homogeneous deformation field is assumed in the sample, each numerical node will be a representative of the overall behavior of the sample. Elasto-plastic formulas are solved in this appendix for one node by assumption of uniform deformation.

A.1 Isotropic Hardening

A.1.1 Elasticity

The well known Hook's isotropic linear elasticity law is adopted to simulate the small deformation elasticity as follows:

$$\varepsilon_{zz}^e = \frac{\sigma_{zz}}{E} - \frac{\nu}{E}(\sigma_{yy} + \sigma_{xx}) \quad (A.1)$$

$$\varepsilon_{yy}^e = \frac{\sigma_{yy}}{E} - \frac{\nu}{E}(\sigma_{xx} + \sigma_{zz}) \quad (A.2)$$

$$\varepsilon_{xx}^e = \frac{\sigma_{xx}}{E} - \frac{\nu}{E}(\sigma_{yy} + \sigma_{zz}) \quad (A.3)$$

For strain controlled approach and triaxial condition, the elastic stiffness matrix is written as:

$$[\underline{C}^E] = \frac{E}{(1+\nu)(1-2\nu)} \begin{bmatrix} 1-\nu & \nu & \nu \\ \nu & 1-\nu & \nu \\ \nu & \nu & 1-\nu \end{bmatrix} \quad (A.4)$$

E is Young's modulus and ν is Poisson's ratio. If one chooses the bulk modulus and shear modulus as elastic material parameters, components of the elastic constitutive matrix change correspondingly. These elastic parameters are interrelated by:

$$E = 2G(1+\nu) = 3K(1-2\nu) \quad (A.5)$$

A.1.2 Yield function

A.1.2.1 Drucker-Prager

The General form of the Drucker-Prager yield function is express as:

$$J_2 - A_{DP} + B_{DP}I_1 = 0 \quad (A.6)$$

Where J_2 is the second invariant of the deviator stress tensor, I_1 is the first invariant of the stress tensor, and A_{DP} and B_{DP} are function of friction angle and cohesion. The Drucker-Prager yield function is written in terms of mean effective stress p and deviator stress q as follows:

$$f = 3\alpha_{DP}p + \frac{q}{\sqrt{3}} - k_{DP} = 0 \quad (A.7)$$

$$\alpha_{DP} = \frac{\sin\varphi}{\sqrt{3}(3 + \sin^2\varphi)^{\frac{1}{2}}} \quad k_{DP} = \frac{\sqrt{3} c \cos\varphi}{(3 + \sin^2\varphi)^{\frac{1}{2}}} \quad (A.8)$$

where c is cohesion, φ is friction angle and θ is load angle whose magnitude defines orientation of stress state within the principal stress space.

This version of the Drucker-Prager yield function was found to be numerically unstable. Hence, alternative forms of α_{DP} and k_{DP} were used. For the version that circumscribes the Mohr-Coulomb yield surface:

$$\alpha_{DP} = \frac{2\sin\varphi}{\sqrt{3}(3 + \sin\varphi)} \quad k_{DP} = \frac{6 c \cos\varphi}{\sqrt{3}(3 + \sin\varphi)} \quad (A.9)$$

And for the version that inscribes the Mohr-Coulomb yield surface:

$$\alpha_{DP} = \frac{2\sin\varphi}{\sqrt{3}(3 - \sin\varphi)} \quad k_{DP} = \frac{6 c \cos\varphi}{\sqrt{3}(3 - \sin\varphi)} \quad (A.10)$$

The version that inscribes the Mohr-Coulomb yield surface produced the closer outcomes compared to the Mohr-Coulomb yield criterion.

A.1.2.2 Mohr-Coulomb

The Mohr-Coulomb yield criterion was the based yield criterion in the analysis.

$$f = p\sin\varphi + \frac{q}{\sqrt{3}}\cos\theta - \frac{q}{3}\sin\theta\sin\varphi - c \cos\varphi = 0 \quad (A.11)$$

$$\frac{-\pi}{6} \leq \theta = \frac{1}{3} \sin^{-1} \left(\frac{-27}{2} \frac{\det[s_{ij}]}{q^3} \right) \leq \frac{\pi}{6} \quad (\text{A.12})$$

$$\det \underline{S} = \det [s_{ij}] = \det \begin{bmatrix} \sigma_{zz} - p & \sigma_{zy} & \sigma_{zx} \\ \sigma_{zy} & \sigma_{yy} - p & \sigma_{yx} \\ \sigma_{zx} & \sigma_{yx} & \sigma_{xx} - p \end{bmatrix} \quad (\text{A.13})$$

$\det \underline{S}$ is determinant of the deviator stress tensor.

A.1.3 Plastic potential function

$$g = p \sin \psi + \frac{q}{\sqrt{3}} \cos \theta - \frac{q}{3} \sin \theta \sin \psi - c \cos \psi = 0 \quad (\text{A.14})$$

ψ is dilation angle which implies shear induced volume change [Saada et. al. 1999]. Dilation angle is always less than the friction angle (i.e. non-associated flow rule) or equal to the friction angle (i.e. associated flow rule). The last term in definition of the plastic potential function has no effect on outcomes because only the gradient of the potential function is used in the constitutive modeling.

Vermeer and Borst (1984) analyzed various rock samples and concluded that the dilation angle is at least 20 degrees less than the friction angle. It has been suggested also that the dilation angle is a quarter of the friction angle for good quality rock and zero for poor rock [Alejano and Alonso 2005]. Choosing a value of zero for the dilation angle in non-associated flow rule is common in rock mechanics while it can be any value, but less than the friction angle. The smaller confining stress results in the greater dilation angle and the greater confining stress leads to the smaller dilation angle (even negative). The reason is that the dilation is suppressed at high confining stress and a ductile response usually occurs instead of a brittle response.

The dilation angle is in relation to the plastic volumetric strain increment. For instance, a zero dilation angle results in a zero plastic volumetric strain increment and vice versa according to the following formula [Vermeer and Borst 1984]:

$$\sin \psi = \frac{\dot{\varepsilon}_{zz}^p + \dot{\varepsilon}_{yy}^p + \dot{\varepsilon}_{xx}^p}{\dot{\varepsilon}_{zz}^p - \dot{\varepsilon}_{xx}^p} \quad (\text{A.15})$$

The dilation angle can be evaluated using the mobilized friction angle as well [Vermeer and Borst 1984]:

$$\sin \psi_m = \frac{\sin \varphi_m - \sin \psi_{cv}}{1 - \sin \varphi_m \sin \psi_{cv}} \quad (A.16)$$

ψ_m and φ_m are mobilized dilation and mobilized friction angle. ψ_{cv} is constant volume dilation angle which is a model parameter.

A.1.4 Hardening law

Hardening parameters were assumed to change by plastic deviator strain. Linear isotropic hardening rule was selected for simplicity. Figs. A1-1 and A1-2 show schematic representation of the chosen isotropic hardening.

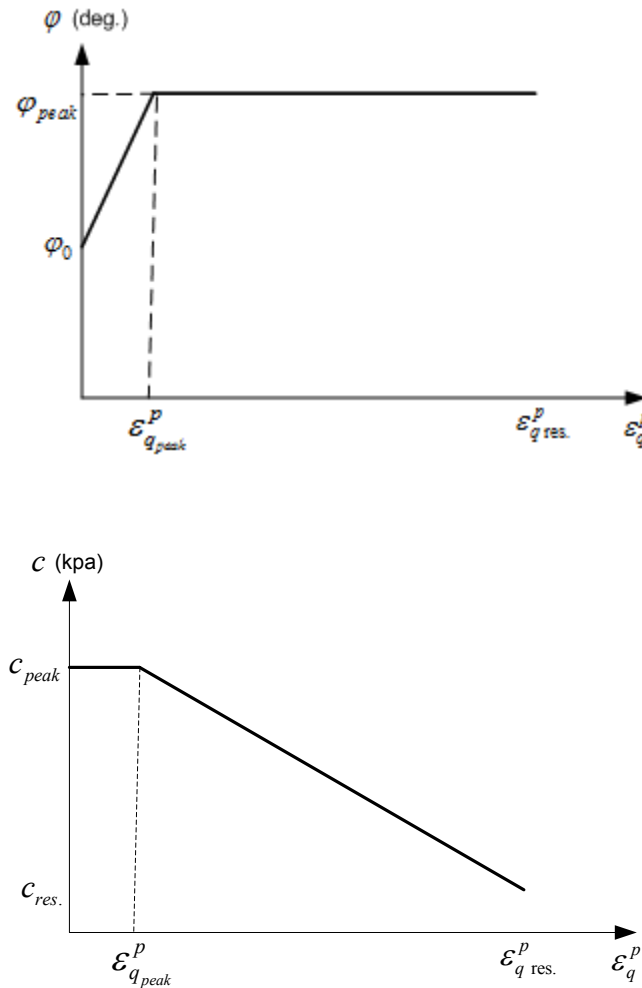


Fig. A1-1 Linear isotropic deviator hardening law

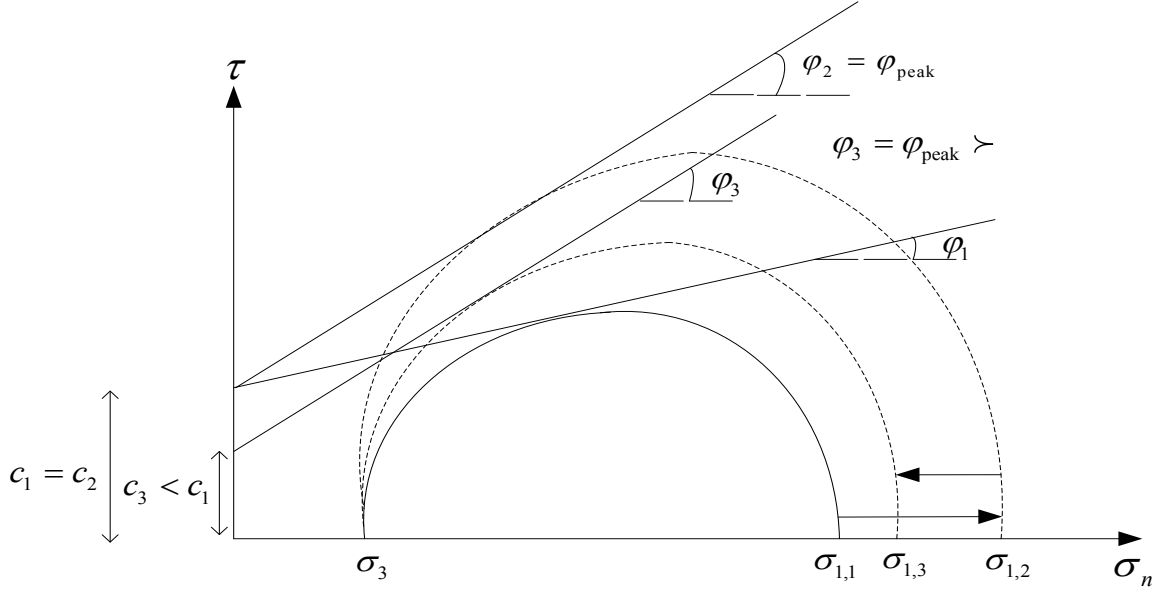


Fig. A1-2 Schematic representation of isotropic hardening with friction angle and cohesion as hardening parameters

A.1.5 Stress-strain relationships

The general stress-strain formula for elasto-plastic analysis is written as:

$$\dot{\sigma}_{ij}^{EP} = C_{ijkl}^{EP} \dot{\epsilon}_{kl} \quad (A.17)$$

By starting from the assumption that change in stress is due to change in elastic strain only, we ultimately arrive at the following formula which is used typically in conventional elasto-plastic analysis.

$$\dot{\sigma}_{ij}^{EP} = (C_{ijmn}^E - C_{ijmn}^P) \dot{\epsilon}_{mn} \quad (A.18)$$

$$C_{ijmn}^P = \frac{C_{ijkl}^E \frac{\partial g}{\partial \sigma_{kl}} \frac{\partial f}{\partial \sigma_{\alpha\beta}} C_{\alpha\beta mn}^E}{H} \quad (A.19)$$

$$H = -\frac{\partial f}{\partial \epsilon_{ij}^p} \cdot \frac{\partial g}{\partial \sigma_{ij}} + \frac{\partial f}{\partial \sigma_{ij}} C_{ijkl}^E \frac{\partial g}{\partial \sigma_{kl}} \quad (A.20)$$

where f , g and H are the yield function, the plastic potential function and the plastic hardening modulus. The first term of H is called strain hardening/softening term (h) and the second is called perfectly plastic term. The strain hardening

occurs if $h > 0$. The strain softening takes place if $h < 0$. There is perfectly plastic response if $h = 0$.

The plastic modulus can be calculated using one of the following forms depends on how the consistency condition is defined.

a) Conventional form:

$$H = - \sum_{n=1}^m \frac{\partial f}{\partial N_n} \frac{\partial N_n}{\partial \varepsilon_{ij}^p} \frac{\partial g}{\partial \sigma_{ij}} + \frac{\partial f}{\partial \sigma_{ij}} C_{ijkl}^E \frac{\partial g}{\partial \sigma_{kl}} \quad df(\sigma_{ij}, \varepsilon_{ij}^p) = 0 \quad (A.21)$$

b) Conventional triaxial (p, q) space:

$$H = - \sum_{n=1}^m \frac{\partial f}{\partial N_n} \left(\frac{\partial N_n}{\partial \varepsilon_p^p} \frac{\partial g}{\partial p} + \frac{\partial N_n}{\partial \varepsilon_q^p} \frac{\partial g}{\partial q} \right) \quad df(p, q, \varepsilon_p^p, \varepsilon_q^p) = 0 \quad (A.22)$$

c) Combination of the two first forms:

$$H = - \sum_{n=1}^m \frac{\partial f}{\partial N_n} \left(\frac{\partial N_n}{\partial \varepsilon_p^p} \frac{\partial g}{\partial p} + \frac{\partial N_n}{\partial \varepsilon_q^p} \frac{\partial g}{\partial q} \right) + \frac{\partial f}{\partial \sigma_{ij}} C_{ijkl}^E \frac{\partial g}{\partial \sigma_{kl}} \quad df(\sigma_{ij}, \varepsilon_p^p, \varepsilon_q^p) = 0 \quad (A.23)$$

N is hardening parameter and m is number of hardening parameters.

The third form was adopted in this study in which:

$$p = \frac{\sigma_{zz} + \sigma_{yy} + \sigma_{xx}}{3} \quad (A.24)$$

$$q = \sqrt{3J_2} \quad (A.25)$$

$$J_2 = \frac{(\sigma_{zz} - \sigma_{yy})^2 + (\sigma_{zz} - \sigma_{xx})^2 + (\sigma_{yy} - \sigma_{xx})^2}{6} + \sigma_{zy}^2 + \sigma_{zx}^2 + \sigma_{yx}^2 \quad (A.26)$$

$$\varepsilon_v = \varepsilon_{zz} + \varepsilon_{yy} + \varepsilon_{xx} \quad (A.27)$$

$$\varepsilon_q = \frac{1}{3} \sqrt{2 \left\{ (\varepsilon_{zz} - \varepsilon_{yy})^2 + (\varepsilon_{zz} - \varepsilon_{xx})^2 + (\varepsilon_{yy} - \varepsilon_{xx})^2 \right\} + 3 \{ \gamma_{zy}^2 + \gamma_{zx}^2 + \gamma_{yx}^2 \}} \quad (A.28)$$

Incremental form of p , q , ε_v and ε_q is defined similarly.

Cohesion and friction angle (and dilation angle for non-associated model) were considered as hardening parameters.

The following relationship was also derived for triaxial conditions:

$$\dot{\varepsilon}_{33} = \frac{\left(\frac{\nu E}{(1+\nu)(1-2\nu)} - C_{3311}^P \right)}{C_{3322}^P + C_{3333}^P - \frac{E}{(1+\nu)(1-2\nu)}} \dot{\varepsilon}_{11} \quad (\text{A. 29})$$

Components of the plastic strain tensor are obtained by the flow rule:

$$\varepsilon_{ij}^p = \lambda_{fr} \frac{\partial g}{\partial \sigma_{ij}} \quad \lambda_{fr} = \frac{df}{H} = \frac{\frac{\partial f}{\partial \sigma_{ij}} C_{ijkl}^E \dot{\varepsilon}_{kl}}{H} \quad (\text{A. 30})$$

Components of the elastic strain tensor are calculated using adopted elasticity law.

The following relationships were also derived in study of the triaxial conditions:

$$\frac{\partial f}{\partial p} = \sin\varphi \quad (\text{A. 31})$$

$$\frac{\partial f}{\partial q} = \frac{\cos\theta}{\sqrt{3}} - \frac{\sin\theta \sin\varphi}{3} \quad (\text{A. 32})$$

$$\frac{\partial f}{\partial \varphi} = p \cos\varphi - \frac{q}{3} \sin\theta \cos\varphi + c \sin\varphi \quad (\text{A. 33})$$

$$\frac{\partial f}{\partial \theta} = \frac{-q}{\sqrt{3}} \sin\theta - \frac{q}{3} \sin\varphi \cos\theta \quad (\text{A. 34})$$

$$\frac{\partial p}{\partial \sigma_{zz}} = \frac{\partial p}{\partial \sigma_{yy}} = \frac{\partial p}{\partial \sigma_{xx}} = \frac{1}{3} \quad (\text{A. 35})$$

$$\frac{\partial q}{\partial \sigma_{zz}} = \frac{(\sigma_{zz} - \sigma_{xx})}{q} \quad (\text{A. 36})$$

$$\frac{\partial q}{\partial \sigma_{yy}} = \frac{(\sigma_{yy} - \sigma_{zz})}{2q} \quad (\text{A. 37})$$

$$\frac{\partial q}{\partial \sigma_{xx}} = \frac{(\sigma_{xx} - \sigma_{zz})}{2q} \quad (\text{A. 38})$$

$$\frac{\partial f}{\partial \sigma_{ij}} = \frac{\partial f}{\partial p} \cdot \frac{\partial p}{\partial \sigma_{ij}} + \frac{\partial f}{\partial q} \cdot \frac{\partial q}{\partial \sigma_{ij}} + \frac{\partial f}{\partial \theta} \cdot \frac{\partial \theta}{\partial \sigma_{ij}} \quad (\text{A.39})$$

$$\frac{\partial p}{\partial \sigma_{ij}} = 0 \quad \frac{\partial q}{\partial \sigma_{ij}} = \frac{3}{q} \sigma_{ij} = 0 \quad \text{if } i \neq j \quad (\text{A.40})$$

$$\frac{\partial \theta}{\partial \sigma_{ij}} = \frac{9}{2 \cos(3\theta) q^3} \left(\frac{3 \det \underline{S}}{q} \frac{\partial q}{\partial \sigma_{ij}} - \frac{\partial \det \underline{S}}{\partial \sigma_{ij}} \right) \quad (\text{A.41})$$

$$\frac{\partial \det \underline{S}}{\partial \sigma_{ij}} = -2 \sigma_{ij} (\sigma_{kk} - p) + 2 \sigma_{ki} \sigma_{kj} \quad k \neq i, j \quad (\text{if } i \neq j) \quad (\text{A.42})$$

$$\frac{\partial \det \underline{S}}{\partial \sigma_{ij}} = 0 \quad \frac{\partial \theta}{\partial \sigma_{ij}} = 0 \quad \frac{\partial f}{\partial \sigma_{ij}} = 0 \quad (\text{if } i \neq j) \quad (\text{A.43})$$

$$\frac{\partial \det \underline{S}}{\partial \sigma_{zz}} = \frac{2}{3} (\sigma_{yy} - p) (\sigma_{xx} - p) - \frac{1}{3} (\sigma_{zz} - p) (\sigma_{xx} - p) - \frac{1}{3} (\sigma_{zz} - p) (\sigma_{yy} - p) \quad (\text{A.44})$$

$$\frac{\partial \det \underline{S}}{\partial \sigma_{yy}} = \frac{2}{3} (\sigma_{zz} - p) (\sigma_{xx} - p) - \frac{1}{3} (\sigma_{yy} - p) (\sigma_{xx} - p) - \frac{1}{3} (\sigma_{zz} - p) (\sigma_{yy} - p) \quad (\text{A.45})$$

$$\frac{\partial \det \underline{S}}{\partial \sigma_{xx}} = \frac{2}{3} (\sigma_{zz} - p) (\sigma_{yy} - p) - \frac{1}{3} (\sigma_{yy} - p) (\sigma_{xx} - p) - \frac{1}{3} (\sigma_{zz} - p) (\sigma_{xx} - p) \quad (\text{A.46})$$

A.1.6 Verification

Since the coordinate directions coincide with the principal directions in triaxial tests, the Mohr-Coulomb yield function in the principal space was used to verify results of the model. The following relationship is easily obtained from the Mohr circles (Fig. A1-3):

$$f = \frac{\sigma_3 - \sigma_1}{2} + \frac{\sigma_1 + \sigma_3}{2} \sin \varphi + c \cos \varphi = 0 \quad (\text{A.47})$$

If the compression is considered negative (which is the case in this 1D model), then:

$$f = \frac{\sigma_3 - \sigma_1}{2} + \frac{\sigma_1 + \sigma_3}{2} \sin\varphi - c \cos\varphi = 0 \quad (A.48)$$

Comparison between calculated values of the constitutive model and those of the above formula verified accuracy of calculated yield axial stresses at different cohesions and friction angles.

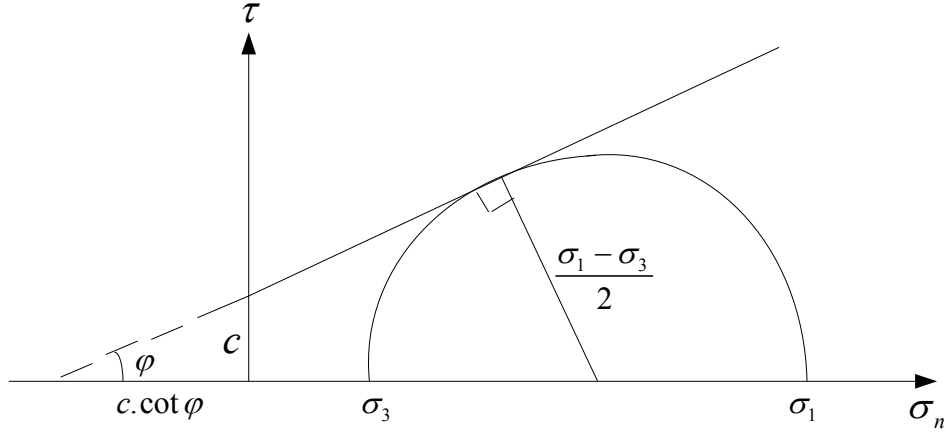


Fig. A1-3 The Mohr circle in $\tau - \sigma_n$ plane

A.1.7 Results

The proposed model has eight material parameters. The following properties were used in the study:

$$E = 200 \text{ Mpa}, \quad \nu = 0.25, \quad \varphi_0 = 20 \text{ deg}, \quad \varphi_{peak} = 40 \text{ deg}, \quad c = 500 \text{ kpa}, \\ c_{res.} = 20 \text{ kpa}, \quad \varepsilon_{q_{peak}}^p = 0.001, \quad \varepsilon_{q_{res.}}^p = 0.101$$

The dilation angle was assumed to be twenty degrees less than the friction angle for simplicity. Figs. A1-4 to A1-8 show model results for conventional drained triaxial compression test with confining stress equals to 500 kpa. Figs. A1-7 to A1-8 imply that the shear induced volume expansion has been suppressed in non-associated flow rule compared to associated flow rule.

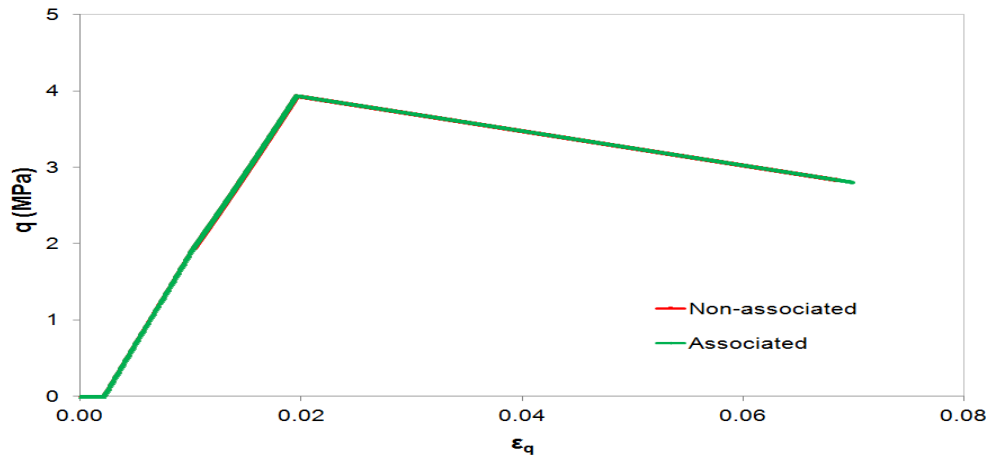


Fig. A1-4 Deviator stress vs. deviator strain for hypothetical conventional drained triaxial compression test

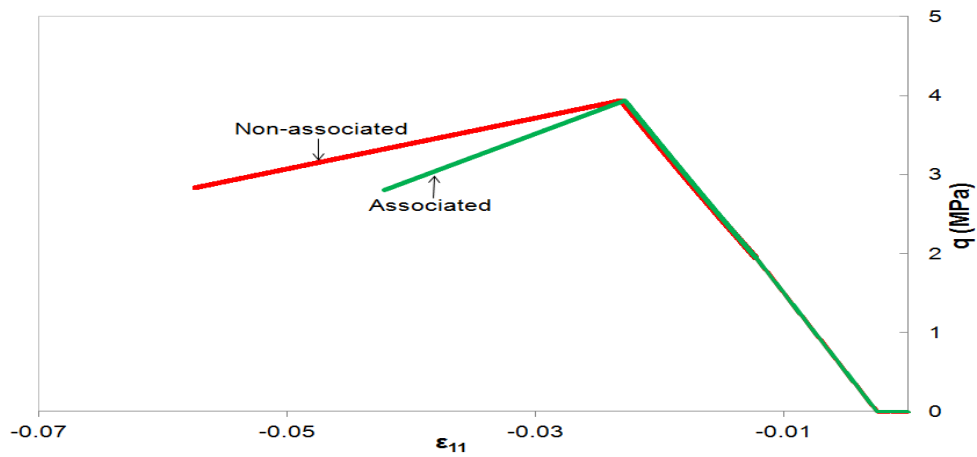


Fig. A1-5 Deviator stress vs. axial strain for hypothetical conventional drained triaxial compression test

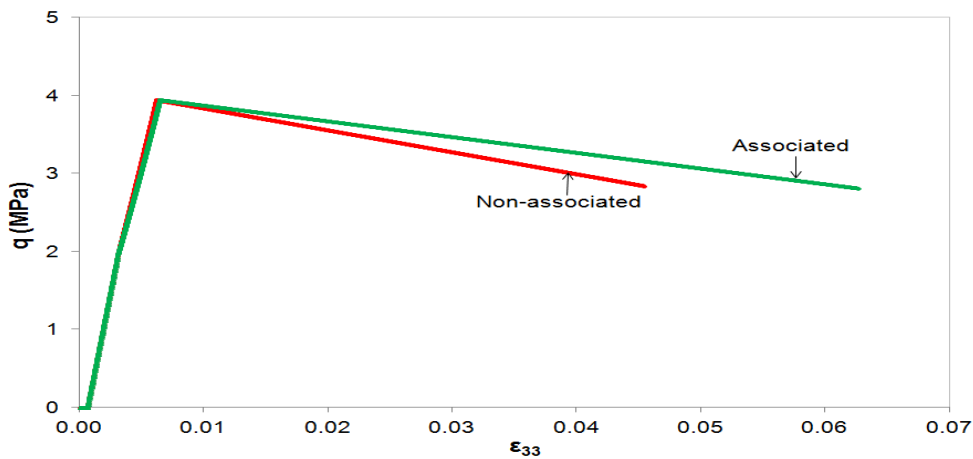


Fig. A1-6 Deviator stress vs. radial strain for hypothetical conventional drained triaxial compression test

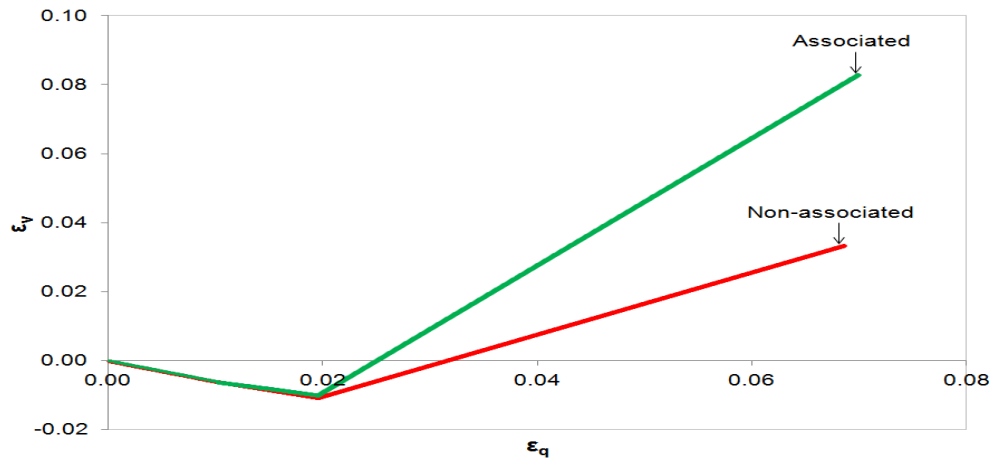


Fig. A1-7 Volumetric strain vs. deviator strain for hypothetical conventional drained triaxial compression test

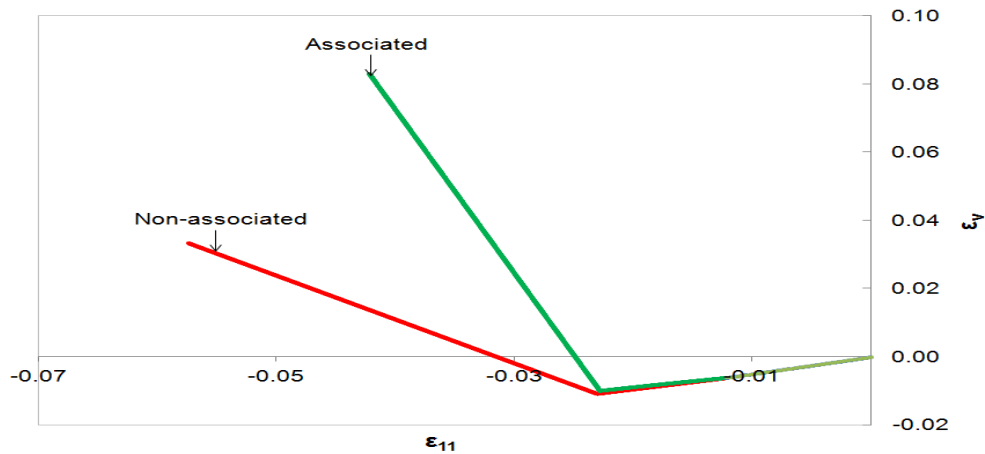


Fig. A1-8 Volumetric strain vs. axial strain for hypothetical conventional drained triaxial compression test

A.2 Kinematic Hardening

A.2.1 Elasticity

Linear isotropic elasticity (i.e. Hook's law) was adopted to govern the elastic behavior.

A.2.2 Yield function

The yield function was assumed to be of the Mohr-Coulomb type yield criterion as follows:

$$f = -|p - p_\alpha| \sin \varphi + \frac{|q - q_\alpha| \cos \theta}{\sqrt{3}} - \frac{|q - q_\alpha| \sin \theta \sin \varphi}{3} - c \cos \varphi = 0 \quad (\text{A.49})$$

in which

$$P_\alpha = \frac{\alpha_{zz} + \alpha_{yy} + \alpha_{xx}}{3} \quad (\text{A.50})$$

$$q_\alpha = \sqrt{\frac{(\alpha_{zz} - \alpha_{yy})^2 + (\alpha_{zz} - \alpha_{xx})^2 + (\alpha_{yy} - \alpha_{xx})^2}{2} + 3(\alpha_{zx}^2 + \alpha_{zy}^2 + \alpha_{yx}^2)} \quad (\text{A.51})$$

It is assumed that the coordinate directions of the stress tensor and those of the back stress tensor (p_α, q_α) coincide.

A.2.3 Plastic potential function

Associated flow rule was adopted in kinematic hardening models for simplicity.

A.2.4 Stress-strain relationships

The stress-strain relationships are written in a strain-controlled approach as follows:

$$[\dot{\sigma}] = \left([C^E] - \frac{[C^E] \left[\frac{\partial g}{\partial \sigma} \right] \left[\frac{\partial f}{\partial \sigma} \right]^T [C^E]}{H} \right) [\dot{\varepsilon}] \quad (\text{A.52})$$

For special case of triaxial conditions:

$$[\dot{\sigma}]_{3 \times 1} = \left([C^E]_{3 \times 3} - \frac{[C^E]_{3 \times 3} \left[\frac{\partial g}{\partial \sigma} \right]_{3 \times 1} \left[\frac{\partial f}{\partial \sigma} \right]_{1 \times 3}^T [C^E]_{3 \times 3}}{H} \right) [\dot{\varepsilon}]_{3 \times 1} \quad (\text{A.53})$$

The plastic modulus depends on type of adopted kinematic hardening law. H is calculated for the following kinematic hardening laws as follows:

A.2.4.1 Prager's rule

$$H = \left[\frac{\partial f}{\partial \sigma} \right]^T [C^E] \left[\frac{\partial g}{\partial \sigma} \right] - \left[\frac{\partial f}{\partial k} \right]^T h_a \left[\frac{\partial g}{\partial \sigma} \right] - \sum_{n=1}^N \left[\frac{\partial f}{\partial N_n} \right] \left[\frac{\partial N_n}{\partial \varepsilon^p} \right]^T \left[\frac{\partial g}{\partial \sigma} \right] \quad (A.54)$$

The first term represents the perfectly plastic behavior, the second term denotes the kinematic hardening behavior, and the third term signifies the strain hardening or softening response.

A.2.4.2 Armstrong and Frederick's rule

$$H = \left[\frac{\partial f^T}{\partial \sigma} \right] [C^E] \left[\frac{\partial g}{\partial \sigma} \right] - \left[\frac{\partial f^T}{\partial k} \right] \frac{2}{3} c_1 \left[\frac{\partial g}{\partial \sigma} \right] + \left[\frac{\partial f^T}{\partial k} \right] c_2 [k] \sqrt{\frac{2}{3}} \sqrt{\left[\frac{\partial g^T}{\partial \sigma} \right] \left[\frac{\partial g}{\partial \sigma} \right]} - \sum_{n=1}^N \left[\frac{\partial f}{\partial N_n} \right] \left[\frac{\partial N_n}{\partial \varepsilon^p} \right]^T \left[\frac{\partial g}{\partial \sigma} \right] \quad (A.55)$$

The first term represents the perfect plastic term. The second term indicates the linear kinematic hardening and the third term signifies non-linear kinematic hardening contribution in the plastic hardening modulus. The last term also denotes the isotropic size hardening of hardening parameter(s) due to plastic strain variations. Note that a pure kinematic hardening law was used for calibration of experimental data.

A.2.4.3 Ziegler's rule

Ziegler's kinematic hardening constant is calculated for (pure) kinematic hardening law as follows:

$$d\mu = \frac{-\frac{\partial f}{\partial \sigma_{ij}} \dot{\sigma}_{ij}}{\frac{\partial f}{\partial \alpha_{ij}} (\sigma_{ij} - k_{ij})} \quad (A.56)$$

There is no way to include kinematic hardening term in the plastic modulus definition since plastic strain has not been included directly in Ziegler's rule. The following formula for plastic strain was later proposed which is at the same form as that of Prager's rule [Yu 2006].

$$\dot{\varepsilon}_{ij}^p = \frac{1}{H} \frac{\frac{\partial g}{\partial \sigma_{ij}}}{\frac{\partial f}{\partial \sigma_{pq}} \frac{\partial g}{\partial \sigma_{pq}}} \frac{\partial f}{\partial \sigma_{kl}} \dot{\sigma}_{kl} \quad (\text{A.57})$$

H is the plastic modulus adopted as a material parameter for Ziegler kinematic hardening. Thus [Yu 2006],

$$\dot{\varepsilon}_{ij} = \dot{\varepsilon}_{ij}^e + \dot{\varepsilon}_{ij}^p = \left(D_{ijkl}^E + \frac{1}{k_p} \frac{\frac{\partial g}{\partial \sigma_{ij}}}{\frac{\partial f}{\partial \sigma_{pq}} \frac{\partial g}{\partial \sigma_{pq}}} \frac{\partial f}{\partial \sigma_{kl}} \right) \dot{\sigma}_{kl} = D_{ijkl}^{EP} \dot{\sigma}_{kl} \quad (\text{A.58})$$

The constitutive relationships can also be written in strain controlled approach using inverse of the elastoplastic compliance tensor as follows:

$$\dot{\sigma}_{ij} = [D_{ijkl}^{EP}]^{-1} \dot{\varepsilon}_{kl} = C_{ijkl}^{EP} \dot{\varepsilon}_{kl} \quad (\text{A.59})$$

A.2.4.4 Derivations

Some of derived formulas in the used pure kinematic Mohr-Coulomb model are as follows:

$$\frac{\partial f}{\partial p} = -\sin \varphi \frac{p - p_\alpha}{|p - p_\alpha|} \quad (\text{A.60})$$

$$\frac{\partial f}{\partial q} = \left(\frac{\cos \theta}{\sqrt{3}} - \frac{\sin \theta \sin \varphi}{3} \right) \left(\frac{q - q_\alpha}{|q - q_\alpha|} \right) \quad (\text{A.61})$$

$$\frac{\partial f}{\partial \varphi} = -|p - p_\alpha| \cos \varphi - \frac{|q - q_\alpha| \sin \theta \cos \varphi}{3} + c \sin \varphi \quad (\text{A.62})$$

$$\frac{\partial f}{\partial \theta} = \frac{-|q - q_\alpha| \sin \theta}{\sqrt{3}} - \frac{|q - q_\alpha| \sin \varphi \cos \theta}{3} \quad (\text{A.63})$$

Other derivations are similar to those for the isotropic hardening model mentioned in the appendix A.1. Also components of the unit normal to the yield surface are calculated by:

$$n_{ij} = \frac{\frac{\partial f}{\partial \sigma_{ij}}}{\sqrt{\left(\frac{\partial f}{\partial \sigma_{ij}}\right)^2 + \left(\frac{\partial f}{\partial \sigma_{ij}}\right)^2}} \quad (A.64)$$

They are obtained in conventional (p, q) space using the following formulas:

$$n_p = \frac{\frac{\partial f}{\partial P}}{\sqrt{\left(\frac{\partial f}{\partial P}\right)^2 + \left(\frac{\partial f}{\partial q}\right)^2}} \quad n_q = \frac{\frac{\partial f}{\partial q}}{\sqrt{\left(\frac{\partial f}{\partial P}\right)^2 + \left(\frac{\partial f}{\partial q}\right)^2}} \quad (A.65)$$

Note that even after forcing stress state to remain on subsequent yield surfaces, still there is likelihood for small deviation from the consistency condition. This deviation can accumulate during subsequent time steps. To fully satisfy the consistency condition, the radial stress return method was implemented in the constitutive modelling as follows:

$$\sigma_{ij}^{corrected} = \sigma_{ij} + \lambda_R \frac{\partial f}{\partial \sigma_{ij}} \quad \lambda_R = \mp f(\sigma_{ij}) / \frac{\partial f}{\partial \sigma_{ij}} \frac{\partial f}{\partial \sigma_{ij}} \quad (A.66)$$

Depends on which way the stress state approaches the yield surface, minus or positive sign is used in definition of λ_R . In this approach, only components of the stress tensor are rectified, meaning no correction is done for the hardening parameter(s).

It is clear that the initial deviation from the consistency condition should not be large since calculated strains do not correspond to the updated stresses.

A.2.4.5 Model predictions

The first set of cyclic loading data was extracted from Michelis (1987). Conventional triaxial cyclic compression test was conducted under confining pressure equals to 3.45 MPa on a specific concrete. Prager and Ziegler's kinematic hardening rules were first tried to calibrate experimental data. Both rules give a linear stress-strain response under a pure kinematic hardening scheme. Thus, only piecewise match can be procured by these rules using

a pure kinematic hardening law. 13 material parameters were used to arrive in the calibration shown in Fig. A2-1 using Ziegler's rule.

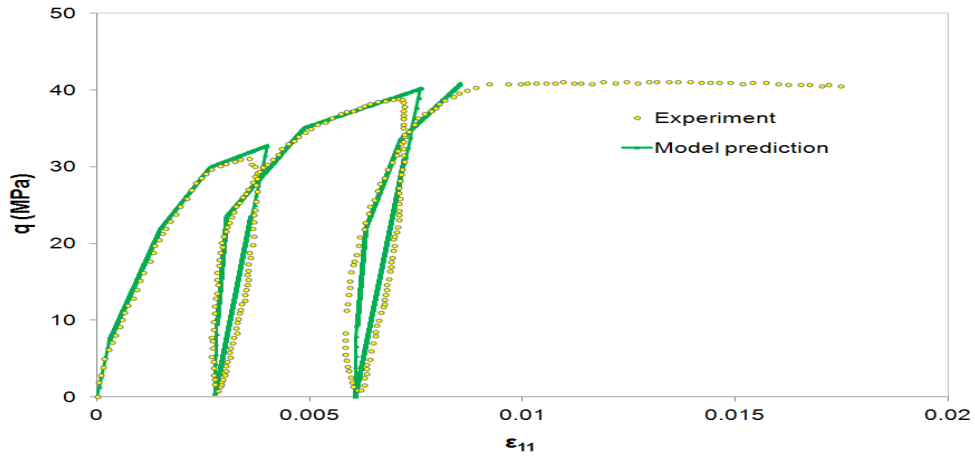


Fig. A2-1 Piecewise calibration of cyclic loading using Ziegler's pure kinematic hardening law

To capture non-linear stress-strain curve using continuously varying plastic modulus under a pure kinematic hardening scheme, use of non-linear kinematic hardening rule is necessary. Table A2.1 shows the material parameters which were used for capturing the experimental observations shown in Figs. A2-2 to A2-6.

Table A2.1 Material parameters used for calibration of cyclic loading using pure kinematic hardening law (2 cycles). N indicates number of cycles.

ν	E (GPa)	c (MPa)	φ (deg)	E_{reload}	c_1 $\times 10^5$	c_1 unload	c_2	c_2 unload	c_1 reload	c_2 reload	h_c
0.25	30	2	15	$4E$	2	$4c_1$	1000	$0.5 c_2$	$c_1/1.55 + (N-1)h_c$	$\frac{c_2}{2.1}$	$0.1c_1$

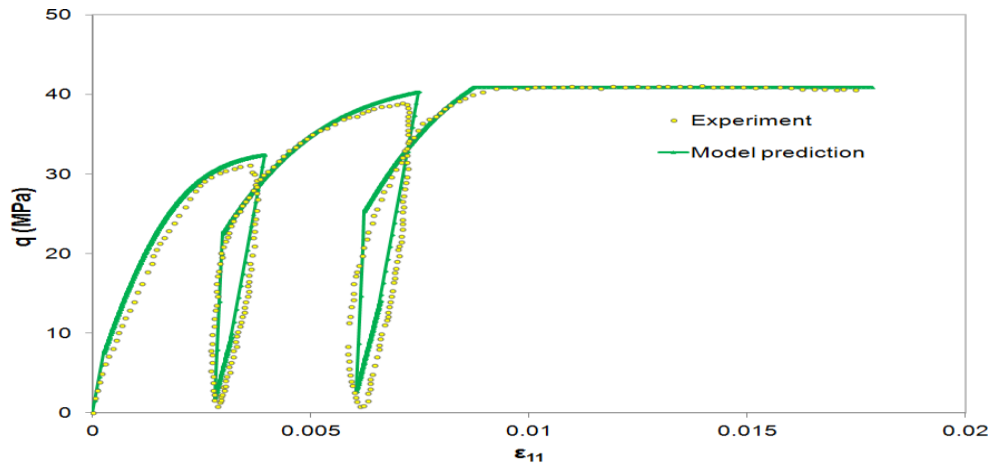


Fig. A2-2 Calibration of cyclic loading using Armstrong and Frederick's pure kinematic hardening rule with confining pressure of 3.45 MPa

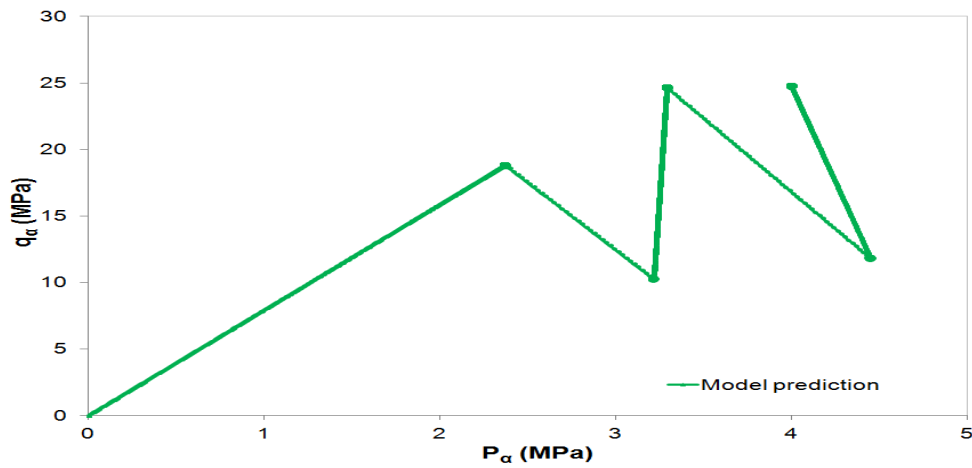


Fig. A2-3 Movement of the yield locus during elastoplastic cyclic loading with confining pressure of 3.45 MPa

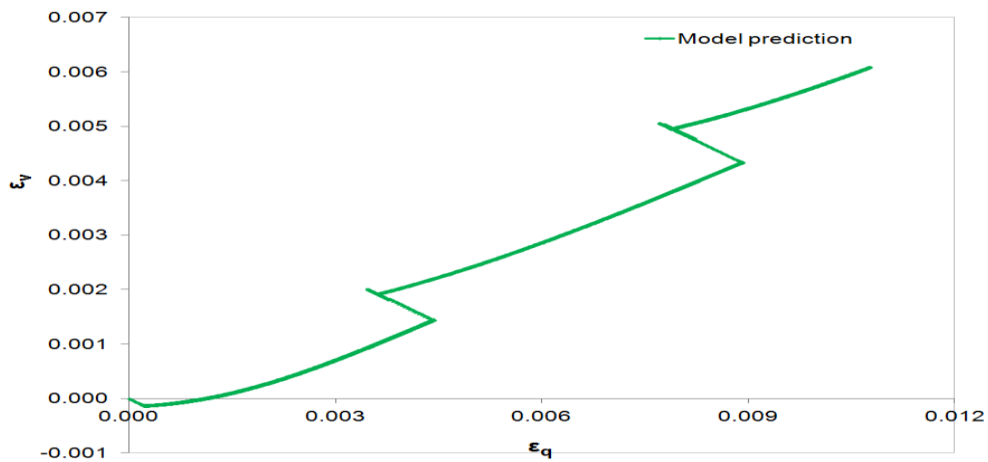


Fig. A2-4 Volumetric behaviour till the constant shear stress (for two complete cycles)

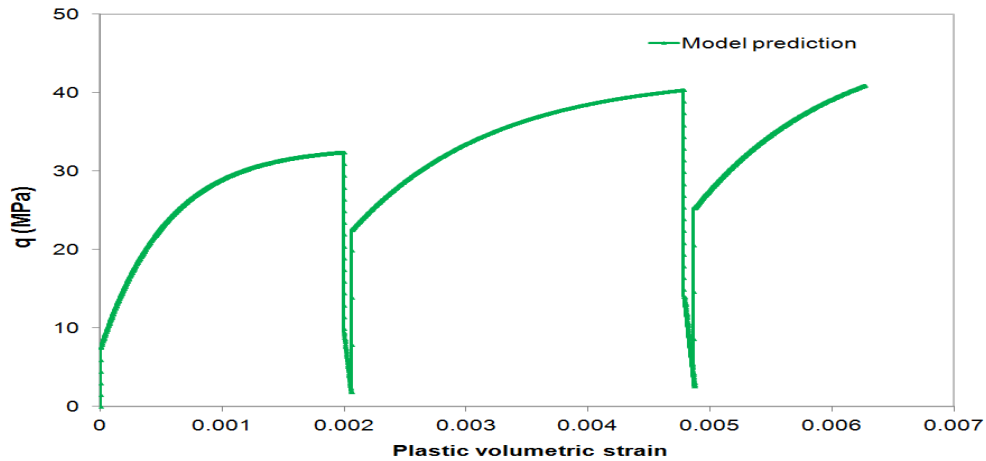


Fig. A2-5 Plastic volumetric strain during cyclic loading till the constant shear stress

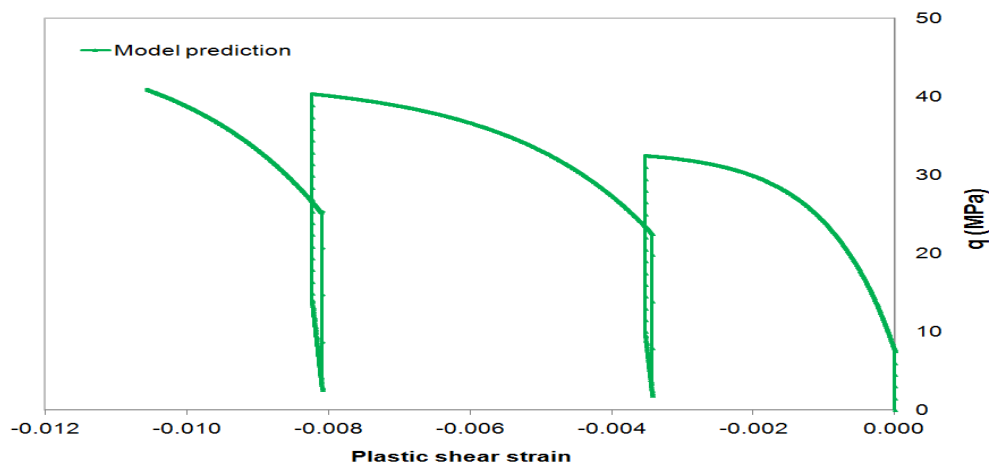


Fig. A2-6 Plastic shear strain during cyclic loading till the constant shear stress

As observed in Fig. A2-4, the deviator/shear strain has a decreasing trend during elastic/plastic unloading in contrast to increasing trend during elastic/plastic reloading. The volumetric expansion, however, continues under plastic unloading/reloading and also elastic unloading. The exception is for elastic reloading during which the sample contracts. The same trend was observed for cumulative plastic volumetric and cumulative plastic shear strain (Fig. A2-5 to A2-6). The same behaviour also was predicted for corresponding curves in the next calibration.

The second set of cyclic loading data comes from the same experiment which was conducted on the same material, but under greater confining pressure, 13.79 *Mpa*. Table A2.2 represents the material parameters used in Figs. A2-7 to A2-10.

Table A2.2 Material parameters used for calibration of cyclic loading using pure kinematic hardening law (4 cycles)

ν	E (GPa)	c (MPa)	φ (deg)	$E_{rreload}$	c_1 $\times 10^5$	c_1 unload	c_2	c_2 unload	c_1 reload	c_2 reload	h_c
0.25	22	2	15	1.8E	2.25	0.8c ₁	530	0.1 c ₂	1.35c ₁ + (N - 1)h _c	1.22c ₂	0

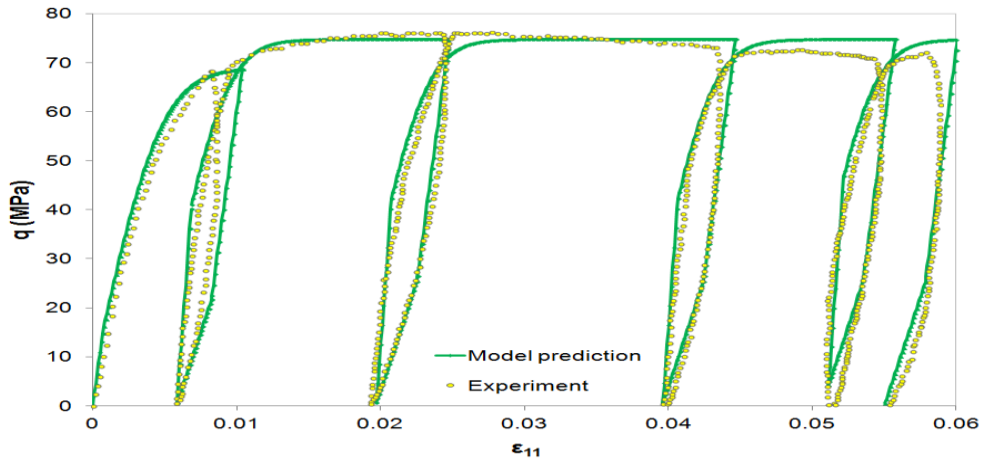


Fig. A2-7 Calibration of cyclic loading using Armstrong and Frederick's pure kinematic hardening rule with confining pressure of 13.79 MPa

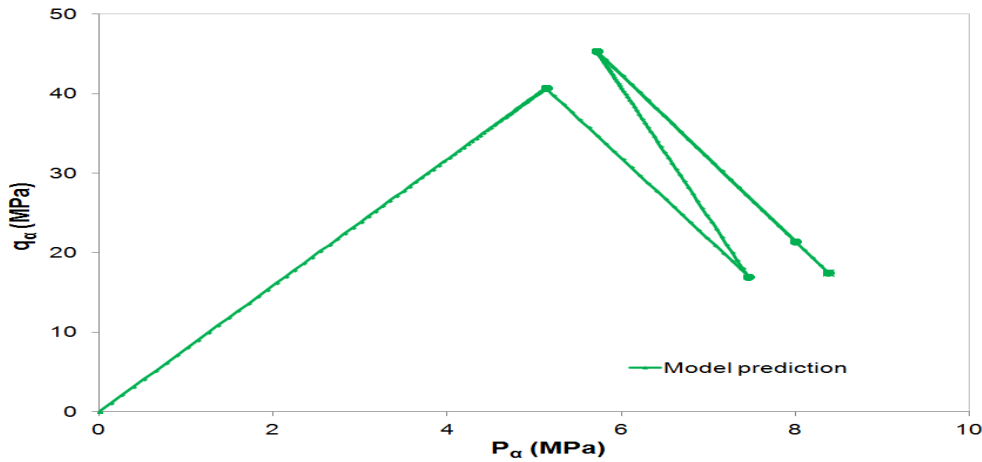


Fig. A2-8 Movement of the yield locus during elastoplastic cyclic loading with confining pressure of 13.79 MPa

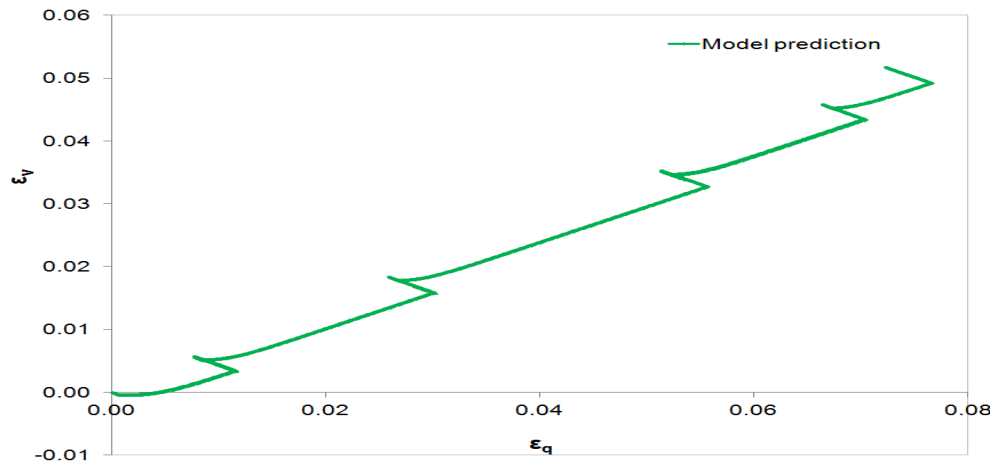


Fig. A2-9 Volumetric behaviour of the sample during cyclic loading

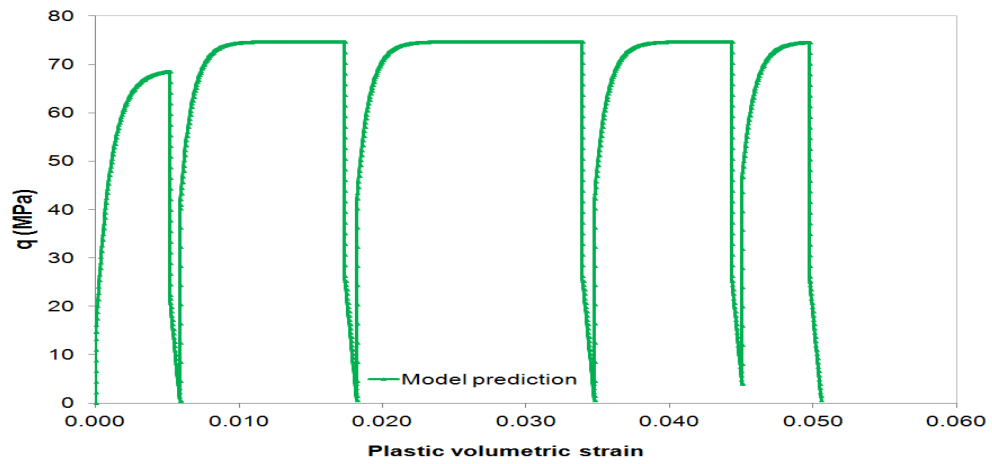


Fig. A2-10 Plastic volumetric strain during cyclic loading

APPENDIX B

GENERAL FORMULATION OF THE CRITICAL STATE CONSTITUTIVE MODEL

B.1 Constitutive modeling

The proposed constitutive model is generalized to include non-triaxial conditions. The total strain increment tensor is defined by:

$$\begin{aligned}\underline{\dot{\varepsilon}} &= \dot{\varepsilon}_{ij} (\underline{e}_i \otimes \underline{e}_j) \\ &= \dot{\varepsilon}_{ij}^e (\underline{e}_i \otimes \underline{e}_j) + \dot{\varepsilon}_{ij}^p (\underline{e}_i \otimes \underline{e}_j) + \dot{\varepsilon}_{ij}^t (\underline{e}_i \otimes \underline{e}_j) + \dot{\varepsilon}_{ij}^T (\underline{e}_i \otimes \underline{e}_j)\end{aligned}\quad (B.1)$$

$\dot{\varepsilon}_{ij}^e$, $\dot{\varepsilon}_{ij}^p$, $\dot{\varepsilon}_{ij}^t$ and $\dot{\varepsilon}_{ij}^T$ are components of the elastic, plastic, creep (viscous/time dependent) and thermal strain increment tensors respectively. Assume the creep and thermal effects are negligible. Hence,

$$\dot{\varepsilon}_{ij} = \dot{\varepsilon}_{ij}^e + \dot{\varepsilon}_{ij}^p \quad (B.2)$$

Components of the total, elastic and plastic strain increment tensors can be decomposed into volumetric and deviator components as follows:

$$\dot{\varepsilon}_v = \dot{\varepsilon}_{kk} = \dot{\varepsilon}_v^e + \dot{\varepsilon}_v^p \quad \dot{\varepsilon}_{ij} = \dot{\varepsilon}_{ij} - \frac{1}{3} \dot{\varepsilon}_v \delta_{ij} = \dot{\varepsilon}_{ij}^e + \dot{\varepsilon}_{ij}^p \quad (B.3)$$

Elastic component of volumetric and shear strains is obtained using the following relationships:

$$\dot{\varepsilon}_v^e = \frac{\dot{p}}{K} \quad \dot{\varepsilon}_{ij}^e = \frac{\dot{s}_{ij}}{2G} \quad (B.4)$$

$$\dot{p} = \frac{\dot{\sigma}_{kk}}{3} \quad \dot{s}_{ij} = \dot{\sigma}_{ij} - \dot{p} \delta_{ij} \quad (B.5)$$

where $\dot{\varepsilon}_v^e$, $\dot{\varepsilon}_{ij}^e$ are elastic volumetric strain and elastic shear strain increments correspondingly, and \dot{s}_{ij} is the deviator stress increment.

Components of plastic strain increment tensor are calculated by:

$$\dot{\epsilon}_{ij}^p = \lambda_{fr} \frac{\partial g}{\partial \sigma_{ij}} \text{sign}(m_{ij}) \quad (B.6)$$

It is possible to postulate another second order tensor $\underline{P} = P_{ij} (\underline{e}_i \otimes \underline{e}_j)$ such that:

$$P_{ij} = \frac{\partial g}{\partial \sigma_{ij}} \text{sign}(m_{ij}) = P'_{ij} \text{sign}(m_q) + p'' \text{sign}(m_p) \delta_{ij} \quad (B.7)$$

Components of the loading surface gradient tensor can also be spitted into the deviator and spherical parts as follows:

$$Q_{ij} = Q'_{ij} + Q'' \delta_{ij} \quad (B.8)$$

$$Q_{ij} = \frac{\partial f}{\partial \sigma_{ij}} \quad Q'_{ij} = \frac{\partial f}{\partial s_{ij}} \quad Q'' = \frac{1}{3} \frac{\partial f}{\partial p} \quad (B.9)$$

Components of the kinematic hardening tensor k_{ij} can be decomposed into its deviator and spherical components similarly as follows:

$$k_{ij} = s_{k_{ij}} + p_k \delta_{ij} \quad (B.10)$$

If Armstrong and Frederick's kinematic hardening law is adopted to govern the evolution of the loading surface, we will have:

$$\dot{k}_{ij} = \frac{2}{3} c_1 \dot{\epsilon}_{ij}^p - c_2 k_{ij} \dot{z} \quad \dot{z} = \sqrt{\frac{2}{3} \dot{\epsilon}_{ij}^p \dot{\epsilon}_{ij}^p} \quad (B.11)$$

The plasticity multiplier is calculated using consistency condition as:

$$\lambda_{fr} = \frac{df}{H} = \frac{Q'_{ij} \dot{s}_{ij} + 3Q'' \dot{p}}{H} \quad (B.12)$$

in which

$$\dot{p} = K(\dot{\epsilon}_v - \lambda_{fr} (3p'') \text{sign}(m_p)) \quad \dot{s}_{ij} = 2G(\dot{\epsilon}_{ij} - \lambda_{fr} (P'_{ij}) \text{sign}(m_q)) \quad (B.13)$$

$$H = -\frac{\partial f}{\partial N_m} \left(\sum_{m=1}^n \frac{\partial N_m}{\partial v^p} (3p'' \text{sign}(m_p)) + \sum_{m=1}^n \frac{\partial N_m}{\partial e_{ij}^p} P'_{ij} \text{sign}(m_q) \right)$$

$$+H^{kinematic} \quad (B.14)$$

$$H^{kinematic} = (3Q'' + Q'_{ij}\delta_{ij}) \left(\frac{2}{9}c_1(3p'')\text{sign}(m_p) - \sqrt{\frac{2}{3}}c_2p_k\beta \right) \\ + Q'_{ij} \left(\frac{2}{3}c_1(P'_{ij}\text{sign}(m_q) + p''\text{sign}(m_p)\delta_{ij}) - \sqrt{\frac{2}{3}}c_2k_{ij}\beta \right) \quad (B.15)$$

$$\beta = \sqrt{P'_{ij}P'_{ij} + 2P'_{ij}p''\text{sign}(m_p)\text{sign}(m_q)\delta_{ij} + 3p''^2} \quad (B.16)$$

If the equations of the stress increments are substituted in definition of the plasticity multiplier, the following formula will result for λ_{fr} after some rearrangements.

$$\lambda_{fr} = \frac{K(3Q'')\dot{\epsilon}_v + 2GQ'_{ij}\dot{\epsilon}_{ij}}{H + K(3Q'')(3p'')\text{sign}(m_p) + 2GQ'_{ij}P'_{ij}\text{sign}(m_q)} \quad (B.17)$$

Explicit forms of a yield function and a plastic potential function are needed for calculating the plasticity multiplier. By substituting this definition of the plasticity multiplier in the flow rule and by knowing $\dot{\epsilon}_v$ and $\dot{\epsilon}_{ij}$, \dot{p} and \dot{s}_{ij} can be calculated. The constitutive relationships are now complete.

Constitutive relationships are also may be expressed using unit tensors. It is beneficial when it is difficult to explicitly define suitable functions for the loading surface and specially the plastic potential surface. Unit normals in this approach are used to define the directions of loading and plastic flow. This approach is also used in generalized plasticity related constitutive models.

Components of the plastic potential function gradient can be written in the following form:

$$n_{p_{ij}} = u_{p_{ij}} + \frac{1}{3}D\delta_{ij} \quad (B.18)$$

$n_{p_{ij}}$ indicates the direction normal to the plastic potential function, $u_{p_{ij}}$ shows the components of a unit tensor normal to the deviator subsurface of the plastic potential surface, and D denotes rate of dilatancy.

Q_{ij} which indicates the loading direction is defined as follows:

$$n_{Q_{ij}} = u_{Q_{ij}} + \frac{1}{3}R\delta_{ij} \quad (B.19)$$

$n_{Q_{ij}}$ shows the direction normal to the loading surface, $u_{Q_{ij}}$ denotes components of a unit tensor normal to the deviator subsurface of the loading surface, and $R = 3Q'' / |Q'|$.

The normalized plasticity multiplier in this approach is determined by:

$$L = \frac{(u_{Q_{ij}}\dot{s}_{ij} + R\dot{p})}{H_n} \quad (B.20)$$

H_n is the normalized plastic modulus which is defined by:

$$H_n = -\frac{\frac{\partial f}{\partial N_m} \left(\sum_{m=1}^n \frac{\partial N_m}{\partial \varepsilon_v^p} D + \sum_{m=1}^n \frac{\partial N_m}{\partial e_{ij}^p} u_{p_{ij}} \right)}{|Q'|} + H_n^{kinematic} \quad (B.21)$$

$$H_n^{kinematic} = (R + u_{Q_{ij}}\delta_{ij}) \left(\frac{2}{9}c_1 D - \sqrt{\frac{2}{3}}c_2 p_k \beta_n \right) + u_{Q_{ij}} \left(\frac{2}{3}c_1 \left(u_{p_{ij}} + \frac{D}{3}\delta_{ij} \right) - \sqrt{\frac{2}{3}}c_2 k_{ij}\beta_n \right) \quad (B.22)$$

$$\beta_n = \sqrt{1 + \frac{2}{3}u_{p_{ij}}D \delta_{ij} + \frac{D^2}{3}} \quad (B.23)$$

Components of the plastic strain increment tensor are calculated by the following equation:

$$\dot{e}_{ij}^p = L u_{p_{ij}} \text{sign}(m_q) \quad \dot{\varepsilon}_v^p = L D \text{sign}(m_p) \quad (B.24)$$

This is the stress controlled formulation. The strain controlled formulation is obtained after some rearrangements as follows:

$$L = \frac{KR\dot{\epsilon}_v + 2Gu_{Q_{ij}}\dot{\epsilon}_{ij}}{H_n + KR D + 2Gu_{Q_{ij}}u_{p_{ij}}} \quad (B.25)$$

Adopting an associated flow rule for the sub deviator part results in $u_{Q_{ij}}u_{p_{ij}} = 1$

The spherical and deviator components of stress increment tensor can be determined by:

$$\dot{p} = K \left(\dot{v} - LD \text{sign}(m_p) \right) \quad \dot{s}_{ij} = 2G \left(\dot{\epsilon}_{ij} - Lu_{p_{ij}} \text{sign}(m_q) \right) \quad (B.26)$$

where

$$m_p = \begin{cases} \frac{D}{\sqrt{1+D^2}} & D \geq 0 \\ -D & D < 0 \end{cases} \quad (B.27)$$

$$m_q = \frac{1}{\sqrt{1+D^2}} \quad (B.28)$$

The following relationships are assumed for unloading conditions:

$$\frac{H_{n,u}}{H_n} = R_u \sqrt{\frac{p}{p_{atm}} |\underline{\eta}|} \quad (B.29)$$

$H_{n,u}$ is unloading normalized plastic modulus. It is also assumed that:

$$m_p^{unloading} = -m_p \quad m_q^{unloading} = m_q \quad (B.30)$$

B.2 Model ingredients

Model ingredients presented already in previous chapters are extended here to the general stress space.

B.2.1 Bounding surface and loading surface

The mathematical definitions of the bounding and loading surfaces are assumed to be of the same form for simplicity. They are defined using the following functions:

$$F = \left(\frac{\sqrt{\frac{3}{2}} (\underline{s}_j - \underline{s}_{k_j})}{p_j - p_{k_j} + p_t} - \underline{\alpha} \right)^2 - M_\alpha^2 \left(1 - \sqrt{\frac{p_j - p_{k_j} + p_t}{p_{b_j}}} \right) = 0 \quad (B.31)$$

$$f = \left(\frac{\sqrt{\frac{3}{2}} (\underline{s} - \underline{s}_k)}{p - p_k + p_t} - \underline{\alpha} \right)^2 - M_\alpha^2 \left(1 - \sqrt{\frac{p - p_k + p_t}{p_b}} \right) = 0 \quad (B.32)$$

in which $\underline{\alpha} = \sqrt{\frac{3}{2}} \frac{\underline{s}_\alpha}{p_\alpha}$ is the tensor that considers anisotropy consolidation effect

(prior to shearing) on the yielding behavior. It is a zero tensor for triaxial conditions (i.e. hydrostatic/isotropic consolidation), but it is a non-zero tensor for non-hydrostatic/anisotropic consolidation. It is assumed that the initial tensor $\underline{\alpha}$ remains unchanged during shearing. The maximum yield pressure for anisotropically consolidated sand is no longer $p = p_c$ but $p = p_\alpha$ which is associated with the stress ratio $\underline{\alpha}$ [Imam 1999]. p_α controls the size (i.e. the length) of the unbounded loading surface and M_p controls its shape (i.e. the width). The value of these parameters during shearing depends on proximity of the current stress to critical state. In general, p_α is not known but depends on the consolidation pressure $\underline{\eta}_c$ and the stress ratio $\underline{\alpha}$ [Imam 1999 and Imam et. al. 2002b].

The subscripts "j" refers to variables of the bounding surface, and underbar sign indicates a tensorial quantity.

The coefficient $\sqrt{3/2}$ is used in these definitions so that stress ratios become directly comparable with those normally used in triaxial tests [Imam 1999]. In 3D principal stress space, this function is presented by a surface whose tip lies at the hydrostatic axis (see Fig. B2-1).

p_k and \underline{s}_k are the spherical and deviator components of the kinematic hardening tensor \underline{k} which evolve with plastic deformation. The kinematic hardening tensor is assumed to lie initially at the origin. This means for the first time loading: $p_k = 0$ and $\underline{s}_k = \underline{0}$.

To avoid crossing of the bounding surface by the loading surface, it is assumed that initial ratio of size of two surfaces does not change during shearing. It is also assumed that components of the kinematic hardening tensor always coincide for two surfaces, i. e. $p_{k_j} = p_k$ and $\underline{s}_{k_j} = \underline{s}_k$.

p_b and p_t which determine size of the loading surface and the tensile strength are defined using the following relationships:

$$p_b = p_\alpha + (1 + \beta)p_o \quad (B.33)$$

$$p_t = \beta p_o \quad (B.34)$$

Destruction of the cementing bonds between sand particles is assumed to result in change in the size of the loading and bounding surfaces only as follows:

$$dp_o = -\gamma p_o d|\underline{e}^p| \quad (B.35)$$

The parameter γ determines rate of the bond breakage.

The scalar M_α^2 is calculated using the tensors $\underline{\alpha}$ and \underline{M}_p as follows:

$$M_\alpha^2 = 5 \underline{M}_p \underline{M}_p - 6 \underline{M}_p \underline{\alpha} + \underline{\alpha} \underline{\alpha} \quad (B.36)$$

in which $\underline{M}_p = \sqrt{3/2} \frac{S_p}{p_p}$. The locus of all stress ratios \underline{M}_p is called the shape hardening surface [Imam 1999].

For a soil consolidated anisotropically along a stress ratio $\underline{\eta}_c$ and to a pressure p_c , $\underline{\alpha}$ and p_α may not be equal to $\underline{\eta}_c$ and p_c respectively. It is, however, assumed for simplicity that they are equal. Thus,

$$\underline{\alpha} = \underline{\eta}_c = \sqrt{\frac{3}{2}} \frac{\underline{s}_c}{p_c} \quad p_\alpha = p_c \quad (B.37)$$

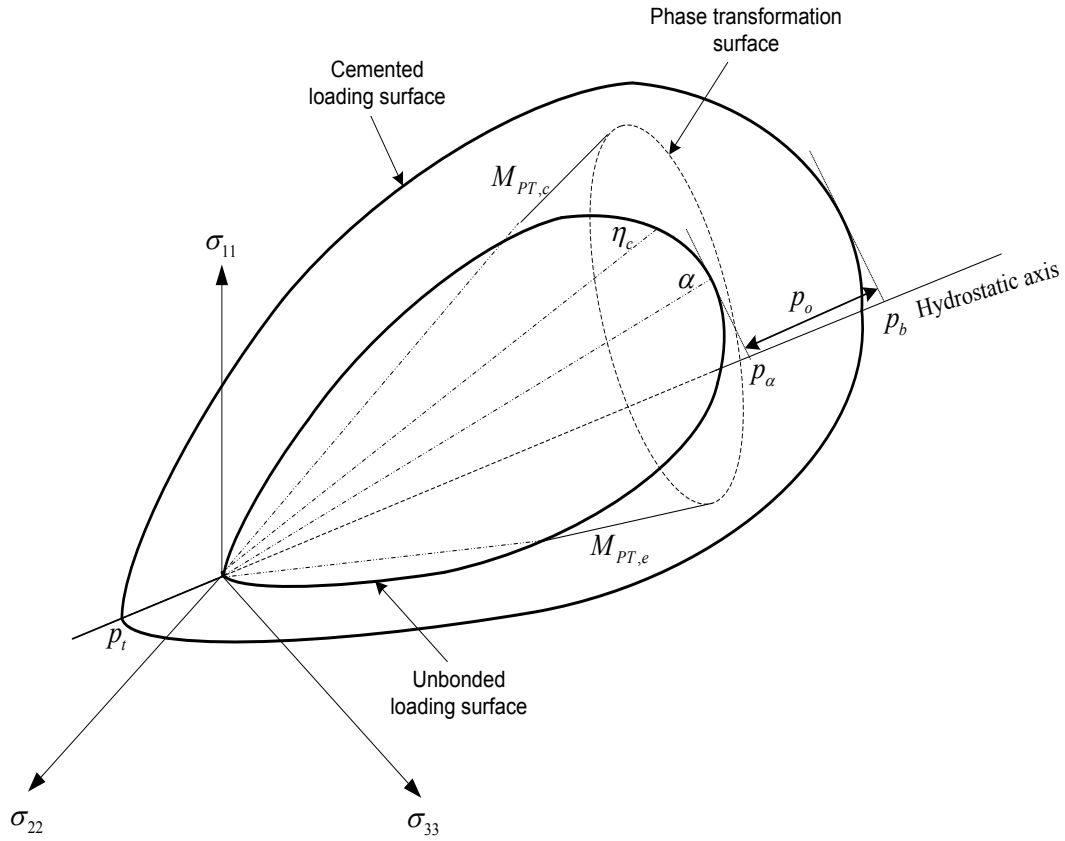


Fig. B2-1 The loading surface in principal stress space (assume coordinate directions coincide with the principal directions)

Geomaterials have different strengths in the direction of anisotropy (usually vertical direction) and in directions perpendicular to it where it is almost isotropic. This is called transverse isotropy. The effect of such inherent anisotropy on the yielding response is accounted using \underline{M}_p [Imam 1999]. \underline{M}_p is independent of anisotropic consolidation stresses since its measured values for isotropic consolidation and anisotropic consolidation (along different ratios of the coefficient of earth pressure) are close to each other [Imam 1999]. This implies that the effects of inherent anisotropy, captured by \underline{M}_p , are independent from those of the stress-induced anisotropy which are captured by $\underline{\alpha}$ [Imam et. al. 2002a]. The tensor \underline{M}_p is determined as follows [Imam 1999]:

$$\underline{M}_p = M_p \underline{u}_s \tag{B.38}$$

where

$$\underline{u}_s = \frac{\underline{s}}{|\underline{s}|} \quad \underline{s} = \underline{\sigma} - p\underline{\delta} \quad |\underline{s}| = \sqrt{\underline{s} \underline{s}} \quad (B.39)$$

The scalar M_p is calculated from the following relationships:

$$M_p = \frac{6(1 - b + b^2)^{1/2} \sin \varphi_p}{3 + (2b - 1) \sin \varphi_p} \quad (B.40)$$

in which:

$$b = \frac{\sigma_2 - \sigma_3}{\sigma_1 - \sigma_3} \quad (B.41)$$

$$\sin \varphi_p = \sin \varphi_\mu - k_p \psi_p - a_p(A) \quad (B.42)$$

$$a_p(A) = \frac{A_c - A}{A_c - A_e} \cdot a_p \quad (B.43)$$

where a_p is a positive material parameter in the original model, A is anisotropic state variable defined in equation (6-21), A_c and A_e are the anisotropic parameters in triaxial compression and triaxial extension, respectively, For triaxial compression $A = A_c$ and $a_p(A) = 0$, and for triaxial extension $A = A_e$ and $a_p(A) = a_p$.

Note that For $b = 0$ and $b = 1$, the equation (B.42) reduces to those of $M_{p,c}$ and $M_{p,e}$, respectively. Therefore equation (B.42) will reduce to equation (B.44) for triaxial compression and equation (B.45) for triaxial extension as follows:

$$\sin \varphi_{p,c} = \sin \varphi_\mu - k_p(e_n - e_\mu) \quad (B.44)$$

$$\sin \varphi_{p,e} = \sin \varphi_\mu - k_p(e_n - e_\mu) - a_p \quad (B.45)$$

where e_n is the normalized void ratio, and e_μ (a material parameter) is the normalized void ratio corresponding to φ_μ . Therefore, $\sin \varphi_{p,e}$ is smaller than $\sin \varphi_{p,c}$ for the same conditions.

The normalized void ratio e_n is determined using an iterative solution scheme from the next equation [Imam et. al. 2002b]:

$$\beta_c e_n^{2.5} \left(\frac{p_c}{p_{atm}} \right) + \ln \left(\frac{e_c}{e_n} \right) = 0 \quad (B.46)$$

in which e_c is pre-consolidation void ratio, and β_c is a material parameter relevant to the sand compressibility.

For a given e_c and p_c , e_n is obtained by moving along the current normally consolidation line to a reference pressure [Imam 1999]. Note that compressibility of sand differs from that of clay. A given sand sample under the same consolidation pressure can exist at different void ratios because sand can be repacked. This means normally consolidation line is not unique in sands.

It should be pointed out that $\psi_p = e - e_p$ can also be used interchangeably in calculation of $\sin \varphi_p$. e_p is critical state void ratio corresponding to the peak of UESP. This definition of ψ_p was used throughout this research.

B.2.2 Flow rule

$$D = \sqrt{\frac{2}{3}} \left(A \left(|\underline{M}_{PT}| - |\underline{\eta}| \right) + \frac{6B}{C} \right) \quad (B.47)$$

It is assumed for general stress conditions that the coefficients of A and C vary with the modified load angle as follows:

$$A = \frac{9}{9 + 3|\underline{M}_{PT}| \cos 3\theta - 2|\underline{M}_{PT}| |\underline{\eta}| + 4B} \quad (B.48)$$

$$B = \frac{c}{p} \sqrt{(2|\underline{M}_{PT}| + 3)(-|\underline{M}_{PT}| + 3)} \quad (B.49)$$

in which c is cohesion, and

$$|\underline{\eta}| = \sqrt{\underline{\eta} \underline{\eta}} = \sqrt{\frac{3}{2} \frac{|\underline{s}|}{p}} \quad (B.50)$$

$|\underline{M}_{PT}|$ is defined as follows [Imam 1999]:

$$|\underline{M}_{PT}| = M_{PT,c} g(\theta) \quad (B.51)$$

$$M_{PT,c} = \frac{6 \sin \varphi_{PT,c}}{3 - \sin \varphi_{PT,c}} \quad g(\theta) = \frac{2c_{PT}}{(1 + c_{PT}) - (1 - c_{PT}) \cos 3\theta} \quad (B.52)$$

$$c_{PT} = \frac{M_{PT,e}}{M_{PT,c}} \quad M_{PT,e} = \frac{6 \sin\varphi_{PT,e}}{3 + \sin\varphi_{PT,e}} \quad (B.53)$$

$$\sin\varphi_{PT,c} = \sin\varphi_{cs} + k_{PT}\psi \quad \sin\varphi_{PT,e} = \sin\varphi_{cs} + k_{PT}\psi + a_{PT} \quad (B.54)$$

θ is the modified load angle which is determined by:

$$\cos 3\theta = \frac{3\sqrt{3}}{2} \frac{J_3}{J_2^{\frac{3}{2}}} \quad 0 \leq \theta \leq \frac{\pi}{3} \quad (B.55)$$

$$J_2 = \frac{1}{2} s_{ij} s_{ji} \quad J_3 = \frac{1}{3} s_{ik} s_{kj} s_{ij} \quad (B.56)$$

Triaxial compression and extension which are two extreme modes of shearing constitute the limits of the modified load angle. That is, $\theta = 0$ corresponds to triaxial compression and $\theta = 60$ degrees corresponds to triaxial extension.

B.2.3 Hardening rule

Variations of p_b and \underline{M}_p during shearing is named size hardening and shape hardening, respectively. However, use of initial value of \underline{M}_p associated with the soil state at the end of consolidation and prior to shearing appears to be sufficient for obtaining acceptable predictions. Thus, the shape hardening is neglected. Hardening can occur due to plastic shear or volumetric strain. It is assumed, however, that the size hardening takes place only due to plastic shear strain as follows:

$$\frac{\partial p_b}{\partial |\underline{e}^p|} = \frac{\partial p_\alpha}{\partial |\underline{e}^p|} + (1 + \beta) \frac{\partial p_o}{\partial |\underline{e}^p|} \quad (B.57)$$

$$\frac{\partial p_\alpha}{\partial |e_p|} = \frac{hG_{ini}}{(p_f - p_\alpha)_{ini}} (p_f - p_\alpha) \quad (B.58)$$

$$\frac{\partial p_o}{\partial |\underline{e}^p|} = -\gamma p_o \quad (B.59)$$

p_f is calculated using an iterative method such as Newton-Raphson method from the following equation:

$$p_f = \frac{p - p_k}{\left(1 - \frac{\left(\frac{(M_f p_f - \sqrt{3/2} s_k)}{p_f - p_k} - \alpha\right) \left(\frac{(M_f p_f - \sqrt{3/2} s_k)}{p_f - p_k} - \alpha\right)}{M_\alpha^2}\right)^2} \quad (B.60)$$

\underline{M}_f is determined using the following relationships [Imam 1999]:

$$\underline{M}_f = |\underline{M}_f| \underline{u}_s = M_{f,c} g(\theta) \underline{u}_s \quad (B.61)$$

$$M_{f,c} = \frac{6 \sin \varphi_{f,c}}{3 - \sin \varphi_{f,c}} \quad \sin \varphi_{f,c} = \sin \varphi_{cs} - k_f \psi \quad (B.62)$$

$g(\theta)$ is the same as that used for calculating the phase transformation stress ratio.

The same value of $g(\theta)$ is used to calculate M_f and M_{pT} at any stage of shearing.

B.2.4 Elastic properties

Elastic properties are the same as those used for triaxial conditions as follows:

$$G = G_a \frac{(2.973 - e)^2}{1 + e} \left(\frac{p}{p_{atm}} \left(1 + \left(\frac{p_o}{p} \right)^m \right) \right)^n \quad (B.63)$$

$$K = K_a \frac{(2.973 - e)^2}{1 + e} \left(\frac{p}{p_{atm}} \left(1 + \left(\frac{p_o}{p} \right)^m \right) \right)^n \quad (B.64)$$

in which n and m are model constants.

For unloading, the elastic moduli are defined as follows:

$$G = |\underline{\eta}| G_a \frac{(2.973 - e)^2}{1 + e} \left(\frac{p}{p_{atm}} \left(1 + \left(\frac{p_o}{p} \right)^m \right) \right)^n \quad (B.65)$$

$$K = |\underline{\eta}| K_a \frac{(2.973 - e)^2}{1 + e} \left(\frac{p}{p_{atm}} \left(1 + \left(\frac{p_o}{p} \right)^m \right) \right)^n \quad (B.66)$$

B.3 Model Calibration

The proposed model uses the following material parameters in its most general form:

- a) Shape hardening parameters: k_p, φ_μ, a_p
- b) Flow rule parameters: $a_{PT}, \varphi_{CS}, k_{PT}, coh, \xi$
- c) Failure: k_f
- d) Elastic parameters: G_a, K_a, R_u
- e) Plastic stiffness parameter: h
- f) Steady state line
- g) Bonding parameters: p_o, β, γ
- h) Kinematic hardening parameters: c_1, c_2
- i) Fabric anisotropy parameters: Δ, M_c, c

There is no need to all material parameters in most cases. For example, fabric anisotropy parameters, a_p , and a_{PT} are not needed if only one-way cyclic conventional triaxial compression tests are calibrated. Some of the above material parameters do not have considerable effects on the results. Methods of determination of material parameters are discussed in the following. These methods are not unique and alternative methods may also be proposed to obtain the material parameters.

The parameters k_p, φ_μ and a_p can be determined from results of undrained TC and TE tests in which the UESP follows a softening path. The actual value of φ_μ is not important since it is an arbitrary reference point on the $\sin\varphi_p$ vs. ψ_p line whose slope gives k_p . However a value smaller than φ_{CS} is usually adopted for φ_μ .

The parameters k_{PT}, φ_{CS} and a_{PT} are estimated from plots of $\sin\varphi_{PT}$ vs. ψ_s obtained from TC and TE tests. φ_{CS} can be measured also directly from drained or undrained tests at large shear strains when no volume change occurs. The parameter coh (cohesion) can be estimated from the peak Mohr-Coulomb yield envelope. Intersection of the peak yield envelope with q axis in $q-p$ plot gives an estimation of intensity of cementation bonds between sand particles. The parameter ξ can be evaluated by fitting theoretical results of the volumetric behaviour to those of experimental observations.

The parameters k_f can be obtained from plots of $\sin\varphi_f$ vs. ψ_s . φ_f is the maximum attainable friction angle at the current stress state which can be obtained using the current state parameter. Consistent with the original model, k_f is taken to be 0.75 under different modes of shearing.

The parameter G_a can be determined using deviator stress-deviator strain plot. It is estimated from the tangent to linear part of the deviator stress vs. deviator strain curve of a drained or undrained test at the origin. The parameter K_a can be determined similarly using volumetric strain vs. deviator strain curve. It can be determined also using estimated shear modulus and a typical value of Poisson's ratio. Estimated values of the elastic moduli using this method usually result in underestimation of the elastic moduli. The reason is that some plastic deformations occur at the points where the slope of the tangent is measured [Imam 1999]. If simulation results underestimate observed (elastic) stiffness in this case, estimated values of the elastic moduli can be increased gradually until the observed (elastic) stiffness can be reproduced by simulation results. The parameter R_u is determined by fitting model predictions to unloading part of experimental stress-strain curve. The smaller the value of R_u , the less stiff the unloading response and the larger unloading-induced plastic strain increment (and vice versa).

The parameter h is determined by fitting model simulations to observed (elasto-plastic) stiffness. Increase in value of h leads to stiffer (elasto-plastic) response. Therefore, a higher value of h can compensate underestimation of observed (elastic) stiffness which originates from underestimation of the elastic moduli.

The ultimate state line can be determined using conventional triaxial tests in which material is loaded until shear deformation occurs under constant volume (i.e. when the critical state is reached). Void ratio, mean effective stress, and deviator stress are recorded at the critical state. If the tests are conducted under different cell pressures, different ultimate state void ratios, mean effective stresses, and deviator stresses are recorded. Linear relationship between ultimate

state deviator stress and mean effective stress gives equation of the ultimate state line in $q-p$ plane. Similarly relationship between ultimate state void ratio and mean effective stress gives equation of the ultimate state line in $e-\ln p$ plane. However the ultimate state line for some sands/cemented sands becomes curved at high pressures in compression plane. Therefore a third order polynomial equation may alternatively also be used to define the ultimate state line based on relationship between ultimate void ratio and mean effective stress.

Methods of determination of the parameters p_o , β , γ , and c_1, c_2 have been discussed in chapters 4 and 5. They are not repeated here.

The parameter Δ can be estimated using acoustic wave anisotropy. Compressional wave velocities are measured along axis of anisotropy/symmetry and bedding plane for a transverse isotropic medium. Then the elastic stiffness along axis of anisotropy and bedding plane are calculated correspondingly based on those of compressional wave velocities and material density. Ratio of the measured stiffness along vertical and horizontal directions gives an estimation for ratio of components of the fabric tensor along vertical and horizontal directions. Hence, Δ can be determined based on this ratio. The parameter M_c (the critical stress ratio under triaxial compression) is determined similar to the method which was suggested to measure the ultimate state line. Measuring the critical state ratio under triaxial extension is required to determine the parameter $c = M_e/M_c$ (the ratio of the critical stress ratio under triaxial extension over that of triaxial compression).

Note that adjustments in measured material parameters often are needed in order to obtain the best fit to a range of experimental observations [Imam 1999]. Moreover, some of the material parameters usually can not be estimated directly from experimental data since extensive experimental tests are required to measure all of the above material parameters. Therefore those material parameters which can not be determined directly due to lack of enough experimental results are chosen based on the best match (i.e. trial and error) to a range of experimental observations.

BIBLIOGRAPHY

Abdulazeez, A. (1994), Constitutive modeling of rocks and numerical simulation of oil reservoirs exhibiting pore collapse, Ph.D. thesis, The university of Oklahoma, Oklahoma, USA.

Abdulla A.A., and Kiousis P.D. (1997), Behaviour of cemented sands- I. testing, International Journal for Numerical and Analytical Methods in Geomechanics, Vol. 21, No. 8, pp. 533-547.

Acock, A., Alexander, J., Andersen, G., Kaneko, T., Venkitaraman, A., Lopez-de-Cardenas, J., Nishi, M., Numasawa, M., Yoshioka, K., Roy, A., Wilson, A. and Twynam, A. (2004), Practical approaches to sand management, Oilfield Review, pp. 10-27.

Alejano, L.R., and Alonso.E. (2005), Consideration of dilation angle and rock masses, International Journal of Rock Mechanics & Mining Sciences, Vol. 42, pp. 481–507.

Al-Tabbaa, A. (1987), Permeability and stress-strain response of Speswhite kaolin, Ph.D. thesis, The University of Cambridge, Cambridge, U.K.

Altaee, A.A. (1992), Finite element implementation validation and deep foundation application of a bounding surface plasticity model, Ph.D. thesis, The University of Ottawa, Ottawa, Canada.

Araujo, M.C. (2002), Non-linear kinematic hardening model for multiaxial cyclic plasticity, M.Sc. thesis, Louisiana State University, Louisiana, USA.

Armstrong, P.J. and Frederick, C.O. (1966), A mathematical representation of the multiaxial Bauschinger effect, CEGB Report, RD/B/N731, Berkeley Nuclear Laboratories.

Asghari, E., Toll, D.G., and Haeri, S.M. (2003), Triaxial behaviour of a cemented gravely sand, Tehran alluvium, Geotechnical and Geological engineering, Vol. 21, No. 1, pp. 1-28.

Atkinson, J. (1993), An introduction to the mechanics of soils and foundations through critical state soil mechanics, McGRAW-HILL Book Company, England.

Bardet, J.P. (1986), Bounding surface plasticity model for sands, Journal of Engineering Mechanics, Vol. 112, No. 11, pp. 1198-1217.

Been, K., and Jefferies, M. G. (1985), A state parameter for sands, Géotechnique, Vol. 35, No. 2, pp. 99-112.

Bellarby, J. (2009), Well completion design, Elsevier, Netherlands.

Cai, Y. (2010), An experimental study of non-coaxial soil behaviour using hollow cylinder testing, Ph.D. thesis, The University of Nottingham, Nottingham, U.K.

Challa, V. (2005), Influence of third invariant of deviatoric stress and intermediate principal stress on constitutive models and localization conditions for high porosity sandstone, Ph.D. thesis, Clarkson University, Potsdam, USA.

Chen, W.F. (1994), Constitutive equations for engineering materials, Elsevier, Netherlands.

Chen, W.F. and Han D.J. (2007), Plasticity for structural engineers, John Ross Publishing, USA.

Choi, S.K., and Huang, W.S. (2011), Impact of water hammer in deep sea water injection wells, SPE 146300, pp. 1-14.

Chung, A.B. (2010), Unifies modeling for sand under generalized stress paths, Ph.D. thesis, Columbia University, New York, USA.

Clough, G.W., Shafii Rad, N., Bachus, R.C., and Sitar, N. (1981), Cemented sands under static loading, Journal of the geotechnical engineering division, Vol. 107, No. 6, pp. 799-817.

Colmenares, L.B., and Zoback, M.D. (2002), A statistical evaluation of intact rock failure criteria constrained by polyaxial test data for five different rocks, International Journal of Rock Mechanics and Mining Sciences, Vol. 39, pp. 695-729.

Consoli, N.C., Cruz, R.C., Fonseca, A.V.D., and Coop, M.R. (2012), Influence of Cement-Voids Ratio on Stress-Dilatancy Behavior of Artificially Cemented Sand, Journal of geotechnical and geoenvironmental engineering, Vol. 138, No. 1, pp. 100-109.

Crouch, R.S., and Wolf, J.P. (1994), Unified 3D critical-state bounding-surface model for soils incorporating continuous plastic loading under cyclic paths. Part I: constitutive relations, International journal for numerical and analytical methods in geomechanics, Vol. 18, No. 11, pp. 735-758.

Crouch, R.S., Wolf, J.P., and Dafalias, Y.F. (1994), Unified critical-state bounding-surface plasticity model for soils, Journal of Engineering Mechanics, Vol. 120, No. 11, pp. 2251-2270.

Dafalias, Y.F. (1986), Bounding Surface Plasticity. I: Mathematical foundation and hypoplasticity, Journal of Engineering Mechanics, Vol. 112, No. 9, pp. 966-987.

Dafalias, Y.F., and Herrmann, L.R. (1982), Bounding surface formulation of soil plasticity, Soil Mechanics-Transient and Cyclic Loads, Wiley, pp. 253-282.

- Dafalias, Y.F., and Herrmann, L.R. (1986), Bounding surface plasticity. II: application to isotropic cohesive soils, *Journal of Engineering Mechanics*, Vol. 112, No. 12, pp. 1263-1291.
- Dafalias, Y.F., and Popov, E.P. (1975), A model of nonlinearly hardening materials for complex loading, *Acta Mechanica*, Vol. 21, pp. 173-192.
- Dafalias, Y.F., and Popov, E.P. (1977), Cyclic loading for materials with a vanishing elastic region, *Nuclear Energy and Design*, Vol. 41, pp. 293-302.
- Desai, C. S. (2001), *Mechanics of materials and interfaces: the disturbed state concept*, CRC Press, USA.
- De Souza, A.L.S., de Souza, J.A.B., Meurer, G.B., Naveira, V.P., and Chaves, R.A.P. (2012), Reservoir geomechanics study for deepwater field identifies ways to maximize reservoir performance while reducing geomechanics risks, *SPE 160329*, pp. 1-19.
- Dunne, F., and Petrinic, N. (2006), *Introduction to computational plasticity*, Oxford University Press, USA.
- Economides, M.J., and Nolte, K.G (2000), *Reservoir stimulation*, Third edition, John Wiley and Sons, USA.
- Elgamal, A., Yang, Z., Parra, E. and Regheb, A. (2003), Modeling of cyclic mobility in saturated cohesionless soils, *International Journal of Plasticity*, Vol. 19, pp. 883-905.
- Ewy, R.T. (1998), Wellbore stability predictions using a modified lade criterion, *SPE/ISRM 47251*, PP. 247-254.
- Fernandez, A.L., and Santamarina, J.C. (2000), Effect of cementation on the small-strain parameters of sands, *Canadian Geotechnical Journal*, Vol. 38, No. 1, pp. 191-199.
- Ferreira, P., and Bica, A. (2006), Problems in identifying the effects of structure and critical state in a soil with a transitional behaviour, *Géotechnique*, Vol. 56, No. 7, pp. 445-454.
- Fjar, E., Holt, R.M., Horsrud, P., Raaen, A.M., and Risnes, R. (2008), *Petroleum related rock mechanics*, Elsevier, U.K.
- Fu, Z., Chen, S., and Peng. C. (2013), Modeling the cyclic behaviour of rockfill materials within the framework of generalized plasticity, *International Journal of Geomechanics*, ASCE.
- Gadde, M.M., and Rusnak, J.A. (2008), Applicability of Drucker-Prager failure criterion to estimate polyaxial rock strength, *ARMA 08-137*.

- Gao, Z., and Zhao, J. (2012), Constitutive modeling of artificially cemented sand by considering fabric anisotropy, *Computers and Geotechnics*, Vol. 41, pp. 57-69.
- Gens, A., and Nova, R. (1993), Conceptual bases for a constitutive model for bonded soils and weak rocks, *Geotechnical engineering of hard soils-soft rocks*, pp. 485-494.
- Grueschow, E. R. (2005), Yield cap constitutive models for predicting compaction localization in high porosity sandstone, Ph.D. thesis, Northwestern University, Chicago, USA.
- Gulhati, S.K., and Datta, M. (2008), *Geotechnical engineering*, McGraw Hill company, India.
- Habte, M.A. (2006), Numerical and constitutive modelling of monotonic and cyclic loading in variably saturated soils, Ph.D. thesis, The University of New South Wales, Sydney, Australia.
- Hashiguchi K. (1989), Subloading surface model in unconventional plasticity, *International Journal of Solids and Structures*, Vol. 25, No. 8, pp. 917-945.
- Hashiguchi, K. (2009), *Elastoplasticity theory*, Springer-verlag, Germany.
- Hashiguchi K., and Chen Z. P. (1998), Elastoplastic constitutive equations of soils with the subloading surface and the rotational hardening, *International Journal for Numerical and Analytical Methods in Geomechanics*, Vol. 22, No. 3, pp. 197-227.
- Hashiguchi, K., and Ueno, M. (1977), Elasto-plastic constitutive laws of granular materials, 9th International Conference on Soil Mechanics and Foundation Engineering, Japan, pp. 73-82.
- Han, G., Ioannidis, M., and Dusseault, M.B. (2003), Semi-analytical solutions for the effect of well shut-down on rock stability, *Journal of Canadian Petroleum Technology*, Vol. 42, No. 12, pp. 46-53.
- Hau, K.W. (2003), Application of a three surface kinematic hardening model to the repeated loading and thinly surfaced pavements, Ph.D. thesis, The University of Nottingham, Nottingham, U.K.
- Hickman, R.J. (2004), Formulation and implementation of a constitutive model for soft rock, Ph.D. thesis, Virginia Polytechnic Institute and State University, Virginia, USA.
- Hoek E. (2007), *Practical Rock Engineering*, www.rocscience.com.
- Holland, T.J. (1997), Numerical methods for implementing the bounding surface plasticity model for clays, Ph.D. thesis, The University of California, Davis, USA.

- Imam, M.R. (1999), Modeling the constitutive behavior of sand for the analysis of static liquefaction, Ph.D. thesis, The University of Alberta, Edmonton, Canada.
- Imam, M.R., and Chan, D.H. (2008), Application of a critical state model for the cyclic loading of sands, In Proceedings from GeoEdmonton: 61st Canadian Geotechnical Conference, Edmonton, pp. 127-134.
- Imam, M.R., Chan, D.H., Robertson, P.K., and Morgenstern, N.R. (2002a), effect of anisotropic yielding on the flow liquefaction of loose sand, *Soils and Foundations*, Vol. 42, No. 3, pp. 33-44.
- Imam, M.R., Morgenstern, N.R., Robertson, P.K., and Chan, D.H. (2002b), Yielding and flow liquefaction of loose sand, *Soils and Foundations*, Vol. 42, No.3, pp. 19-31.
- Imam, M.R., Morgenstern N.R., Robertson P.K., and Chan, D.H. (2005), A critical-state constitutive model for liquefiable sand, *Canadian Geotechnical Journal*, Vol. 42, No. 3, pp. 830-855.
- Imam, M. R., Rasouli, R. (2010), Introduction of inherent anisotropy into a critical-state constitutive model for sands, proceedings of the 63rd Canadian Geotechnical Conference, Calgary, Canada. pp. 168-175.
- Ishihara, K. (1993) Liquefaction and flow failure during earthquake. *Géotechnique*, Vol. 43, No. 3, pp. 351-415.
- Ishihara, K., Tatsuoka, F., and Yasuda, S. (1975), Undrained deformation and liquefaction of sand under cyclic stresses, *Soils and Foundation*, Vol. 15. No. 1, pp. 29-44.
- Iwan, W.D. (1967), On a class of models for the yielding behaviour of continuous and composite systems, *Journal of Applied Mechanics*, Vol. 34, pp. 612-617.
- Jardine, S.I., Johnson A.B., and Stibbs, W. (1993), Hard or soft shut-in: which is the best approach?, SPE 25712.
- Jefferies, M.G. (1993), Nor-Sand: a simple critical state model for sand, *Géotechnique*, Vol. 43, No. 1, pp. 91-103.
- Jefferies, M., and Been, K. (2000), Implications for critical state theory from isotropic compression of sand, *Geotechnique*, Vol. 50, No.4, pp. 419-429.
- Kan, M. E, Taiebat, H.A., and Khalili, N. (2014), Simplified mapping rule for bounding surface simulation of complex loading paths in granular materials, *International journal of Geomechanics*, Vol. 14, No. 2, pp. 239-253.
- Kappos, A. J. (2002), *Dynamic loading and design of structures*, Taylor & Francis Group, USA.

Kavvas, M., and Amorosi, A. (2000), A constitutive model for structured soils, *Géotechnique*, pp. 263 –273.

Khalili, N., Habte, M. A., and Valliappan S. (2005), A bounding surface plasticity model for cyclic loading of granular soils, *International Journal For Numerical Methods In Engineering*, Vol. 63, pp. 1939–1960.

Khalili, N., Habte, M. A., and Valliappan S. (2006), Monotonic and cyclic analysis of granular soils, *Computational Methods in Engineering and Science, China*, pp. 59-70.

Khalili, N., and Liu, M.D. (2008), A bounding surface plasticity model for soils with stress increment direction dependent plastic potential, 12th international conference of international association for computer methods and advances in geomechanics, Goa, India.

Khong, CD. (2004), Development and numerical evaluation of unified critical state models, PhD thesis, The University of Nottingham, Nottingham, U.K.

Krieg, R.D. (1975), A practical two-surface plasticity theory, *Journal of Applied Mechanics*, Vol. 42, No. 3, pp. 641-646.

Lee, K.H., Chan, D.H., and Lam, K.C. (2004), Constitutive model for cement treated clay in a critical state framework, *Soils and Foundations*, Vol. 44, No. 3, pp. 69-77.

Leeson, J., and Campbell, D. (1983), The variation of soil critical state parameters with water-content and its relevance to the compaction of two agricultural soils, *Journal of Soil Science*, Vol. 34, No. 1, pp. 33-44.

Lenart, S. (2008), The response of saturated soils to a dynamic load, *Acta Geotechnica Slovenica*, Vol. 5, No. 1, pp. 37-49.

Li, X.S. (2005), Calibration of an anisotropic sand model, In *Proceedings from GeoFrontiers: Calibration of Constitutive Models*, ASCE, Austin, pp. 1-12.

Li, X.S., and Dafalias, Y.F. (2002), Constitutive modeling of inherently anisotropic sand behaviour, *Journal of Geotechnical and GeoEnvironmental Engineering*, Vol. 128, No. 10, pp. 868-880.

Li, X.S., Ming, H.Y.(2000), Unified modeling of flow liquefaction and cyclic mobility, *Soil Dynamics and Earthquake Engineering*, Vol. 19, pp. 363-369.

Ling, H.I., and Yang, Y. (2006), Unified sand model based on the critical state and generalized plasticity, *Journal of Engineering Mechanics*, Vol. 132, No. 12, pp. 1380-1391.

Liu, Y., Wan, R.G., and Jian, Z. (2008), Effects of foamy oil and geomechanics on cold production, *Journal of Canadian Petroleum Technology*, Vol. 47, No. 4, pp. 1-7.

- Manzari, M.T., and Dafalias, Y. F. (1997), A critical state two-surface plasticity model for sands, *Géotechnique*, Vol. 47, No. 2, pp. 255-272.
- Marri, A. (2010), The mechanical behaviour of cemented granular materials at high pressures, Ph.D. thesis, The University of Nottingham, Nottingham, U.K.
- Martinez, B. N. (2003), Strength properties of granular materials, M.Sc. thesis, Louisiana State University, Louisiana, USA.
- Martinez, J.M. (2014), Elastic properties of sedimentary rocks, Ph.D. thesis, The university of Alberta, Edmonton, Canada.
- Mathis, S.P. (2003), Sand management: A review of approaches and concerns, SPE 82240, pp. 1-7.
- McDowell G.R., and Hau K.W. (2004), A generalised Modified Cam Clay model for clay and sand incorporating kinematic hardening and bounding surface plasticity, *Granular Matter*, Vol. 6, No. 1, pp. 11-16.
- Mielke, A., and Roubicek, T. (2003). A rate-independent model for inelastic behavior of shape-memory alloys, *Multiscale Modeling and Simulation*, Vol. 1, No. 4, pp. 571-597.
- Michelis, P. (1987), True triaxial cyclic behavior of concrete and rock in compression, *International Journal of Plasticity*, Vol. 3, pp. 249-270.
- Minassian, G.H. (2003), Behavior of granular materials under cyclic and repeated loading, Ph.D. thesis, University of Alaska Fairbanks, Alaska, USA.
- Mitchell, J. K., and Soga, K. (2005), *Fundamentals of soil behavior*, Third edition, John Wiley & Sons, USA.
- Mohsin, A.K.M. (2008), Automated Gmax measurement to explore degradation of artificially cemented carbonate sand, Ph.D. thesis, The University of Sydney, Sydney, Australia.
- Morita, N., Davis, E., and Whitebay, L. (1998), Guidelines for solving sand problems in water injection wells, SPE 39436, pp. 189-200.
- Morita, N., and Fuh, G.F. (1998), Prediction of sand problems of a horizontal well from sand production histories of perforated cased wells, SPE 48975, pp. 113-119.
- Mroz, Z., (1967), On the description of anisotropic hardening, *Journal of the Mechanics and Physics of Solids*, Vol. 15, pp. 163-175.
- Mroz, Z., Norris, V. A. and Zienkiewicz, O.C. (1978), An anisotropic hardening model for soils and its application to cyclic loading, *International Journal for Numerical and Analytical methods in Geomechanics*, Vol. 2 ,pp. 203-221.

- Mroz, Z., Norris, V. A. and Zienkiewicz, O.C. (1979), Application of an anisotropic hardening model in the-analysis of elasto-plastic deformation of soils, *Géotechnique*, Vol. 29, No. 1, pp. 1-34.
- Nasr, M.S., and Edbieb, S.M. (2012), Effect of sand production on the productivity of oil wells in unconsolidated sandstone reservoirs in Sirte basin Libya (field case study), 19th Annual India Oil & Gas Review Summit & International Exhibition, Mumbai.
- Navarro, V., Alonso, J., Calvo, B., and Sanchez, J. (2010), A constitutive model for porous rock including effects of bond strength degradation and partial saturation, *International Journal of Rock Mechanics & Mining Sciences*, Vol. 47, No. 8, pp. 1330–1338.
- Nawrocki, P.A. (2010), Critical wellbore pressures using different rock failure criteria, ISRM International Symposium and 6th Asian Rock Mechanics Symposium, New Delhi, India.
- Nouri, A., Kuru, E. and Vaziri, H. (2009), Elastoplastic modeling of sand production using fracture energy regularization method, *Journal of Canadian Petroleum Technology*, Vol. 48, No. 4, pp. 64-71.
- Nouri, A., Vaziri, H., Belhaj, H., and Islam, R.(2003), A comprehensive approach to modeling sanding during oil production, *SPE 81032*, pp. 1-7.
- Nouri, A., Vaziri, H., Kuru, E., and Islam, R. (2006), A comparison of two sanding criteria in physical and numerical modeling of sand production, *Journal of Petroleum Science and Engineering*, Vol. 50, pp. 55-70.
- Nova, R. (2005), A simple elastoplastic model for soils and soft rocks, In *Soil Constitutive Models: Evaluation, Selection, and Calibration*, ASCE pp. 380-399.
- Nova, R. (2006), Modelling of bonded soils with unstable structure, *Springer Proceedings in Physics, Modern Trends in Geomechanics*, Vol. 106, pp. 129-141.
- Nova, R., Castellanza, R., and Tamagnini, C. (2003), A constitutive model for bonded geomaterials subject to mechanical and/or chemical degradation, *International Journal for Numerical and Analytical Methods in Geomechanics*, Vol. 27, No. 9, pp. 705–732.
- Oda, M. and Nakayama, H. (1989), Yield function for soil with anisotropic fabric, *Journal of Engineering Mechanics*, Vol. 115, No. 1, pp. 89-104.
- Oluyemi, G.F., and Oyemeyin, M. B. (2010), Analytical critical drawdown (CDD) failure model for real time sanding potential prediction based on Hoek and Brown failure criterion, *Journal of Petroleum and Gas Engineering*, Vol. 1, No. 2, pp. 16-27.
- Orense, R., and Pender M. (2012), Liquefaction characteristics of pumice sands, EQC project 10/589, The University of Auckland, Auckland, New Zealand.

- Ostadhassan, M., Zeng, Z., Jabbari, H. (2011), Using advanced acoustic data to determine stress state around wellbore, ARMA, pp. 1-7.
- Pastor, M., Zienkiewicz, O.C., and Chan A.H.C. (1990), Generalized Plasticity and the Modelling of Soil Behaviour, International journal for numerical and analytical methods in geomechanics, Vol. 14, pp. 151-190.
- Pastor, M., Zienkiewicz, O.C., and Leung, K.K. (1985), Simple model for transient soil loading in models for sands earthquake analysis. II. Non-associated models for sands, International Journal for Numerical and Analytical Methods in Geomechanics, Vol. 9, pp. 477-498.
- Pradhan, T. B. S. (1989), The behavior of sand subjected to monotonic and cyclic loadings, PhD thesis, Kyoto University.
- Pradhan, T.B.S., Tatsuoka, F., and Sato, Y. (1989), Experimental stress-dilatancy relations of sand subjected to cyclic loading, Soild and Foundations, Vol. 29, pp. 45-64.
- Querol, S.L., and Blázquez, R. (2006), Liquefaction and cyclic mobility model for saturated granular media, International Journal for Numerical and Analytical Methods in Geomechanics, Vol.30, pp. 413-439.
- Rahim, Amir (2002), Simple cyclic loading model based on Modified Cam Clay, CRISP company.
- Rahmati, H., Jafarpour, M., Azadbakht, S., Nouri, A., Vaziri, H., Chan, D., and Xiao, Y. (2013), Review of sand production prediction models, Journal of Petroleum Engineering, Review Article, pp. 1-16.
- Ranjan, G., and Rao A.S. (2005), Basic and applied soil mechanics, New age international publisher, India.
- Rascal, E. (2009), Cyclic Properties of Sand: Dynamic behaviour for seismic applications, Ph.D. thesis, University of EPFL, Lausanne, Switzerland.
- Rasouli, R. (2010), Modelling of anisotropic behaviour of sands, M.Sc. thesis, Amir Kabir University of technology, Tehran, Iran.
- Reilly, M.P.O, and Brown, S.F. (1991), Cyclic loading of soils: from theory to design, Blackie and son limited, U.K.
- Roscoe, K. H., Schofield, A. N., and Wroth, C. P. (1958), On the yielding of soils, Getechnique, Vol. 8, No. 1, pp. 22-52.
- Roshan, H. (2011), Three dimensional non-linear anisotropic thermo-chemo-poro-elastoplastic modeling of borehole stability in chemically active rocks, Ph.D. thesis, University of New South Wales, Sydney, Australia.

- Rowe, P.W. (1962), The stress-dilatancy relation for static equilibrium of an assembly of particles in contact, *Proceedings of Royal Society, London*, Vol. 269, pp. 500-527.
- Russel, A., and Khalili N. (2004), A bounding surface plasticity model for sands exhibiting particle crushing, *Canadian Geotechnical Journal*, Vol. 41, No. 6, pp. 1179-1192.
- Saada, A.S., Liang, L., Figueroa, L., and Cope, C.T. (1999), Bifurcation and shear band propagation in sands, *Geotechnique*, Vol. 49, No. 3, pp. 367-385.
- Sadrpanah, H., Allam, R., Acock, A., Norris, M., O'Rourke, T., Murray, L.R., and Wood, D.J. (2005), Designing effective sand control systems to overcome problems in water injection wells, *SPE 93564*, pp. 1-11.
- Santarelli, F.J., Sanfilippo, F., Embry, J.M., and Turnbull, J. (2011), The sanding mechanisms of water injectors and their quantification in terms of sand production: example of the Buzzard field (UKCS), *SPE 146551*, PP. 1-13.
- Santarelli, F.J., Skomedal, E. Markestad, P., Berge, H.I., Nasvig, H. (1998), Sand production on water injectors: just how bad can It get?, *SPE/ISRM 47329*, pp. 107-115.
- Servant, G., Marchina, P., and Nauroy, J.F. (2007), Near-wellbore: sand production issues, *SPE 109894*.
- Schnaid, F., Prietto, P.D.M., and Consoli, N.C. (2001), Characterization of cemented sand in triaxial compression, *Journal of Geotechnical and Geoenvironmental Engineering*, Vol. 127, No. 10, pp. 857-868.
- Schofield, A. (1993), *Original Cam-Clay*, International Conference on Soft Soil Engineering, Guangzhou, China.
- Schofield, A., and Wroth, P. (1968), *Critical state soil mechanics*, McGraw-Hill, U.K.
- Silva, C. W. (2005), *Vibration and shock handbook*, Taylor & Francis Group, USA.
- Skjaerstein A., Tronvoll, J., Santarelli, F.J., and Joranson, H. (1997), Effect of water breakthrough on sand production: experimental and field evidence, *SPE 38806*.
- Stallebrass, S. E. (1990), Modeling the effect of recent stress history on the deformation of overconsolidated soils, Ph.D. thesis, The City University, London, U.K.
- Stavropoulou, M., Papanastasiou, P., and Vardoulakis (1998), Coupled wellbore erosion and stability analysis, *International Journal for numerical and analytical Methods in Geomechanics*, Vol. 22, No. 9, pp. 749-769.

Suebsuk, J., Horpibulsuk, S., and Liu, M.D. (2010), Modified structured cam clay: a generalised critical state model for destructured, naturally structured and artificially structured clays, *Computers and Geotechnics*, Vol. 37, No. 7-8, pp. 956, 968.

Suebsuk, J., Horpibulsuk, S., and Liu, M.D. (2011), A critical state model for overconsolidated structured clays, *Computers and Geotechnics*, Vol. 38, No. 5, pp. 648-658.

Sulem, J., and Ouffroukh, H. (2005), Shear banding in drained and undrained triaxial tests on a saturated sandstone: porosity and permeability evolution, *International Journal of Rock Mechanics & Mining Science*, Vol. 43, pp. 292-310.

Sulem, J., Vardoulakis, I., Papamichos, E., Oulahna, A. and Tronvoll, J. (1999), Elasto-plastic modelling of red wildmoor sandstone, *Journal of Mechanics of Cohesive-Frictional Materials*, Vol. 4, No. 3, pp. 215–245.

Syed, A., Bertran, A., Donald, A., Sinha, B., Bose, S. (2011), Continuous statistical indicator of stress-induced dipole flexural wave anisotropy, 52th annual logging symposium, Colorado, USA.

Tatsuoka, F., and Ishihara, K. (1974), Drained deformation of sand under cyclic stresses reversing direction, *Soils and Foundations*, Vol. 14, No. 3, pp. 51-65.

Towhata, I. (2008), *Geotechnical Earthquake Engineering*, Springer, Germany.

Tronvoll, J., Morita, N., and Santarelli, F.J. (1992), Perforation Cavity Stability: comprehensive laboratory experiments and numerical analysis, SPE 24799, PP. 339-349.

Vardoulakis, I., and Papamichos, E. (2003), A continuum theory for erosion in granular media, *Rivista Italiana Di Geotecnica*.

Vardoulakis, I., Stavropoulou, M., and Papanastasiou, P. (1996), Hydro-mechanical aspects of the sand production problem, transport in porous media, Vol. 22, pp. 225-244.

Vatsala, A., Nova, R., and Murthy, B.R.S. (2001), Elastoplastic model for cemented soils, *Journal of Geotechnical and Geoenvironmental Engineering*, Vol. 127, No. 8, pp. 679-687.

Vaziri, H., Nouri, A., Hovem, K., and Wang, X. (2007), Computation of sand production in water injectors, SPE 107695, pp. 1-9.

Veeken, C.A.M., Davies, D.R., Kenter, C.J., and Kooijman, A.P. (1991), Sand production prediction review: developing an integrated approach, SPE 22792.

Venkatramaiah, C. (2006), *Geotechnical engineering*, New age international publishers, India.

- Vermeer, P.A., and de Borst, R. (1984), Non-associated plasticity for soils, concrete and rocks, *Heron*, Vol. 29, No. 3, pp. 1-64.
- Wan, R.G., and Guo, P.J. (2001a), Drained cyclic behavior of sand with fabric dependence, *Journal of Engineering Mechanics*, Vol. 127, No. 11, pp. 1106-1116.
- Wan, R.G., and Guo, P.J. (2001b), Effect of microstructure on undrained behaviour of sands, *Canadian Geotechnical Journal*, Vol. 38, No. 1, pp. 16-28.
- Wan, R.G., and Guo, P.J. (2004), Stress dilatancy and fabric dependencies on sand behavior, *Journal of Engineering Mechanics*, Vol. 130, No. 6, pp. 635-645.
- Wang., Y., and Leung, S.C. (2008), Characterization of cemented sand by experimental and numerical investigations, *Journal of Geotechnical & Geoenvironmental Engineering*, Vol. 134, No. 7, pp. 992-1004.
- Wang, Y., and Lu, B. (2001), A Coupled reservoir-geomechanics model and applications to wellbore stability and sand prediction, *SPE 69718*, pp. 1-14.
- Wang, J., Yale, D., and Dasari, G. (2011), Numerical modeling of massive sand production, *SPE 147110*, pp. 1-14.
- Wood, D.M. (1990), *Soil behavior and critical state soil mechanics*, The Cambridge University Press, USA.
- Wu, B., Tan, C.P., and Lu, N. (2005), Effect of water cut on sand production-an experimental study, *SPE 92715*.
- Yang. C., Huang, M.S., and Cui, Y.J. (2011), Constitutive model of unsaturated structured soils under cyclic loading, Taylor & Francis group, pp. 987-992.
- Yoshimine, M., Ishihara, K., and Vargas, W. (1998), Effects of principal stress direction and intermediate principal stress on undrained shear behaviour of sand, *Soils and Foundations*, Vol. 38, No. 3, pp. 179–188.
- Yoshinaka, R., Tran, T.V., and Osada M. (1998), Non-linear, stress and strain dependent behaviour of soft rocks under cyclic triaxial conditions, *International Journal of Rock Mechanics and Mining Sciences*, Vol. 35, No. 7, pp. 941-955.
- Younessi, A. and Rasouli, V. (2012), Numerical simulations of sanding under different stress regimes, *ARMA 12-373*.
- Yu, H.S. (1998), CASM: A unified state parameter model for clay and sand, *International Journal of Numerical and Analytical Methods in Geomechanics*, Vol. 22, pp. 621-653.
- Yu, H.S. (2006), *Plasticity and geotechnics*, Springer, USA.
- Yu, H.S., Khong, C., and Wang J. (2007), A unified plasticity model for cyclic behaviour of clay and sand, *Mechanics Research Communications*, Vol. 34, No. 2, pp. 97-114.

Yu, H.S., Tan, S.M., and Schnaid, F. (2007), A critical state framework for modeling bonded geomaterials, *Geomechanics and Geoengineering*, Vol. 2, No. 1, pp. 61-74

Ziegler, H. (1959), A modification of Prager's hardening rule, *Quarterly of Applied Mathematics*, Vol 17, pp. 55-65.

Zienkiewicz, O.C., Leung, K.K., and Pastor, M. (1985), Simple model for transient soil loading in earthquake analysis. I. basic model and its application, *International Journal for Numerical and Analytical Methods in Geomechanics*, Vol. 9, pp. 453-476.

Zoback, M.D. (2007), *Reservoir geomechanics*, Cambridge University Press, USA.